

**SYNTHESIS OF MOLECULAR IMPRINTED POLYMERS BY [6]-  
GINGEROL EMBEDDED QUANTUM DOTS AND THEIR  
APPLICATIONS IN ENVIRONMENTAL ASPECTS**

Thesis Submitted for the Award of the Degree of

**DOCTOR OF PHILOSOPHY**

**IN**

**Chemistry**

**By**

**Azad Qayoom Malik**

**Registration Number:11916641**

**Supervised by**

**Dr Deepak Kumar**

**Department of Chemistry (Assistant Professor)**

**Lovely Professional University**

**Co-Supervised by**

**Dr Ajit Kumar Sharma**

**Department of Chemistry (Associate Professor)**

**Lovely Professional University**



**Lovely Professional University, Punjab**

**2022**

## DECLARATION

I, hereby declared that the presented work in the thesis entitled “SYNTHESIS OF MOLECULAR IMPRINTED POLYMERS BY [6]-GINGEROL EMBEDDED QUANTUM DOTS AND THEIR APPLICATIONS IN ENVIRONMENTAL ASPECTS” in fulfilment of degree of **Doctor of Philosophy (Ph. D.)** is outcome of research work carried out by me under the supervision of Dr Deepak Kumar, working as Assistant Professor, in the Department of Chemistry, School of Chemical Engineering and Physical Sciences, Lovely Professional University, Punjab, India. In keeping with general practice of reporting scientific observations, due acknowledgements have been made whenever work described here has been based on findings of another investigator. This work has not been submitted in part or full to any other university or Institute for the award of any degree.



Name of the scholar: Azad Qayoom Malik

Registration No.:11916641

Department of Chemistry, School of Chemical engineering and Physical Sciences,  
Lovely Professional University,  
Punjab, India

## CERTIFICATE

This is to certify that the work reported in the Ph. D. thesis entitled “SYNTHESIS OF MOLECULAR IMPRINTED POLYMERS BY [6]-GINGEROL EMBEDDED QUANTUM DOTS AND THEIR APPLICATIONS IN ENVIRONMENTAL ASPECTS” submitted in fulfillment of the requirement for the reward of degree of **Doctor of Philosophy (Ph.D.)** in the Department of Chemistry, School of Chemical Engineering and Physical Sciences of Lovely Professional University, is a research work carried out by Azad Qayoom Malik, 11916641, is bonafide record of his original work carried out under my supervision and that no part of thesis has been submitted for any other degree, diploma or equivalent course.



**(Signature of Supervisor)**

Name of supervisor: Dr Deepak Kumar

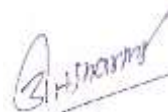
Designation: Assistant Professor

Department;

School of Chemical Engineering

and Physical Science

University: Lovely Professional University



**(Signature of Co-Supervisor)**

Name of Co-Supervisor: Dr Ajit Kumar Sharma

Designation: Associate Professor

Department; School of Chemical Engineering

and Physical Science

University: Lovely Professional University

## Abstract

In this chapter Molecular Imprinting Polymers were synthesized using [6]-gingerol as a template, 2 hydroxy-methacrylate as monomer and ethyl glycol dimethacrylate as crosslinker. The obtained polymers were doped with hybrid Mn-ZnS nanocomposite. [6]-gingerol was isolated from a natural herb using a Soxhlet and characterized in its purity and structure. Synthesized polymers and their precursors were also characterized in structure, morphology and thermal stability. The obtained Imprinting Polymer was ultimately used as a UV-dependent photocatalyst in the photodegradation of relevant pharmaceuticals that are utilized elsewhere and are a common concern in wastewater treatment facilities. The determined removal of Norfloxacin (NOFX) was 84% and for Paracetamol, a maximum degradation of 80% was achieved.

In this chapter MIPs were synthesized using Cadmium sulphide QDs mobilised in the matrix of Molecular imprinted polymer. The MIPs was developed using [6]-gingerol as template molecule and the reaction was proceeded through Exsitu polymerisation method to prepare MIPs composite. The physicochemical properties of the hybrid polymer nano catalyst were investigated using a variety of spectroscopic and microscopic techniques. FTIR, NMR, XRD, FESEM, are few of the analysis techniques which were employed for the characterization of synthesized sample. Thermogravimetric and differential scanning calorimeter were used to study thermal properties of the composite. Electrochemical study was also performed by using cyclic voltammetry and impedance spectroscopy. The compound was employed to investigate the photocatalytic of imidacloprid and Buprofezin under visible light source.

In this Chapter, Molecular imprinted polymers (MIPs) were developed by carrying out cocktail solution of Template ([6]-gingerol), monomer, crosslinker and Ag<sub>2</sub>S Quantum Dots (QDs) dissolved in an appropriate solvent resulting in an efficient crosslinked polymer composite. The synthesis was performed in an inert atmosphere and QDs was incorporated through Exsitu polymerization method. The Structure and Morphology of nanocomposite were well characterized by Using X-Ray diffraction (XRD), Transmission Electron Microscopy(TEM) Thermogravimetric analysis, Fluorescence spectroscopy,

Zeta potential analyzer and Scanning Electron Microscopy (SEM) equipped with Energy dispersive spectroscopy analysis. The MIPs composite prepared was employed for the first time as a photocatalyst for the degradation of Alizarin Red S (ARS) dye and yellowish sunset (SY) azo dye under visible light irradiation. Impact of affecting parameters on Ag<sub>2</sub>S-MIPs composite have been studied and analyzed. The result shows efficient photocatalyst activity of Ag<sub>2</sub>S-MIPs composite for the degradation of AR and SY dye with degradation% (80%) and (84%) in an aqueous wastewater.

In this chapter The CuS/ZnO nanocomposite was prepared by using a simple mechanical method. CuS/ZnO nanocomposite synthesized were analysed with XRD and SEM. The average particle size of CuS/ZnO was found to be 30-35nm. The electrochemical study of nanocomposite was done by using electrochemical impedance and Cyclic voltammetry analysis. CuS nanoparticles mechanically combined with ZnO nanoparticles served as an electron absorber in the nanocomposite, assisting in the enhancement of ZnO photocatalysis. CuS served as an electron collector in the nanocomposite, which aided in the enhancement of ZnO photocatalysis. Experiment performed under visible light source also showed that CuS could aid ZnO in the degradation of Congo red and Phenol. From the UV analysis it was found that CuS/ZnO nanocomposite exhibited better photochemical stability. All of these results suggested that prepared sample could be useful in practical applications.

In this chapter Cadmium Sulfide (CdS) Quantum dots (QDs) has been prepared by using simple co-precipitation method. Structural and morphological characteristics of CdS QDs were measured by XRD, FT-IR, and FESEM techniques. The thermal studies of nanomaterial were also analysed by thermogravimetric and differential scanning calorimetry. Tauc plot was used to calculate band gap energy of nanomaterial. The synthesized material was employed as a photocatalyst for the photodegradation of 2-chlorophenol (2-CP) under UV light source. The impact of pH for photodegradation of the catalyst has also been investigated and shows higher efficiency at high pH. The photodegradation efficiency was found to be 80% with increasing amount of catalyst. Antimicrobial activities against E. coli and Aeromonas hydrophilia

were also performed by this CdS QDs. This work demonstrates the potential applications of CdS for photodegradation and antimicrobial activity.

In this chapter an affordable solid state reaction technique was used to make pristine and Ni doped ZnS nanoparticles. FTIR, UV–Vis, XRD and SEM were used to characterise the products' functional, Structural and morphological properties. The polycrystalline nature of the nanoparticles with cubic crystal structure was confirmed by X-ray diffraction. FTIR spectroscopy was used to analyse the functional group linked with a molecule's vibration. The photocatalytic efficiency results showed that doping of Ni has increased the ZnS photocatalytic activity. As a result, Ni-ZnS could be employed as a photocatalyst to degrade the environmental contaminant Methyl red dye. Among nanocomposites, ZnS have the highest photoactivity. To optimise the photodegradation process of dyes, the influence of sample pH and ZnS dosage were changed. With a concentration of 50 mg/l, Efficient degradation was obtained for Methyl red. In samples with a pH of 6-10, the ZnS indicates the stability.

In this chapter a simple precipitation method was used to develop a Zn Doped CuS-Graphene Oxide nano composite. The prepared compound was annealed at high temperature and synthesis and characterized by using X-ray powder diffraction (XRD) and Scanning electron microscopy (FESEM). To determine major functional groups of nanocomposites “Fourier, transform infrared spectroscopy” (FTIR) was used. The crystalline and average size of nanocomposite was systematically characterized by X-ray powder diffraction (XRD) and Scanning electron microscopy (FESEM) and the particle size of Zn.CuS Quantum Dots (QDs) was found to be 7-10nm and the average particle size of Zn.CuS/GO was determined to be 183-185nm. The thermal stability of composite was studied by using thermogravimetric analysis confirming effective interaction between GO and Zn.CuS nanocomposite. The electrophoretic stability of nanocomposite was analysed by using zeta potential and was found to be -15.2mV and size of agglomerated compound to be 185nm. The electrochemical analysis was also done using Cyclic voltammetry and

impedance spectroscopy and results obtained confirms supercapactive nature of our sample. Zn.CuS/GO nanocomposite demonstrated excellent photocatalytic degradation% (82%) of rhodamine B, as well as high antifungal activity. The Zn.CuS-GO has a high potential for water treatment applications due to its simple and low-energy synthesis process, as well as its excellent degradation and antifungal performance.

## Acknowledgements

First, I bow in reverence to Almighty \God" the cherisher and sustainer to benediction give me the required zeal for completion of my research work. The successful completion of any research work is a matter of great endeavourance but, because of the personal and practical support of numerous people makes the job entirely enjoyable and simple. It is a pleasant aspect that I have now the opportunity to express my gratitude for them.

First and foremost, I would like to express my deep sense of gratitude and everlasting indebtedness to my supervisor Dr. Deepak Kumar, Assistant Professor, Department of Chemistry, School of Chemical Engineering and Physical Sciences, Lovely Professional University, Phagwara-Punjab, for his patience, continuous encouragement, and guidance throughout my research work. Without his guidance it would not have been possible for me to complete the work. I could not wish a better friendly supervisor.

I feel privileged to my sincere regards and gratitude to Dr. Ajit Kumar Sharma, for his valuable guidance and constant encouragement throughout the course of my research work. I am also thankful to all the faculty members of the university for their generous support, encouragement, and valuable suggestions to improve the present work.

I am greatly indebted my father Ab Qayoom Malik and my mother Smt.

Nusrat Begum for their invaluable support and blessings. I must record my sincere thanks to my esteemed siblings Mr. Kaiser Qayoom Malik and Mr. Babar Qayoom for their steady encouragement, timely support, unconditional love and moral support, without whom I would never have enjoyed so many opportunities.

I particularly thank my colleagues those sleepless nights, we were working together before deadlines and for all the fun we have during this research work. Without their precious support, it would not have been possible to conduct this research.

I would like to express my gratitude towards their moral and emotional support that helped me in completion of this thesis and inspired me to work tirelessly to accomplish this task. I also express my gratitude to all who knowingly and unknowingly contributed in completion of this thesis.



## List of Contents

<b>Declaration of Authorship</b>	i
<b>Certificate</b>	ii
<b>Abstract</b>	iii
<b>Acknowledgements</b>	vi

### List of Tables

<b>(Chaper 1)Table 1.</b>	Advantages and disadvantages of Polymerization methods used for Synthesis.
<b>(Chapter 2)Table 1.</b>	List of solvents based on their on their solubility
<b>(Chapter 2) Table 2.</b>	Functional groups present in the [6]-gingerol
<b>(Chapter 5)Table 1.</b>	Photocatalytic activity of Different catalyst against Congo red and phenol in aqueous solution
<b>(Chapter 8) Table 1.</b>	Minimum Inhibitory Concentration (MIC) and Minimum fungicidal concentration (MFC) of Doped Zn.CuS/GO and GO.

## List of Figures

<b>Chapter 1</b>	
Figure 1	Volatile components of gingerol
Figure 2	Non-volatile components of ginger
Figure 3	Scheme of Molecular imprinting polymers
Figure 4	Different polymerization techniques in MIPs synthesis
Figure 5	Schematic representation of Mechanism of precipitation polymerization
Figure 6	Chemical structure of Taxol (paclitaxel), functional monomer and crosslinker
Figure 7	molecule and the imprinting cavity on the poly(MAP/MMA/EGDMA) microbeads
Figure 8	Schematic illustration of the IMD molecular imprinting procedure
Figure 9	Mechanism of Quercetin imprinted polymer synthetic
Figure 10	Schematic representation of camptothecin
Figure 11	Mechanism of 2,4,6, T.C.P MIP synthesis
Figure 12	Pictorial representation of Fluorescent Quantum Dots
<b>Chapter 2</b>	
Figure 1	DFT optimized (uB3LYP/6-311G) chemical Structure of [6]-gingerol based Molecular
Figure 2	Process flow chart for the extraction of [6]-gingerol
Figure 3	HPLC chromatogram of [6]-gingerol from ginger extract
Figure 4	FTIR spectra of [6]-gingerol
Figure 5	<sup>1</sup> HNMR (400MHz, DMSO-d <sup>6</sup> ) spectrum of [6]-gingerol
Figure 6	<sup>13</sup> CNMR (100MHz, DMSO-d <sup>6</sup> ) spectra of [6]-gingerol.
Figure 7	Negative ion electrospray product ion mass spectrum of [6]-gingerol
Figure 8	FTIR images of [6]-gingerol and [6]-gingerol MIP
Figure 9	XRD of Mn doped ZnS and MIPs coated Mn doped ZnS.
Figure 10	SEM images of Mn-doped ZnS at different magnifications ( <b>10<math>\mu</math>m, 1 <math>\mu</math>M</b> ) FESEM images of MIPs coated Mn doped ZnS of different resolution ( <b>10<math>\mu</math>m, 1<math>\mu</math>m</b> ).
Figure 11	TGA-DSC plot of MIPs/QDS with 10°C heating rate under nitrogen atmosphere
Figure 12	Selected geometrical Mn doping and MIP deposition effect over Mullikan charge in ZnS
Figure 13	Density of States analysis showing the semiconductor band system in ZnS and ZnS derivates.
Figure 14	Starting geometry for ZnS matrix
Figure 15	Frontier molecular orbitals and photocatalytic potential for optimized ZnS material

Figure 16	Uv spectra of Mn doped ZnS and Mn.ZnS/MIPs nanocomposite.
Figure 17	Photodegradation of NOFX by Mn-doped ZnS at different catalyst doses
Figure 18	Degradation efficiency of Mn.ZnS/MIPs against NOFX and paracetamol
Figure 19	Zeta potential of MIPs/ZnS at pH 11 alkaline solution
<b>Chapter 3</b>	
Figure 1	FT-IR spectrum of CdS QDs
Figure 2	XRD diffraction pattern of CdS, MIPs@CdS and NIPs@CdS composite.
Figure 3	(A-D) SEM images of Pure CdS (B) MIPs/CdS(E) and NIPs/CdS(F) composite
Figure 4	Fluorescence spectra of CdS MIPs
Figure 5	DSC- TGA of CdS MIPs CdS nanocomposite.
Figure 6	Electrochemical study of CdS QDs and CdS/MIPs composite.
Figure 7	Photocatalytic degradation of Imidacloprid and Buprofezin insecticide by CdS/MIPs composite at different catalyst doses, pH values, temperature variation and pollutant concentration.
Figure 8	Photocatalytic removal efficiency of Imidacloprid and Buprofezin insecticide by CdS/NIPs composite at different catalyst doses, pH values, pollutant concentration and temperature variation.
Figure 9	Optical band gap energy of MIP/CdS nanocomposite.
Figure 10	DFT energy optimization of CdS-MIPs.
Figure 11	a) DOS spectrum of CdS and CDs-MIPs catalysts; b) Total energy determination for composite CdS-MIPs.
Figure 12	Band gap energy of CdS QDs and CdS MIPs composite.
Figure 13	Schematic representation of photodegradation mechanism of CdS
<b>Chapter 4</b>	
Figure 1	Schematic representation of Ag <sub>2</sub> S-MIPs
Figure 2	XRD and EDX of Ag <sub>2</sub> S (B)XRD of Ag <sub>2</sub> S-MIPS composite
Figure 3	TEM images Ag <sub>2</sub> S Quantum Dots
Figure 4	FESEM images of (A, B) Ag <sub>2</sub> S-MIPs and (C, D) Ag <sub>2</sub> S-NIPs composite

Figure 5	FTIR Spectra of Ag <sub>2</sub> S QDs and AgS-MIPs composite
Figure 6	Fluorescence spectra and Zeta potential analysis of Ag <sub>2</sub> S-MIPs composite (a,b,d and Zeta potential of Ag <sub>2</sub> S QDs(c).
Figure 7	TGA-DSC analysis of AgS-MIPs composite
Figure 8	(A) Degradation % of Alizarin red and Sunset at different time and (B) $\ln C_0/C_t$ versus irradiation time
Figure 9	Photodegradation of alizarin red and yellowish sunset yellow by Ag <sub>2</sub> S-MIPs composite under different parameters.
Figure 10	Photodegradation of alizarin red and yellowish sunset yellow by Ag <sub>2</sub> S-NIPs composite under different parameters.
<b>Chapter 5</b>	
<b>Figure 1.</b>	FTIR spectrum of IR spectra of CuS, ZnO and ZnO/CuS nanocomposites
<b>Figure 2.</b>	XRD pattern of CuS, ZnO and ZnO/CuS composite
	<b>Figure 3.</b> FESEM images of synthesized crystalline forms of ZnO and CuS QDs
<b>Figure 4.</b>	SEM images of prepared CuS/ZnO Nanocomposite
<b>Figure 5.</b>	Electrochemical impedance spectroscopy and Cyclic Voltammetry of CuS-ZnO nanocomposite
<b>Figure 6.</b>	CuS/ZnO as an efficient photocatalyst for Congo Red and phenol degradation(b) Effect of pH on photodegradation of Congo Red and phenol under Visible light influence.
<b>Figure 7.</b>	kinetics curves of degradation of Congo red under visible light
<b>Figure 8.</b>	UV-Vis results demonstrating reaction rate kinetics of phenol under the influence of Visible light
<b>Figure 9</b>	photocatalytic degradation mechanism of ZnO/CuS.
<b>Chapter 6</b>	
Figure 1	FTIR spectra of Cadmium Sulphide QDs
Figure 2	XRD Spectrum of CdS (B)-SEM images of CdS Quantum Dots at different resolution.
Figure 3	Tauc Plot to obtain band gap energy of CdS QDs
Figure 4	TGA-DSC characterization of CdS QDs
Figure 5	Calibration curve showing a plot of electronic absorbance vs. conc. (ppm). The maximum wavelength was 280 nm (B) Graph

	showing degradation effect of concentration on 2-CP. (C) Effect of concentration of nanoparticles on organic pollutant with respect to time. (D) calibration curve was drawn against the concentration of 2-chlorophenol
Figure 6	Mechanistic Investigation of Photodegradation by CdS
Figure 7	Bactericidal Images of E. coli and Aeromonas hydrophilia
<b>Chapter 7</b>	
Figure 1	XRD and FESEM images of cubic pristine and Ni doped ZnS QDs.
Figure 2	Photodegradation of Methyl Red by Ni doped ZnS.
Figure 3	Effect of ZnS on photodegradation of Methyl Red
<b>Chapter 8</b>	
Figure 1	Schematic representation of synthesis of Zn.CuS/GO
Figure 2	XRD analysis of GO nanosheets, Zn-CuS QDs and Zn-CuS-GO nanocomposite
Figure 3	SEM and EDS analysis of (a, b) GO, (c, d) Zn-CuS and (E,F) Zn-CuS-GO.
Figure 4	FTIR spectrum of GO, Zn/CuS and Zn.CuS/GO nanomaterial
Figure 5	TGA-DSC characterization of ZnCuS-GO nanocomposite
Figure 6	Electrochemical study of Zn.CuS-GO nanocomposite using CV and Impedance spectroscopy
Figure 7	Zeta potential of Zn.CuS/GO composite.
Figure 8	A plot between $(\alpha h\nu)^2$ versus $h\nu$ of Zn.CuS and Zn.CuS/GO nanocomposite for energy gap calculation
Figure 9	Effect of catalyst at different concentrations, at different pH values, varying pollutant concentration and different time period

## List of Appendices

<b>Abbreviations</b>	<b>Expansion</b>
AIBN	2,2'-azo-bis(isobutyronitrile)
ACN	Acetonitrile
DMSO	Dimethyl sulfoxide
EtOH	Ethanol
THF	Tetrahydrofuran
EGDMA	Ethylene glycol dimethacrylate
QDs	Quantum dot
UV-VIS	Ultraviolet-visible spectroscopy
FTIR	Fourier transform infrared
SEM	Scanning Electron Microscopy
MIPs	Molecular imprinting polymers
TGA	Thermogravimetric analysis

# Contents

## CHAPTER I

### 1. Introduction

#### MOLECULAR IMPRINTING POLYMERS: A REVIEW

1. A brief History of Ginger.....	19
1.2. <i>Botanical description of Ginger</i> .....	20
1.3. <i>Ginger varieties and production.</i> .....	20
1.4. <i>Ginger's chemical composition</i> .....	21
1.5. <i>The Volatile components of ginger</i> .....	21
1.7 <i>Extraction and Isolation of phenolic compounds of ginger</i> .....	22
1.8 <i>Medicinal properties of phenolic compounds of ginger</i> .....	23
1.9 MOLECULAR IMPRINTED POLYMERS .....	25
1.10. <i>Molecular imprinting strategy</i> .....	27
1.11. <i>Various approaches of molecular imprinting</i> .....	28
(i) <i>Covalent approach Functional monomers</i> .....	29
(ii) <i>Non-covalent approach Crosslinkers</i> .....	29
1.12. <i>Molecular recognition of imprinted polymers</i> .....	30
1.13. <i>Parameters affecting spatial molecular recognition in imprinted polymers</i> ....	31
I. <i>Templates</i> .....	31
II. <i>Functional monomers</i> .....	32
III. <i>Crosslinkers</i> .....	33
IV <i>Porogenic solvents</i> .....	34
V <i>Initiators</i> .....	35
1.14. <i>Preparation Methods of MIP</i> .....	36
1.14.1. <i>Bulk Polymerization</i> .....	37
1.14. 2. <i>Multi-step Swelling Polymerization</i> .....	38
1.14.3. <i>Suspension Polymerization</i> .....	39
1. 14. 4. <i>Precipitation Polymerization</i> .....	40
1.14.5. <i>Surface Imprinting Polymerization</i> .....	41
1.14.6. <i>Emulsion polymerization</i> .....	42
1.14.7. <i>Monolithic molecular imprinted method</i> .....	43
1.15. <i>Applications of molecular imprinting polymer</i> .....	44
i. <i>Affinity separation</i> .....	45
II. <i>Antibody binding mimics</i> .....	46
III. <i>Enzyme mimic for catalytic/synthetic applications</i> .....	47
iv. <i>Biosensor-like devices</i> .....	49
v. <i>MIPs for extraction prepose</i> .....	51
1.16. <i>Quantum Dots</i> .....	52
1.17. <i>Semiconductors III-V</i> .....	53



<i>i. Group III-V (Boron and Nitrogen Family)</i> .....	54
<i>ii. IV-VI (Lead chalcogenide group)</i> .....	55

## CHAPTER 2

Ginger derived polymer modified with Mn Quantum Dots as photocatalyst in the elimination of pharmaceutical pollutants norfloxacin and paracetamol

2. 1. <i>Introduction</i> .....	68
2.2 <i>Materials and methods</i> .....	70
2.3. <i>Results and Discussion</i> .....	73
2.3.1. <i>Characterization of [6]-gingerol</i> .....	78
2.3.7. <i>Photodegradation of norfloxacin and paracetamol by MIPs encapsulated QDs</i> .....	84
2.4. <i>Conclusions</i> .....	90

## CHAPTER 3

Fluorescent CdS QDs modified with Molecular imprinted polymer for the effective photodegradation of imidacloprid and buprofezin pesticides under Visible light.

3.1. <i>Introduction</i> .....	94
3.2. <i>Experimentation</i> .....	97
3.3. <i>Results and discussion</i> .....	98
3.4. <i>Photocatalytic activity evaluation of Imidacloprid and buprofezin</i> .109	
3.5. <i>Conclusion</i> .....	121

## CHAPTER 4

Photocatalytic activity tuning in a Novel Ag<sub>2</sub>S QDs embedded in Molecular imprinted polymer matrix.....

6.1. <i>Introduction</i> .....	126
6.1.1. <i>Experimentation</i> .....	127
6.1.2 <i>Reagents and chemicals</i> .....	128
6.3 <i>Results and Discussion</i> .....	130
6.4 <i>Photocatalysis activity</i> .....	135
6.5. <i>Conclusion</i> .....	142

## CHAPTER 5

Synthesis, Characterization, Photocatalytic effect of CuS-ZnO nanocomposite on photodegradation of Congo Red and phenol pollutant.....

4. <i>Introduction</i> .....	148
4. 1. <i>Experimental Details</i> .....	149
4. 1. <i>Results and Discussions</i> .....	154
4. 3. <i>Effect of different parameters on photodegradation</i> .....	156
4.5 <i>Conclusion</i> .....	160

## CHAPTER 6

Preparation of Cadmium Sulphide Quantum Dots and their mechanistic investigations towards aqueous 2-Chlorophenol degradation and antimicrobial activity .....	114
5.1. <i>Introduction</i> .....	114
5.2. <i>Characterization</i> .....	115
5.3. <i>Results and Discussions</i> .....	117
5.4. <i>Photodegradation of 2-CP</i> .....	121
5.4.1. <i>Photodegradation of 2-CP in the visible region</i> .....	122
5.6. <i>Antibacterial activity of CdS nanoparticles using disc diffusion process</i> .....	124
5.7 <i>Conclusions</i> .....	125

## CHAPTER 7

Facile synthesis of ZnS and Ni doped ZnS Quantum dots and enhanced photocatalytic property of Ni doped ZnS nanoparticle .....	178
7.1. <i>Introduction</i> .....	178
7.2. <i>Experimental Section</i> .....	180
7.3. <i>Results and discussions</i> .....	181
7.4. <i>Photocatalytic activity</i> .....	184
7.5. <i>Mechanism of Photocatalytic activity</i> .....	186
7.6. <i>Conclusion</i> .....	189

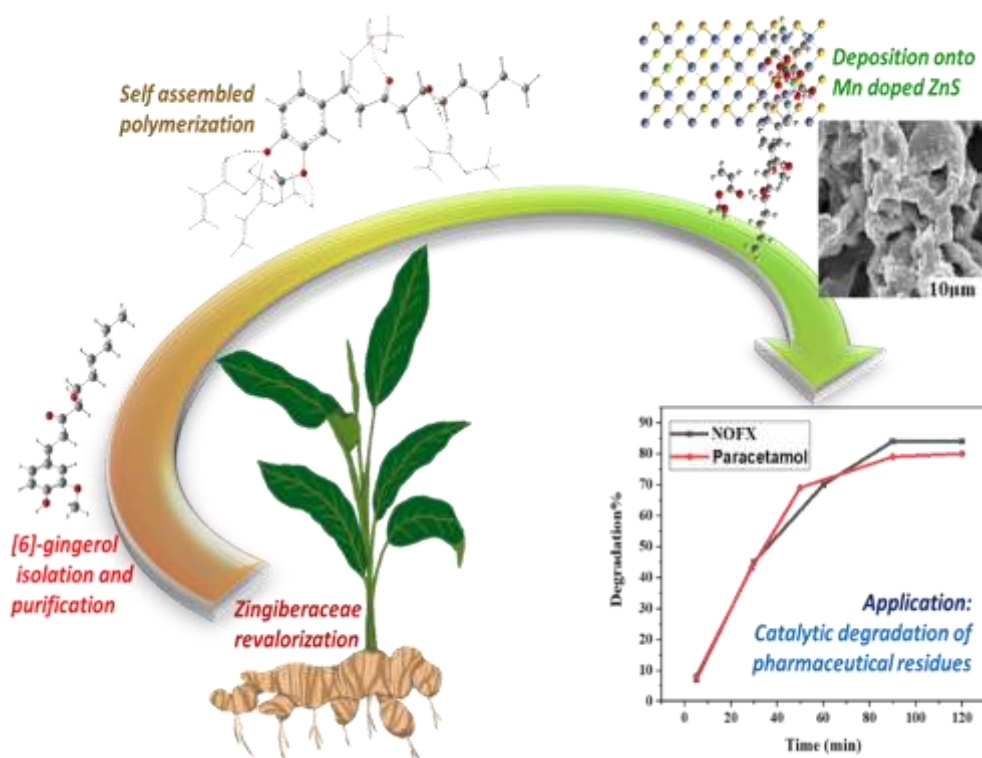
## CHAPTER 8

8.1. Assessment of photocatalytic efficiency and antifungal activity of Zinc doped Copper Sulfide composite embedded with Graphene Oxide nanosheets .....	191
8.2. <i>Introduction</i> .....	192
8.3. <i>Experimental Section</i> .....	195
8.4. <i>Results and Discussions</i> .....	203
8.6. <i>Photocatalytic properties</i> .....	205
8.7. <i>Minimum Inhibitory Concentration</i> .....	206
8.9. <i>Conclusion</i> .....	208

## CHAPTER 9

<b>Conclusion and Future Recommendations</b> .....	210
--	-----

# CHAPTER 1



## 1.1. Introduction

Ginger (*Zingiber officinale* Rosc.) a significant commercial crop that is widely distributed in tropical and subtropical countries, according to the current study. Ginger is described in ancient literature as 'an aromatic of Paradise,' and it's been used as a spice for a long time. Ginger's underground rhizome stem is used as a spice to marinate a wide range of foods and other food products. It is also utilized in medicine, especially traditional medicine. It was well-known to English palates by the 13th and 14th centuries and, also with pepper, was the most prevalent spice. Commercial cultivation occurs in India, China, South East Asia, Mexico, and other regions of the world[1]. Its Spice value addition has grown as a large business with significant commercial relevance [2]. *Zingiber Officinale Roscoe* is the botanical name for ginger " Ginger is known by several other names, including Adrak (Hindi, Punjabi, and Urdu), Shunti (Kannada), Inji (Tamil), Ada (Bengali, Oriya), Allamu, Sonthi (Telgu), Adu (Gujarati), Inchi (Malayalam), and Ale (Marathi). Ginger has numerous uses in both food and medicine[3]. It is widely used in Asian cuisine as a flavouring additive in a variety of items such as sweets, tea, curry

powders, pickles, soft drinks, and alcoholic beverages. It's used as a preservative in confectionery and fortified meals. The Greeks used to wrap ginger in bread and eat it after meals to help with digestion. Ginger can now be directly incorporated into bread, which is known as ginger-bread. Because of its medicinal characteristics, ginger is used not only as a spice but also as a medicine[4]. Ginger, one of the world's best medicines since antiquity, was given the Sanskrit term "Mahoushadha" (meaning "excellent remedy"). It has the ability to cure a variety of common disorders in the human body. It is used to treat catarrh, rheumatism, gingivitis, gastrointestinal discomfort, chronic lung disease, toothache, brain attack, motion sickness, constipation, and diabetes and neurological disorders in Chinese, Ayurvedic, and Tibb-Unani herbal remedies, [5]. It is utilised as an analgesic, anti-arthritis, anti-ulcer, hypo-cholesteric, cardiogenic. without any adverse side-effects. [n]-Gingerols and [n]-shogaols have been identified as the bioactive constituents of primary ginger-derivatives[6].

## **1.2. Botanical description of Ginger**

The ginger plant, botanically known as *Zingiber officinale*, is a thin herbaceous perennial herb. It is a member of the Zingiberaceae family, a monocotyledonous plant in the Zingiberales order. It is made up of approximately 52 genera and 1100 species. The plant grows 30 to 100 cm tall dark green leafy stems with clusters of white and pink flower buds that open into yellow blooms with purple streaks. A triangular-oval capsule with various asymmetrical and blackish seeds makes up the unusual fruiting body. Its rhizomes (underground stems) are the plant's functional components, which are variable in shape and size, often thick lobed, and pale yellow in colour [7].

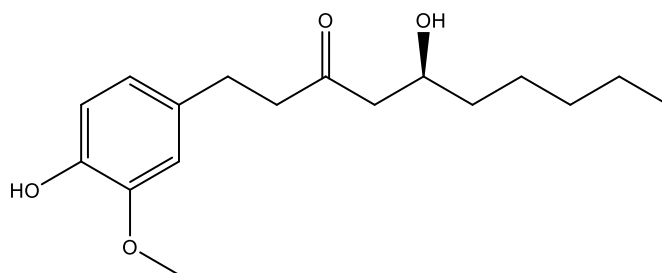
## **1.3. Ginger varieties and production**

Ginger comes in a variety of commercial variants. Nigerian ginger is darker, smaller in size, and has a more pungent flavour than other types. Ginger from Cochin (Kerala, India) is typically huge, well-scraped, high in starch content. African ginger has fewer taste components but stronger molecules. Jamaican ginger is less pungent. The ideal environmental conditions for ginger cultivation are warm and humid[8]. Though many countries cultivate ginger, India is the world's greatest producer, with a trade history dating back to the Middle Ages. The Indian contribution to global ginger production is 36.5%. In 2014-15, ginger production in India was 683160 Tonnes from an area of 138200 hectares. Ginger exports totalled 23300 tonnes in 2013-14, with a market value

of 25614 lakhs. Ginger is grown in several Indian states; however, Kerala and Meghalaya are the main producers, accounting for 70% of total production in India[9].

#### 1.4. Ginger's chemical composition

Ginger is made up of various chemical ingredients; its composition is determined by its origin and the physical state of the rhizome. It is mostly regarded for its scent and moderate pungency, which contribute to its distinct flavour. The presence of chemical components differs greatly between fresh and dried ginger. Ginger contains phenolic chemicals and volatile oils, as well as moisture, carbs, proteins, fat, fibre, and minerals. Ginger's chemical ingredients can be divided into volatile and non-volatile components. The identified and purified gingerols have been named [6]-, [5]-, [3]-, [4]-, [8]-, and [10]-Gingerol in relation to these chains. The shogaols (phenylalkanones), products of dehydration of Gingerol, are more pungent but present in lower concentrations, and during drying and storage process their yield increases. gingediols, gingediacetates, gingerdione and gingerenones are other pungent elements[10].



Synonyms :1-(4'-Hydroxy-3'-methoxyphenyl)-5-hydroxy-3-decanone

Molecular Weight: 294.4

Molecular Formula: C<sub>17</sub>H<sub>26</sub>O<sub>4</sub>

#### 1.5. The Volatile components of ginger

The odour is mostly caused by the volatile oil of ginger. The overall proportion of ginger volatile oil is between 1 and 3%. Steam distillation of ginger is commonly used to produce volatile oil. The aroma's quality, content, and physicochemical properties are determined by the raw material and total distillation time. Ginger volatile oil contains around 50 chemicals, the majority of which are monoterpenoids and sesquiterpenoids. - phellandrene, cineole, geraniol, geranial, Citral, terpineol, and borneol farnesene, curcumene, and zingiberene and few mentioned in **Figure 1**[11].

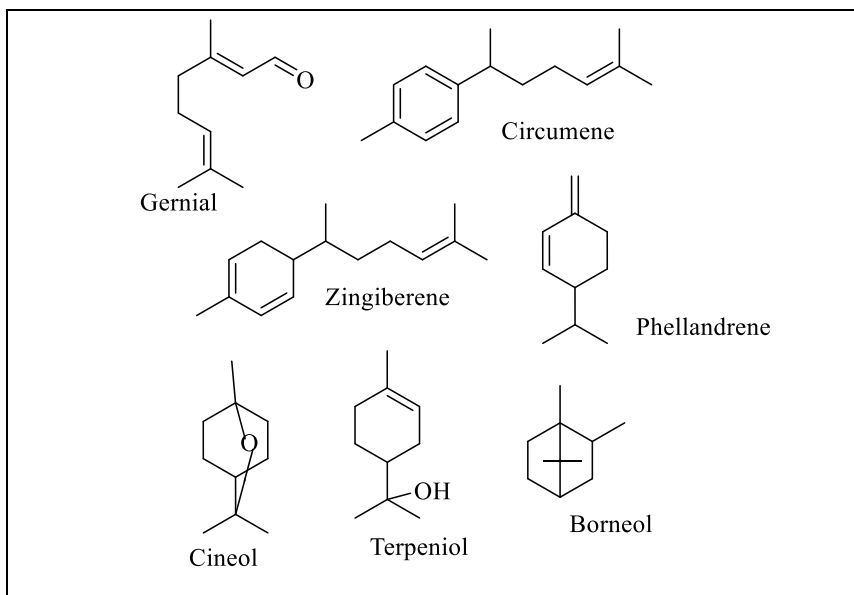


**Figure 1.** volatile components of gingerol

### 1.6. The Phenolic compounds of Ginger

Phenolic chemicals are important secondary metabolites found in plants. The significance of phenolic compounds as natural antioxidants and other bioactive substances has long been recognised. Since the nineteenth century, researchers have been trying to figure out how many phenolic chemicals are responsible for ginger's pungency. The structure of most ginger's phenolic compounds has been determined through the process of separation and purification by chromatography. They are further validated using spectroscopic characterization[12].

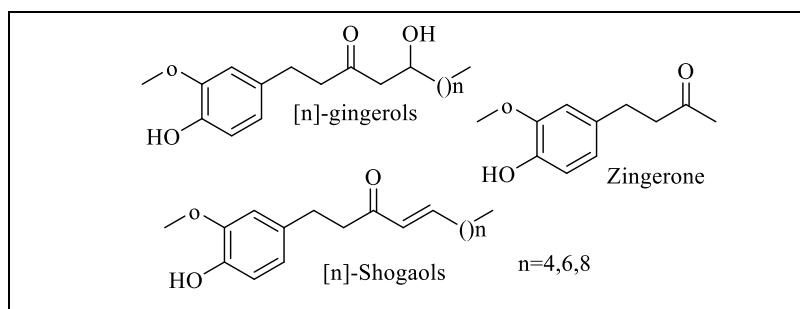


**Figure 2.** Non-volatile components of ginger

The phenolic chemicals are primarily responsible for ginger's pungency (Fresh ginger's main phenolic constituent is [6]-gingerol, while dry ginger's main component is [6]-shogaol. Other phenolic compounds found in ginger include paradols, zingerone, and dehydrozingerone[13]. There are also trace amounts of gingerols, shogaols, and paradols with varying chain lengths and few of them mentioned in **Figure 2**. The activated aromatic nucleus of gingerols, shogaols, and paradols is structurally similar, with minor changes in the side chain. Gingerols have a -hydroxyl ketone moiety, whereas shogaol

has an unsaturated ketone[14]. The alkyl side chain of paradols has simply a ketone group. Shogaols are dehydrated gingerols, and paradols are shogaols that have been hydrogenated.

The most common pungent chemicals in fresh rhizomes are [n]-gingerols. The most frequent ingredient is [6]-gingerol (n = 4), followed by minor constituents such as [8]- and [10]-gingerols (n = 6 and 8, respectively). Only trace amounts of [n]-shogaols are present in fresh roots; they are primarily present in dried and thermally treated roots, with [6]-shogaol being the most prevalent. [15].

The structural formula for [6]-gingerol is 5-hydroxy-1-(4-hydroxy-3-methoxyphenyl) decan-3-one, C<sub>17</sub>H<sub>26</sub>O<sub>4</sub> with a molecular weight of 294.38. The yellow oily feature of [6]-gingerol can be determined physically. In ethanol, the oil has a UV (max) of 282 nm and an extinction coefficient of 2560[16].

### **1.7. Extraction and Isolation of phenolic compounds of ginger**

It is difficult to isolate a single phenolic ingredient from ginger extract since ginger includes several phenolic compounds such as [6]-,[8]-,[10]-gingerols, shogaols, paradols, and zingerone[17]. Kubra et al. investigated microwave-assisted extraction of ginger phenolic compounds and adjusted the extraction technique by varying variables such as temperature, duration, and solvent. In 50% aqueous ethanol, high yields of gingerols are produced[18].

After pre-treatment with enzymes, the bioactive components of ginger were extracted with a suitable solvent. They pre-treated ginger with -amylase, viscozyme, cellulase, pectinase, and protease enzymes before extracting it using various solvents. It was discovered that an ethanol extract of ginger pre-treated with cellulase enzyme yielded the highest quantity of phenolic chemicals. There are few alternative low-yielding methods for isolating [6]-gingerol from ginger. The methods for describing the high yield of gingerols isolation are described below[19].

- [6]-Gingerol is extracted from ginger roots using supercritical CO<sub>2</sub> and ultrasound. The extraction rate and yield were both boosted in the presence of ultrasound[20].
- Wang et al. Al used high-speed counter-current chromatography to extract and purify gingerol components from a crude extract of ginger. A two-phase solvent system composed of light petroleum, ethyl acetate, methanol, and water (5:5:6.5:3.5, v/v/v/v) is used. In this study, A single step purification method is used in this study to produce

different concentration of 6-gingerol,8-gingerol, and of [10]-gingerol in 170 mins from 200 mg of crude extract [21].

### **1.8. Medicinal properties of phenolic compounds of ginger**

Plants have long been used in traditional medical systems such as Ayurveda in India, traditional Chinese medicine, Greco-Roman and Egyptian medicine, and have since been refined for use in modern medicine systems. Despite the fact that the contemporary medical system relies heavily on synthetic pharmaceuticals as therapeutic agents, plants continue to play an important role and serve as a model for the pharmaceutical industry[22]. Many chemicals extracted from plants are either employed as medicinal medications or as a source for pharmaceutical compound synthesis. They serve as prototypes for synthetic and semi-synthetic medications.

Ginger also contains a plethora of bioactive chemicals. Phenolic compounds with bioactive properties include [n]-gingerols, [n]-shogaols, and [n]-paradol. [6]-Gingerol has long been studied in the literature for a variety of bioactive properties. [6]-gingerol has anti-cancer, anti-tumour actions that are connected to cytotoxic and antiproliferative effects and inhibit angiogenesis in vitro and in vivo[23].

A few key instances from the literature that highlight the importance of [n]-gingerols as a medicinal and nutraceutical molecule are shown below. [6]-gingerol inhibits angiogenesis in vivo and invitro. Human endothelial cell proliferation induced by VEGF and bFGF is inhibited in vitro by [6]-gingerol, which also causes apoptosis in the G1 phase. It also inhibits VEGF-induced endothelial cell formation of capillary-like tubes, as well as VEGF-induced endothelial cell sprouting in the aorta of rat and formation of new blood vessel formation in the cornea of mouse. [6]-Gingerol reduces angiogenesis and may be effective in the treatment of cancers and other illnesses involving angiogenesis[24]. [6]-Gingerol specifically suppresses macrophage production of pro-inflammatory cytokines while having no effect on APC activity or cell surface expression of MHC II and co-stimulatory components[25]. Antiplatelet treatment is commonly used to prevent ischemic heart disease. For decades, aspirin has been the basis of therapeutic anti-platelet therapy. However, there have been instances of aspirin side effects, most notably gastric ulcers and gastrointestinal bleeding. Gingerol suppresses human platelet activation more than aspirin when their effects on arachidonic acid-induced platelet serotonin release and aggregation are compared in vitro [26]. [6]-Gingerol has a suppressive effect on HIV-1 replication. Gingerol has potential to be a safe and effective



immune-boosting treatment for AIDS patients. [6]-Gingerol has anticancer action, as demonstrated by a two-stage mouse skin carcinogenesis model[27]. [6]-Gingerol has medicinal promise for Alzheimer's disease management. [6]-Gingerol has anti-inflammation, antioxidant, and analgesic properties. In human breast cancer cell lines, [6]-gingerol inhibits cell adhesion, invasion, and motility activity. 6-Gingerol is an alpha amylase inhibitor that occurs naturally.

## **1.9. MOLECULAR IMPRINTED POLYMERS**

Molecular imprinting is a low-cost technique for fabricating polymeric separation media with specific biochemical recognition for the target molecule. In this procedure, the molecule is mixed with the appropriate host monomer, a massive volume of solvent, and a crosslinking agent. Non-covalent molecular interactions can cause the template molecule and the host monomer to assemble, which can then be crosslinked and polymerized to create molecular imprinted separation media [28].

The template molecule is allowed to preconfigure in the presence of one or more monomers with distinct functional groups that can interact with the target molecule prior to polymerization. After polymerization, the target molecules are removed, leaving a polymeric network of three-dimensional pores with spatially oriented functional groups [29] Pre-polymerization prearrangement can make use of covalent and noncovalent interactions between the template and the functional monomer. The presence of a monomer that generates stable self-assembled complexes is necessary for non-covalent interactions. Although non-covalent bonding interactions like hydrogen bonding, electrostatic attraction, and hydrophobic interactions are employed to create pre-polymerization complexes, covalent bonds are still necessary. After grinding and sieving, free radical bulk polymerization is conventionally used to prepare stiff monolith. The primary benefits of this method are its simplicity and accessibility. Unfortunately, the shape, size and interior morphology of the particles obtained during the grinding and sieving processes vary. Several other approaches, such as nano beads or thin imprint films, have recently been developed to produce more homogeneous products, although they have significant drawbacks, such as employment of a large amount of templates[30]. To better comprehend molecular specific interaction mechanisms in biological systems and to develop novel compounds that mimic biological functions and can be applied in analytical applications, research has concentrated on the design and synthesis of artificial

receptor molecules. Molecular imprinting is well known as a reliable technique for developing synthetic receptors that resemble polymers. This method involves polymerizing monomers and crosslinkers in the presence of a template molecule. The template is then taken out of the resulting polymer network to leave a cavity that fits the template[31]. The functional monomers used should be arranged in a way that reinforces the chemical features of the template. This is due to interaction of the functional monomers to the template molecule during polymerization. The most significant aspect of designing a molecularly imprinted system for a specific target molecule is the identification of suitable functional monomers and the determination of their stoichiometry. Bulk polymerization to generate glassy polymer blocks that are then crushed, powdered, and sieved is one of the most successful molecular imprinting techniques utilized to date[32]. Due to these time-consuming and tedious experimental processes, Even though polymer production is simple and quick, the entire process of creating and evaluating molecular imprinted polymers typically takes several days. As a result, identifying an appropriate monomer group by studying a variety of molecular imprinted polymers generated under different conditions has proven difficult. As a result, a method based on combinatorial chemistry that can easily undertake the creation and asses of molecular imprinted polymers in order to construct an ideal functional monomer in a short time has been sought. [33].

The distinction and binding of a molecular receptor (host) and a substrate are necessary for molecular recognition in a matrix of structurally related molecules (guest). This is only possible if the host and guest molecules' binding sites are complementary in size, shape, and chemical functionality. Natural selection has resulted in the evolution of molecular recognition properties in biological systems such as antigen-antibody, enzyme-substrate and hormone-receptor systems. The presumption that polymerization locks the pre-polymer complex in place forms the basis of the binding site structure working hypothesis for molecular imprinted polymers. In order to facilitate convergent interactions with the template, it is assumed that a cavity containing functional groups in a complementary array will form [34].

Molecular imprinting appears to be a suitable schema for the development of transition metal catalysts within an imprinted active site's interior. The imprinting process involves the copolymerization of organic or inorganic templates into highly crosslinked organic polymers. Their modification resulted in molecularly imprinted polymers that retained

the original template's chemical details. Even though the majority of MIP efforts have concentrated on analytical applications, recent advancements have seen the use of comparable techniques to address synthesis and catalysis issues [35].

### **1.10. Molecular imprinting strategy**

Wulff and colleagues' key study revealed the importance of crosslinkers with increase in the amount of crosslinkers boosts the specific sites by covalently imprinted polymers[33]. A novel monomer design method that combines interactive monomer functionality with a crosslinking format has been used to create non-covalent molecular imprinted polymers with improved performance. Studies of quantitative structure-selective relationships have shown significant advancement in the design of monomers and the template interactive functional group in a crosslinking monomer format [36]. The proper functioning of living systems depends on molecular recognition, in which biological macromolecules such as Saccharides, nucleic acids, and proteins (which can act as enzymes, antibodies, and receptors) all play important roles in biological activity. The difficulty of creating synthetic molecules capable of molecular recognition has attracted a lot of interest to this field of chemistry because recognition should be based on fundamental chemical interactions between chemical units [37]. In laboratories all over the world, extensive research into supramolecular design, synthesis, and evaluation is being done in order to produce host molecules with precise identification of guest species. The time-consuming multi-step preparative methods required for molecular receptors, on the other hand, frequently result overall in a low yield of the final compound a significantly less complicated template [38] The "molecular imprinting" polymerization technique is an alternative method for producing host molecules that can recognise specific guest species shown in **Figure 3**. The monomer forms a covalent or non-covalent bond with the template molecule or ionic species. A matrix-forming crosslinker is then used to polymerize this complex, creating a three-dimensional crosslink network. When the template species is removed, cavities form in the polymer matrix. Because the cavities remembered the template's spatial properties and bonding preferences, The imprinted polymer will rebind the template preferentially from a mixture of chemical species.

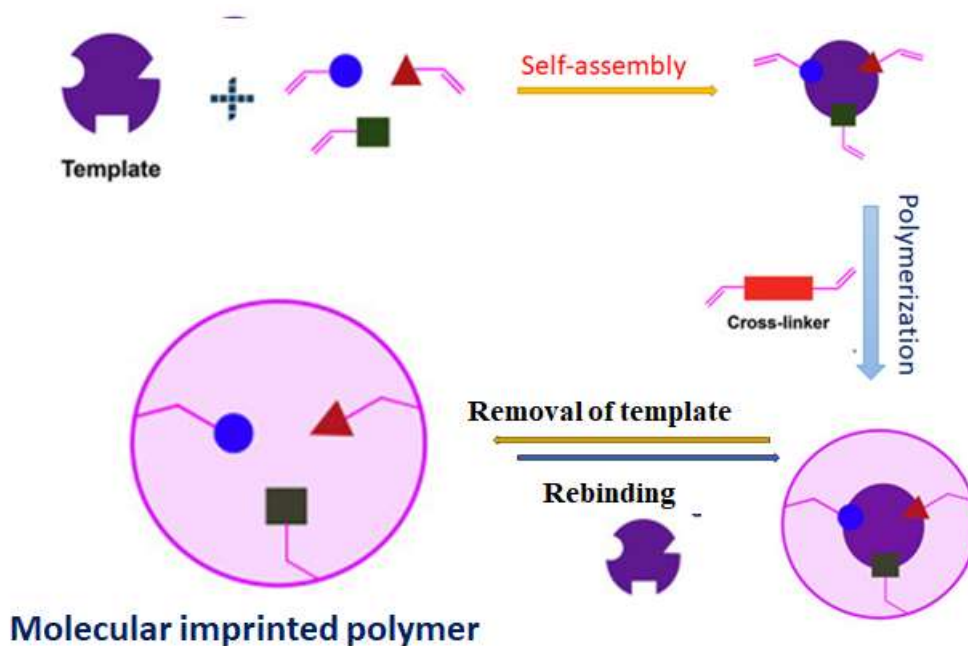


**Figure 3.** Schematic representation of Molecular imprinting polymers.

We use the term "molecular imprinting" to describe a process for producing high-affinity polymers for large templates such as viruses, not to imply that imprinting has occurred at the molecular level. The three-dimensional polymer created if the individual reagents (such as the polymer and template) aggregated together would have cavities complementary to such aggregate formations, enhancing non-specific binding to the target molecule and decrease selectivity [38]. The simplicity with which the template can be released to create complementary recognition sites in the crosslinked polymer is another thing to consider. The complementary voids that are left empty are what make molecular imprinted polymers so effective at sticking to the target molecule in a preferred manner. No recognition site will form to rebind the target molecule if the wash solution is unable to remove the template from the crosslinked hydrogel. To complete the molecular imprinting procedure, strategies for minimising template removal and it is necessary to develop methods for reducing aggregate formation before polymerization and for crosslinking the imprinted polymer [39].

### 1.11. Various approaches of molecular imprinting

In general, the two primary types of molecular imprinting techniques that have been developed are based on interactions that are both covalent and non-covalent between the target molecule and functional monomers. The functional monomers are chosen to interact with the template molecule's functional groups, and they undergo polymerization [40]. The functional group of the template interacts covalently or more frequently non-

covalently with the monomer to create the spatial binding sites, which is then followed by crosslinked co-polymerization. The non-covalent strategy has been applied more frequently than the other due to the following factors: The non-covalent approach is simple to implement because it avoids the time-consuming preparation of pre-polymerization complexes, (ii) target molecule removal is much easier, usually accomplished through continuous extraction, and (iii) non-covalent methods can introduce a wide range of functionality into the imprinted binding site [41].

**(i) Covalent approach**

In the Covalent method template is attached to a polymerizable monomer through reversible covalent force. Using a crosslinker to copolymerize, the template molecule is then chemically differentiated from the strongly crosslinked polymer [42]. Wulff and colleagues began by imprinting certain amino acids and sugars with a polymerizable function covalently. After polymerization, the sugar moiety was degraded and the polymer was used for specific binding. In covalent molecular imprinting, the amount of crosslinker used increases the specificity of the imprinted polymer. Furthermore, covalent imprinting requirements differ from non-covalent imprinting requirements, particularly in terms of functional monomer, crosslinker, and template ratio. However, reversible covalent interactions with polymerizable monomers are rare and frequently require an acid hydrolysis procedure to separate the covalent bonds between the template and the functional monomer because both the number of potential templates and reversible covalent interactions are significantly constrained [40].

**(ii) Non-covalent approach**

The most popular technique for creating molecularly imprinted polymers is the non-covalent technique because it is so straightforward. The monomer and template Self-assemble between followed by crosslinking co-polymerization, produces the spatial binding sites during the non-covalent method. Imprint molecules can interact through non-covalent means such as ionic, hydrophobic, and hydrogen bonding. The non-covalent imprinting strategy seems to hold more promise for the future of molecular imprinting due to the wide range of chemicals, including bioactive molecules, proficient of non-covalent interactions with functional monomers[43]. The unexpected molecular

recognition requirements define the boundaries of non-covalent molecular imprinting. In hydrophobic environments, the connections between the monomer and template are stabilised; however, in polar environments, they are quickly severed. The requirement for multiple different points of interaction is another drawback. Some compounds, such as an isolated carboxyl, have only one interacting group, resulting in imprinted polymers with confined molecular recognition properties that aren't very important in real-world applications[44]. The technique offers more affinity binding sites than covalent methods and is significantly less complicated, for two reasons, understanding the fundamentals of non-covalent method optimization is critical. The trends in binding and specificity in non-covalent imprinted polymers can best be explained by the use of numerous functional monomers at the binding sites with the highest affinity [44].

The polymer binding site's stringent accuracy increases with the number of binding interactions present, which also improves the site's affinity and selectivity. This would suggest that rather than being directly determined by the solution phase prepolymer complex, the number of functional groups in the polymer binding site is determined during polymerization. The real reason determining the ultimate binding site structure continue to present significant challenges due to the difficulties in describing the binding site configurations [45].

### **1.12. Molecular recognition of imprinted polymers**

Despite the number of studies produced on molecular imprinting polymers in recent decades, the recognition procedure and its rational management appear to be irresolvable, preventing enhancement of the imprinting technique. There are many factors, including complementarities in form and function and contributions from the environment, have an impact on a molecular recognition capacity. Despite the fact that all non-covalent interactions between a template and a molecular recognition site created during molecular imprinting are applicable to molecular recognition, the performance and quality of the final polymer are determined by the type of template, monomers, and polymerization reaction itself [46].

Polymer recognition creates a molecular memory, enabling the recognition sites to predominantly recognise the imprinted species. In molecularly imprinted polymers,

hydrogen bonds are most used as a molecular recognition interaction. Due to the carboxyl group's dual roles as a hydrogen bond giver and acceptor, acrylic acid and methacrylic acid are frequently used as functional monomers [48]. Following polymerization, the template molecule can be easily removed from the network by reversing these non-covalent contacts, typically with a wash in an aqueous solution of an acid, base, or methanol. This more general approach not only offers greater versatility, but also quick and reversible template binding [47].

### **1.13. Parameters affecting spatial molecular recognition in imprinted polymers**

The synthesis of molecularly imprinted polymers is a chemically demanding task that demands a thorough understanding of chemical equilibrium, molecular recognition theory, thermodynamics, and polymer chemistry to achieve a high level of molecular recognition. The polymeric materials should be comparatively stiff to keep the cavity structure after separating off the template. However, the discharge and reuptake of templates in the cavity must quickly reach equilibrium, making it essential to use flexible polymers. Due to the opposition between these two characteristics, careful optimization is required. The idea of creating and synthesising a molecularly imprinted polymer can be intimidating to a novice scientist, not least because there are so many experimental variables to consider, such as template type and concentration, functional monomer, crosslinker, solvent and initiator, initiation method, and polymerization length. The optimization of imprinted goods is further complicated by the fact that there are multiple factors to consider, some or all of which may affect the morphological, chemical and molecular recognition qualities of the molecular imprinted materials. Fortunately, in some cases, it is simple to predict how altering any one of these factors will impact these characteristics, such as the crosslink ratio [48].

#### **I. Templates**

The template is critical to all MIPs process because it monitors the configuration of bonding to functional monomers. Templates should ideally be chemically inert under polymerization conditions in order to be compatible with free radical polymerization. If the template is capable of radical reactions or is erratic under process conditions for any other reason, alternative imprinting methods might be needed. It is now common practise to imprint small chemical molecules, such as hormones, antibiotics, insecticides, amino acids, peptides, nucleotide bases, and sugars[48]. During optimization, optically active templates were used in the

majority of situations. The precision of the imprint structure was determined in these circumstances by its ability to separate racemic mixture, which was evaluated using a batch technique or chromatographic supports made of polymeric materials. One of the many appealing aspects of molecular imprinting is the fact that it can be performed with a variety of analytes, although not all templates are immediately accessible to molecular imprinting techniques. Many ordinary imprinted polymers used tiny organic compounds as templates. Large organic substances, such as proteins, require specially tailored methods. It is still difficult to imprint such a huge structure. The fundamental issue is that these templates are less rigid, making well-defined binding cavities difficult to define during the imprinting process [49]. Furthermore, when large biomolecules like proteins are subjected to the thermal or photolysis treatment used to create imprinted polymers, their secondary and tertiary structures may change. Because it is difficult for large molecules, like peptides and proteins, to enter the polymer network and reoccupy spaces left by them, rebinding is more difficult.

The authors outline a concise imprinting technique for fabricating molecular imprinted magnetic nanowires inside the pores of a nano porous alumina membrane. The pore walls of the alumina membrane nanopores have immobilised the template molecule [50]. After that, the nano porous were filled with a pre-polymerization mixture comprising superparamagnetic  $\text{MnFe}_2\text{O}_4$  Nano crystallites[51]. The alumina membrane was chemically removed after polymerization to reveal magnetic polymer Nano wires with template binding sites that were unique to the surface and saturation magnetization. The resulting magnetic imprinted polymer nanowires could bind the template more effectively than non-imprinted nanowires. Using an alumina membrane as a template, superparamagnetic nano crystallites can be entrapped in polymer nanowires. Magnetic nanoparticles immobilised with biological receptors have found widespread use in medicine and biotechnology. Engineered receptors on magnetic nanowires could be used for biochemical sensors, drug delivery, and target tracking [52].

## **II. Functional monomers**



The most significant element in ensuring comparable interactions with the template and precursors is the careful selection of functional monomers. The drawback on the number of functional monomers that can be covalently linked by the template and the stoichiometric nature of their bonding, The ratio of functional monomer to template does not need to be altered for covalent molecular imprinting. The ideal target compound to monomer ratio for non-covalent imprinting is empirically determined by testing numerous polymers created using various formulations and a higher template concentration [51]. The binding or selectivity of the imprinted polymer increases with the amount of final binding sites. The general mechanism of molecular imprinted binding site development states that functional monomers oversee binding interactions. To encourage the development of template functional monomer assemblies, non-molecular covalent molecular imprinting techniques are frequently used more than the number of moles of template. To maximise complex formation and the imprinting effect (H-bond donor with H-bond acceptor), the functional monomer's functionality must be enhanced by the template's functionality [53]. To create a molecular imprinted system that is specifically tailored to work with a given target molecule, the functional monomers chosen, and their stoichiometry are crucial. The selectivity of molecularly imprinted materials has been demonstrated to be enhanced by a novel monomer design technique for non-covalently imprinted polymers. The increased selectivity was influenced by two characteristics of the crosslinking agents[54]. Initial crosslinking is optimised without taking functional group concentrations into account. Second, the conformational entropy that would otherwise prevent selective binding is reduced by covalently attaching the functional group to the matrix of the binding site. Finally, it was discovered that diastereomeric compounds significantly impacted the selectivity of imprinted polymers.

A surface molecular imprinting technique was used to create zinc-imprinted polymers and novel organophosphorus functional monomers. The template effect and the challenging adsorption behaviour of zinc and copper ions on surface-imprinted polymers were investigated. The functional monomer's ability to recognise molecules on the surface of imprinted polymers was found to depend on the aromatic rings presence, a long enough straight alkyl chain and a

high affinity for the target metal ions [55]. The presence of three important parameters, including a longer alkyl chain with high interfacial activity, ensures significant adsorption and selectivity for target metal ions, (ii) aromatic rings with high binding affinity, and (iii) organophosphorus groups with high binding affinity. Surface template polymers have high chemical and physical stability and are easy to make. Investigations were done into the significance of the vinyl group location in functional monomers for successful imprinting of oligopeptides and derivatives of amino acids in water [56]. A semi-automated small-scale method for producing and evaluating molecularly imprinted polymers is described. By combining molecular imprinting and combinatorial chemistry, this technique allows for rapid screening and optimization of imprinted polymer libraries. To create molecular imprinted polymers, functional monomers such as acrylamide, methacrylate, 4-vinylpyridine (4-VP), acrylic acid, and styrene have been combined to Porogenic solvents such as acetonitrile and toluene. A pharmaceutical compound with aromatic, hydroxyl, and amide functional groups served as the study's template molecule. The findings demonstrated that the functional monomer used in the polymer synthesis with MAA had the highest binding affinity, and it was therefore selected to develop this specific template molecule. [57].

### **III. Crosslinkers**

The nature and amount of crosslinking agent used in the production of imprinted polymers has a major impact on binding affinity. The crosslinker in an imprinted polymer performs three important functions. The type of polymer gel-type matrix, pore volume, or micro gel powder—must be determined first. Furthermore, it helps keep the imprinted binding sites stable and contributes to the polymer's mechanical stability [58]. In polymerization, high crosslink ratios are frequently utilised to make permanently porous (macro porous) materials with appropriate mechanical stability. As a result, the amount of crosslinker should be sufficient to maintain the stability of the recognition sites. This could be because of the strong crosslinking, which enables the micro cavities to maintain a three-dimensional structure that complements the template in terms of shape and chemical functionality even after the template is removed. As a result, the functional groups remain in the optimal position for rebinding the

template, allowing the sensor to recognize the original substrate [59]. Commonly used polymers have crosslink ratios of more than 80%. But according to recent research, imprinted systems with higher selectivity and specificity can form with only a moderate amount of crosslinking (40–50%). Many crosslinkers can be used with molecular imprinting, and Some of them can integrate with the template simultaneously and become useful monomers. Catalytic activity was higher in the EGDMA-crosslinked copolymer with a high imidazole content. The hydrophobic interaction and cooperative function of DVB as a crosslinking agent improved the imprinted copolymer's catalytic activity[60].

#### **(IV) Porogenic solvents**

Porogenic solvents are employed to generate the porous structure of imprinted polymers, also known as macroporous polymers. The type and concentration of Porogenic solvents are known to affect polymer shape and non-covalent contact strength, which obviously affects the functionality of imprinted polymers. The template molecule, the initiator, the monomer, and the crosslinker must all be soluble in the Porogenic solvents. The Porogenic solvents should induce large pores in order to ensure smooth flow-through of the resulting polymer's pores.[61]. To avoid interferences during the complex formation between the imprint molecule and the monomer, which is essential for obtaining molecularly imprinted polymers with good selectivity, the Porogenic solvents should also be significantly less polar. Larger holes and materials with a lower surface area result from Porogenic liquids that phase separate too early. On the other hand, phase separation occurs later in the polymerization process with Porogenic solvents with increased solubility. As a result, materials with a large surface area and narrow pore size distribution are produced [62]. Polymers with well-developed pore architectures and high specific surface areas result from the use of a thermodynamically excellent solvent. The use of a thermodynamically weak solvent results in polymers with poorly formed pore architectures and low specific surface areas. However, porosity appears to have no effect on binding and selectivity in imprinted polymers [63]. Molecular imprinting is an effective method for producing an enantioselective TSA imprinted polymer catalyst for the hydrolysis of amino acid esters. The effectiveness of the two porogens used

to synthesise TSA imprinted polymers was compared, and the DMSO-prepared catalyst outperformed the chloroform-prepared catalyst [64]. Despite the fact that molecular recognition outcomes get worse as solvent polarity rises, it's important to remember that sufficiently potent template-monomer interactions have occasionally been observed in fairly polar solvents. As the volume of Porogenic liquids rises, the size of the pores also expands [65]. A non-covalent imprinting polymerization requires careful solvent design to increase the possibility of template-functional monomer complex formation in furthermore to its dual features as a solvent and pore-generating agent. Because they stabilise hydrogen bonding, polar, non-protic solvents like toluene are typically preferred. Water might be the preferred solvent if hydrophobic forces are what are causing the complexation [66].

#### (V) Initiators

As a source of free radicals in free radical polymerization, a few chemical initiators with different physical and chemical properties can be used. In comparison to the monomer, they are frequently used in small amounts, typically 1 weight% or 1 mole% of the total moles of polymerizable double bonds [67]. Depending on the chemical composition of the initiator, a variety of triggers and controls, such as heat, light, chemicals, or electrochemical methods, can be used to control the rate and mode of an initiator's breakdown into radicals. For instance, the photolysis or thermolysis of the azo-bis-iso-butyronitrile (AIBN) azo initiator yields stabilised, carbon-centered radicals that can begin the synthesis of a number of vinyl monomers [68].

#### 1.14. Preparation Methods of MIP

Various techniques are employed for the preparation of MIPs. The advantages and limitations of different polymerization are summarised in Table 4. These methods are are briefly described below in **Figure 4**.

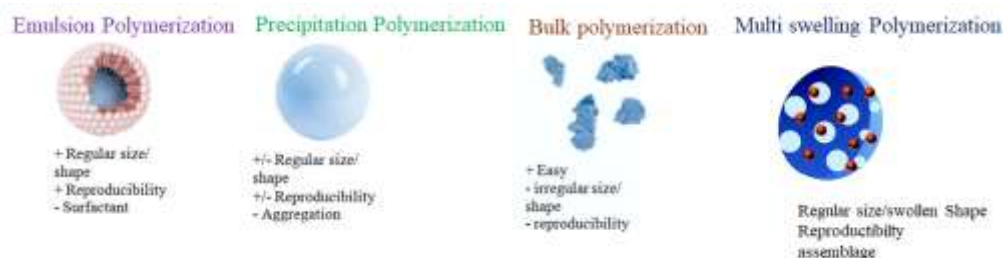


**Figure 4.** Different polymerization techniques in MIPs synthesis

### **1.14.1. Bulk Polymerization**

There are numerous ways to produce molecularly imprinted polymers. Solution polymerization, in which the monomer is immersed in a non-reactive solvent, is the proper technique for creating MIP. Initiators and useful monomers make up the reaction mixture. The bulk polymer obtained is mechanically ground to furnish tiny particles and sieving the ground particles into the desired size scales, whose width lies usually in the range of micrometer [69]. This strategy is very popular and offers many advantageous qualities, particularly to new users. This method produces highly transparent high molecular weight polymers quickly and without the requirement for specialized operator skills [70]. Bulk polymerization is an easy and simple technique. Bulk polymerization has lower heat of polymerization and reactivity and is therefore applicable for step-growth polymerization. Bulk polymerization can be carried out either in homogeneous or heterogeneous fashion depending on the solubilization of the expanding polymer chains in the monomer. vinyl chloride is an example of heterogeneous polymerization. however, the technique has also possessed many drawbacks. After the last sieving stage in bulk polymerization, the nanoparticles gathered have an uneven form and size. Additionally, the crushing and screening process is a laborious one, and during bulk polymerization, there is a large loss of useful polymer, estimated to be between 50 and 75% of the initial volume of bulk material. Because only a portion of the polymer may be used as packing material, this process used a lot of template molecules. Additionally, because bulk polymerization is exothermic, it cannot be done without running the danger of overheating the unit. According to theoretical values, reduced chromatographic efficiency and low MIPs adsorption loading capacity result from the destruction of certain contacts during grinding [71]. Gonzalez utilized non-covalent interaction to generate bulk MIP [72]. As a template molecule, digoxin was used throughout the synthesis. By switching the monomers (methacrylic acid or 2-vinyl pyridine) and the Porogenic solvents (acetonitrile or dichloromethane), the bulk polymerization has been created under various conditions. polymers with distinct structural symmetries and features have been created by bulk polymerization method was proceeded either under a thermostat-controlled water bath or in a UV radiation. The surface morphology of polymer determines the binding affinity, specificity, chemical and thermal capabilities of MIPs[70].

### **1.14.2. Multi-step Swelling Polymerization**

Significant effort has gone into creating imprinted stationary phases with small size, high efficiency, and mass transfer qualities. To create homogenous spherical particles, a multi-step swelling process was applied [99-102]. Microsphere spherical beads of a specific size can be manufactured directly. The multi-step swelling process yields particles with reasonably homogeneous shape and size, making it ideal for chromatographic applications. However, for reaction setup, complicated modes and harsh reaction conditions are required, and the binding and decay selectivity may have interfered with the aqueous suspensions utilized in this system. Furthermore, the imprinting process might have been hampered using aqueous emulsions, and the particle specificity is still not totally satisfactory.

The multi-step swelling polymerization process was utilized, coupled with a combination of phosphate buffer and acetonitrile as the mobile phase, to produce equally sized MIP for d-chlorpheniramine (Cp) and brompheniramine (bp). The bulk of CP and BP enantiomers were preserved as monovalent cations on MAA-co-EDMA polymers and divalent cations on TFMAA-co-EDMA polymers. Ion-exchange, hydro-organic mobile phase, and hydrophobic interactions are predominantly employed to act for the retention and enantio-separation of CP and BP on both MAA-co-EDMA and TFMAA-co-EDMA polymers [73].

### **1.14.3. Suspension Polymerization**

Suspension polymerization is a straightforward heterogeneous radical polymerization method for creating imprinted polymers without mechanical contact. When the system is sufficiently diluted, it generates a structure of spherical particles and microspheres of uniform size. The process is used to produce a variety of resins, including polyvinyl chloride, polystyrene, and polymethacrylate [74]. The uniform molecular imprinted microsphere with efficient chromatographic, high selectivity has been synthesized through suspension polymerization. To eliminate disruption in the multi-step swelling approach, perfluorocarbon solvents have been investigated in suspension polymerization. The applicability and practicality of this approach have diminished due to the practice of fluorocarbon solvent and fluor surfactant in polymerization. Utilizing inverse-phase seeded suspension polymerization, imprinted polyacrylamide gel beads of bovine serum albumin were synthesized using a crosslinker having low-density polyacrylamide gel as the imprinting shell and high-density crosslinked gel beads as the core [75]. Furthermore, the technique is simple, using just water as a solvent, and the imprinting beads exhibited

a faster adsorption rate and better recovery qualities than those created directly by inverse-phase suspension polymerization.

#### 1.14.4 Precipitation Polymerization

Another approach for developing the molecular imprinted polymer is precipitation polymerization. This polymerization begins in a homogeneous solution that is in a continuous unbroken phase. At first, functional monomer and low concentrations of initiator are totally miscible in each other. However, with the addition of initiator, the polymer becomes insoluble and eventually precipitates throughout the reaction. The polymer composition initiates polymerization by incorporating both the monomer and the initiator [76]. Precipitation polymerization does not require stabilizers, and polymer beads are produced in high yield during the polymerization operation shown in **Figure 5**. Precipitation polymerization by homogeneous nucleation is the most common method for producing microgels.

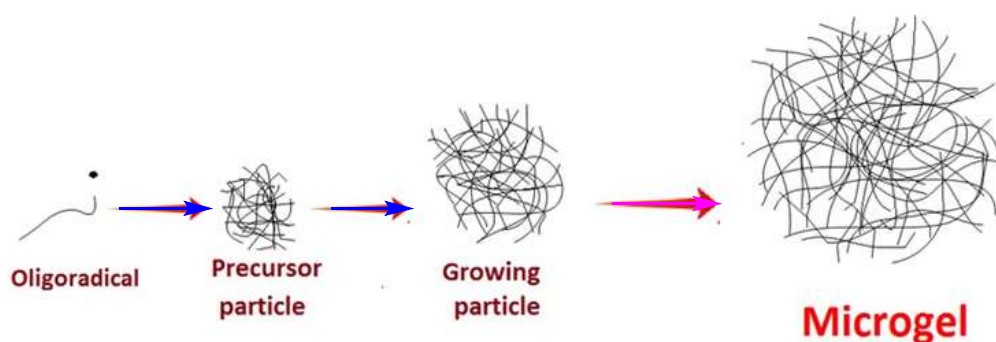


**Figure 5.** Schematic representation of Mechanism of precipitation polymerization. Adopted from reference [78]

Precipitation polymerization, which spans across a vast surface area by regulating its proportions, was used to obtain micro spherical MIPs with more uniform diameters. The coagulation of nano-gel beads composed of Precipitation polymerization is caused by the recovery of oligomers from the surrounding solution[77]. In this way, the size and porosity of near-monodispersed micro spherical beads can be precisely controlled, changing the polymerization status. MIP-based immunoassays capillary electrochromatography [78] and capillary electrochromatography[79] have described this process. Furthermore, precipitation polymerization has been identified as an efficient method for producing chromatography-grade molecularly imprinted beads.

By using precipitation polymerization, Ye and Puoci et al. have created molecularly imprinted microspheres [80]. Despite the high yield, the polymerization dilution factor is considerable, necessitating the use of many target molecules throughout the preparation process. Ho et al. used precipitation polymerization to create MIPs for morphine. The precipitation polymerization process, a viable approach for constructing MIP, is used to create homogenous particles. In comparison to the usual approach of crushing and sieving, these particles generated through precipitation polymerization demonstrate a more specific identification binding affinity in detecting morphine. Furthermore, the precipitation polymerization of morphine rebinded with MIP in a solution performed better than NMIP. However, the response has been hampered by the acquisition of agglomerates rather than individual beads [81].

#### **1.14.5. Surface Imprinting Polymerization**

Recently, the exciting and comprehensive method of surface imprinting prepared beads with MIP films to obtain imprinted materials at the chromatographic level has been introduced. Thin imprinted layers were coated on silica grade porous chromatography-level utilizing various ways to test the surface-initiated radical polymerization of the beads in this procedure [82]. An imprinted layer was prepared by Sreenivasan specific to molecules on the polymer surface designed without affecting bulk characteristics. Piacham et al. prepared ultra-thin films MIP on substrates coated with metal using surface-initiated radical polymerization. Straight polymer films are produced atop a gold-coated circular quartz crystal, enabling for safe monitoring of polymerization extension [83]. As a result, it is simple to manage the width of the thin film MIP to be less than 50 nm, where the underlying quartz crystal resonator can readily detect the selective memory of target analytes. Furthermore, the quantum sensor showed a quick temporal response (1 min) and particular stereoselectivity towards (S)-propranolol [84].

#### **1.14.6. Emulsion polymerization**

Emulsion Polymerization is a high-yielding polymerization process. The process entails the creation of spherical particles and allows us to predict the size of polymer particles. This process is a bit complicated since it is difficult to separate the surfactants and stabilizers that aid in the synthesis following the production of molecular imprinted polymers[85]. Emulsion-free polymerization begins with the emulsion of surfactant and functional monomer in water. The oil-in-water emulsion is the most well-known example



of emulsion polymerization. It is a complicated polymerization procedure, making it less suited than bulk or precipitation polymerization [86].

#### **1.14.7. Monolithic molecular imprinted method**

Monolithic molecular imprinting technology has attracted substantial interest in recent years as a revolutionary approach for the production of stationary phases. These are made using a simple technique that integrates the monolithic column and the imprinting process immediately within the stainless steel column, eliminating the need for time-consuming grinding, sieving, and column packing operations[87]. Because of their ease of preparation, high reproducibility, and large surface area, monolithic MIPs have been widely used as stationary phases in HPLC, CEC, and CLC. Through the use of a monolithic column and an imprinted molecular method, it is anticipated that the isolation and direct interpretation with high performance and high rate following in-situ polymerization will improve [88]. Matsui et al. used in-situ polymerization to create molecularly imprinted monoliths. The approach continues by dissolving a template with a suitable monomer in porous solvents (cyclohexanol and 1-dodecanol) and performing the reaction in a column after removing the gas from the mixture. Following polymerization, the target compound and porous solvents were thoroughly washed away with methanol-acetic acid. The monolithic molecular imprinted technology is simple to construct and has high selectivity, sensitivity, and rapid mass transport. In recent years, monolithic molecular imprinted polymer conjugated with chromatographic column has become a rapidly growing technique in the field of chromatographic stationary phase preparation. Mayes et al. employed -blockers in MIPs to create three types of MIP via bulk, multistep-swelling, and grafting to investigate the various polymerization processes [89].

**Table 1. Advantages and Limitations of Polymerization methods used for Synthesis.**

Method	Advantages	Limitations	References
Suspension Polymerization	Spherical particles, highly reproducible results, and potential for huge scales	Complex phase partitioning system Many imprinting techniques need the use of specialized surfactant polymers because they are incompatible with water.	[90]
Bulk Polymerization	It is easy to execute polymerization, and it doesn't require specialized knowledge or high-tech equipment.	Column packing, screening, and grinding all take a lot of time. The size and form of particles are amorphous. low effectiveness	[91]
Multi-step swelling polymerization	Extremely good particle for to perform HPLC, monodisperse beads are of balanced diameter.	Procedures and reacting circumstances are challenging	[92]
Surface polymerization	Thin imprints with layers	Complicated and time-consuming	[93]
Precipitation polymerization	imprinted microspheres that are high yielding	The dilution factor is high.	[94]

### 1.15. Applications of molecular imprinting polymer

Molecular imprinting preparation is inexpensive and straightforward, and the synthesis of MIPs is stable there, making them the perfect analogs for molecular recognition elements synthesized through sensible design[95]. Molecular imprinted polymers have

been found to be effective in four areas: (1) Enzyme mimics (2) affinity separation, (3) antibody binding mimics and (4) bio mimic sensors.

**i. Affinity separation**

- ii. The MIPs allow the construction of custom-made supports with preset selectivity, which has recently surfaced as a possible use in affinity separation. A wide variety of imprinted compounds have been utilized in various imprinted ways to separate tiny entities (amino acids, pharmaceuticals, and carbohydrates) from bigger entities (proteins)[96]. The specifically produced molecular imprinting materials have mostly been employed as chiral stationary phases in chiral HPLC. This stationary phase is distinguished by a preset order of enantiomer elution. For example, if the R- isomer is employed as a template, the S-form will be eluted first, and vice versa. Most chiral medications, however, are executed as racemic mixes; MIPs, on the other hand, offers major prospective utility in racemic resolution [97].
- iii. The bulk polymerization process is often used for HPLC stationary phase configuration material. After fragmentation of the resulting resin, approximately 25µm particles in diameter are produced. However, the polymer has several limitations, such as lower potential and heterogeneous binding sites[98]. As a result, various attempts have been undertaken to generate MIP particles with uniform morphology [size and shape] and parameters that affect flow rate in chromatography.

**iv. Antibody binding mimics**

- v. MIPs were initially developed as antibody mimics. Antibody and receptor binding mimics that are intellectually engaging correlatives to their natural analogues have been produced via molecular imprinting. According to some research on MIPs, MIPs can function as artificial binding mimics of natural antibodies and as artificial receptors in immunoassay-type investigations [99]. The energy and binding efficiency between an imprinted polymer and a target template are comparable to those between an antibody and an antigen. In terms of application, antibody binding MIPs imitators provide a quick and inexpensive path into well-built molecular artificial matrices in immunoaffinity separation of antibodies and antigens chromatography, bioanalytical immunoassay techniques, and immunosensors. MIPs' ability to bind resulted in a number of advantages over natural antibodies. For example, imprinted polymers' physiochemical resistance

leads to high strength and durability, while the possibility of purifying the polymers aids in the precise artificial binding recognition qualities and lower manufacturing costs. Another significant advantage is the elimination of foreign antigens in antibody formation [100].

**vi. Enzyme mimic for catalytic/synthetic applications**

One of the most intriguing uses of molecular imprinting is their use as enzyme mimics (mimicking the role of genuine enzymes), which have strong regioselectivity and enzyme stereoselectivity, better convenience, higher stability, and the ability to execute a wide range of processes. This was achieved by allowing the molecular imprinted polymer to work as an artificial enzyme. The most common approach in the imprinting protocol is the use of transition state analogues in an enzyme-catalyzed reaction by stabilizing the transition state of reaction and improving the rate of product formation. Molecular imprinted polymers are used to control the formation of the product either directly or indirectly [101].

**vii. Biosensor-like devices**

One of the most interesting applications of molecular imprinted polymers is the creation of MIPs as artificial receptors in biosensor-like devices. MIP has the potential to become a very durable sensing component. an immobilized sensing component, such as an enzyme, antibody, or receptor, at the interface between the sensor and the target analyte. The process of analyte attaching to the artificial receptor element generates "a selected chemical signal," which is then translated into an electrical signal, amplified, and organized in a "manageable" manner [102]. The main features of sensing devices contiguity between the sensing part and the transducing element. In Biosensors, there are specific artificial binding receptors of proper chemical substances which are utilized as analytical devices. The biomaterial whether antibody, enzyme, the antigen is used as recognition elements by binding with the transducer first. Substrate concentration is transformed into an electrical signal by the transducer which is then amplified and processed. biological catalysts if used in biosensors are called catalytic biosensors[103]. These kinds of biosensors are in excess, and they have a lot of applications in medicine, ecological environment, and monitoring biomolecules with poor chemical and physical stability. By replacing natural sensing

components, the MIP has potential benefits like antibodies. They have great stability and can function in a difficult environment. They are the greatest possibilities when no biologically recognized element can function. Xue et al. employed MIP-coated gold nanoparticles as electrochemical sensors. for amperometric detection of dopamine. AuNPs were used as the functional monomer, dopamine was used as the template, and p-amino benzenethiol (p-ATP) was selected as the cross-linker [104].

#### viii. MIPs for extraction prepose

MIPs with template paclitaxel has been synthesized and characterized. The synthesis has been done using methacrylic acid as a functional monomer and to increase hydrophilicity of reaction 2-hydroxyethyl methacrylate (HEMA) was Chosen of the obtained microparticles. Trimethylolpropane trimethacrylate (TRIM) and ethylene glycol dimethacrylate (EGDMA) were both used as crosslinkers to compare how they affected the properties of the final materials depicted in **Figure 6**. The obtained microparticles' physicochemical characteristics and paclitaxel adsorption characteristics have been studied. To the best of our knowledge, it is the first study outlining the synthesis of MIPs microparticles with paclitaxel imprinted on them [105].

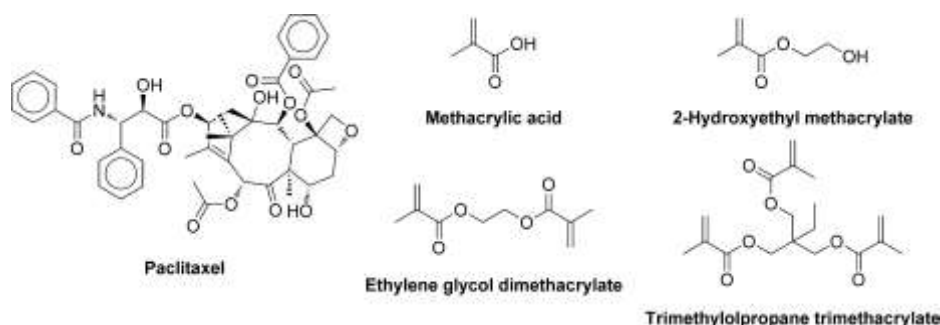


**Figure 6.** Chemical structure of Taxol (paclitaxel), functional monomer and crosslinker

MIPs have been studied for the separation and purification of [6]-gingerol from ginger [106]. The approach employs a molecular template, with zingerone serving as a mimic template. The polymerization was carried out in an aqueous solution with the functional monomer methyl acrylic acid (MAA). The polymerization procedure used ethylene glycol dimethyl acrylate as a crosslinker (EGDMA). As an initiator, 2,2, azobisisobutyronitrile (AIBN) is used. Ester was chosen as the porogen, while glycerol

monostearate was chosen as the emulsifier. MIPs were utilized exclusively as sorption for preconcentration of bisphenol A from aqueous samples. Precipitation polymerization was used to create the bisphenol imprinted polymer illustrated in **Figure 7**. Bisphenol A has a significant binding capability with MIPs [107].

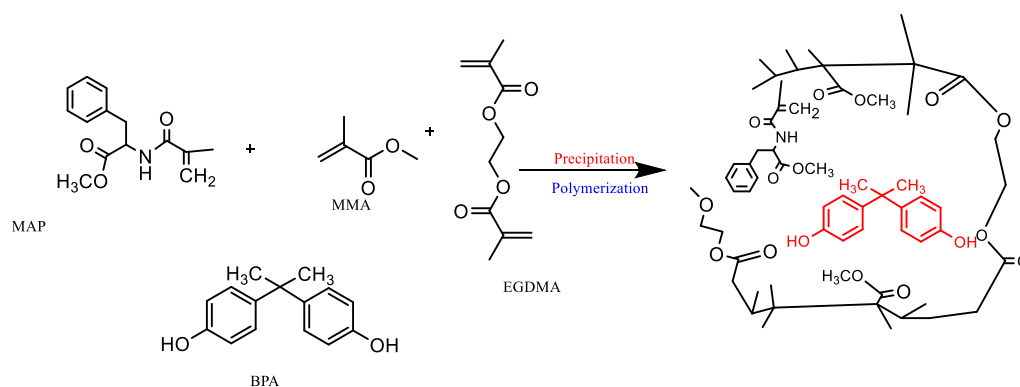


**Figure 7.** Schematic illustration of the complexation of the polymer with the bisphenol A molecule and the imprinting cavity on the poly(MAP/MMA/EGDMA) microbeads. approved adoption from reference [110]

The identification components for the detection of imidacloprid were created using emulsion polymerization by photo-initiated emulsion polymerization on a capacitive-based sensor integrated with MIPs. Imidacloprid is one of the most widely used insecticides, with a broad global user base. Its many applications include plant protection, veterinary products, and seed coating. As a result of its widespread use, it has been identified as a harmful contaminant. Imidacloprid is a common pesticide that can interfere with neurotransmitters in certain invertebrates. To address these concerns, a molecular imprinted polymer embedded with a capacitive sensor was developed to detect their existence in a different matrix. As shown in **Figure 8**, the synthesis was carried out with IMD as a template, MAA as a monomer, and EGDMA as a crosslinker in a molar ratio of 1:4:20 [108].

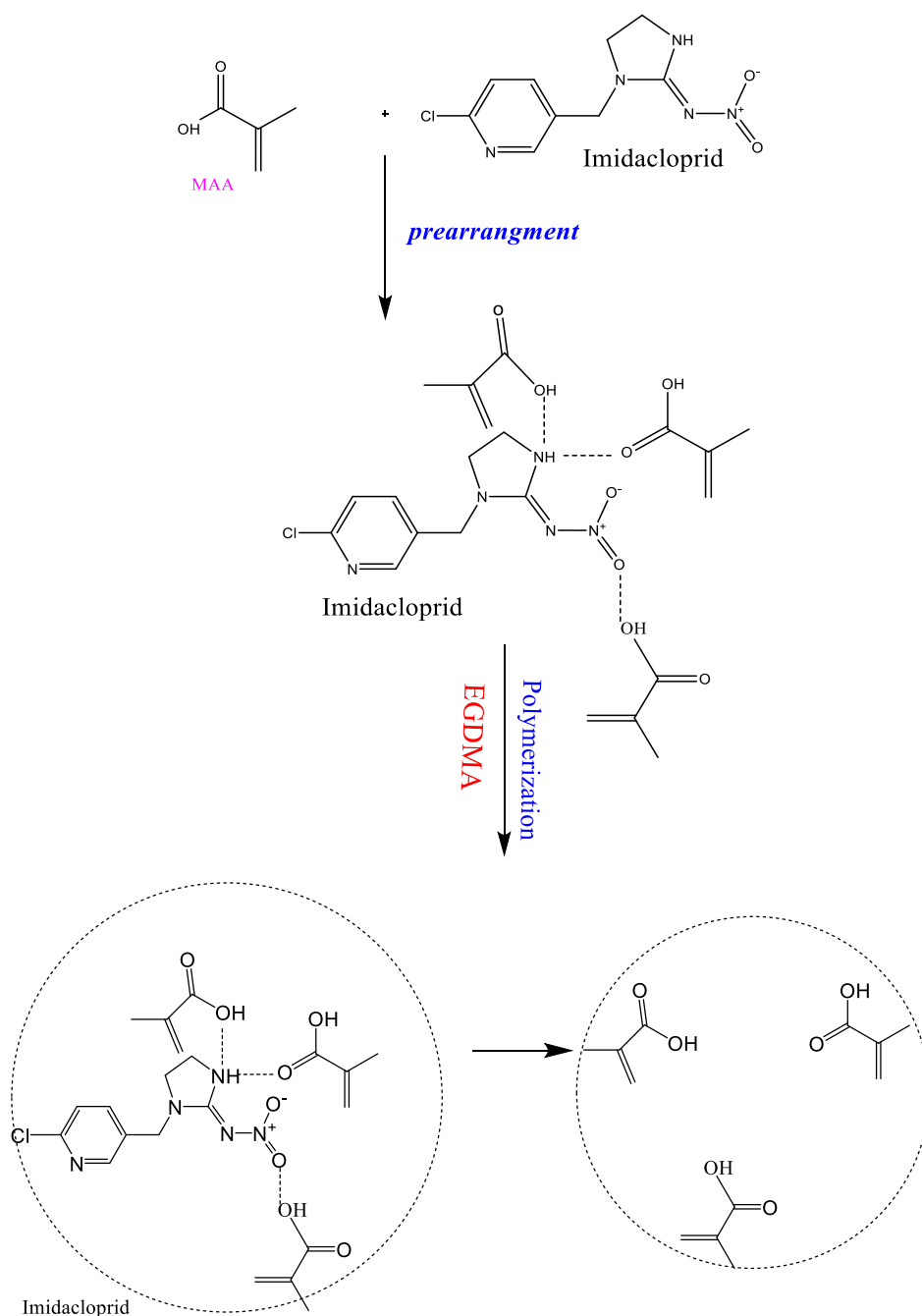


**Figure 8.** Schematic illustration of the IMD molecular imprinting procedure.

Adopted from reference [111]

MIPs has been prepared to bind specifically to quercetin and related compounds [141]. Quercetin is a pigment found in plants that belongs to the flavonoid family. There is emerging evidence that quercetin may be useful in illness prevention and therapy. Quercetin has been demonstrated to have antioxidant, anti-inflammatory, and anticancer properties. Quercetin is a bitter-tasting polyphenolic molecule. It has a yellow tint and is weakly soluble in hot and cold water, although it is soluble in alcohol. Quercetin may be found in a variety of foods, including onions, grapes, berries, and citrus fruits. Quercetin,

like another water-soluble pigment Anthocyanin found in fruits, is widely ingested in the human diet. Depending on the pH, anthocyanin can be red, purple, or blue. Because of its anti-inflammatory and antiviral properties, anthocyanin has emerged as a significant flavonoid bioactive component. Anthocyanin was extracted using a molecularly imprinted polymer that was bonded with quercetin; the synthesis begins with quercetin attaching to a monomer in the presence of a crosslinker to bind at certain places. Anthocyanin was extracted from the crude extract of mangosteen polymer using a polymer imprinted with quercetin [109] **Figure 9** depicts the bulk polymerization method used to develop a quercetin imprinted polymer.

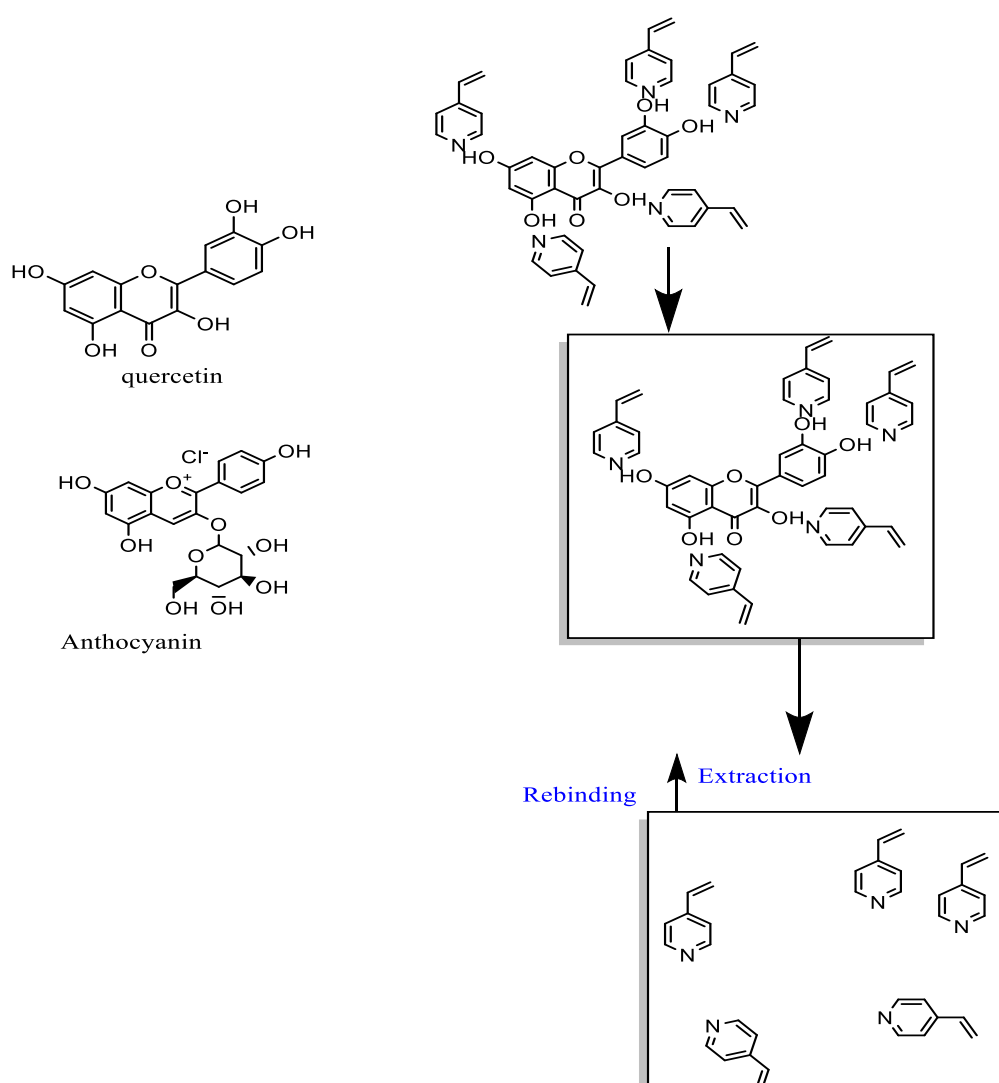


**Figure 9.** Mechanism of Quercetin imprinted polymer synthetic. Source. Adopted from reference [112]



MIPs were employed for camptothecin extraction and purification. A carbon nanotube-based solid-phase technique coated with molecularly imprinted polymers was developed to extract and analyse camptothecin in *Camptotheca acuminata* fruit from bark. EGDMA was employed as a crosslinker in the synthesis, while methacrylic acid was used as a functional monomer. The molecular imprinting approach was used with high-performance liquid chromatography for the analytic measurement of camptothecin [110]. Emulsion suspension polymerization was used to create camptothecin-based molecular imprinted polymer microspheres. Camptothecin is used as a template, ethylene glycol maleic rosinate acrylate as a crosslinker, and acrylic acid as a monomer, as indicated in **Figure 10** [111].

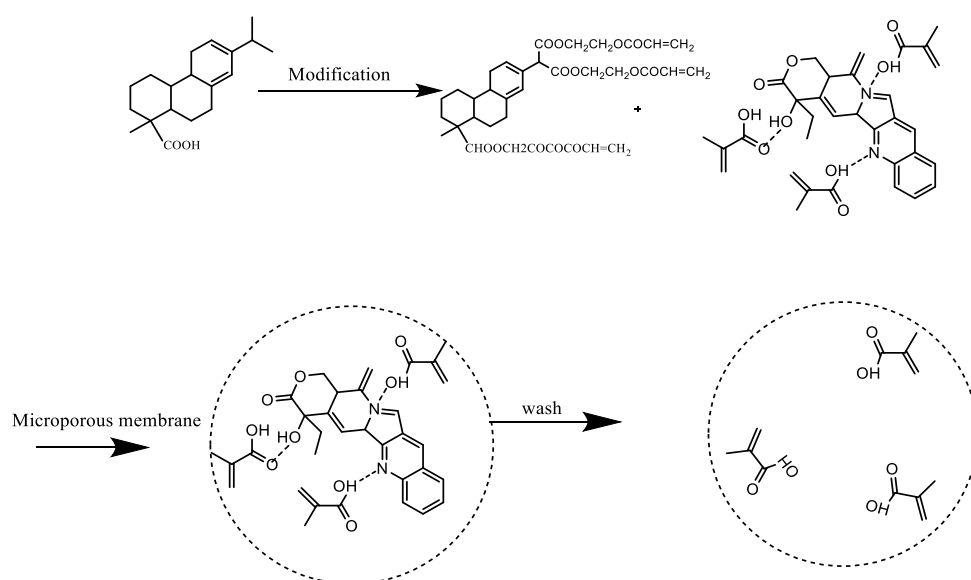
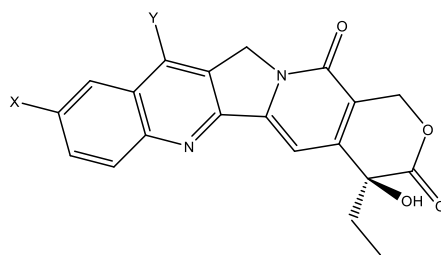


**Figure 10.** Schematic representation of camptothecin adopted from reference [114]

MIPs were utilized to characterize the presence of irinotecan in human serum samples. The reaction was carried out in dichloromethane as a solvent using irinotecan as a template and methacrylic acid and 4-vinyl pyridine as functional monomers. EGDMA was utilized as a cross linker. The polymer was extracted in high yield before being crushed and packaged into a cartridge.[112].



Structure of Irinotecan.

2,4,6 trichlorophenol is one of the most dangerous contaminants, its separation and sensitive identification are in high demand. MIPs were created by polymerizing methacrylic acid (MAA) using the template presented in Fig.10 to separate and purify 2, 4, 6-TCP. In the synthesis of 2,4,6-TCP-MIP, the binding includes covalent contact, with the carboxyl group of MAA facilitating H-bonding between the C-H groups of the templates. Many functional halogen bonds exist between the Cl group of the template and the hydrogen groups of the functional monomers **Figure 11**[113].

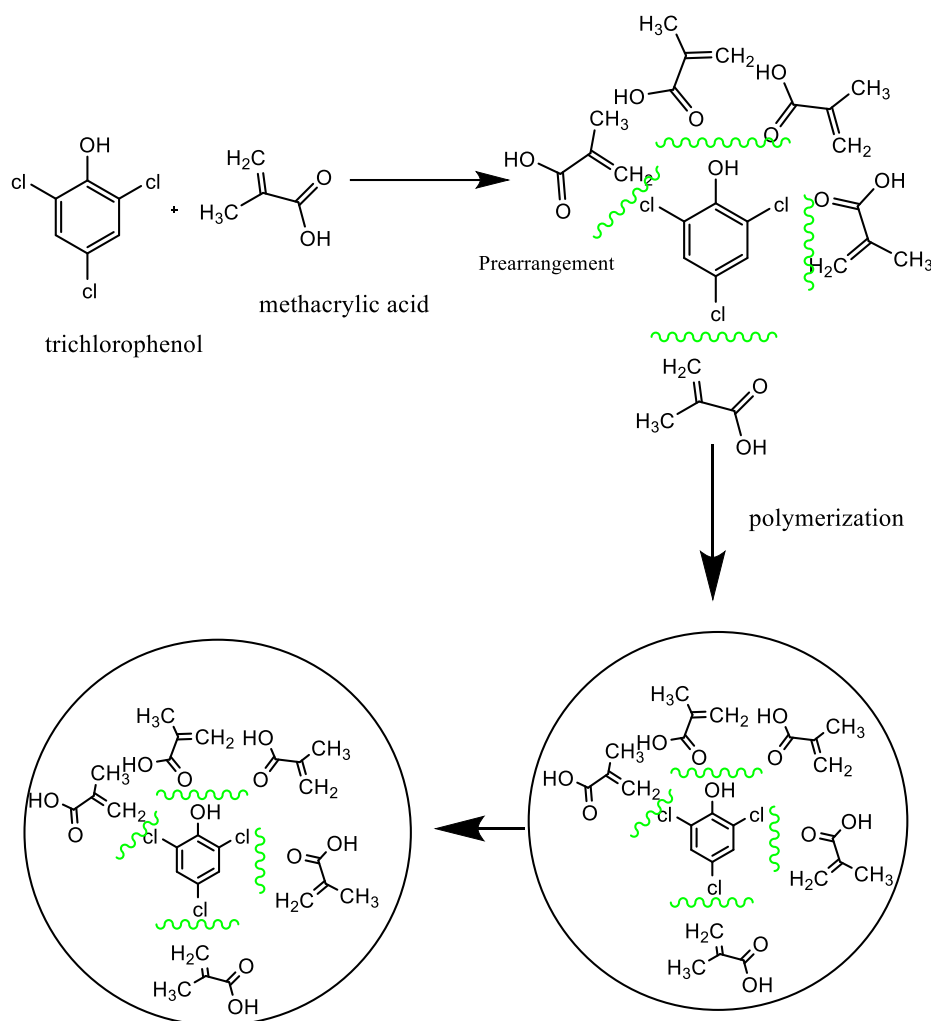


**Figure 11.** Mechanism of 2,4,6, T.C.P MIP synthesis. Source adopted from reference [116]

### 1.16. Quantum Dots

Quantum dots (QDs), also referred to as "artificial atoms," have distinct energy levels, and their optical band gap can be precisely altered by adjusting their size. QDs are described as semiconductor crystals containing elements from groups II to VI or III to V and nanoparticles with physical dimensions narrower than the exciton Bohr radius [114]. The smallest diameters detectable at the nanoscale, ranging from 2 to 10 nm, are found in QDs, which are nanocrystal-semiconducting materials (10–50 atoms). QDs are available in various sizes and are smaller than tennis ball by a million times. QDs that are 3 nm in size are known as smaller QDs and emit blue or light at comparable wavelength. This is because the precise QD composition, which chose the precise colours

based on their different sizes, produced the desired results. QDs are considered as artificial atoms due to their small size, ability to attenuate their bandgap and distinct energy levels precisely [115]. This is because the precise QD composition, which chose the precise colours based on their different sizes, produced the desired results. Due to their tiny size, ability to accurately regulate their bandgap, and distinct energy levels, QDs are referred as artificial atoms [116]. In general, the energy difference between the lowest conduction band and the highest valence band grows as QD size lowers. Dot excitation necessitates extra energy owing to a colour shift in emitted light from the larger wavelength (red) to the shorter wavelength (green), which is released when their crystal returns to its ground state (blue colour) shown in **Figure 12**. The location of the electron-hole pair in a nanocrystal semiconductor, which is typically delocalized at a distance greater than the lattice constant, determines how excited the semiconductor is electronically [117]. The QD size effect (QDE), which results from a starting shift in QD electronic properties, happens when a nanocrystal semiconductor's diameter approaches the exciton Bohr diameter. A QD forms when its nano diameter is close to or less than the exciton diameter of 6 nm (3,000-4,000 atoms), which was first discovered 30 years ago [118]. Most of the atoms in QDs are on or very close to the surface and operate in the small-size regime. 15% of the atoms in a 5 nm quantum dots cadmium sulphide are on the surface. The properties of the nanocrystal were affected by the presence of a sizable interface with its surroundings. When stimulated optically, nanocrystals have an uneven surface and electron-hole traps as a result. Because of the trapped electrons and holes, the optical characteristics of the nanocrystals altered. Because of size differences, the identical semiconductor nanocrystal employed in QDs can emit any colour of light. This refers to the wide control over QD size that may be exerted during synthesis methods to produce any colour of light. Larger dots, such as red, emit longer wavelengths, whereas smaller dots, such as green, emit shorter wavelengths. A guitar string, like a QD tune, generates a higher pitch when it is shorter and a lower pitch when it is longer. When the bandgap falls inside the visible wavelength spectrum, the colour of the light emitted changes at the same time as its size changes. The amount of energy required to transport an electron from the valence to conduction bands is referred to as the bandgap. The amount of magnetic memory (coercive force) required to turn a magnetic field inside a quantum dot is also determined by the quantum dot's size [119].

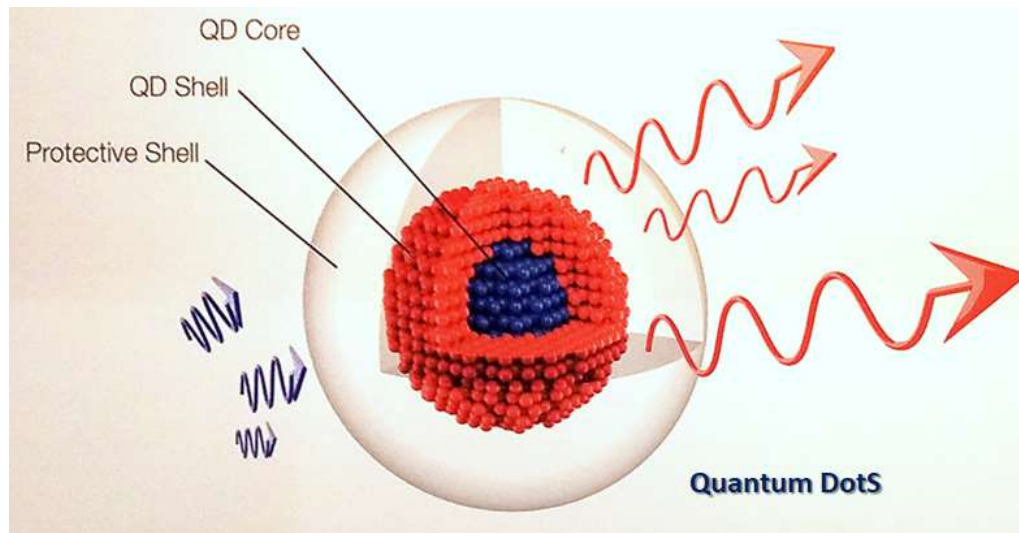


**Figure 12. Pictorial representation of Fluorescent Quantum Dots.**

The excitons are squeezed into a smaller nanocrystalline semiconductor twice the size of the exciton Bohr radius, resulting in quantum confinement. The most notable impact of the quantum confinement effect is the size dependence of the bandgap, which tunes to a certain energy dependent on nanocrystal dimensions and degree of confinement [120]. As a result, the electron Bohr radius, the hole wave functions, and the size of the QD determine the three confinement regimes. The energy of exciton confinement can be changed by changing the quantum dot size. A substantial quantum confinement effect is found in tiny QDs because of the splitting of energy levels in the valence and conduction bands. The stationary wave functions of different QD shapes are influenced by the splitting energy levels.[121]. Box-shaped dots' energy states are more s-type and p-type in nature while still maintaining orbital symmetry. The asymmetry confinement effect leads to the mixing of the wave functions in pyramid-shaped dots. Although QDs typically have 200–3,000,000 atoms, they only have 100 or fewer free electrons. Based on electron confinement, a variety of structures can be differentiated. The first QD experiments were conducted on planar structures, resulting in dimensions of almost 100 nm for electrostatic confinement and dimensions of about 10 nm for vertical confinement. Due to electrostatic confinement, pyramidal QDs are more beneficial for laser applications than flat and vertical structures despite their pyramidal or lens-shaped 10 nm diameters [122]. In general, quantization effects in nanocrystalline semiconductor devices result in size reduction dependent on the direction of charge carriers confined in various dimensions. Due to differences in quantum confinement effects and confinement energies, the properties of quantum dots (QDs) differ from those of bulk semiconductors.

Due to their reduced three dimensions, QDs are remarkable optical materials with extraordinary optical characteristics that have recently been used in bio and laser applications[123]. There are three primary classes of QD semiconductors based on the periodic table elements:

### **1.17. Semiconductors III-V**

#### **I. Group III-V (Boron and Nitrogen Family)**

Semiconductors are composed of elements from the periodic table III (Boron, Aluminium, Gallium, and Indium) and V (Nitrogen, Phosphorous, Arsenic, antimony, and Bismuth). Gallium arsenide (GaAs) has exceptional performance, particularly in optical data processing, where GaAs-QDs are light sources that are used as gain mediums in lasers. This type of QDs, on the other hand, appears to be designated for specialised purposes and is not equivalent to Si-QDs in the semiconductor sector[124]. Semiconductors II-VI are made up of elements II (Zn and Cd) and VI (O, S, Se, and Te). CdSe and CdTe are excellent examples of this QD family[125].

#### **II. IV-VI (Lead chalcogenide group)**

Semiconductors are made up of elements from the periodic table IV (Carbon, Silicon, Germanium, Tin, and lead) and VI (Oxygen, Sulphur, Selenium and Tellurium). However, Si-QD development is not as far along as QDs from other groups semiconductors. Because of its applicability in photovoltaics, Si-QDs are a required component of processors, optical chips, and optical sensors, and offer a great potential for integration into contemporary silicon electronics. Because of their high costs, Si materials are currently predominantly favoured for usage in the aircraft sector [126] .

Their optical properties differ significantly depending on the size observed. As a result, QDs have the unrivalled ability to convert light easily and efficiently to any colour in the visible spectrum. QDs 5 nm are referred to as larger QDs due to their red or orange emission colour at longer wavelengths. To mention a few of its distinctive luminescence and electrical features, QDs have a broad and continuous absorption spectrum, limited emission spectra, and great light stability. They absorb white light and then, depending on the bandgap of the material, re-emit a certain colour a few nanoseconds later[127]. The surface atoms of QDs, which typically have 200 to 10,000 atoms, greatly affect the

photocatalytic, catalytic, optical, electromagnetic properties of nanomaterials. This is due to QDs' high surface-to-volume ratio. Quantum dots have characteristics that fall somewhere between those of discrete molecules and bulk semiconductors because their excitons are quantized in all three spatial dimensions. Moreover, QDs could have a core made of ZnS, ZnO, CdSe, CdS, TiO<sub>2</sub>, CeO<sub>2</sub>, or SnO<sub>2</sub> and a shell covering the core made of ZnO, ZnS, ZnSe, or CdS. Pertinently, metal ions can be doped into the nanocrystal core to improve photoluminescence and photocatalytic properties. The most popular method for maintaining QD stability is to chemically attach a monolayer of organic molecules (such as capping groups, ligands, or linkers) to the atoms on the surface of nanocrystals. The creation of novel ligands is crucial for the synthesis of QDs because they will be essential in determining the physico-chemical properties of QDs[128].

## 1.18 Reference

- [1] R.-H. Ma, Z.-J. Ni, Y.-Y. Zhu, K. Thakur, F. Zhang, Y.-Y. Zhang, F. Hu, J.-G. Zhang, Z.-J. Wei, A recent update on the multifaceted health benefits associated with ginger and its bioactive components, *Food Funct.* 12 (2021) 519–542. <https://doi.org/10.1039/D0FO02834G>.
- [2] R.R. Dalsasso, G.A. Valencia, A.R. Monteiro, Impact of drying and extractions processes on the recovery of gingerols and shogaols, the main bioactive compounds of ginger, *Food Research International.* 154 (2022) 111043. <https://doi.org/10.1016/j.foodres.2022.111043>.
- [3] S.H. Hassan Ahmed, T. Gonda, A. Hunyadi, Medicinal chemistry inspired by ginger: exploring the chemical space around 6-gingerol, *RSC Advances.* 11 (2021) 26687–26699. <https://doi.org/10.1039/D1RA04227K>.
- [4] L.A. Akamine, D.A. Vargas Medina, F.M. Lanças, Magnetic solid-phase extraction of gingerols in ginger containing products, *Talanta.* 222 (2021) 121683. <https://doi.org/10.1016/j.talanta.2020.121683>.
- [5] J.B. Johnson, J.S. Mani, S. White, P. Brown, M. Naiker, Quantitative profiling of gingerol and its derivatives in Australian ginger, *Journal of Food Composition and Analysis.* 104 (2021) 104190. <https://doi.org/10.1016/j.jfca.2021.104190>.
- [6] Q. Sun, X. Yu, L. Zhang, A.E. A. Yagoub, Y. Tang, H. Wahia, C. Zhou, Effects of vacuum ultrasonic infiltration and combined drying on rehydration quality of ginger (*Zingiber officinale* Roscoe), *Industrial Crops and Products.* 187 (2022) 115381. <https://doi.org/10.1016/j.indcrop.2022.115381>.
- [7] S.R. Sommano, T. Tangpao, Chapter 4 - Aromatic profile of rhizomes from the ginger family used in food, in: C.M. Galanakis (Ed.), *Aromatic Herbs in Food*, Academic Press, 2021: pp. 123–165. <https://doi.org/10.1016/B978-0-12-822716-9.00004-4>.
- [8] S. Flores, M. Retana-Cordero, P.R. Fisher, R. Freyre, C. Gómez, Effect of Photoperiod, Propagative Material, and Production Period on Greenhouse-grown Ginger and Turmeric Plants, *HortScience.* 56 (2021) 1476–1485. <https://doi.org/10.21273/HORTSCI16025-21>.
- [9] A.M. El-kady, W.A.I. Al-Megrin, I.A.M. Abdel-Rahman, E. Sayed, E.A. Alshehri, M.H. Wakid, F.M. Baakdah, K. Mohamed, H. Elshazly, H.M. Alobaid, S.H. Qahl, H.A. Elshabrawy, S.S. Younis, Ginger Is a Potential Therapeutic for Chronic Toxoplasmosis, *Pathogens.* 11 (2022) 798. <https://doi.org/10.3390/pathogens11070798>.
- [10] Ü. Erdoğan, Antioxidant Activities and Chemical Composition of Essential Oil of Rhizomes of *Zingiber officinale* (Ginger) and *Curcuma longa* L.(Turmeric), *International Journal of Secondary Metabolite.* 9 (2022) 137–148. <https://doi.org/10.21448/ijsm.993906>.
- [11] D.-X. Yu, S. Guo, J.-M. Wang, H. Yan, Z.-Y. Zhang, J. Yang, J.-A. Duan, Comparison of Different Drying Methods on the Volatile Components of Ginger (*Zingiber officinale* Roscoe) by HS-GC-MS Coupled with Fast GC E-Nose, *Foods.* 11 (2022) 1611. <https://doi.org/10.3390/foods11111611>.
- [12] A. Imran, C. Quispe, A. Zeeshan, M. Imran, M. Nadeem, S.A. Gilani, T.A. Gondal, T. Tufail, F. Aslam, C.F. Rodrigues, B. Salehi, J. Sharifi-Rad, M. Martorell, N. Cruz-Martins, Development and antioxidant characterization of Ginger-Mint drink prepared through different extraction techniques, *Food Measure.* 15 (2021) 2576–2590. <https://doi.org/10.1007/s11694-021-00843-8>.
- [13] J.B. Johnson, J.S. Mani, S. White, P. Brown, M. Naiker, Pungent and volatile constituents of dried Australian ginger, *Current Research in Food Science.* 4 (2021) 612–618. <https://doi.org/10.1016/j.crfs.2021.08.010>.
- [14] E.F. Ali, H.M. Al-Yasi, A.A. Issa, K. Hessini, F.A.S. Hassan, Ginger Extract and Fulvic Acid Foliar Applications as Novel Practical Approaches to Improve the Growth and Productivity of Damask Rose, *Plants.* 11 (2022) 412. <https://doi.org/10.3390/plants11030412>.
- [15] R.E. Amoah, F.D. Wireko-Manu, I. Oduro, F.K. Saalia, W.O. Ellis, A. Dodoo, C. Dermont, M.E. Manful, Effects of Pretreatment and Drying on the Volatile Compounds of Sliced Solar-Dried



- Ginger (*Zingiber officinale* Roscoe) Rhizome, *Journal of Food Quality*. 2022 (2022) e1274679. <https://doi.org/10.1155/2022/1274679>.
- [16] A. Ravindran, J. Ettannil, A. K. Post-harvest processing, chemistry and culinary applications of major spices used in south Indian cuisines, (2022) 2429–2441.
- [17] K. Yoshida, H. Satsu, A. Mikubo, H. Ogiwara, T. Yakabe, T. Inakuma, M. Shimizu, 6-Shogaol, a Major Compound in Ginger, Induces Aryl Hydrocarbon Receptor-Mediated Transcriptional Activity and Gene Expression, *J. Agric. Food Chem.* 62 (2014) 5492–5499. <https://doi.org/10.1021/jf405146j>.
- [18] Z. Drinić, M. Jovanović, D. Pljevljakušić, N. Čujić-Nikolić, D. Bigović, K. Šavikin, Microwave-assisted extraction of essential oil from ginger (*Zingiber officinale* Rosc.), *Lekovite Sirovine*. 41 (2021) 22–27. <https://doi.org/10.5937/leksir2141022D>.
- [19] H. Wohlmuth, D.N. Leach, M.K. Smith, S.P. Myers, Gingerol Content of Diploid and Tetraploid Clones of Ginger (*Zingiber officinale* Roscoe), *J. Agric. Food Chem.* 53 (2005) 5772–5778. <https://doi.org/10.1021/jf050435b>.
- [20] p Yanxia, Zhang p>, Studies on Compositions of Ginger Oleoresin by Supercritical CO<sub>2</sub> Extraction Compare with Ultrasonic Solvent Extraction, *Academic Journal of Engineering and Technology Science*. 4 (2021). <https://doi.org/10.25236/AJETS.2021.040803>.
- [21] E. Gunaydin, G. Goncagul, Ç. Güceyü, Ö. Kardoğan, What about the Antibacterial Activity of Fresh Ginger Juice (*Zingiber officinale*)?, *Journal of Advances in Medicine and Medical Research*. 33 (2021) 163–172. <https://doi.org/10.9734/JAMMR/2021/v33i1931092>.
- [22] N.M. Roudsari, N.-A. Lashgari, S. Momtaz, B. Roufogalis, A.H. Abdolghaffari, A. Sahebkar, Ginger: A complementary approach for management of cardiovascular diseases, *BioFactors*. 47 (2021) 933–951. <https://doi.org/10.1002/biof.1777>.
- [23] O. Chou, A. Ali, V. Subbiah, C.J. Barrow, F.R. Dunshea, H.A.R. Suleria, LC-ESI-QTOF-MS/MS Characterisation of Phenolics in Herbal Tea Infusion and Their Antioxidant Potential, *Fermentation*. 7 (2021) 73. <https://doi.org/10.3390/fermentation7020073>.
- [24] C. Li, J. Li, F. Jiang, N.T. Tzvetkov, J.O. Horbanczuk, Y. Li, A.G. Atanasov, D. Wang, Vasculoprotective effects of ginger (*Zingiber officinale* Roscoe) and underlying molecular mechanisms, *Food Funct.* 12 (2021) 1897–1913. <https://doi.org/10.1039/D0FO02210A>.
- [25] A. Jafarzadeh, S. Jafarzadeh, M. Nemati, Therapeutic potential of ginger against COVID-19: Is there enough evidence?, *Journal of Traditional Chinese Medical Sciences*. 8 (2021) 267–279. <https://doi.org/10.1016/j.jtcms.2021.10.001>.
- [26] K. Wala, W. Szlasa, N. Sauer, P. Kasperkiewicz-Wasilewska, A. Szewczyk, J. Saczko, N. Rembiałkowska, J. Kulbacka, D. Baczyńska, Anticancer Efficacy of 6-Gingerol with Paclitaxel against Wild Type of Human Breast Adenocarcinoma, *Molecules*. 27 (2022) 2693. <https://doi.org/10.3390/molecules27092693>.
- [27] A. Keyhani, I. Sharifi, E. Salarkia, A. Khosravi, R. Tavakoli Oliaee, Z. Babaei, P. Ghasemi Nejad Almani, S. Hassanzadeh, R. Kheirandish, M. Mostafavi, M. Hakimi Parizi, S. Alahdin, F. Sharifi, S. Dabiri, S. Shamsi Meymandi, A. Khamesipour, A. Jafarzadeh, M. Bamorovat, In vitro and in vivo therapeutic potentials of 6-gingerol in combination with amphotericin B for treatment of *Leishmania major* infection: Powerful synergistic and multifunctional effects, *International Immunopharmacology*. 101 (2021) 108274. <https://doi.org/10.1016/j.intimp.2021.108274>.
- [28] G. Vasapollo, R.D. Sole, L. Mergola, M.R. Lazzoi, A. Scardino, S. Scorrano, G. Mele, Molecularly Imprinted Polymers: Present and Future Prospective, *International Journal of Molecular Sciences*. 12 (2011) 5908–5945. <https://doi.org/10.3390/ijms12095908>.
- [29] S. Ramanavicius, A. Jagminas, A. Ramanavicius, Advances in Molecularly Imprinted Polymers Based Affinity Sensors (Review), *Polymers*. 13 (2021) 974. <https://doi.org/10.3390/polym13060974>.
- [30] C. Dong, H. Shi, Y. Han, Y. Yang, R. Wang, J. Men, Molecularly imprinted polymers by the surface imprinting technique, *European Polymer Journal*. 145 (2021) 110231. <https://doi.org/10.1016/j.eurpolymj.2020.110231>.

- [31] N. Leibl, K. Haupt, C. Gonzato, L. Duma, Molecularly Imprinted Polymers for Chemical Sensing: A Tutorial Review, *Chemosensors*. 9 (2021) 123. <https://doi.org/10.3390/chemosensors9060123>.
- [32] S. He, L. Zhang, S. Bai, H. Yang, Z. Cui, X. Zhang, Y. Li, Advances of molecularly imprinted polymers (MIP) and the application in drug delivery, *European Polymer Journal*. 143 (2021) 110179. <https://doi.org/10.1016/j.eurpolymj.2020.110179>.
- [33] K.K. Dar, S. Shao, T. Tan, Y. Lv, Molecularly imprinted polymers for the selective recognition of microorganisms, *Biotechnology Advances*. 45 (2020) 107640. <https://doi.org/10.1016/j.biotechadv.2020.107640>.
- [34] P. Rebelo, E. Costa-Rama, I. Seguro, J.G. Pacheco, H.P.A. Nouws, M.N.D.S. Cordeiro, C. Delerue-Matos, Molecularly imprinted polymer-based electrochemical sensors for environmental analysis, *Biosensors and Bioelectronics*. 172 (2021) 112719. <https://doi.org/10.1016/j.bios.2020.112719>.
- [35] S. Pardeshi, R. Dhodapkar, Advances in fabrication of molecularly imprinted electrochemical sensors for detection of contaminants and toxicants, *Environmental Research*. 212 (2022) 113359. <https://doi.org/10.1016/j.envres.2022.113359>.
- [36] O.I. Parisi, M. Ruffo, F. Puoci, 5 - Molecularly imprinted polymers for selective recognition in regenerative medicine, in: V. Guarino, M. Iafisco, S. Spriano (Eds.), *Nanostructured Biomaterials for Regenerative Medicine*, Woodhead Publishing, 2020: pp. 141–163. <https://doi.org/10.1016/B978-0-08-102594-9.00005-X>.
- [37] E.I. Paruli, O. Soppera, K. Haupt, C. Gonzato, Photopolymerization and Photostructuring of Molecularly Imprinted Polymers, *ACS Appl. Polym. Mater.* 3 (2021) 4769–4790. <https://doi.org/10.1021/acsapm.1c00661>.
- [38] G.J. Soufi, S. Iravani, R.S. Varma, Molecularly imprinted polymers for the detection of viruses: challenges and opportunities, *Analyst*. 146 (2021) 3087–3100. <https://doi.org/10.1039/D1AN00149C>.
- [39] K. Karim, F. Breton, R. Rouillon, E.V. Piletska, A. Guerreiro, I. Chianella, S.A. Piletsky, How to find effective functional monomers for effective molecularly imprinted polymers?, *Advanced Drug Delivery Reviews*. 57 (2005) 1795–1808. <https://doi.org/10.1016/j.addr.2005.07.013>.
- [40] H. Yan, K.H. Row, Characteristic and Synthetic Approach of Molecularly Imprinted Polymer, *International Journal of Molecular Sciences*. 7 (2006) 155–178. <https://doi.org/10.3390/i7050155>.
- [41] J.O. Mahony, K. Nolan, M.R. Smyth, B. Mizaikoff, Molecularly imprinted polymers—potential and challenges in analytical chemistry, *Analytica Chimica Acta*. 534 (2005) 31–39. <https://doi.org/10.1016/j.aca.2004.07.043>.
- [42] R. Schirhagl, Bioapplications for Molecularly Imprinted Polymers, *Anal. Chem.* 86 (2014) 250–261. <https://doi.org/10.1021/ac401251j>.
- [43] V. Pichon, Selective sample treatment using molecularly imprinted polymers, *Journal of Chromatography A*. 1152 (2007) 41–53. <https://doi.org/10.1016/j.chroma.2007.02.109>.
- [44] S.N.N.S. Hashim, R.I. Boysen, L.J. Schwarz, B. Danylec, M.T.W. Hearn, A comparison of covalent and non-covalent imprinting strategies for the synthesis of stigmasterol imprinted polymers, *Journal of Chromatography A*. 1359 (2014) 35–43. <https://doi.org/10.1016/j.chroma.2014.07.034>.
- [45] W.J. Cheong, F. Ali, J.H. Choi, J.O. Lee, K. Yune Sung, Recent applications of molecular imprinted polymers for enantio-selective recognition, *Talanta*. 106 (2013) 45–59. <https://doi.org/10.1016/j.talanta.2012.11.049>.
- [46] K. Mosbach, Molecular imprinting, *Trends in Biochemical Sciences*. 19 (1994) 9–14. [https://doi.org/10.1016/0968-0004\(94\)90166-X](https://doi.org/10.1016/0968-0004(94)90166-X).
- [47] S.E. Elugoke, A.S. Adekunle, O.E. Fayemi, E.D. Akpan, B.B. Mamba, E.-S.M. Sherif, E.E. Ebenso, Molecularly imprinted polymers (MIPs) based electrochemical sensors for the determination

- of catecholamine neurotransmitters – Review, *Electrochemical Science Advances*. 1 (2021) e2000026. <https://doi.org/10.1002/elsa.202000026>.
- [48] A.N. Hasanah, N. Safitri, A. Zulfa, N. Neli, D. Rahayu, Factors Affecting Preparation of Molecularly Imprinted Polymer and Methods on Finding Template-Monomer Interaction as the Key of Selective Properties of the Materials, *Molecules*. 26 (2021) 5612. <https://doi.org/10.3390/molecules26185612>.
- [49] M. Zhong, Y.-H. Wang, L. Wang, R.-Q. Long, C.-L. Chen, Preparation and application of magnetic molecularly imprinted polymers for the isolation of chelerythrine from *Macleaya cordata*, *J Sep Sci*. 41 (2018) 3318–3327. <https://doi.org/10.1002/jssc.201800245>.
- [50] Y. Li, X.-F. Yin, F.-R. Chen, H.-H. Yang, Z.-X. Zhuang, X.-R. Wang, Synthesis of Magnetic Molecularly Imprinted Polymer Nanowires Using a Nanoporous Alumina Template, *Macromolecules*. 39 (2006). <https://doi.org/10.1021/ma0526185>.
- [51] A. Anene, R. Kalfat, Y. Chevalier, S. Hbaieb, Design of Molecularly Imprinted Polymeric Materials: The Crucial Choice of Functional Monomers, *Chemistry Africa*. 3 (2020) 769–781. <https://doi.org/10.1007/s42250-020-00180-1>.
- [52] Z. Liu, Y. Wang, F. Xu, X. Wei, J. Chen, H. Li, X. He, Y. Zhou, A new magnetic molecularly imprinted polymer based on deep eutectic solvents as functional monomer and cross-linker for specific recognition of bovine hemoglobin, *Analytica Chimica Acta*. 1129 (2020). <https://doi.org/10.1016/j.aca.2020.06.052>.
- [53] A.J. Hall, P. Manesiotis, J.T. Mossing, B. Sellergren, Molecularly Imprinted Polymers (MIPs) Against Uracils: Functional Monomer Design, Monomer-Template Interactions In Solution And MIP Performance In Chromatography, *MRS Online Proceedings Library (OPL)*. 723 (2002). <https://doi.org/10.1557/PROC-723-M1.3>.
- [54] G.D. Olsson, B.C.G. Karlsson, S. Shoravi, J.G. Wiklander, I.A. Nicholls, Mechanisms underlying molecularly imprinted polymer molecular memory and the role of crosslinker: resolving debate on the nature of template recognition in phenylalanine anilide imprinted polymers, *Journal of Molecular Recognition*. 25 (2012) 69–73. <https://doi.org/10.1002/jmr.2147>.
- [55] L. Zhao, Z. Ma, L. Pan, J. Wang, MISPE Combined with GCMS for Analysis of Organophosphorus Pesticides from Environmental Water Sample, *Advanced Materials Research*. 239–242 (2011) 3216–3220. <https://doi.org/10.4028/www.scientific.net/AMR.239-242.3216>.
- [56] L. Yang, X. Zhang, L. Jiang, Determination of Organophosphorus Pesticides in Fortified Tomatoes by Fluorescence Quenching of Cadmium Selenium – Zinc Sulfide Quantum Dots, *Analytical Letters*. 52 (2018) 1–16. <https://doi.org/10.1080/00032719.2018.1490311>.
- [57] C. Alexander, H.S. Andersson, L.I. Andersson, R.J. Ansell, N. Kirsch, I.A. Nicholls, J. O’Mahony, M.J. Whitcombe, Molecular imprinting science and technology: a survey of the literature for the years up to and including 2003, *Journal of Molecular Recognition*. 19 (2006) 106–180. <https://doi.org/10.1002/jmr.760>.
- [58] M. Moreno-Bondi, F. Navarro-Villoslada, E. Benito-Peña, J. Urraca, Molecularly Imprinted Polymers as Selective Recognition Elements in Optical Sensing, *Current Analytical Chemistry*. 4 (2008) 316–340. <https://doi.org/10.2174/157341108785914925>.
- [59] R.M. Garcinuño, I. Chianella, A. Guerreiro, I. Mijangos, E.V. Piletska, M.J. Whitcombe, S.A. Piletsky, The stabilisation of receptor structure in low cross-linked MIPs by an immobilised template, *Soft Matter*. 5 (2009) 311–317. <https://doi.org/10.1039/B804476G>.
- [60] W. Winingsih, S. Ibrahim, S. Damayanti, Purification of Andrographolide Methanolic Extract Using Molecularly Imprinted Polymer Prepared by Precipitation Polymerization, *Scientia Pharmaceutica*. 90 (2022) 27. <https://doi.org/10.3390/scipharm90020027>.
- [61] B. Hermawan, M. Mutakin, A. Nur Hasanah, Role of porogenic solvent type on the performance of a monolithic imprinted column, *Chemical Papers*. 75 (2020) 1–11. <https://doi.org/10.1007/s11696-020-01399-5>.

- [62] S. Yu, F. Ng, K. Ma, A. Mon, F.L. Ng, Y. Ng, Effect of Porogenic Solvent on the Porous Properties of Polymer Monoliths, *Journal of Applied Polymer Science*. 127 (2013). <https://doi.org/10.1002/app.37514>.
- [63] R. Vendamme, W. Eevers, M. Kaneto, Y. Minamizaki, Influence of Polymer Morphology on the Capacity of Molecularly Imprinted Resins to Release or to Retain their Template, *Polym. J.* 41 (2009) 1055–1066. <https://doi.org/10.1295/polymj.PJ2009098>.
- [64] S.M.E. Nilsson, S. Suriyanarayanan, S. Kathiravan, J. Yli-Kauhaluoma, T. Kotiaho, I.A. Nicholls, Enantioselective hyperporous molecularly imprinted thin film polymers, *RSC Adv.* 9 (2019) 33653–33656. <https://doi.org/10.1039/C9RA07425B>.
- [65] B. Selligren, R.N. Karmalkar, K.J. Shea, Enantioselective Ester Hydrolysis Catalyzed by Imprinted Polymers. 2, *J. Org. Chem.* 65 (2000) 4009–4027. <https://doi.org/10.1021/jo000014n>.
- [66] D. Mathew, B. Thomas, K.S. Devaky, Transition state analogue imprinted polymers as artificial amidases for amino acid p-nitroanilides: morphological effects of polymer network on catalytic efficiency, *Artificial Cells, Nanomedicine, and Biotechnology*. 46 (2018) 1830–1837. <https://doi.org/10.1080/21691401.2017.1394871>.
- [67] I. Mijangos, F. Navarro-Villoslada, A. Guerreiro, E. Piletska, I. Chianella, K. Karim, A. Turner, S. Piletsky, Influence of initiator and different polymerisation conditions on performance of molecularly imprinted polymers, *Biosens Bioelectron.* 22 (2006) 381–387. <https://doi.org/10.1016/j.bios.2006.05.012>.
- [68] M. Viltres-Portales, M.D.L. Alberto, L. Ye, Synthesis of molecularly imprinted polymers using an amidine-functionalized initiator for carboxylic acid recognition, *Reactive and Functional Polymers*. 165 (2021). <https://doi.org/10.1016/j.reactfunctpolym.2021.104969>.
- [69] L. Wang, K. Zhi, Y. Zhang, Y. Liu, L. Zhang, A. Yasin, Q. Lin, Molecularly Imprinted Polymers for Gossypol via Sol–Gel, Bulk, and Surface Layer Imprinting—A Comparative Study, *Polymers*. 11 (2019) 602. <https://doi.org/10.3390/polym11040602>.
- [70] F. Schneider, S. Piletsky, E. Piletska, A. Guerreiro, M. Ulbricht, Comparison of thin-layer and bulk MIPs synthesized by photoinitiated in situ crosslinking polymerization from the same reaction mixtures, *Journal of Applied Polymer Science*. 98 (2005) 362–372. <https://doi.org/10.1002/app.22112>.
- [71] J.-X. He, H.-Y. Pan, L. Xu, R.-Y. Tang, Application of molecularly imprinted polymers for the separation and detection of aflatoxin, *Journal of Chemical Research*. 45 (2021) 400–410. <https://doi.org/10.1177/1747519820980373>.
- [72] M.A. García Mayor, G. Paniagua González, R.M. Garcinuño Martínez, P. Fernández Hernando, J.S. Durand Alegría, Synthesis and characterization of a molecularly imprinted polymer for the determination of spiramycin in sheep milk, *Food Chemistry*. 221 (2017) 721–728. <https://doi.org/10.1016/j.foodchem.2016.11.114>.
- [73] K. Nishimura, N. Okamura, T. Kimachi, J. Haginaka, Evaluation of molecularly imprinted polymers for chlorpromazine and bromopromazine prepared by multi-step swelling and polymerization method—The application for the determination of chlorpromazine and its metabolites in rat plasma by column-switching LC, *Journal of Pharmaceutical and Biomedical Analysis*. 174 (2019) 248–255. <https://doi.org/10.1016/j.jpba.2019.05.063>.
- [74] S.A. Nabavi, G.T. Vladislavljević, Y. Zhu, V. Manović, Synthesis of Size-Tunable CO<sub>2</sub>-Philic Imprinted Polymeric Particles (MIPs) for Low-Pressure CO<sub>2</sub> Capture Using Oil-in-Oil Suspension Polymerization, *Environ. Sci. Technol.* 51 (2017) 11476–11483. <https://doi.org/10.1021/acs.est.7b03259>.
- [75] Q. Liu, L. Wang, A. Xiao, Research progress in macroporous styrene-divinylbenzene co-polymer microspheres, *Designed Monomers and Polymers*. 10 (2007) 405–423. <https://doi.org/10.1163/156855507781833620>.

- [76] S. Pardeshi, S.K. Singh, Precipitation polymerization: a versatile tool for preparing molecularly imprinted polymer beads for chromatography applications, *RSC Adv.* 6 (2016) 23525–23536. <https://doi.org/10.1039/C6RA02784A>.
- [77] Q. Xia, Y. Yun, Q. Li, Z. Huang, Z. Liang, Preparation and characterization of monodisperse molecularly imprinted polymer microspheres by precipitation polymerization for kaempferol, *Des Monomers Polym.* 20 (2016) 201–209. <https://doi.org/10.1080/15685551.2016.1239174>.
- [78] N. Tarannum, O.D. Hendrickson, S. Khatoon, A.V. Zherdev, B.B. Dzantiev, Molecularly imprinted polymers as receptors for assays of antibiotics, *Crit Rev Anal Chem.* 50 (2020) 291–310. <https://doi.org/10.1080/10408347.2019.1626697>.
- [79] B. Tóth, G. Horvai, *Chromatography, Solid-Phase Extraction, and Capillary Electrochromatography with MIPs*, *Topics in Current Chemistry.* 325 (2012) 267–306. [https://doi.org/10.1007/128\\_2010\\_100](https://doi.org/10.1007/128_2010_100).
- [80] F. Puoci, F. Iemma, R. Muzzalupo, U. Spizzirri, S. Trombino, R. Cassano, N. Picci, Spherical Molecularly Imprinted Polymers (SMIPs) via a Novel Precipitation Polymerization in the Controlled Delivery of Sulfasalazine, *Macromolecular Bioscience.* 4 (2004) 22–6. <https://doi.org/10.1002/mabi.200300035>.
- [81] K.-C. Ho, W.-M. Yeh, T.-S. Tung, J.-Y. Liao, Amperometric detection of morphine based on poly(3,4-ethylenedioxythiophene) immobilized molecularly imprinted polymer particles prepared by precipitation polymerization, *Analytica Chimica Acta.* 542 (2005) 90–96. <https://doi.org/10.1016/j.aca.2005.02.036>.
- [82] S.A. Zaidi, Molecular imprinting: A useful approach for drug delivery, *Materials Science for Energy Technologies.* 3 (2020) 72–77. <https://doi.org/10.1016/j.mset.2019.10.012>.
- [83] A. Abo Dena, A. Ali, I. El-Sherbiny, Surface-Imprinted Polymers (SIPs): Advanced Materials for Bio-Recognition, 8 (2020) 1–19.
- [84] G. Ertürk, B. Mattiasson, Molecular Imprinting Techniques Used for the Preparation of Biosensors, *Sensors (Basel).* 17 (2017) 288. <https://doi.org/10.3390/s17020288>.
- [85] H. Chen, S. Son, F. Zhang, J. Yan, Y. Li, H. Ding, L. Ding, Rapid preparation of molecularly imprinted polymers by microwave-assisted emulsion polymerization for the extraction of florfenicol in milk, *J Chromatogr B Analyt Technol Biomed Life Sci.* 983–984 (2015) 32–38. <https://doi.org/10.1016/j.jchromb.2015.01.003>.
- [86] A. Herrera-Chacón, X. Cetó, M. del Valle, Molecularly imprinted polymers - towards electrochemical sensors and electronic tongues, *Anal Bioanal Chem.* 413 (2021) 6117–6140. <https://doi.org/10.1007/s00216-021-03313-8>.
- [87] M. Nakamura, M. Ono, T. Nakajima, Y. Ito, T. Aketo, J. Haginaka, Uniformly sized molecularly imprinted polymer for atropine and its application to the determination of atropine and scopolamine in pharmaceutical preparations containing Scopolia extract, *J Pharm Biomed Anal.* 37 (2005) 231–237. <https://doi.org/10.1016/j.jpba.2004.10.017>.
- [88] Y. He, S. Zeng, A.M. Abd El-Aty, A. Hacimüftüoğlu, W. Kalekristos Yohannes, M. Khan, Y. She, Development of Water-Compatible Molecularly Imprinted Polymers Based on Functionalized  $\beta$ -Cyclodextrin for Controlled Release of Atropine, *Polymers.* 12 (2020) 130. <https://doi.org/10.3390/polym12010130>.
- [89] R. Suedee, T. Srichana, G.P. Martin, Evaluation of matrices containing molecularly imprinted polymers in the enantioselective-controlled delivery of  $\beta$ -blockers, *Journal of Controlled Release.* 66 (2000) 135–147. [https://doi.org/10.1016/S0168-3659\(99\)00261-8](https://doi.org/10.1016/S0168-3659(99)00261-8).
- [90] X. Liu, F. Wu, C. Au, Q. Tao, M. Pi, W. Zhang, Synthesis of molecularly imprinted polymer by suspension polymerization for selective extraction of p-hydroxybenzoic acid from water, *Journal of Applied Polymer Science.* 136 (2019) 46984. <https://doi.org/10.1002/app.46984>.
- [91] X. Ma, G. Wen, Development history and synthesis of super-absorbent polymers: a review, *J Polym Res.* 27 (2020) 136. <https://doi.org/10.1007/s10965-020-02097-2>.
- [92] H. Sambe, K. Hoshina, J. Haginaka, Molecularly imprinted polymers for triazine herbicides prepared by multi-step swelling and polymerization method: Their application to the

- determination of methylthiotriazine herbicides in river water, *Journal of Chromatography A*. 1152 (2007) 130–137. <https://doi.org/10.1016/j.chroma.2006.09.003>.
- [93] L. Lafferentz, V. Eberhardt, C. Dri, C. Africh, G. Comelli, F. Esch, S. Hecht, L. Grill, Controlling on-surface polymerization by hierarchical and substrate-directed growth, *Nature Chem.* 4 (2012) 215–220. <https://doi.org/10.1038/nchem.1242>.
- [94] J. Kundu, D. Pradhan, Controlled Synthesis and Catalytic Activity of Copper Sulfide Nanostructured Assemblies with Different Morphologies, *ACS Appl. Mater. Interfaces*. 6 (2014) 1823–1834. <https://doi.org/10.1021/am404829g>.
- [95] O. Brüggemann, K. Haupt, L. Ye, E. Yilmaz, K. Mosbach, New configurations and applications of molecularly imprinted polymers, *Journal of Chromatography A*. 889 (2000) 15–24. [https://doi.org/10.1016/S0021-9673\(00\)00350-2](https://doi.org/10.1016/S0021-9673(00)00350-2).
- [96] V. Pichon, K. Haupt, Affinity Separations on Molecularly Imprinted Polymers with Special Emphasis on Solid-Phase Extraction, *Journal of Liquid Chromatography & Related Technologies*. 29 (2006) 989–1023. <https://doi.org/10.1080/10826070600574739>.
- [97] J. Haginaka, Molecularly imprinted polymers as affinity-based separation media for sample preparation, *Journal of Separation Science*. 32 (2009) 1548–1565. <https://doi.org/10.1002/jssc.200900085>.
- [98] C. Zheng, Y.-P. Huang, Z.-S. Liu, Recent developments and applications of molecularly imprinted monolithic column for HPLC and CEC, *Journal of Separation Science*. 34 (2011) 1988–2002. <https://doi.org/10.1002/jssc.201100164>.
- [99] K. Haupt, P.X. Medina Rangel, B.T.S. Bui, Molecularly Imprinted Polymers: Antibody Mimics for Bioimaging and Therapy, *Chem. Rev.* 120 (2020) 9554–9582. <https://doi.org/10.1021/acs.chemrev.0c00428>.
- [100] L. Ye, K. Mosbach, Molecularly imprinted microspheres as antibody binding mimics, *Reactive and Functional Polymers*. 48 (2001) 149–157. [https://doi.org/10.1016/S1381-5148\(01\)00050-5](https://doi.org/10.1016/S1381-5148(01)00050-5).
- [101] K. Severin, Applications of Molecularly Imprinted Materials as Enzyme Mimics, in: *Molecularly Imprinted Materials*, CRC Press, 2004.
- [102] D. Kriz, O. Ramström, K. Mosbach, Peer Reviewed: Molecular Imprinting: New Possibilities for Sensor Technology, *ACS Publications*. (2011). <https://doi.org/10.1021/ac971657e>.
- [103] S. Rajpal, P. Mishra, Next generation biosensors employing molecularly imprinted polymers as sensing elements for in vitro diagnostics, *Biosensors and Bioelectronics: X*. 11 (2022) 100201. <https://doi.org/10.1016/j.biosx.2022.100201>.
- [104] Fabrication of DNA, o-phenylenediamine, and gold nanoparticle bioimprinted polymer electrochemical sensor for the determination of dopamine, *Biosensors and Bioelectronics*. 66 (2015) 490–496. <https://doi.org/10.1016/j.bios.2014.12.009>.
- [105] M. Cegłowski, J. Kurczewska, P. Ruszkowski, G. Schroeder, Application of paclitaxel-imprinted microparticles obtained using two different cross-linkers for prolonged drug delivery, *European Polymer Journal*. 118 (2019) 328–336. <https://doi.org/10.1016/j.eurpolymj.2019.06.010>.
- [106] W. Ji, X. Ma, J. Zhang, H. Xie, F. Liu, X. Wang, Preparation of the high purity gingerols from ginger by dummy molecularly imprinted polymers, *Journal of Chromatography A*. 1387 (2015) 24–31. <https://doi.org/10.1016/j.chroma.2015.02.002>.
- [107] C. Cáceres, C. Bravo, B. Rivas, E. Moczko, P. Sáez, Y. García, E. Pereira, Molecularly Imprinted Polymers for the Selective Extraction of Bisphenol A and Progesterone from Aqueous Media, *Polymers (Basel)*. 10 (2018) 679. <https://doi.org/10.3390/polym10060679>.
- [108] S. El-Akaad, M.A. Mohamed, N.S. Abdelwahab, E.A. Abdelaleem, S. De Saeger, N. Beloglazova, Capacitive sensor based on molecularly imprinted polymers for detection of the insecticide imidacloprid in water, *Sci Rep*. 10 (2020) 14479. <https://doi.org/10.1038/s41598-020-71325-y>.

- [109] X. Song, J. Li, J. Wang, L. Chen, Quercetin molecularly imprinted polymers: Preparation, recognition characteristics and properties as sorbent for solid-phase extraction, *Talanta*. 80 (2009) 694–702. <https://doi.org/10.1016/j.talanta.2009.07.051>.
- [110] Y. Ma, M. Jiang, X. Liu, X. Xu, X. Jiang, L. Chen, N. Niu, Functionally modified cross-linked molecularly imprinted resins: separation and purification of camptothecin and its theoretical study, *Industrial Crops and Products*. 184 (2022) 115078. <https://doi.org/10.1016/j.indcrop.2022.115078>.
- [111] T. Wang, P. Li, Y. Sun, X. Song, H. Li, L. Qin, J. Zhou, Q. Huang, F. Lei, Camptothecin-imprinted polymer microspheres with rosin-based cross-linker for separation of camptothecin from *Camptotheca acuminata* fruit, *Separation and Purification Technology*. 234 (2019) 116085. <https://doi.org/10.1016/j.seppur.2019.116085>.
- [112] B. Roy, S. Vo Duy, J.-Y. Puy, C. Martin, J. Guitton, C. Dumontet, C. Périgaud, I. Lefebvre-Tournier, Synthesis and Evaluation of a Molecularly Imprinted Polymer for Selective Solid-Phase Extraction of Irinotecan from Human Serum Samples, *Journal of Functional Biomaterials*. 3 (2012) 131–142. <https://doi.org/10.3390/jfb3010131>.
- [113] S.A. Bhawani, S. Bakhtiar, S.R. Shafqat, Synthesis of Molecularly Imprinted Polymers for the Selective Extraction /Removal of 2,4,6-trichlorophenol, *The Open Chemical Engineering Journal*. 13 (2019). <https://doi.org/10.2174/1874123101912010122>.
- [114] A.L. Efros, L.E. Brus, Nanocrystal Quantum Dots: From Discovery to Modern Development, *ACS Nano*. 15 (2021) 6192–6210. <https://doi.org/10.1021/acsnano.1c01399>.
- [115] S. Mazumder, R. Dey, M.K. Mitra, S. Mukherjee, G.C. Das, Review: Biofunctionalized Quantum Dots in Biology and Medicine, *Journal of Nanomaterials*. 2009 (2009) e815734. <https://doi.org/10.1155/2009/815734>.
- [116] C. Murray, D. Norris, M. Bawendi, Murray, C.B., Norris, D.J. & Bawendi, M.G. Synthesis and characterization of nearly monodisperse CdE (E = S, Se, Te) semiconductor nanocrystallites. *J. Am. Chem. Soc.* 115, 8706–8715, *Journal of The American Chemical Society - J AM CHEM SOC*. 115 (1992). <https://doi.org/10.1021/ja00072a025>.
- [117] S. Basak, R. Venkatram, R.S. Singhal, Recent advances in the application of molecularly imprinted polymers (MIPs) in food analysis, *Food Control*. 139 (2022) 109074. <https://doi.org/10.1016/j.foodcont.2022.109074>.
- [118] D. Loreck, P. Schmidt, H. Hüge, I. Heerdeggen, G. Bühler, [Liquid crystal thermography of the hands in comparison to roentgen diagnosis, clinical aspects and capillary microscopy in arthritis psoriatica, *Radiol Diagn (Berl)*. 24 (1983) 783–798.
- [119] M. Li, T. Chen, J.J. Gooding, J. Liu, Review of Carbon and Graphene Quantum Dots for Sensing, *ACS Sens.* 4 (2019) 1732–1748. <https://doi.org/10.1021/acssensors.9b00514>.
- [120] S.M. Reimann, M. Manninen, Electronic structure of quantum dots, *Rev. Mod. Phys.* 74 (2002) 1283–1342. <https://doi.org/10.1103/RevModPhys.74.1283>.
- [121] F. Bian, L. Sun, L. Cai, Y. Wang, Y. Zhao, Quantum dots from microfluidics for nanomedical application, *WIREs Nanomedicine and Nanobiotechnology*. 11 (2019) e1567. <https://doi.org/10.1002/wnan.1567>.
- [122] A. Sahu, D. Kumar, Core-shell quantum dots: A review on classification, materials, application, and theoretical modeling, *Journal of Alloys and Compounds*. 924 (2022) 166508. <https://doi.org/10.1016/j.jallcom.2022.166508>.
- [123] Z. Tachan, I. Hod, M. Shalom, L. Grinis, A. Zaban, The importance of the TiO<sub>2</sub>/quantum dots interface in the recombination processes of quantum dot sensitized solar cells, *Phys. Chem. Chem. Phys.* 15 (2013) 3841–3845. <https://doi.org/10.1039/C3CP44719G>.
- [124] M.A. Cotta, Quantum Dots and Their Applications: What Lies Ahead?, *ACS Appl. Nano Mater.* 3 (2020) 4920–4924. <https://doi.org/10.1021/acsanm.0c01386>.
- [125] K. James Singh, T. Ahmed, P. Gautam, A.S. Sadhu, D.-H. Lien, S.-C. Chen, Y.-L. Chueh, H.-C. Kuo, Recent Advances in Two-Dimensional Quantum Dots and Their Applications, *Nanomaterials*. 11 (2021) 1549. <https://doi.org/10.3390/nano11061549>.

- [126] J.H. Warner, A. Hoshino, K. Yamamoto, Richard.D. Tilley, Water-Soluble Photoluminescent Silicon Quantum Dots, *Angewandte Chemie International Edition*. 44 (2005) 4550–4554. <https://doi.org/10.1002/anie.200501256>.
- [127] G. Conibeer, M. Green, E.-C. Cho, D. König, Y.-H. Cho, T. Fangsuwannarak, G. Scardera, E. Pink, Y. Huang, T. Puzzer, S. Huang, D. Song, C. Flynn, S. Park, X. Hao, D. Mansfield, Silicon quantum dot nanostructures for tandem photovoltaic cells, *Thin Solid Films*. 516 (2008) 6748–6756. <https://doi.org/10.1016/j.tsf.2007.12.096>.
- [128] H. Preier, Physics and applications of IV-VI compound semiconductor lasers, *Semicond. Sci. Technol.* 5 (1990) S12–S20. <https://doi.org/10.1088/0268-1242/5/3S/004>.



## CHAPTER 2

### **Ginger derived polymer modified with Mn Quantum Dots as photocatalyst in the elimination of pharmaceutical pollutants norfloxacin and paracetamol**

#### **2.1. Introduction**

Groundwater contamination by persistent organic substances such as drugs is a global environmental issue, and complete remediation remains a challenge. Photocatalytic degradation (PD) has been proposed as a feasible, long-term, and scalable technology to address drug pollutant[129]. Norfloxacin and paracetamol, which are quinoline and analgesics with a life time of days to years depending on the surrounding conditions, are two of the most commonly used drug compounds. Excessive consumption of drugs has resulted in an increase in their concentration in wastewaters, sediments, and many other aquatic systems[130]. The development and design of novel compounds has received increased attention. A substantial number of Nonmetal, metal oxides, metal sulphides, metal nitrides, and other pure or hybrid materials have been developed and studied for the Photocatalytic application. Among the numerous types of Sulphides have been widely used as potential catalyst materials. because of the ease with which it can be used as a photocatalyst material for environmental remediation Synthesis, high efficiency, and exceptional photoelectric properties[131].

Zinc sulphide (ZnS) has recently received a lot of attention due to high negative reduction and rapid electron-hole generation electrons with potentials that exited under the influence of light. ZnS is a significant II-VI semiconducting and crystalline material with a 3.68 eV dielectric constant [132]. It also has a high exciton binding energy (40 meV) due to which it has been found to have better efficiency in photodegradation. A three-dimensional confinement effect was observed when ZnS QDs were prepared using various capping agents. ZnS is more stable, nontoxic, environmentally friendly and an ideal host for the development of composite formation with semiconductors [133]. To improve optoelectronic properties, as well as magnetic properties of QDs doping is usually conducted with appropriate elements [134]. The properties and applications of semiconductor nanomaterials doped with controlled impurities have encouraged research into dopants in semiconductor-based devices. Many technologies have been adopted for the inclusion of dopants or impurities to regulate material behaviour. The effect of dopants on semiconductor nanocrystals is consequently important. The most widely researched doped QDs, Mn doped ZnS are usually advocated as appropriate fluorescent and photodegradation probes [135]. Mn-doped ZnS QDs have been prepared using different techniques such as chemical

precipitation method, oxidation method, hydrothermal method wet chemical procedures and laser-assisted thermal [136]. Mn-doped ZnS QDs have aroused interest in recent years due to their remarkable physical, chemical and optical properties and this efficiency can be stimulated further by encapsulating them with molecular imprinting polymer.

Molecular imprinting polymer (MIPs) is one of the most commonly studied and used methods for generating biomimetic receptors. MIPs has been widely exploited in areas such as Nano sensors, artificial antibody mimics, therapeutics, photocatalysis and, particularly in, chromatography as Solid-Phase Extraction sorbents (SPEs) [137]. MIPs have been used to selectively adsorb traces of organic pollutants in water [138]. MIPs has been synthesized using Ofloxacin as a template on the surface of mesoporous carbon nanoparticles to demonstrate that MIP may remove fluoroquinolone drugs from saltwater. Fluoroquinolone imprinted polymers have also been developed for the extraction and identification of important antibiotics in real-world water samples [139]. Norfloxacin is a fluoroquinolone antibiotic with a relatively stable chemical structure and low biodegradability, whereas Paracetamol is a widespread anti-inflammatory drug. Due to their low concentration and considerable bio-toxicity, Conventional technologies are insufficient to successfully remove Norfloxacin (NOFX) and Paracetamol [140]. As a result, it is vital to create effective technologies to remove NOFX and Paracetamol from drinking water and wastewater [141]. Molecular imprinting technology (MIT) provides the potential to provide Mn doped ZnS-based materials with great selectivity by combining tailor-made receptors that can detect and bind target molecules with binding specificity. This technique often refers to a process in which the template molecules engage with the chosen functional monomer to build major host-guest complexes, and then a particular quantity of cross-linking agent and initiator are combined into the complexes to produce macromolecule polymers.

This study aims to create a new, environmentally friendly type of nanocomposite material for application in waste water treatment through in-situ polymerization method. The MIPs has been synthesized using [6]-gingerol as the template, 2-hydroxymethacrylic acid as a functional monomer, 2,2'-azobisisobutyronitrile (AIBN) as initiator and ethyl glycol dimethacrylate (EGDMA) as crosslinker. The [6]-gingerol molecule is an aromatic phenolic compound and has been chosen as template molecule due to its variety of pharmacological and physiological properties against various drugs and structure of [6]-gingerol was optimized using DFT study shown in **Figure 1**. The [6]-gingerol has been previously studied as having hepatoprotective activity against acetaminophen-liver induced toxicity in a mice model and [6]-gingerol has been found significantly reduce biochemical parameters. The polymer is encapsulated with

Mn-doped ZnS QDs and combines the advantages of molecular technology with the photocatalytic property of Mn-doped ZnS QDs for photodegradation of drugs such as norfloxacin and paracetamol.

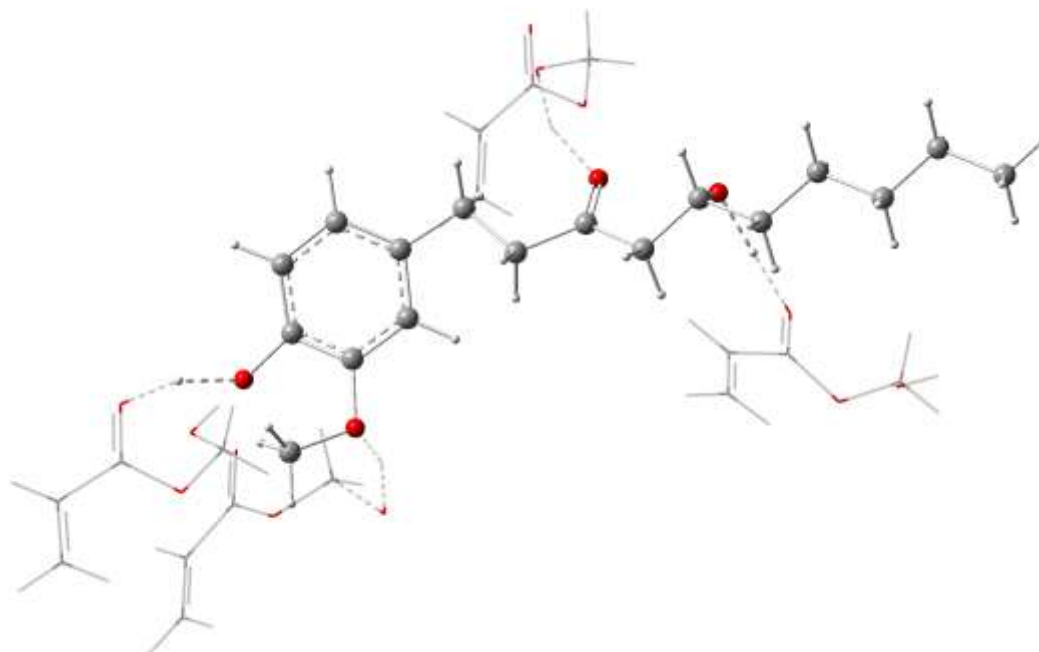


**Figure 1.** DFT optimized (uB3LYP/6-311G) chemical Structure of [6]-gingerol based Molecular imprinted polymer. (The red dot indicates oxygen atom of [6]-gingerol and black colour indicates presence of carbon atoms).

## 2.2 Materials and methods

$^1\text{H}$ NMR and  $^{13}\text{C}$ NMR were recorded on Bruker-500 and 400MHz instruments using DMSO- $d_6$  as solvent and tetramethyl-silane as an internal reference standard. High-resolution mass spectra measurements were carried out to determine the molar mass of our sample. X-ray diffraction and FESEM techniques were employed to analyze the size and morphology of the synthesized sample. Thermogravimetric analysis-differential scanning calorimetry was carried out on Perkin Elmer DSC-7 instruments operating at a  $10^\circ$  heating rate in an  $\text{N}_2$  atmosphere with 1 to 2 mg of the sample. Computational modelling was achieved using Gaussian 16 software using Density Functional Theory for optimization of geometries and energy states using a HSEh1PBE/LANL2DZ basis set [142].

### 2.2.1 Extraction of [6]-gingerol

The ginger rhizome was purchased at a local store. Figure 2 demonstrated the graphical representation of the samples. The Rhizomes were collected and washed in tap water three to four times to remove soil, converted into small pieces and dried in the presence of sunlight.

This material was pulverized with the help of an electric grinder for 60 minutes after that dried powder of ginger was obtained. The Soxhlet extraction method was utilized to extract gingerol from powdered ginger. A total of 200 grams of ginger powder was uniformly packed with 1000 millilitre of methanol for the extraction process. The reaction was allowed to continue for 48 hours at the boiling temperature of the solvent until the solvent became colourless. The resulting extract fractions were concentrated, resulting in the formation of a thick paste. This paste was then dried in an oven at 45°C. Following this, a crude extraction of gingerol yield was obtained, as depicted in **Figure 2**.

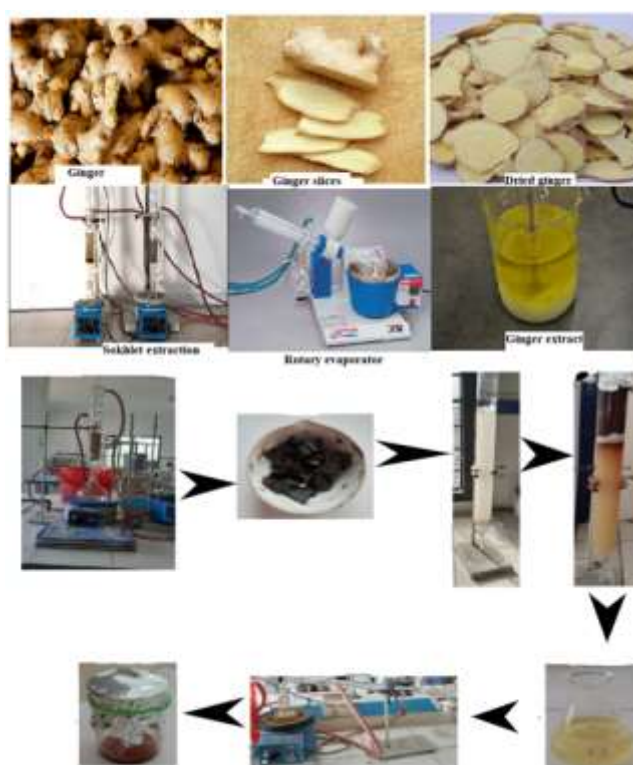


**Figure 2.** Process flow chart for the extraction of [6]-gingerol

### 2.2.1 Synthesis of Mn-doped ZnS

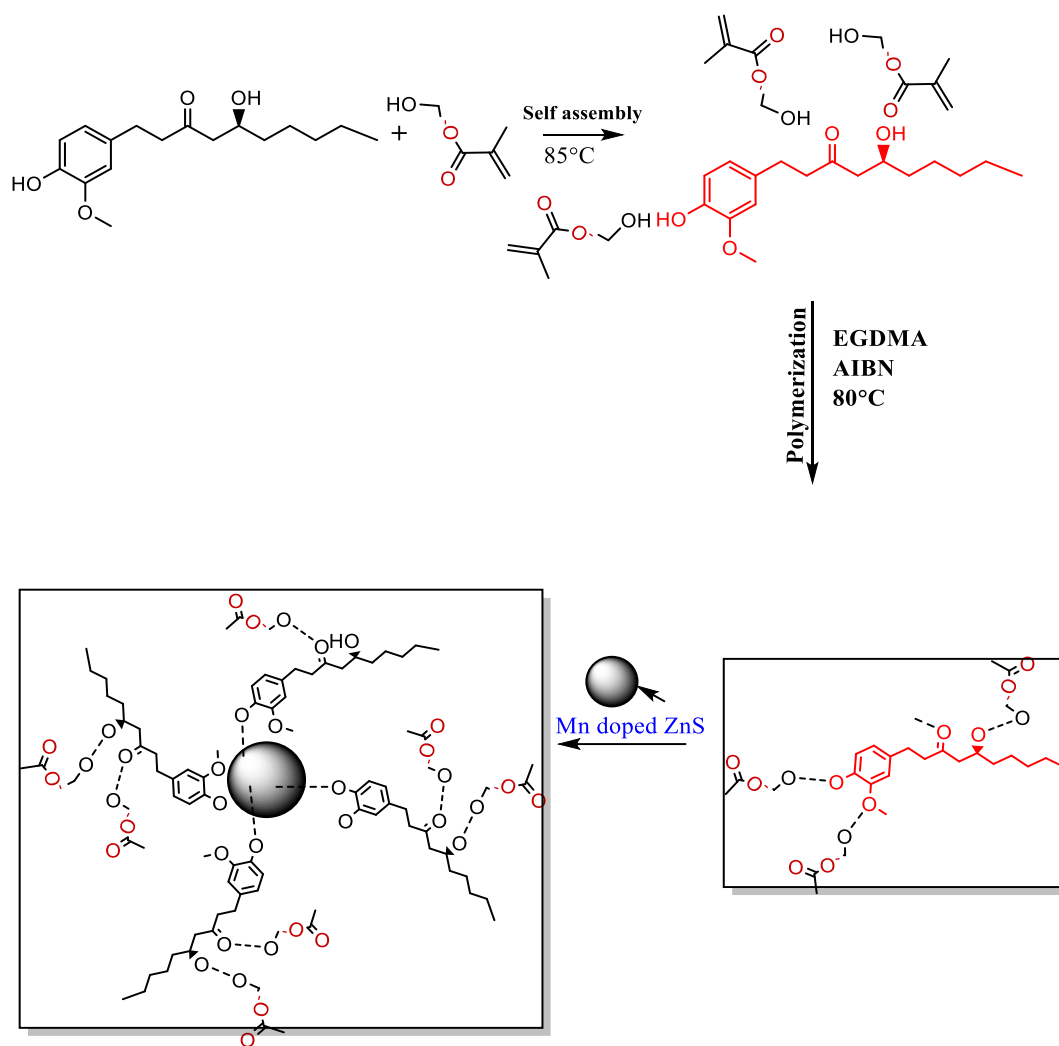
The Mn-doped ZnS was prepared by the chemical precipitation method. Prepared the 1M Zinc chloride ( $ZnCl_2$ ) anhydrous solution by using 20ml of deionized water. The solution was treated with 1 M sodium Sulfide ( $Na_2S$ ) solution. The mixture was stirred at 65 °C, and after that mixture was precipitated in colloidal form. This precipitate was washed several times with double distilled water to eliminate impurities. The resulting product was calcinated for 20 minutes at 200°C. The Synthesized QDs were further used for the preparation of Mn-doped ZnS by adding 0.1 moles of Manganese (Mn) as a doping agent and mercaptoethanol was used

as a capping agent in the solution. The resulting product was calcinated for roughly 3 hours at 200°C to obtain Mn doped ZnS. The sample was further confirmed by different spectroscopic techniques such as XRD and FESEM.

0.0.0.32.326.

#### +2.2.3 *Synthesis of molecular imprinted polymer (MIP) By Insitu Polymerization*

A template of 1.0 mmol of [6]-gingerol was utilized and dissolved in a conical flask containing a mixture of 5 mL diethyl ether and 5 mL acetonitrile. These solvents were chosen as porogen solvent. Due to the limited solubility of [6]-gingerol in diethyl ether, a miscible mixture of diethyl ether and acetonitrile was employed. In this solution, 4 mmol of HEMA was added as the functional monomer, followed by the addition of 16 mmol of Ethylene glycol dimethacrylate (EGDMA) as the cross-linking monomer. The molar ratio was maintained at 1:4:16. To initiate the free-radical polymerization process, 0.030 g of 2,2-azobisisobutyronitrile (AIBN) was added as the polymerization initiator, along with 0.89g of Mn-doped ZnS. The reaction was conducted under a nitrogen atmosphere by purging N<sub>2</sub> gas for 15 minutes at a flow rate of 0.1 L/min. The contents of the conical flask were allowed to polymerize in a water bath at 80°C for 3 hours and purified by using methanol. Consequently, a composite of Molecularly Imprinted Polymers (MIPs) was obtained according to (Scheme 1) and further characterization was carried out using FTIR, XRD, and FESEM.



**Scheme 1.** Schematic illustration of MIPs coated with QDs

## 2.3. Results and Discussion

### 2.3.1 Characterization of [6]-gingerol

The following formula was used to obtain the % yield:

$$(W_1/W_2) \times 100 = \%Yield \quad (1)$$

$W_1$  represents the weight of the dried ginger thick paste obtained from the hot air oven, and  $W_2$  represents the weight of the pulverized ginger after drying. To prepare the fine powder, 20 grams of ginger thick paste was triturated with 3g silica gel, resulting in a final powder weight of 23 grams.

A column chromatography technique was employed at different ratios of DCM and petroleum ether (9:1,8:2,7:3). As three spots were obtained on TLC with each ratio, purification was

forwarded to the next solvent ratio. The [6]-gingerol was, however, obtained at a 6:4 ratio of DCM and petroleum ether and 5mg of [6]-gingerol was collected from 20g of ginger crude extract.

*High-Performance Liquid Chromatography (HPLC)*: The HPLC analysis was performed using an eluent of HPLC grade acetonitrile and water (55:45 v/v) at a flow rate of 1.0ml/min and the temperature was set at 30°C by applying a reverse phase C-18 column with isocratic elution. A 282 nm Variable Wavelength Detector (VWD) was employed. A prominent peak was observed with a retention time of 2.75 minutes. This peak exhibited an area representing approximately 17% of the total peak area, indicating the presence of 6-gingerol. The compound [6]-gingerol was identified and quantified based on a retention time of 2.75 min (**Figure 3**).

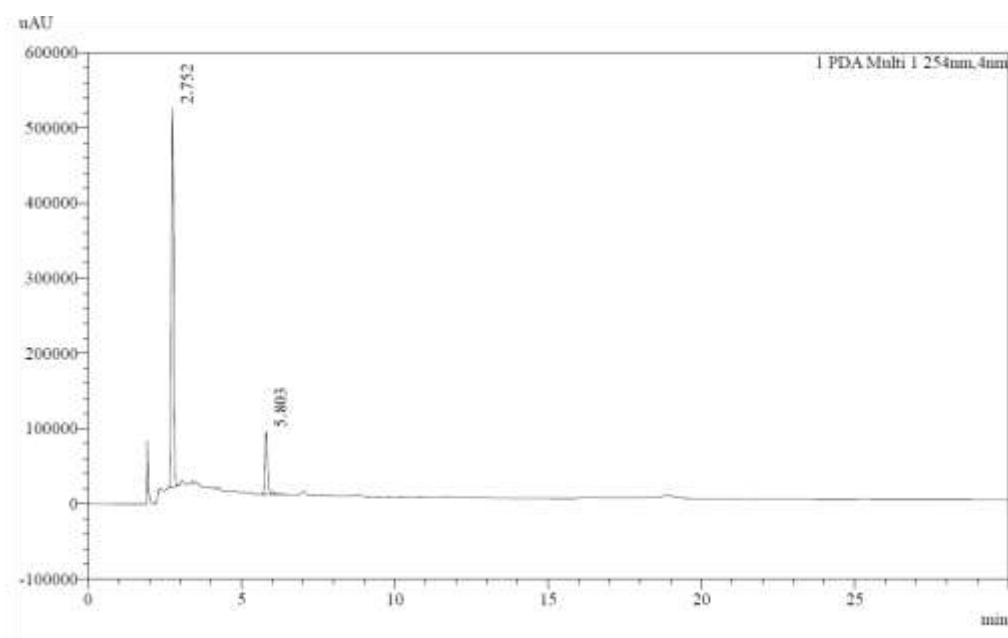


**Figure 3.** HPLC chromatogram of [6]-gingerol from ginger extract.

*Fourier Transform Infrared Spectroscopy (FTIR)*: FTIR spectrum of the extracted 6-gingerol is evident in **Figure 4**. In this spectrum, 3000 to 3200  $\text{cm}^{-1}$  peaks attributed to OH stretching. Another sharp peak observed at 1737  $\text{cm}^{-1}$  indicates the stretching vibrations of the carbonyl group. A small and low-intensity peak at 1383.01  $\text{cm}^{-1}$  indicates the bending vibrations of the -OH group. The stretching vibrations of -OCH<sub>3</sub> are indicated by a peak at 1236.41  $\text{cm}^{-1}$ , while another small peak at 1039.67  $\text{cm}^{-1}$  indicates the stretching vibrations of -CHOH. All these peaks are attributed to [6]-gingerol which will be further confirmed by other spectroscopic techniques, such as NMR spectroscopy.

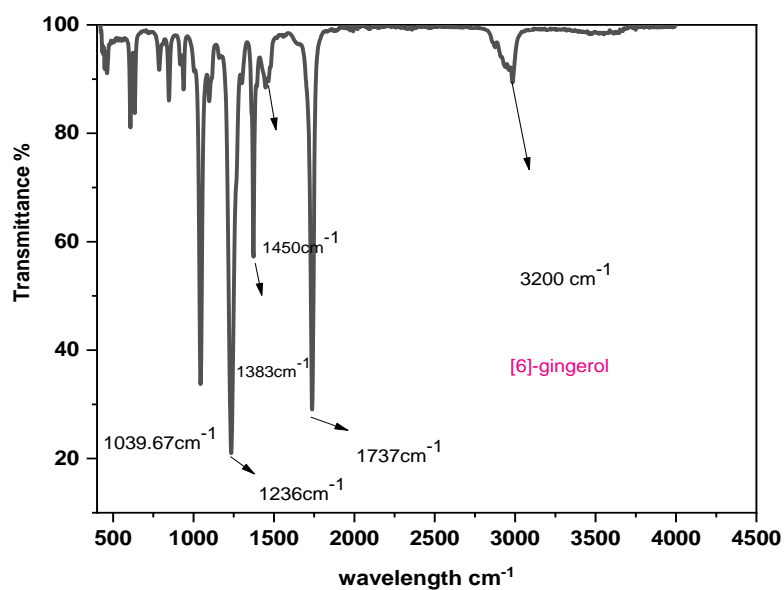


**Figure 4.** FT-IR spectra of [6]-gingerol.

$^1\text{H}$  and  $^{13}\text{C}$  Nuclear Magnetic Resonance (NMR): (DMSO- $d_6$ ).  $^1\text{H}$ NMR shows the following peaks (**Figure 5**): 0.6-1.5 (3H, t,  $j=6.6\text{Hz}$ ), 1.9-2.2 (8H, m), 2.2-2.5 (1H, d,  $j=8\text{Hz}$ ), 2.67-2.85 (2H, s), 3.8 (3H, s,  $-\text{OCH}_3$ ), 6.63 (1H, s), 6.77 (1H, s), 6.7 (1H, s). In this spectrum  $^1\text{H}$ NMR exhibits separate signals for the presence of  $-\text{OCH}_3$  group with a chemical shift at 3.837 and signals of three aromatic protons were assigned to chemical shift at 6.63, 6.77 and 6.78. In this spectrum  $\delta$  value at 0.6-1.5 is relevant to  $-\text{CH}_3$  groups and the rest of protons such as  $\delta$  value at 1.6-1.9, 2.2-2.5, 2.67-2.85 is corresponds to  $-\text{CH}_2-$  groups in aliphatic region.



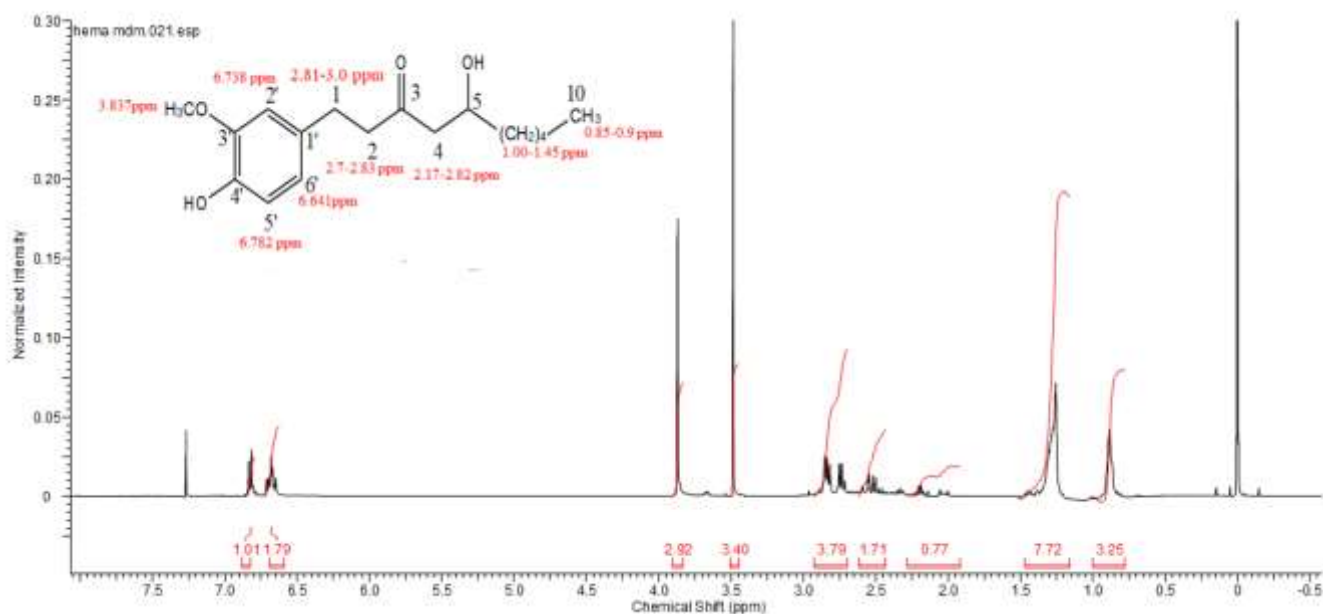


**Figure 5.**  $^1\text{H}$ NMR (400MHz,  $\text{DMSO-d}_6$ ) spectra of [6]-gingerol.

The  $^{13}\text{C}$  NMR(DEPT) spectrum in **Figure 6** indicates the compound [6]-gingerol based on the 17 peaks for 17 carbons in the molecule.  $\delta$ : 13.7 (C-10), 22.35 (C-9), 24.79 (C-7) 29.28 (C-8), 30.84 (C-1), 36.6 (C-6), 45.44(C-2), 49.11 (C-4), 55.50 (-OCH<sub>3</sub>), 67.69 (C-5), 110.91 (C-2), 114.63 (C-5), 121.0 (C-6), 133.4 (C-1), 143.7 (C-4), 146.38 (C-3), 211.2 (C-3).  $^{13}\text{C}$  NMR (DEPT) spectrum shows signals of one methoxy group at  $\delta\text{C}=55.50$ , one carbonyl carbon at ( $\delta\text{C}=211.2$ ) as well as two oxygen groups of one aromatic ring [( $\delta\text{C}=146.38$ , C-3 and 143.7, C-4)].

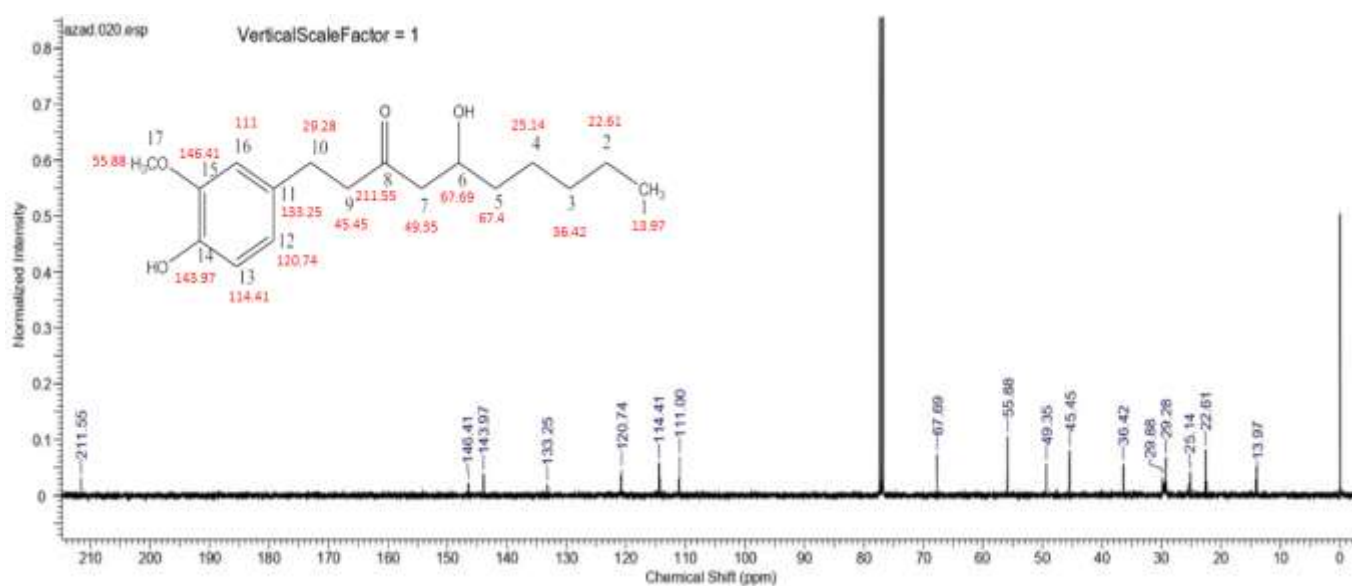


**Figure 6.**  $^{13}\text{C}$ NMR (100MHz,  $\text{DMSO-d}^6$ ) spectra of [6]-gingerol.

*ESI- mass spectrometry:* **Figure 7** shows the deprotonated form [6]-gingerol with the  $m/z$  value of 294. One of the prominent peaks of 276 is generated by the loss of a water molecule from the  $m/z$  294. [6]-gingerol produces abundant product ions of  $m/z$  137 and 192, as well as small fragment ions of  $m/z$  179, 205 and 235 due to cleavage of the C4-C5 bonds. The loss of the methyl radical from the ion of  $m/z$  192 results in the formation of the product ion of  $m/z$  179, while the elimination of the hexanal (100u) results in the formation of an ion of  $m/z$  192.

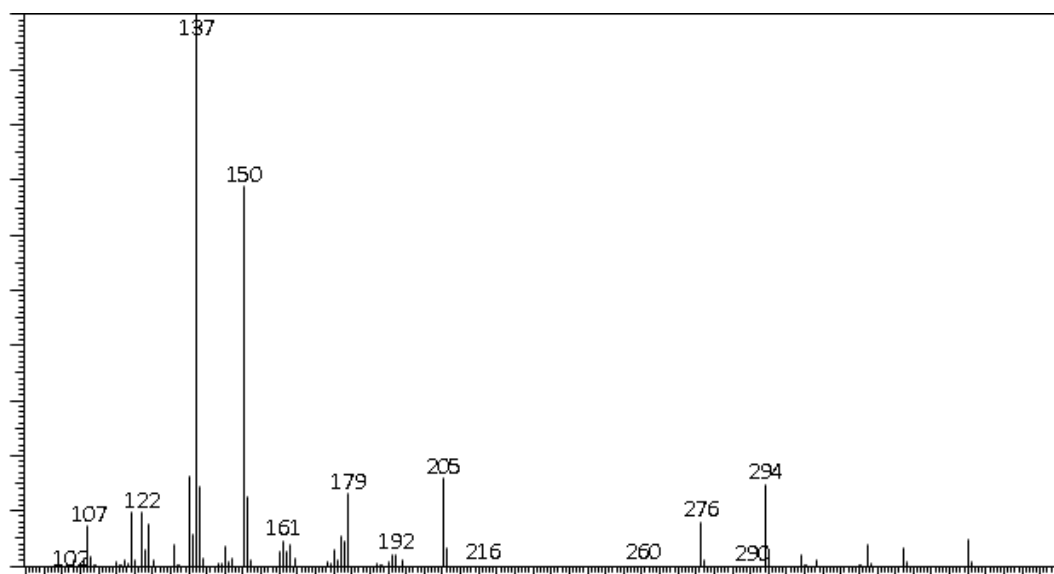


**Figure 7.** Negative ion electrospray product ion mass spectrum of [6]-gingerol.

### 2.3.2 Characterization of MIPs

The appearance of broad band  $3200\text{cm}^{-1}$  in the spectrum can be attributed to -OH stretching vibrations that are stretched as a result of crosslinked formation as seen in (**Figure 8**). The presence of bands with strong to medium intensities, due to the carbonyl, were observed at  $1737\text{cm}^{-1}$ . Peaks at  $1631.83\text{cm}^{-1}$ ,  $1535\text{cm}^{-1}$ , and  $1425\text{cm}^{-1}$  indicated stretching vibrations of the aromatic ring, -OH bending vibrations were indicated by a little and low-intensity peak at  $1383.01\text{cm}^{-1}$  and -OCH<sub>3</sub> stretching vibrations were indicated by a small and low-intensity peak at  $1266.41\text{cm}^{-1}$ , while another minor peak at  $1139.67\text{cm}^{-1}$  indicates -CHOH stretching vibrations.

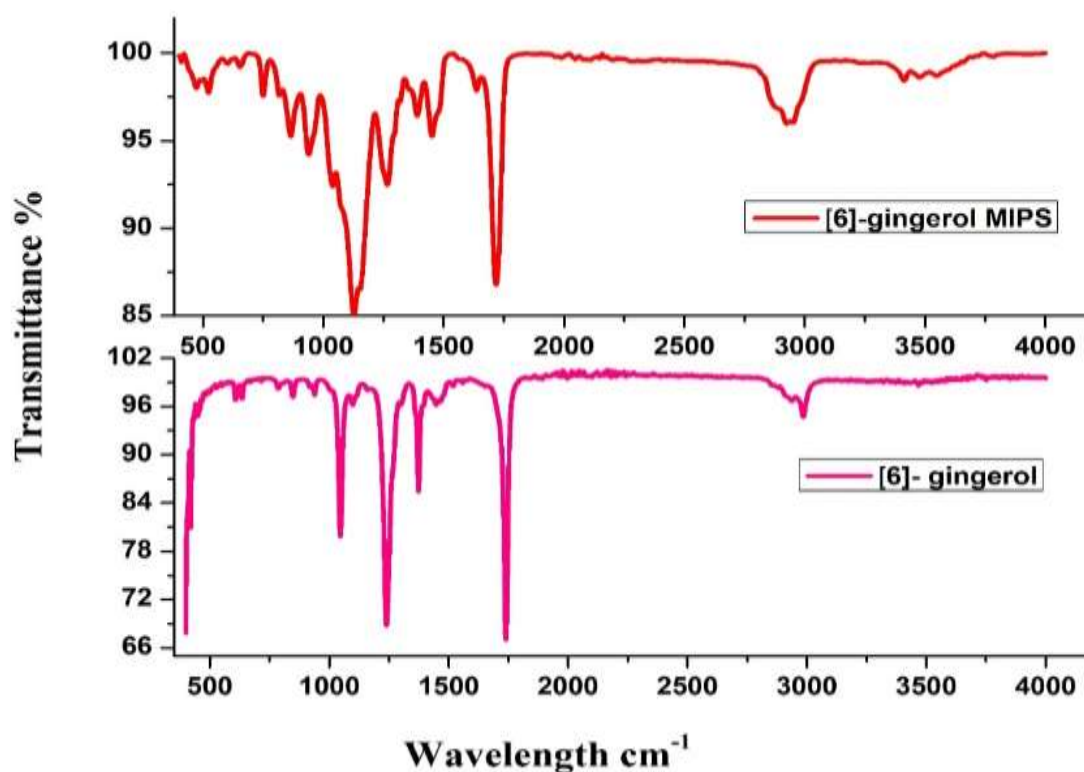


**Figure 8.** FTIR images of [6]-gingerol and [6]-gingerol MIP

### 2.3.3 Characterization of Mn-doped ZnS molecular imprinted polymer (MIP)

The structure of Mn<sup>2+</sup>-doped ZnS samples was investigated using the monochromatic X-ray diffraction technique (**Figure 9**). The X-ray diffraction pattern was recorded in the range from 20 to 90°. The X-ray diffraction peaks were obtained at 22.70°, 30.08° and 46.42° corresponding to the diffraction planes (111), (220) and (311) with (JCPDS) database, no.80-0020), which confirms the zinc blende structure of the compound. The presence of peaks suggested the crystalline nature of the compound. The crystallite size was calculated using the Debye-Scherrer relation. [15]. The most intense peak was observed at (111) plane and the average crystalline size was found to be 2-5nm. Due to their cross-linking and rigid nature of the polymer, when QDs are embedded into the matrix of the MIPs the peaks of XRD were broadened, which accelerates the rigidness of the composite material and is confirmed by the SEM images (**Figure 9**). The increased crosslinked results in the aggregation of particles, the size of the composite was discovered to be greater in size than XRD and was around 60-80 nm in SEM investigation.

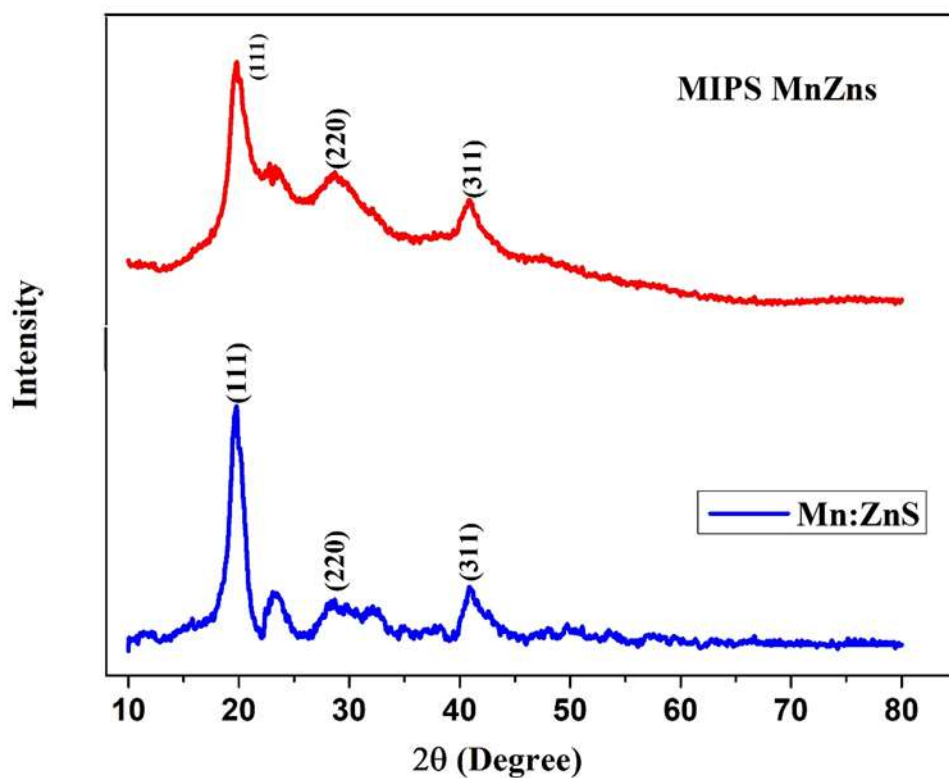


**Figure 9.** XRD of Mn doped ZnS and MIPS coated Mn doped ZnS

The morphological structure of  $\text{Mn}^{2+}$  doped ZnS QDs was studied using SEM analysis. The Powder exhibited blocked particles and irregular shapes due to agglomeration among particles. The SEM images revealed the size of QDs size to be in the range of 8-10nm in (**Figure 10**). MIPS encapsulated Mn-doped ZnS QDs were found to be larger than Mn-doped ZnS, indicating that the QDs were successfully embedded in the matrix of MIPS.

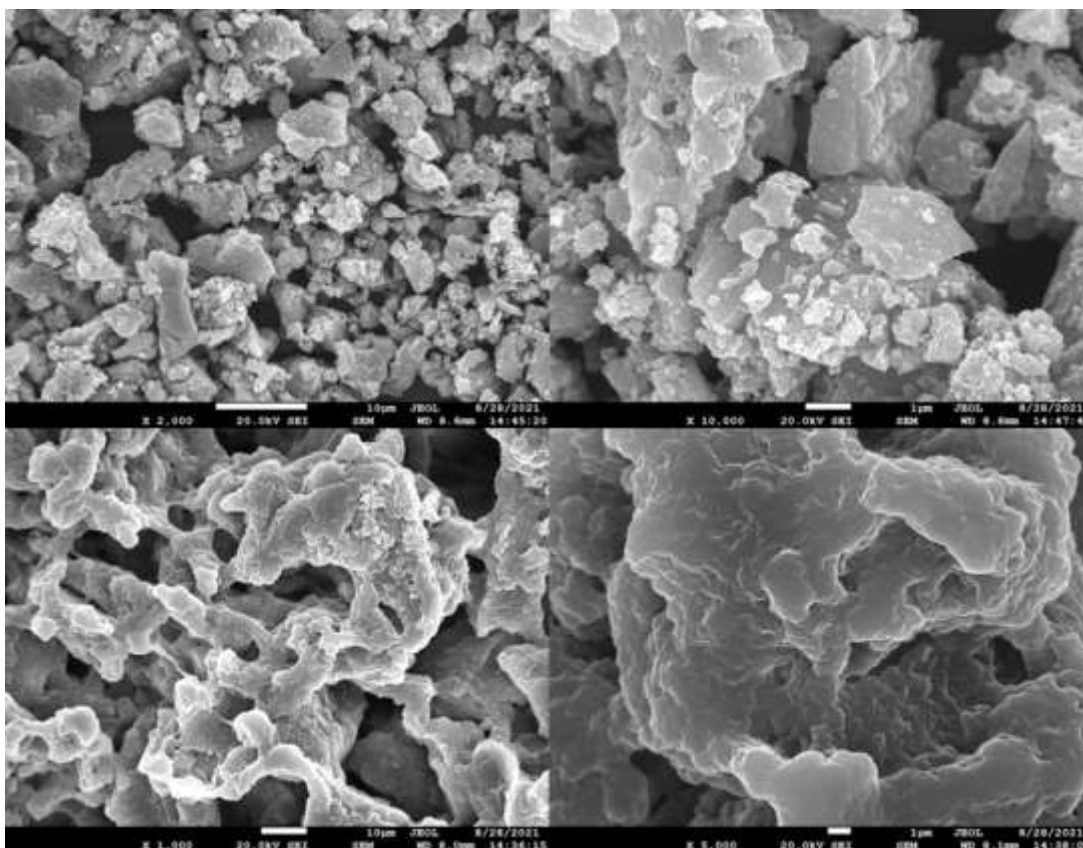


**Figure 10.** SEM images of Mn-doped ZnS at different magnifications (**10 $\mu$ m, 1  $\mu$ m**) FESEM images of MIPs coated Mn doped ZnS of different resolution (**10 $\mu$ m, 1 $\mu$ m**).

#### 2.3.4 Thermal studies of MIP composite

The thermogravimetric analysis-differential scanning calorimetry (TGA-DSC) method was used to study the polymers' thermal characteristics. The loss of the adsorbed water and residual solvent molecules generated the first weight loss (4%) seen at temperatures below 213°C, as illustrated in **Figure 11**. From 250 to 450 °C, the polymer's thermal decomposition was characterized by a main weight loss. The polymer was totally degraded at 450°C. Below 220 °C, weight loss (4%) was caused by the desorption of water and residual solvent molecules, the characteristic is determined by the shape and crystallinity of the polymer. The removal of water molecules and the entrapped solvent molecules created two endothermic peaks on the imprinted polymer (MIPs QDs) in DSC thermogram at 221°C and 329 °C. Crosslinker and gingerol molecule loss was speculated to be responsible for the significant endothermic peak at 329°C. Decomposition of polymer could explain the final endothermic peak at 431°C. Glass-transition temperature ( $T_g$ ) of the polymer composite was 221°C, according to DSC thermograms. Polymer composite has a melting point of 329 °C. The features of the solid-state, like  $T_g$ , can be used to determine polymer miscibility [143].

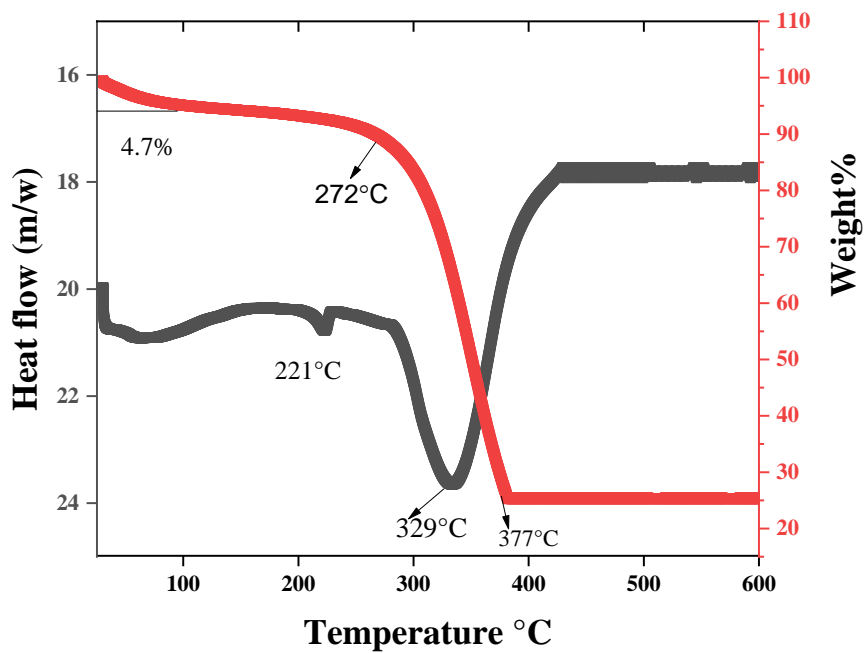


**Figure 11.** TGA-DSC plot of MIPs/QDS with 10°C heating rate under nitrogen atmosphere

### 2.3.5 MIPS encapsulated QDs theoretical modelling

The modelling of an MIP-QDs system was performed following the experimental procedure. In the initial part, a two-layer ZnS wurtzite was constructed with formula:  $Zn_{32}S_{32}$  and  $x=21.6$  Å,  $y=9.79$  Å and  $z=6.03$  Å dimensions, with a final volume of  $1275.12$  Å<sup>3</sup> and a density of  $4054.9$  kg/m<sup>3</sup> which is relatable to that reported for ZnS:  $4090$  kg/m<sup>3</sup> at STP conditions **Figure 12**. The increased theoretical mass density comes from the assumption that no defects are present and therefore there are no atom vacancies.

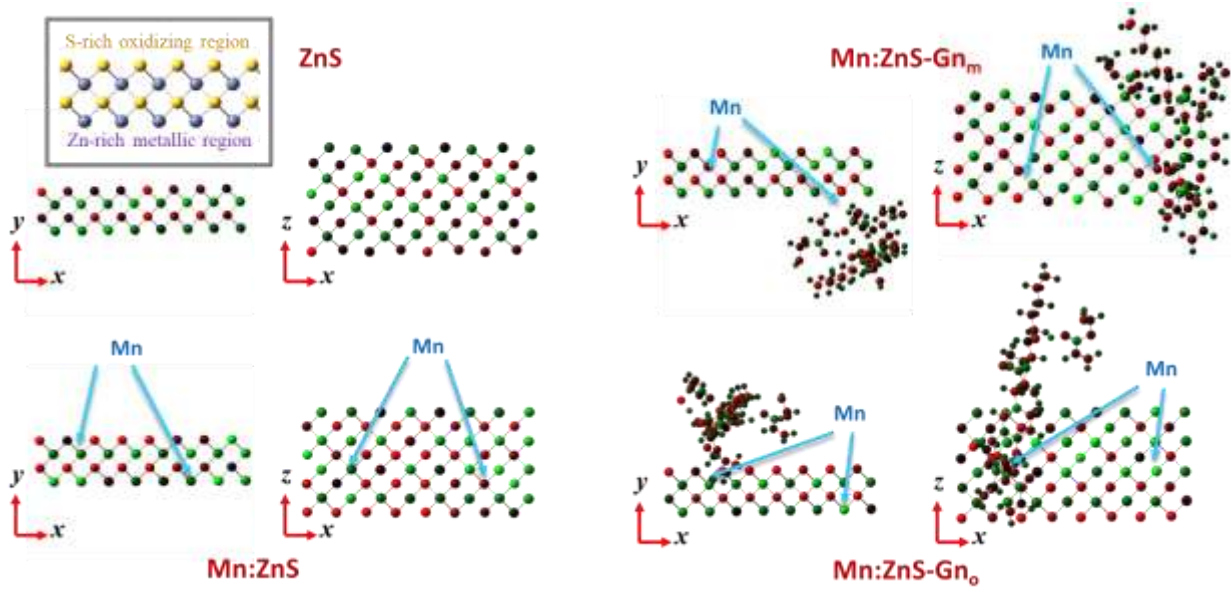


**Figure 12.** Selected geometrical Mn doping and MIP deposition effect over Mulliken charge in ZnS derived materials.

Optimization of ZnS shows that there are two identifiable regions in the layer, the outer S-rich region and the inner Zn-rich region. Mulliken charge analyses reveals that S region has a tendency towards negative dipole which is understandable given the oxidizing nature of sulfur [144]. On the other side, embedded  $Zn^{2+}$  ions give a positive charge to the local environment in ZnS, it would be easier to replace Zn for Mn during doping process[145]. In the model, two metal substitution sites were studied: Mn substitution at the metallic region and substitution at oxidizing region. In Mn: ZnS, manganese atoms create a local defect in charges. The smaller size of the atom would quench steric hindrance allowing electron transfer within the cell. Mn acts as an electron sink where highly energetic electrons could be allocated. This observation is confirmed in Mulliken Charge analyses, where the presence of Mn creates a local imperfection that unbalances atomic charges **Figure 13**.



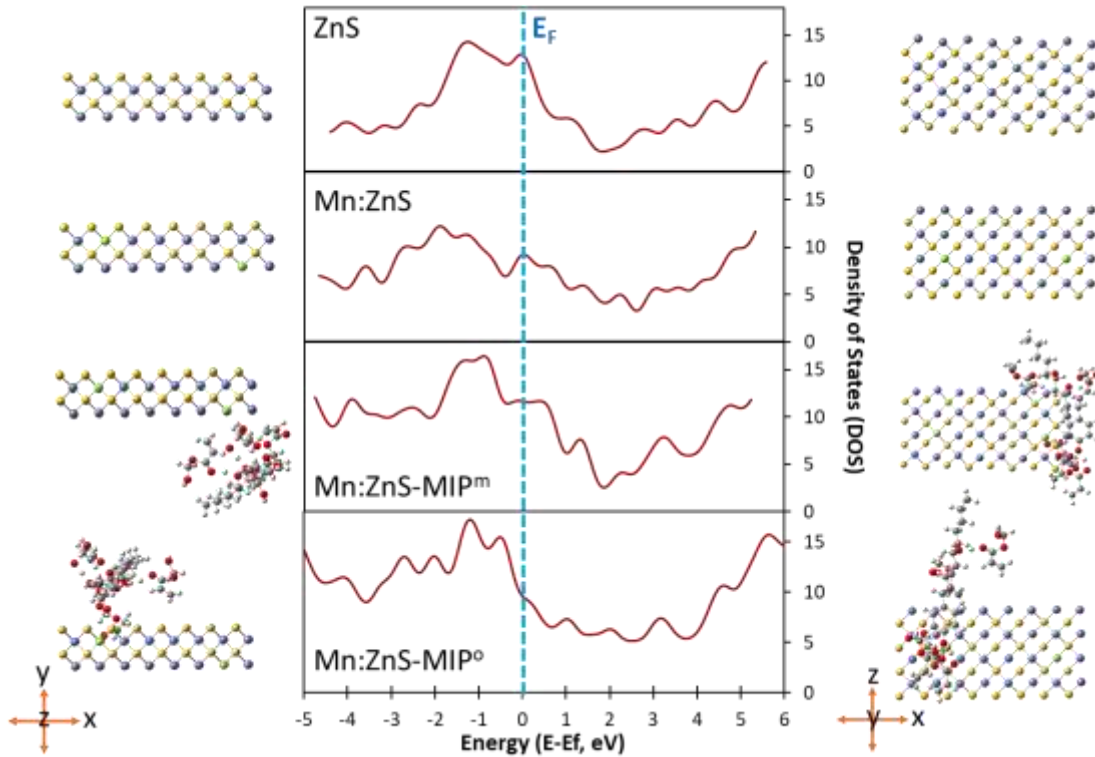


**Figure 13.** Density of States analysis showing the semiconductor band system in ZnS and ZnS derivatives.

Valence band is located at the sulfur side because of its oxidizing nature. However, Zn atoms can also provide intermediate states from expanded and conjugated  $\pi$  molecular orbitals [146]. The changes in energy between different d arrangements ( $d_{xy}$ ,  $d_{xz}$ ,  $d_{yz}$ ,  $d_{x^2-y^2}$  and  $d_{z^2}$ ) [147] and the geometrical differences [148] could therefore explain the bumpy diffuse conduction band that was identified at  $E > 3.5$  eV as shown in **Figure 14**.

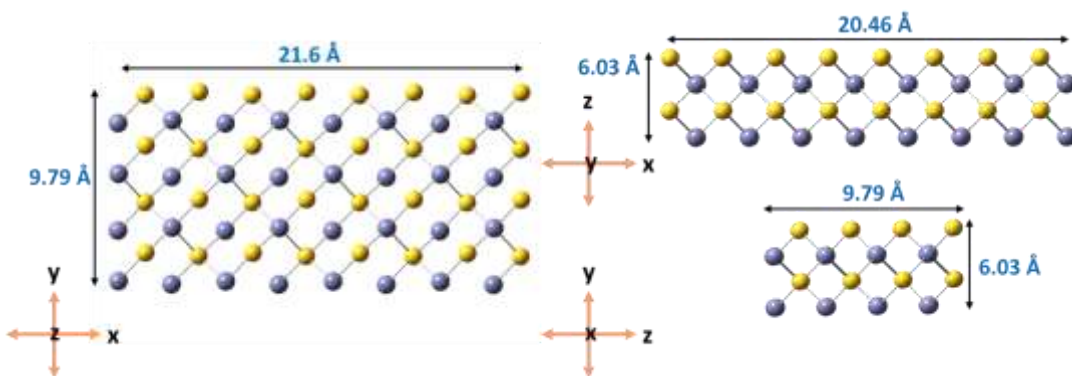


**Figure 14.** Starting geometry for ZnS matrix



**Figure 15** depicts the frontier molecular orbitals of ZnS materials at Valence ( $V_b$ ), First conduction ( $C_{b1}$ ) and Second Conduction band ( $C_{b2}$ ). Calculated bandgap energy of ZnS was 3.61 eV, on close accordance with the typical 3.5-3.6 eV usually reported [149]

Charge transport effect from MIP molecule is clear and tends to grow as polymer length increases [150]. However, the position of MIP center does not seem to have important changes to semiconductor's band composition; this result shows that addition of MIPs can enhance photocatalytic behavior, no matter the orientation.

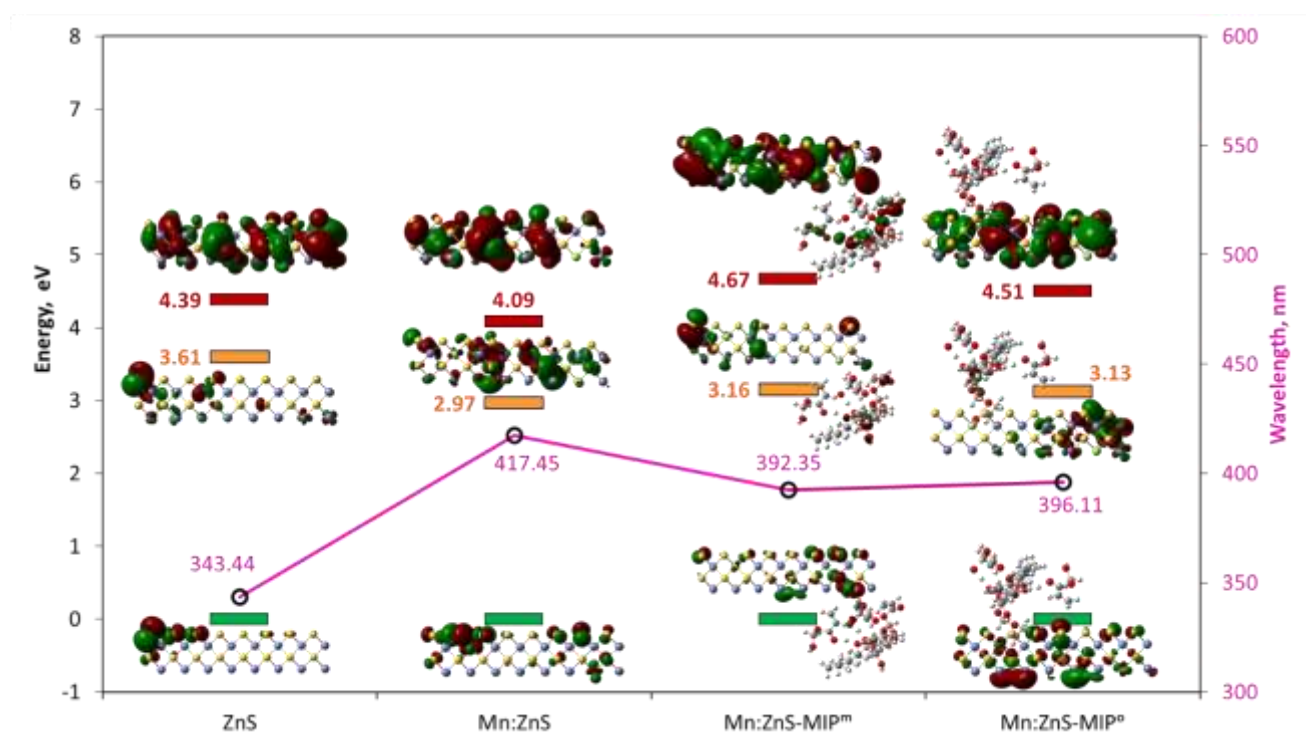


**Figure 15.** Frontier molecular orbitals and photocatalytic potential for optimized ZnS materials.

### 2.3.6 Photodegradation of norfloxacin and paracetamol by MIPs encapsulated QDs

The photocatalytic degradation efficiency of MIPs coated QDs were tested against Norfloxacin and Paracetamol in an aqueous solution under Irradiation by using a 40 W Xe lamp Uv light. The photocatalytic studies were investigated by dissolving (0.2 mg/mL) of NOFX and paracetamol in an aqueous solution. To optimize the effect of catalyst and pH values,

concentration was kept constant (0.2 mg/mL) in the solution. The reaction was conducted on a batch reactor at room temperature. Different reaction solutions were prepared by adding varying doses of catalyst and pH values. Sample aliquots from the solution were centrifuged at various time intervals to examine drug degradation in UV spectra. The efficiency of MIPs coated Mn-doped ZnS QDs was demonstrated by a decrease in the absorbance of drug samples after irradiation for a given time interval.

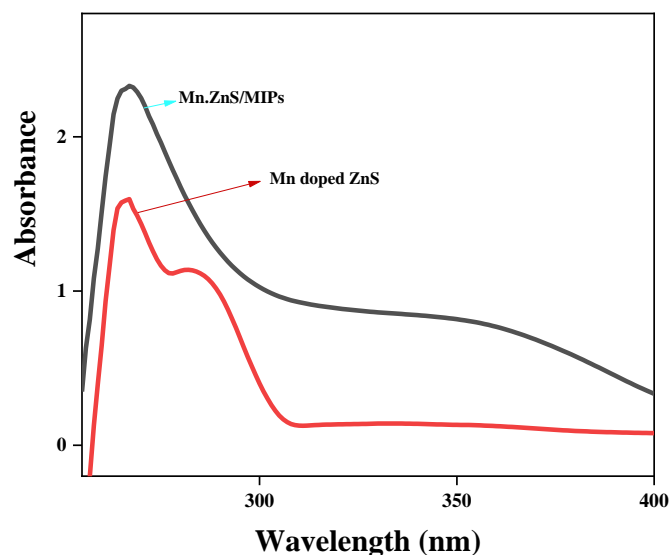


**Figure 16.** Uv spectra of Mn doped ZnS and Mn.ZnS/MIPs nanocomposite.

1. *Effect of catalysis dosage:* The amount of photocatalyst dose is an important parameter in the photodegradation of pollutants. The concentration of catalyst was varied from 20 to 50 mg and the concentration of the pollutant was maintained constant at 20mg/L. The degradation efficiency of the pollutant accelerates during the increased amount of catalyst against NOFX and paracetamol to 84% and 80%. Active sites of the catalyst may enhance the degradation of drug pollutants. However, adding more catalysts will reduce light penetration, resulting in a reduction in the volume of photoactive suspension. **Figure 17A and 17E** below shows that a catalyst concentration of 50 mg/25 mL is appropriate for maximum degradation of pollutants.

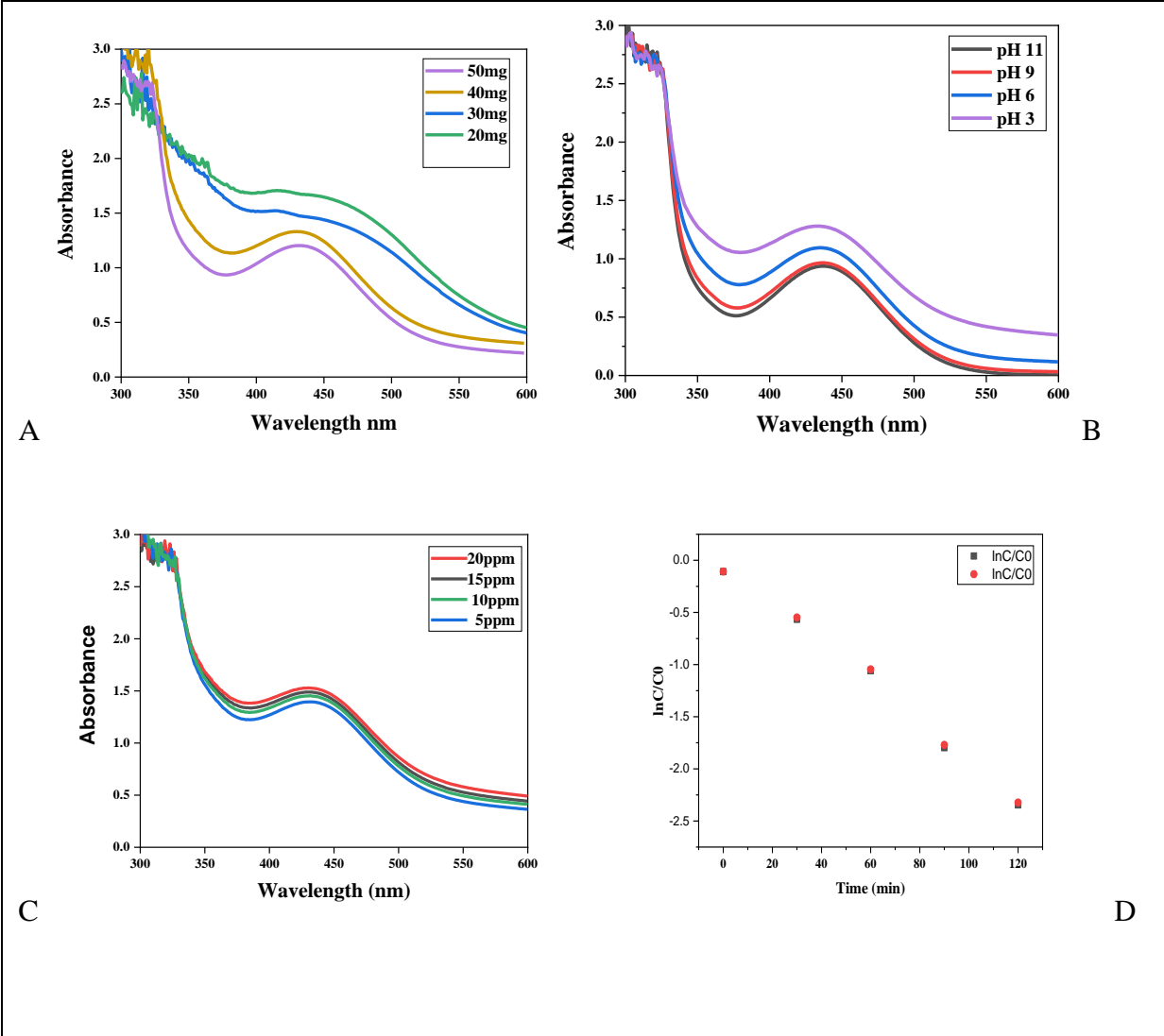
2. *Effect of pH:* The effect of pH on the degradation of Norfloxacin and Paracetamol are shown in **Figure 17B** and **17F**, respectively. The optimum pH for norfloxacin degradation appears to be 9-11 and shows low degradation at an acidic pH value. The optimum pH for Paracetamol decomposition appears to be 11 and shows a lower degradation rate between 3 and 6. The reaction rate constants are lower at acidic pH values between 2 and 4 because the  $\cdot\text{OH}$  generated in the reaction medium weakly interacts with paracetamol drug due to the possibility of recombination of these  $\cdot\text{OH}$  with  $\text{H}^+$  and hydronium ions ( $\text{H}_3\text{O}^+$ ) in the photocatalytic process

to form water molecules. The magnitude of the reaction rate is constant and consequently, the photodegradation efficiency is greater at pH 11, which may be due to the increased production of hydroxyl radicals at high pH values as more  $\cdot\text{OH}$  groups are available on the Nano catalyst surface to easily oxidize. The polar groups and aromatic moiety of paracetamol engage specifically with MIPs coated Mn-doped ZnS, resulting in good adsorption, whereas free produced and accessible  $\cdot\text{OH}$  species interact with paracetamol molecules more to degrade them. The kinetic analysis of the obtained results revealed that the current heterogeneous photocatalytic process follows the pseudo-first-order kinetics in different pH values ( $\ln(C_t/C_0) = -kt$ ), where  $C_0$  and  $C_t$  are the concentration of dye at time = 0 and time = t (in mg/L), respectively,  $k$  is the reaction rate constant ( $\text{min}^{-1}$ ) [151]. The fitted kinetic model in the presence of MIPs covered ZnS QDs yielded the following result. The photodegradation of NOFX catalyzed by MIPs coated ZnS QDs follows pseudo-first-order kinetics, as shown in the **Figure 17D** and **G** which shows a linear relationship between  $\ln(C_t/C_0)$  and time with appropriate correlation coefficients ( $R^2$ ) [152].

### 3. *Effect of pollutant concentration;*

**Figure 17C** and **17G** depicted the degradation efficiency of Norfloxacin and Paracetamol for Mn.ZnS/ MIPs. It was observed that the degradation efficiency decreased with an increase in concentration. This can be attributed to the fact that higher concentrations of the pollutant led to increased adsorption of the pesticide on the active sites of the catalyst. Consequently, there was a decrease in the competitive adsorption of  $\text{O}_2$ ,  $\text{H}_2\text{O}$ , and  $\text{OH}^-$  on the same site, resulting in fewer  $\text{OH}$  radicals being formed.  $\text{OH}$ , radicals are the primary oxidants required for achieving high degradation efficiency.

This decrease in degradation efficiency can be explained by the fact that as the concentration of drug increases, the path length of photons entering the solution becomes shorter. As a result, there is less photon adsorption on the catalyst surface, leading to a lower observed degradation rate.



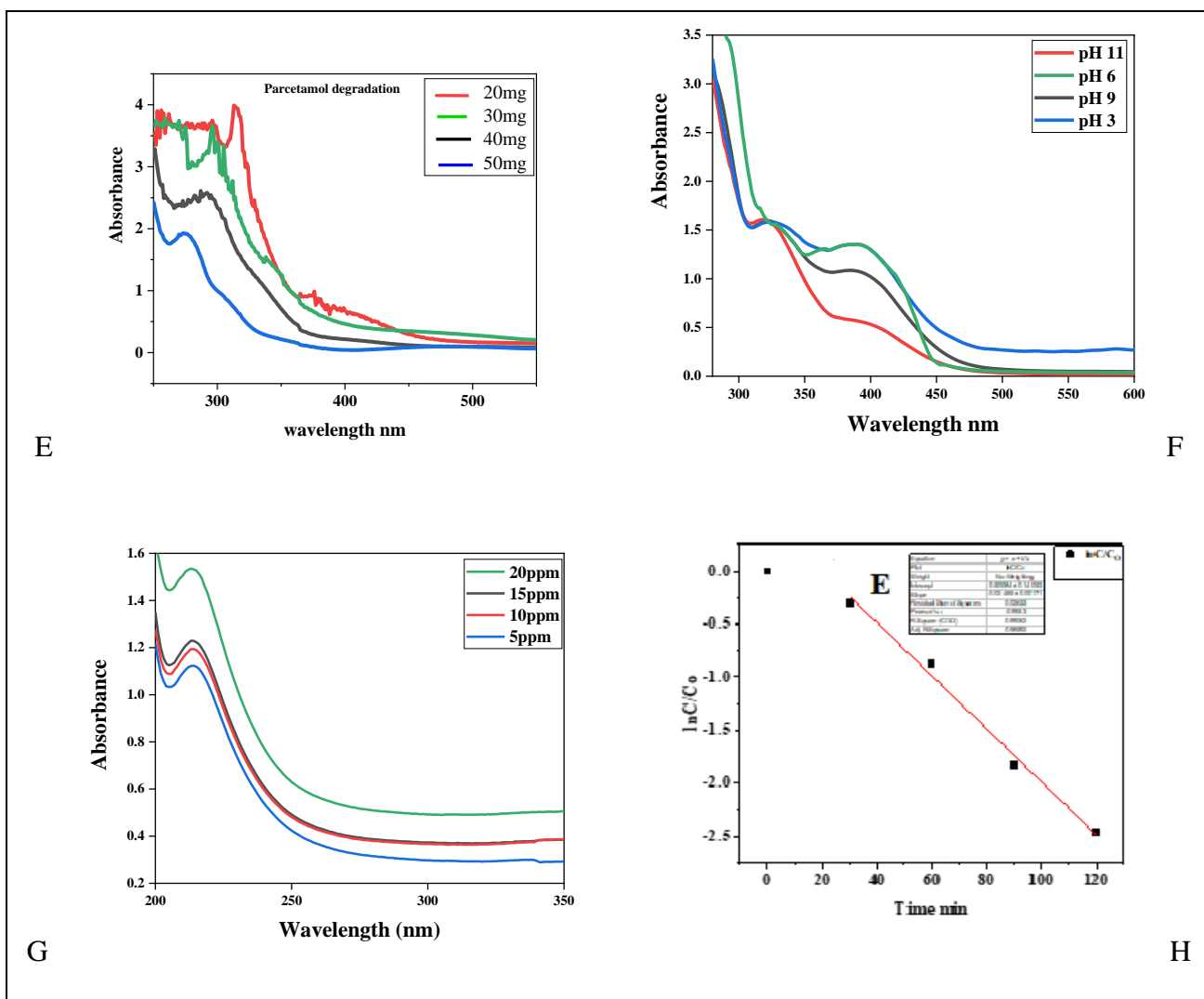


**Figure 17.** Photodegradation of NOFX and Paracetamol by Mn-doped ZnS at different catalyst doses.

#### 2.4 Degradation kinetics

The degradation rates of Mn-doped ZnS MIPs composite under UV irradiation were estimated in **Figure 18**. The degradation rates of NOFX and paracetamol were found to be 84% and 80%, respectively indicating that photocatalytic degradation of NOFX and paracetamol is the most efficient under UV irradiation. The radicals generated can only react with pharmaceuticals that have been dissociated, photocatalytic activities are usually carried out in water.

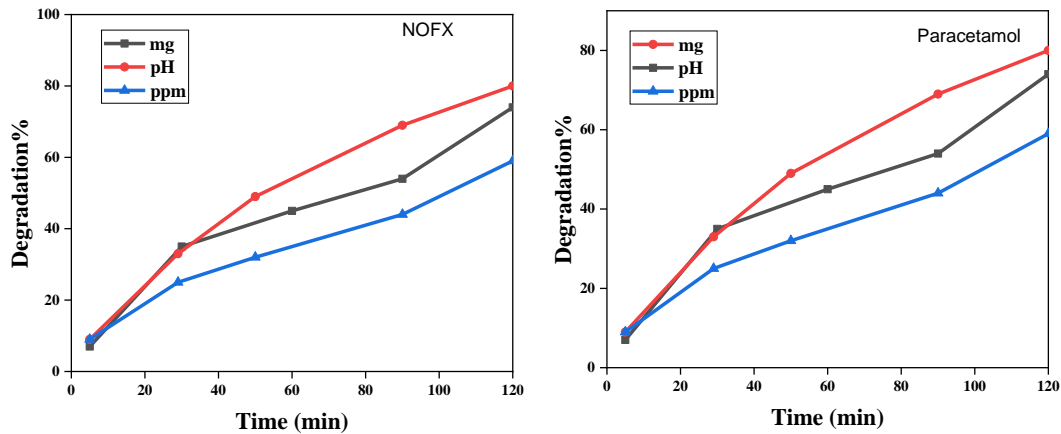


**Figure 18.** Degradation efficiency of MN. ZnS/MIPs against NOFX and paracetamol.

The degradation process can be explained with the help of bandgap energy. When the Semiconducting material is bombarded with photons of light that are equivalent to or slightly higher than the bandgap of the semiconductor photocatalyst, the excitation of semiconducting QDs takes place. This produces an exciton ( $e^-/h^+$  pair) at the surface of the charge carriers [153]. When these  $e^-$  and  $h^+$  recombine or float to the photocatalyst surface, photo-active centres occur. The degradation efficiency is influenced by the overall number of charge carriers at the photocatalyst surface. Because of its high oxidation potential,  $h^+$  can oxidize organic materials (NOFX, Paracetamol) both indirectly and directly [154]. Under alkaline conditions, the surface of Mn/ZnS can acquire a negative charge. This negative charge arises from the dissociation of water molecules and the subsequent adsorption of hydroxide ions ( $\text{OH}^-$ ) onto the surface of the Mn/ZnS QDs. The hydroxide ions contribute to the negative zeta potential shown in **Figure 19**, which results in the repulsion of protons ( $\text{H}^+$ ) from the surface [155].

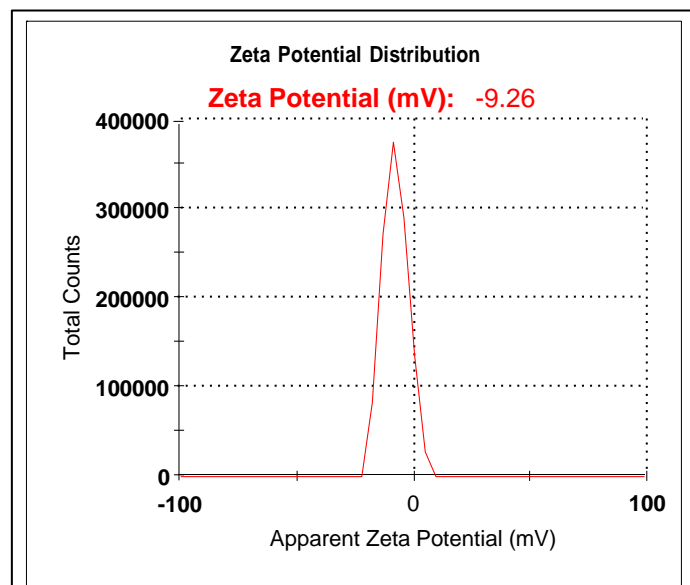


**Figure 19.** Zeta potential of MIPs/ZnS at pH 11 alkaline solution.

It is important to note that while the negative zeta potential repels protons, it does not directly produce them. The production of protons ( $H^+$ ) typically occurs through other chemical processes, such as the dissociation of water or the release of protons from acidic substances. The reactive hydroxide radicals ( $\cdot OH$ ) are formed during indirect oxidation when  $h^+$  reacts with  $H_2O$  or hydroxide anions,

This  $\cdot OH$  is a powerful oxidant ( $E= 3.06$  V) that oxidizes pharmaceuticals and other organic materials to mineral species in a non-selective manner. Furthermore, oxygen atoms on the surface as well as the doped metal act as a sink for  $e^-$  improving the exciton separation. The conduction band on the surface of ZnS has the potential to convert molecular oxygen ( $O_2$ ) into the superoxide anion  $O_2\cdot^-$ . After that, the  $O_2$  interacts with  $H_2O$  to produce  $H_2O_2$ , produces  $\cdot OH$  radicals [155]. The  $h^+$ ,  $e^-$ ,  $\cdot OH$ ,  $O_2\cdot^-$  and  $O_2$  itself play an important role in the photodegradation pathway depending on the specific experimental condition. As a result, the  $\cdot OH$  created by  $e^-$  in the conduction band can trigger organic matter mineralization.

The generation of extra  $\cdot OH$  and  $O_2\cdot^-$  improves photocatalytic degradation when the catalyst is doped with transition metal ions. Because doping allows charge carriers ( $e^-$  and  $h^+$ ) to be trapped and their lives to be extended, dopants improve photocatalytic efficiency[156].

## 2.5 Conclusions

In this paper [6]-gingerol was successfully extracted by the Soxhlet method and fully characterized by different spectroscopic techniques. Molecular imprinted polymer was synthesized by using [6]-gingerol as a template molecule, 2-hydroxymethacrylic as the monomer, EGDMA as the crosslinker and AIBN as the initiator. The reaction was proceeded by Ex-situ polymerization method using Mn-doped ZnS QDs as a inorganic nanocomposite porous material. The material was characterized using IR, HPLC, Mass Spectra, NMR, XRD and SEM. This material was evaluated as a photocatalyst for the degradation of Norfloxacin and paracetamol, both are considered organic in the presence of UV and visible light, the photocatalyst demonstrated excellent degradation efficiency of more than 80% in 120 min. Variation of photocatalytic concentration (20, 30, 40, 50 mg) can be utilised to degrade norfloxacin and paracetamol and optimized at different pH values. The degradation of the catalyst follows a pseudo-first-order reaction kinetics. Experimental and theoretical findings support the claim that addition of MIPs actively enhance semiconductor charge carriers in order to trigger photocatalytic degradation of pharmaceutical drugs.

## 2.6 References

- [129] Y. Chen, Chapter 8 - Photodegradation of pharmaceutical waste by nano-materials as photocatalysts, in: P. Singh, A. Borthakur, P.K. Mishra, D. Tiwary (Eds.), *Nano-Materials as Photocatalysts for Degradation of Environmental Pollutants*, Elsevier, 2020: pp. 143–152. <https://doi.org/10.1016/B978-0-12-818598-8.00008-0>.
- [130] M. El-Kemary, H. El-Shamy, I. El-Mehasseb, Photocatalytic degradation of ciprofloxacin drug in water using ZnO nanoparticles, *Journal of Luminescence - J LUMINESC.* 130 (2010) 2327–2331. <https://doi.org/10.1016/j.jlumin.2010.07.013>.
- [131] S.K. Fanourakis, J. Peña-Bahamonde, P.C. Bandara, D.F. Rodrigues, Nano-based adsorbent and photocatalyst use for pharmaceutical contaminant removal during indirect potable water reuse, *Npj Clean Water.* 3 (2020) 1–15. <https://doi.org/10.1038/s41545-019-0048-8>.
- [132] R.N. Bhargava, D. Gallagher, X. Hong, A. Nurmikko, Optical properties of manganese-doped nanocrystals of ZnS, *Phys. Rev. Lett.* 72 (1994) 416–419. <https://doi.org/10.1103/PhysRevLett.72.416>.
- [133] P.H. Borse, N. Deshmukh, R.F. Shinde, S.K. Date, S.K. Kulkarni, Luminescence quenching in ZnS nanoparticles due to Fe and Ni doping, *Journal of Materials Science.* 34 (1999) 6087–6093. <https://doi.org/10.1023/A:1004709601889>.
- [134] I.A. Banerjee, L. Yu, H. Matsui, Room-Temperature Wurtzite ZnS Nanocrystal Growth on Zn Finger-like Peptide Nanotubes by Controlling Their Unfolding Peptide Structures, *J. Am. Chem. Soc.* 127 (2005) 16002–16003. <https://doi.org/10.1021/ja054907e>.
- [135] P.J. Binu, S. Muthukumar, Band Gap Tailoring, Size Modulation and Photoluminescence Properties of Mn/Cu doped ZnS Nanostructures, *In Review*, 2021. <https://doi.org/10.21203/rs.3.rs-216184/v1>.
- [136] R.K. Chandrakar, R.N. Baghel, V.K. Chandra, B.P. Chandra, Synthesis, characterization and photoluminescence studies of Mn doped ZnS nanoparticles, Superlattices and Microstructures. 86 (2015) 256–269. <https://doi.org/10.1016/j.spmi.2015.07.043>.
- [137] T. Thi, N. Hien, D. Thu, V. Quoc Trung, Thin films containing Mn-doped ZnS nanocrystals synthesised by chemical method and study of some of their optical properties, *Journal of Experimental Nanoscience.* 8 (2013) 530–538. <https://doi.org/10.1080/17458080.2011.599045>.
- [138] L. Fang, K. Tang, D. Wei, Y. Zhang, Y. Zhou, Photocatalytic Degradation of Norfloxacin By Magnetic Molecularly Imprinted Polymers: Influencing Factors And Mechanisms, 2021. <https://doi.org/10.21203/rs.3.rs-392691/v1>.
- [139] I. Shahnavi, R. Bano, S. Musharraf, M. Sheraz, S. Hussain, S. Ahmed, H. Tahir, Q. Ul Arfeen, M.S. Bhatti, Z. Shad, Photodegradation of Norfloxacin in Aqueous and Organic Solvents: A Kinetic Study, *Journal of Photochemistry and Photobiology A Chemistry.* 302 (2015) 1–10. <https://doi.org/10.1016/j.jphotochem.2015.01.005>.
- [140] L. Li, X. Zheng, Y. Chi, Y. Wang, X. Sun, Q. Yue, B. Gao, S. Xu, Molecularly imprinted carbon nanosheets supported TiO<sub>2</sub>: Strong selectivity and synergic adsorption-photocatalysis for antibiotics removal, *Journal of Hazardous Materials.* 383 (2020) 121211. <https://doi.org/10.1016/j.jhazmat.2019.121211>.
- [141] M. Cantarella, A. Di Mauro, A. Gulino, L. Spitaleri, G. Nicotra, V. Priviter, G. Impellizzeri, Selective photodegradation of paracetamol by molecularly imprinted ZnO nanonuts, *Applied Catalysis B: Environmental.* 238 (2018). <https://doi.org/10.1016/j.apcatb.2018.07.055>.
- [142] C.A. Huerta-Aguilar, A.A. Ramírez-Alejandre, P. Thangarasu, J.A. Arenas-Alatorre, I.A. Reyes-Dominguez, M. de la L. Corea, Crystal phase induced band gap energy enhancing the photocatalytic properties of Zn–Fe<sub>2</sub>O<sub>4</sub>/Au NPs: experimental and theoretical studies, *Catal. Sci. Technol.* 9 (2019) 3066–3080. <https://doi.org/10.1039/C9CY00678H>.



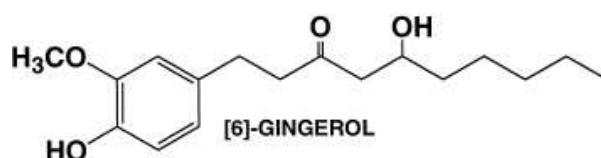
- [143] G. Murugadoss, Synthesis, optical, structural and thermal characterization of Mn<sup>2+</sup> doped ZnS nanoparticles using reverse micelle method, *Journal of Luminescence*. 131 (2011) 2216–2223. <https://doi.org/10.1016/j.jlumin.2011.03.048>.
- [144] H.-J. SUN, Y.-Y. LI, S.-H. LI, Y.-X. ZHANG, S.-C. LIU, Z.-Y. LIU, B.-Z. REN, ZnSO<sub>4</sub> and La<sub>2</sub>O<sub>3</sub> as Co-Modifier of the Monoclinic Ru Catalyst for Selective Hydrogenation of Benzene to Cyclohexene, *Acta Physico-Chimica Sinica*. 30 (2014) 1332–1340. <https://doi.org/10.3866/PKU.WHXB201405072>.
- [145] S. Sapra, A. Prakash, A. Ghangrekar, N. Periasamy, D.D. Sarma, Emission Properties of Manganese-Doped ZnS Nanocrystals, *J. Phys. Chem. B*. 109 (2005) 1663–1668. <https://doi.org/10.1021/jp049976e>.
- [146] M.L. Steigerwald, L.E. Brus, Semiconductor crystallites: a class of large molecules, *Acc. Chem. Res.* 23 (1990) 183–188. <https://doi.org/10.1021/ar00174a003>.
- [147] W.-X. Wu, X.-Z. You, A.-B. Dai, S.-P. Jing, Indo/Giao calculations of the NMR shielding constant including d orbitals, *Polyhedron*. 9 (1990) 1849–1854. [https://doi.org/10.1016/S0277-5387\(00\)83997-2](https://doi.org/10.1016/S0277-5387(00)83997-2).
- [148] N. Chestnoy, R. Hull, L.E. Brus, Higher excited electronic states in clusters of ZnSe, CdSe, and ZnS: Spin-orbit, vibronic, and relaxation phenomena, *J. Chem. Phys.* 85 (1986) 2237–2242. <https://doi.org/10.1063/1.451119>.
- [149] X. Wang, H. Huang, B. Liang, Z. Liu, D. Chen, G. Shen, ZnS Nanostructures: Synthesis, Properties, and Applications, *Critical Reviews in Solid State and Materials Sciences*. 38 (2013) 57–90. <https://doi.org/10.1080/10408436.2012.736887>.
- [150] T. Liu, J. Qian, C. Wang, Y. Wang, Y. Yang, B. Kong, Y. Qian, W. Wu, Enhanced photocatalytic degradation performance of mono-disperse ZnS nano-flake on biocarbon sheets, *Inorganic Chemistry Communications*. 119 (2020) 108142. <https://doi.org/10.1016/j.inoche.2020.108142>.
- [151] M. Roushani, M. Mavaei, Graphene quantum dots as novel and green nano-materials for the visible-light-driven photocatalytic degradation of cationic dye, *Journal of Molecular Catalysis A: Chemical*. 409 (2015) 102–109. <https://doi.org/10.1016/j.molcata.2015.08.011>.
- [152] H.R. Rajabi, O. Khani, M. Shamsipur, V. Vatanpour, High-performance pure and Fe<sup>3+</sup>-ion doped ZnS quantum dots as green nanophotocatalysts for the removal of malachite green under UV-light irradiation, *J Hazard Mater*. 250–251 (2013) 370–378. <https://doi.org/10.1016/j.jhazmat.2013.02.007>.
- [153] H.R. Pouretedal, H. Eskandari, M. Keshavarz, A. Semnani, Photodegradation of organic dyes using nanoparticles of cadmium sulfide doped with manganese, nickel and copper as nanophotocatalyst, *Acta Chimica Slovenica*. 56 (2009) 353–361.
- [154] T. Oyama, A. Aoshima, S. Horikoshi, H. Hidaka, J. Zhao, N. Serpone, Solar photocatalysis, photodegradation of a commercial detergent in aqueous TiO<sub>2</sub> dispersions under sunlight irradiation, *Solar Energy*. 77 (2004) 525–532. <https://doi.org/10.1016/j.solener.2004.04.020>.
- [155] M. Montazerzohori, M. Nasr-Esfahani, S. Joohari, Photocatalytic degradation of an organic dye in some aqueous buffer solutions using nano titanium dioxide: A kinetic study, *Environment Protection Engineering*. 38 (2012) 45–55. <https://doi.org/10.5277/EPE120305>.
- [156] A. Fujishima, X. Zhang, Titanium dioxide photocatalysis: present situation and future approaches, *Comptes Rendus Chimie*. 9 (2006) 750–760. <https://doi.org/10.1016/j.crci.2005.02.055>.

## CHAPTER 3

### Fluorescent CdS QDs modified with Molecular imprinted polymer for the effective photodegradation of imidacloprid and buprofezin pesticides under Visible light: Synthesis and Characterization

#### 3.1. Introduction

Gingerols are the most abundant pungent phenolic compounds found in fresh roots of ginger containing several gingerols with varying chain lengths ( $n=6$  to  $n=10$ ), the most abundant being 6-gingerol compound distinguished by the length of their unbranched alkyl chains[157]. Among the main pungent components of gingerol, [6]-gingerol is the major bioactive pungent compound with various biological and therapeutic effects including antioxidant anti-inflammatory, antipyretic and antibacterial properties[158]. [6]-gingerol can be extracted by various conventional methods including Soxhlet method, Microwave extraction, Cold extraction, Reflux extraction, Ultrasonic extraction. To boost the solubility and mass transfer rate, these approaches require the right agitation, power and solvent.



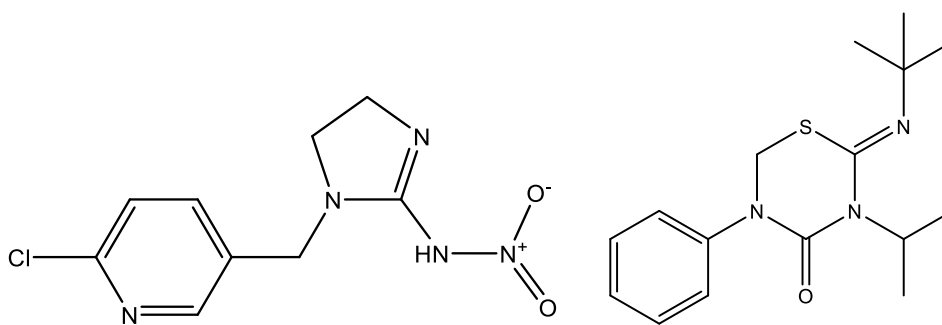
Chemical Structure of [6]-gingerol (5-hydroxy-1-(4'hydroxy- 3' methoxyphenyl)-3-decanone)

Cadmium sulphide (CdS) is a significant nanomaterial belonging to II–VI semiconductor with a band gap energy ( $E_g = 2.42$  eV (515 nm)) of outstanding application. CdS has intriguing applications in a variety of technical fields such as photocatalysis, gas sensing, solar cells, laser and infrared detector, optoelectronic materials, luminescent device and so on[159]. CdS is also the most important photocatalyst material and can be synthesized in thin films or in powder form using various chemical methods such as hydrothermal/solvothermal techniques, precipitation, mechanical grinding and other processes. Recently, efforts have been made to synthesise high-quality CdS nanoparticles and investigate their optical characteristics. The ability to tune the properties of particles by manipulating their sizes and shapes necessitates the development of novel experimental procedures that produce nanoparticles with very low size and shape dispersion[160]. To synthesise sea-urchin-like cadmium sulphide nanoparticles with nanorod-based morphology the solvothermal approach has been used where cadmium chloride

and thiourea reagents were dissolved in ethylenediamine solution[161]. CdS has also been prepared through green route using sodium sulphate and cadmium sulphate as precursors where Tea Decoction is employed as a natural stabilizing agent[162]. Similarly, A novel method for developing nanoparticle films on biological membrane substrates has been proposed in which CdS has been synthesized by chemical reaction of Cadmium Acetate and Thiourea aqueous solutions[163]. CdS has been synthesized using various methods and from various precursors. In this work to prepare novel nanocomposite material CdS QDs has been synthesized by a simple precipitation method which is embedded into a Molecular imprinted polymer matrix (MIPs).

MIPs are bio-inspired synthetic compounds that attach to an active target site selectively using a lock and key process[164]. Molecular imprinting is now presumed to be a modified strategy for developing synthetic receptors composed of highly cross-linked porous-rich polymers with specific recognition binding sites that are complementary in shape, size, and functional groups to a template molecule [165]. It is a simple concept based on lock and key theory and comparable to that includes the creation of specialised recognition sites, most typically within synthetic polymers. Recently, development of MIPs synthesis and its application have been acknowledge in various areas [166].MIPs including covalent interaction, noncovalent interaction, and hybridization of both have been synthesized through various approaches (the creation of complexes between the template molecule and the functional groups of the monomers). MIPs are broadly classified as covalent imprinting, noncovalent imprinting, and hybridization of the two. MIPs are prepared using free-radical polymerization (bulk, precipitation, suspension, emulsion, multistep swelling polymerization and the sol-gel technique[117].

Recently, MIPs have been developed to form composite material to enhance the efficiency of nanoparticles in many applications, such as Adsorption, Sensing, Fluorescence and photodegradation. Within these applications, photocatalysis is one of the prominent of the composite materials. In the current study, efforts have been made to develop CdS/MIPs nanomaterial.



Chemical Structure of Imidacloprid and buprofezin

To understand the limitations of the absorption spectrum of CdS QD's, a photocatalysts with excellent selectivity, as well as robust visible light absorption, is created. Finally, to establish excellent physical and chemical characteristics of CdS/MIPs are employed. Herein the aim of the MIPs is to increase the particle size and distribution of CdS QDs that are implanted together and to induce catalytic degradation of organic contaminants using visible light. The study hopes that the findings presented will find significant application and appeal within waste water remediation.

## 3.2 Experimentation

### 3.2.1 Reagents and chemicals

The chemical reagents used were of analytical grade. Sigma Aldrich supplied the Itaconic acid, Ethylene glycol dimethacrylate (EGDMA), Azoisobutyronitrile (AIBN) and TCI provided acetonitrile and tetrahydrofuran. The template molecule was [6]-gingerol, which was isolated from natural ginger.

### 3.2.2. Extraction of [6]-gingerol By Reflux Method

The fresh rhizomes of ginger (*Zingiber officinale* Roscoe) were collected from a local market. Ginger was washed several times and sliced. The sliced ginger was dried in a natural environment avoiding direct exposure to sunlight. The reflux apparatus was employed to avoid time loss as observed in Soxhlet method and to maximize the yield. The reaction was setup by using 20g of dried rhizomes with 150ml of methanol where the raw sample was refluxed for 2–5 hours at 50–70°C. The experiment was repeated several times until an abundant amount of extracted compound was obtained. The raw extract of ginger sample was filtered and concentrated using rotary evaporator. The extracted compound contains non-volatile homologues compounds in which [6]-gingerol was the major bioactive component. The extracted compound forms precipitates by adding 5-10 ml of H<sub>2</sub>O and the precipitates were

cooled to 5-10°C. The yellow oily precipitation mixture was poured into separating funnel. The pH of the immiscible compound was increased to 11-12 range by adding standard solution of sodium hydroxide. The ethyl acetate was also added till two layers were obtained. Here the upper organic layer and aqueous layer formed below in separating funnel. The aqueous layer was separated and HCl was added until pH becomes less than 1, after a few minutes of separation precipitates start collecting downward which were collected and filtrated further for analysis. The ginger extract is soluble in methanol, ethanol, chloroform, and Dimethylsulphoxide and sulphoxide (DMSO) below is the list of solvents showing the solubility of [6]-gingerol in **Table 1**.

**Table 1.** List of solvents based on their on their solubility

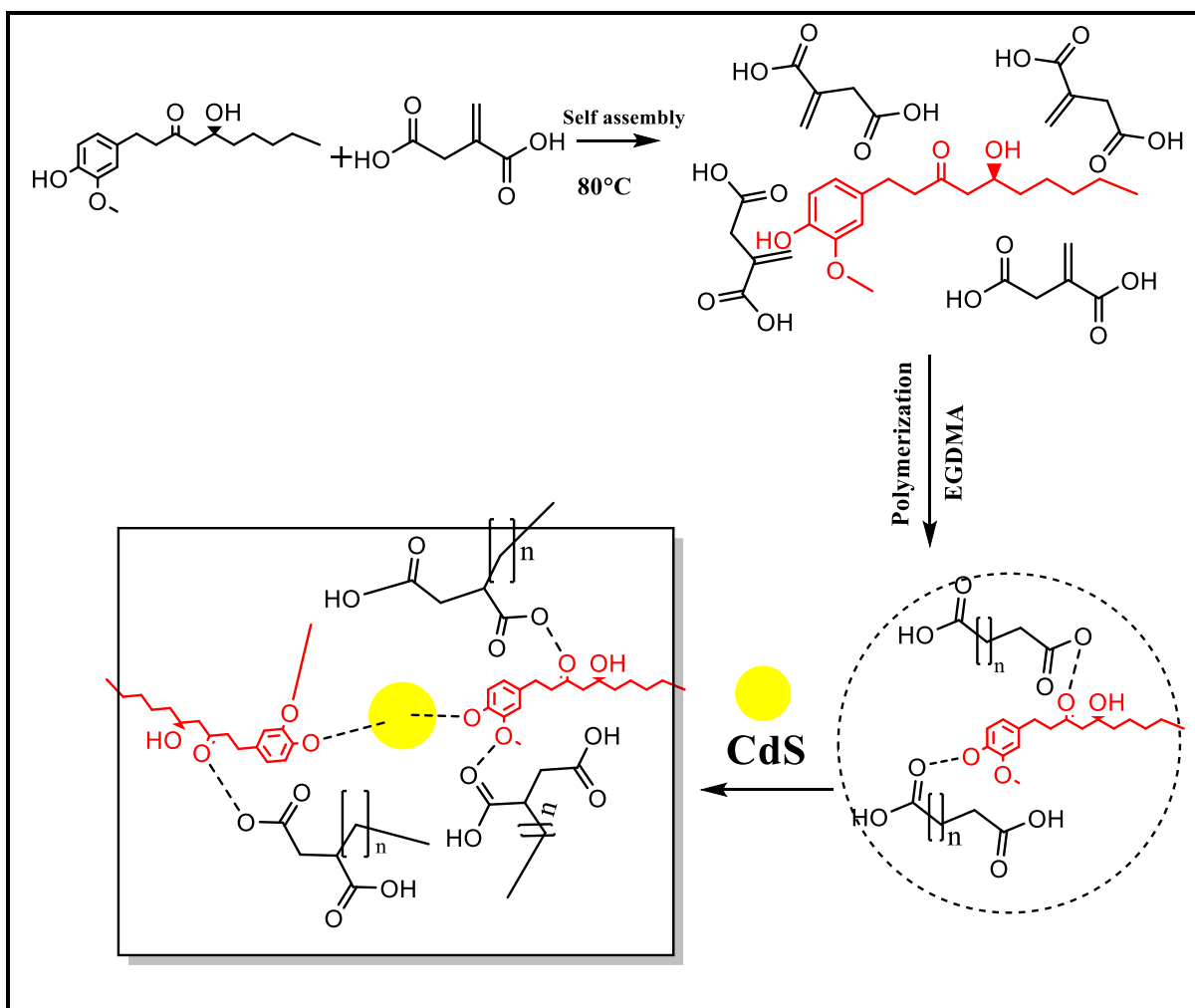
Solubility	behaviour
Chloroform	Soluble
Toluene	Insoluble
Methanol	Soluble
Ethanol	Soluble
DMSO	Soluble
Acetone	Insoluble
Water	Insoluble

### 3.2.3 Synthesis of CdS QDs

CdS QDs were prepared in an aqueous solution at ambient temperature and pressure using basic chemical precipitation method. Cadmium nitrate ( $\text{Cd}(\text{NO}_3)_2 \cdot 4\text{H}_2\text{O}$ ), Ammonium sulphide ( $\text{NH}_4)_2\text{S}$ , sodium sulphide was obtained from Sigma Aldrich. All of the chemicals were analytical grade and used without further purification. The synthesis is summarized below. 100mL  $\text{Cd}(\text{NO}_3)_2 \cdot 4\text{H}_2\text{O}$  (0.08M) aqueous solution was dropwise added to a 100ml ( $\text{NH}_4)_2\text{S}$  (0.10M) aqueous solution with continuous stirring. After 5 minutes, 20 ml sodium sulphide solution was added dropwise under continuous stirring. The reaction was carried for 3 hours at constant stirring and a yellow precipitate of CdS developed, which was washed with ethanol and acetone and dried at room temperature. CdS QDs were obtained as dark yellow precipitates which were further mechanically calcinated to obtain quantum size nanoparticles.

### **3.2.4. Synthesis of molecular imprinted polymer encapsulated with cadmium sulphide QDs by Exsitu polymerization**

1.16g of [6]-gingerol was used as a template which was dissolved in a 10ml mixture of tetrahydrofuran and acetonitrile in a conical flask.[6]-gingerol is poorly soluble in tetrahydrofuran so a mixture of Tetrahydrofuran/acetonitrile was employed to act as Porogenic solvent in the reaction.4.43g of monomer itaconic acid was added into the conical flask followed by the addition of 7.8ml of crosslinking agent Ethylene glycol dimethyl acrylate (EGDMA). The molar ratio was maintained as 1:4:16. 0.05g for the 2,2-azobisisobutyronitrile (AIBN) that was used as the polymer initiator which proceeded reaction through a free radical polymerization process. The reaction was performed in the presence of nitrogen atmosphere by purging N<sub>2</sub> gas for 15min with access flow of 0.1L/min. This purging process was continued for 3hrs until an amorphous polymer was obtained Following this Cadmium sulphide QDs were added into the amorphous polymer. The contents of the conical flask containing the mixture were allowed to polymerize in a hotplate at 80°C for the 3h. To obtain molecular imprinted polymer (MIPs) composite the methanol was used to purify the polymer. The solid polymer obtained was grinded and crushed with mortar and pestle into fine powder which was further analysed with FTIR, XRD and FESEM.



**Scheme 1.** Schematic representation of CdS/MIPs nanocomposite.

### 3.3 Characterization

#### 3.3.1 $^1\text{H}$ NMR

The [6]-gingerol compound was isolated from gingerol and the structure was elucidated with the  $^1\text{H}$ NMR.  $^1\text{H}$ NMR were recorded on Bruker-500 and 400MHz instruments using  $\text{DMSO-d}_6$  as solvent and tetramethyl-silane as an internal reference standard. ( $\text{DMSO-d}_6$ )  $^1\text{H}$ NMR in **Figure 5 (Chapter 2)**. shows the following peaks: 0.6-1.5 (3H, t,  $j=6.6\text{Hz}$ ), 1.6-1.9 (8H, m), 2.2-2.5 (1H, d,  $j=8\text{Hz}$ ), 2.67-2.85 (2H, s), 3.8 (3H, s,  $-\text{OCH}_3$ ), 6.63 (1H, s), 6.77 (1H, s), 6.7 (1H, s). In this spectrum  $^1\text{H}$ NMR exhibits separate signals for the presence of  $-\text{OCH}_3$  group with a chemical shift at 3.837 and signals of three aromatic protons were assigned to chemical shift at 6.63, 6.77 and 6.78. In this spectrum  $\delta$  value at 0.6-1.5 is relevant to  $-\text{CH}_3$  groups and the rest of protons such as  $\delta$  value at 1.6-1.9, 2.2-2.5, 2.67-2.85 is corresponds to  $-\text{CH}_2-$  groups in aliphatic region.

**Figure 1.** shown the FTIR result for the pure CdS Quantum Dots. The pure CdS nanoparticle FTIR spectrum revealed peaks at 1013, 1411, 1650, 2094, 2342 and 3438 $\text{cm}^{-1}$ . The 3352 $\text{cm}^{-1}$  absorption peak is stretched by the relatively strong hydrogen bond O-H and frequently overlap the C-H absorbance. Similarly, the peak at 1650 $\text{cm}^{-1}$  corresponds to medium intensity bending vibration of O-H group of H<sub>2</sub>O molecules. A medium high absorption peak of Cd-S stretching has been detected in nanoparticles at 637 $\text{cm}^{-1}$ . The absorption peak at 1013  $\text{cm}^{-1}$  correspond to C-N stretch, whereas the peak at 1411  $\text{cm}^{-1}$  relates to C-O stretching.

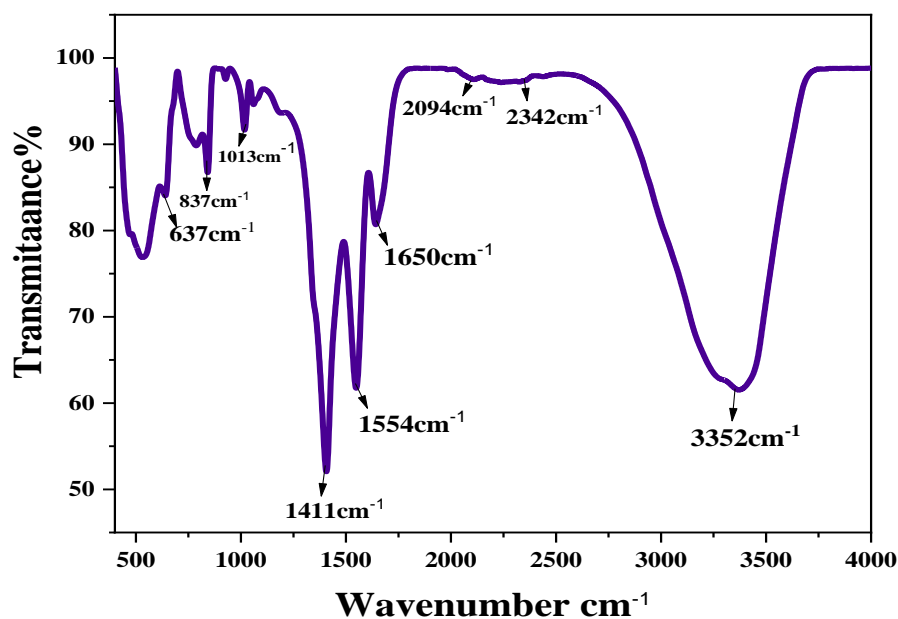


**Figure 1.** FT-IR spectrum of CdS QDs

**Figure 4 (Chapter 2)** shown FTIR spectrum of [6]-gingerol. FTIR spectrum of 6-gingerol contains a peak at 3300  $\text{cm}^{-1}$  is corresponds to -OH str., 900-1300  $\text{cm}^{-1}$  is relevant to -C-O str., 1600-1900  $\text{cm}^{-1}$  is related to >C=O str. and 1398, 1448  $\text{cm}^{-1}$  is corresponding to aromatic stretching.

**Table 2.** Functional groups present in the [6]-gingerol

The information revealed from [6]-gingerol FTIR summarized in **Table 2.**



Functional Group (cm <sup>-1</sup> )	Theoretical Peaks (cm <sup>-1</sup> )	Practical Peaks
O-H (stretch)	2700-3300	3000cm <sup>-1</sup>
C-O (stretch)	900-1300	1258cm <sup>-1</sup>
C=O (stretch)	1600-1900	1737cm <sup>-1</sup>
C=C aromatic stretching	1500-1600	1448,1398cm <sup>-1</sup>

The XRD pattern shown in the **Figure 2** corresponds to the CdS spectrum. In this Figure the peaks observed in the XRD pattern of CdS at  $2\theta$  values of 25.04°, 26.80°, 28.55°, 36.9°, 43.70°, 48.7°, 51.3°, 52.2°, 53°, 58°, 66°, 71.34°, 72.86°, 75.86° match perfectly with the (100), (002), (101), (102), (110), (103), (112), (201), (004), (202), (203), (211), (114) and (105) crystalline planes reflections may be indexed to hexagonal CdS (JCPDS No. 06-0314) quite well. Using the Scherrer formula, the crystallite sizes of the as-synthesised CdS QDs, were estimated from the principal diffraction peaks of the base[167]:

$$D = K \lambda / \beta \cos\theta \quad (1)$$

where K is a constant (approx. 0.9) (33),  $\lambda$  is the X-ray wavelength employed in XRD (1.5418),  $\cos\theta$  is the Bragg angle, and  $\beta$  is the pure diffraction broadening of a peak at half-height, that is, broadening owing to crystallite size. The XRD spectrum was compared with CdS/MIPs composite. The diffraction peak of template molecule was invisible which may be on the surface of CdS QDs and failed to change the crystalline structure of nanomaterial. The zero change in the  $2\theta$  value indicated that pure crystallinity and slight broadening of peaks were observed which was a result of the size variation in the CdS/MIPs nanocomposite. The Scherrer formula was used to calculate size of CdS QDs nanomaterial which was found to be in the range of 8-9nm and increase to 30-40nm in case of MIPs and NIPs composite. The crystalline nature of the synthesized Cadmium QDs is suggested by the narrow diffraction peaks.

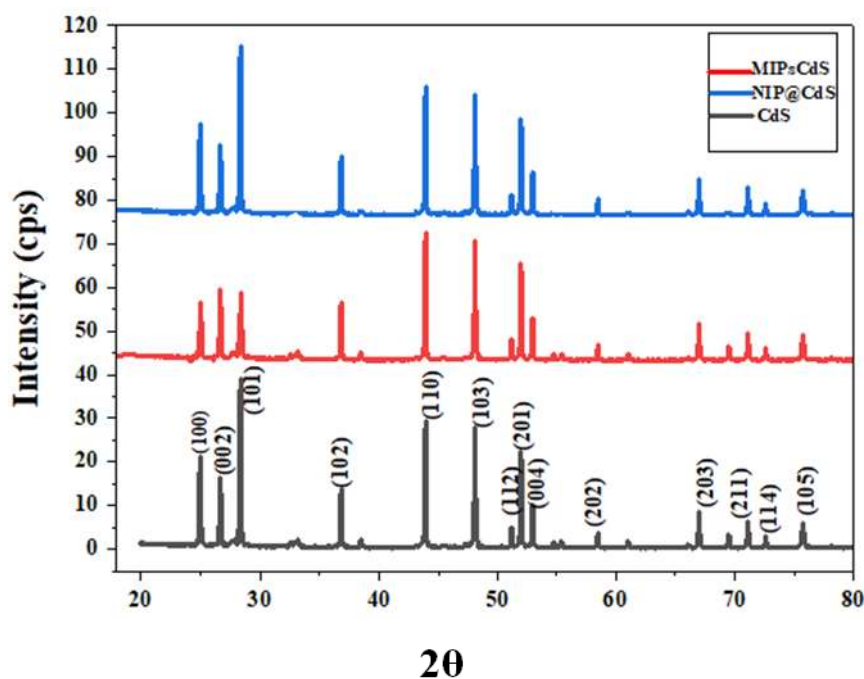


**Figure 2.** XRD diffraction pattern of CdS, MIPs@CdS and NIPs@CdS composite.

FESEM images of CdS quantum dots are shown in the **Figure 3(A-D)**. When the cadmium sulphide layer is deposited using sulphur, the larger grains are generated by a combination of smaller grains, which may lead to an increase in the charge carrier diffusion length by providing a conducting connection. CdS quantum dots reveals highly agglomerated, crystalline and monodispersed semi-spherically shaped particles. The prepared CdS has powdered quantum range particles with sizes ranging from 3.98 to 5.90 nm shown, after embedding the CdS in MIPs matrix the surface of the particles becomes coarser which aggregates the size of nanocomposite material prepared at 80°C. The nanomaterial has semi-spherical particles with sizes ranging from 30-70nm. The cavitation structures of CdS/MIPs (E) shown in **Figure 3** were found to be more prevalent than those of NIPs(F) (as shown in **Figure**), respectively. This suggests that the template molecule has an impact on the microstructure formation during the synthesis process. Further, the regularity and average of NIPs were found to be lower than those of MIPs and the cavitation content of MIPs was higher. Overall, these results indicate that imprinted materials containing hyperbranched polymers with degradable disulphide bonds were successfully prepared.

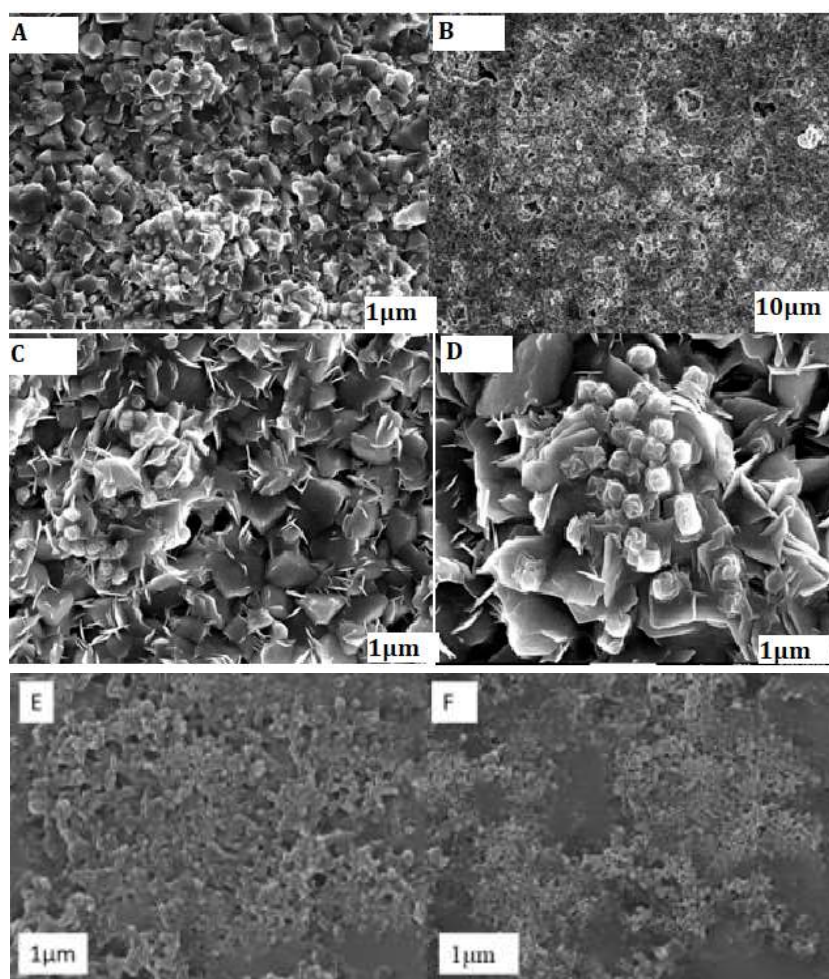


**Figure 3.** (A-D) SEM images of Pure CdS (E) MIPs/CdS(F) NIPs/CdS composite.

Fluorescence property of CdS/MIPs was studied by using Scanning confocal laser microscopy. The molecule absorbs beam of photons and gets excited at a wavelength of 428.8 nm. The intense fluorescence peak with a maximum at around 428 nm and a wave peak at 621nm were recorded in the spectra **Figure 4**. The spectra in close proximity of fluorescence spectra were investigated using 1800 lines per mm diffraction grating and a spectral resolution of 0.027 nm, which revealed two near peaks. The positions of the peaks are 428 and 621 nm can be explained by the excitement of absorbed photon in the composite which enters an excited state. The system can relax by emitting a photon and therefore shedding energy. The Stokes shift occurs when the energy of the released photon is smaller than that of the absorbed photon. If the emitted photon has more energy, the energy difference is referred to as an anti-Stokes shift[168].

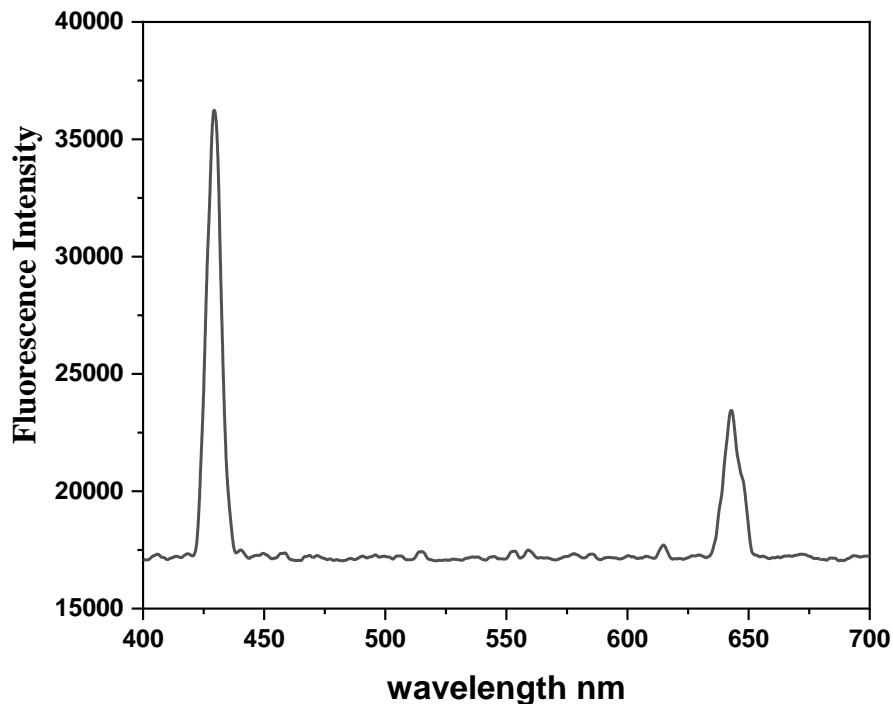


**Figure 4.** Fluorescence spectra of CdS MIPs.

### 3.4 Thermal Study

TGA is commonly used to determine degradation, moisture content, chemical changes, and thermal stability of components. TGA was used to evaluate thermal stability of composite as well as percent of CdS present[169]. Weight changes are caused by the breaking and/or formation of physical and chemical bonds[170]. The polymeric material began to disintegrate at 337°C and were completely decomposed at 454°C. The initial weight loss in the temperature range below 205°C is primarily due to evaporation of residual solvent and begins to disintegrate at 337 °C possibly due to breakage in crosslinked monomers with a weight loss of 80% appearing as an endothermic peak in the DSC curve. All of the composites' residual weights were found to be 18%. To evaluate different transitions such as glass transition temperature, melting and crystallization temperature Differential scanning calorimetry (DSC) analysis was also performed. TGA–DSC coexistence measurement not only improves output values but also simplifies interpretation. DSC data allows for the distinguishing endothermic and exothermic states[171]. The DSC curve of MIPs-CdS nanocomposite was investigated from 50 to 500°C. The DSC curve of MIPs CdS nanoparticles is shown in **Figure 5**. The composite curve demonstrates two distinct endothermic peaks. The first peak, which occurs between 212 and 226°C, is a result of the dehydration process of organic solvents both inside and outside of the cavity. The second peak, observed at a high temperature of 397°C, is related to the melting of

the MIPs polymer. The strength of the hydrogen bonding network between the polymer, which is due to the presence of many hydroxyl groups, is the key factor determining the crystalline nature of the CdS/MIPs solid structure.

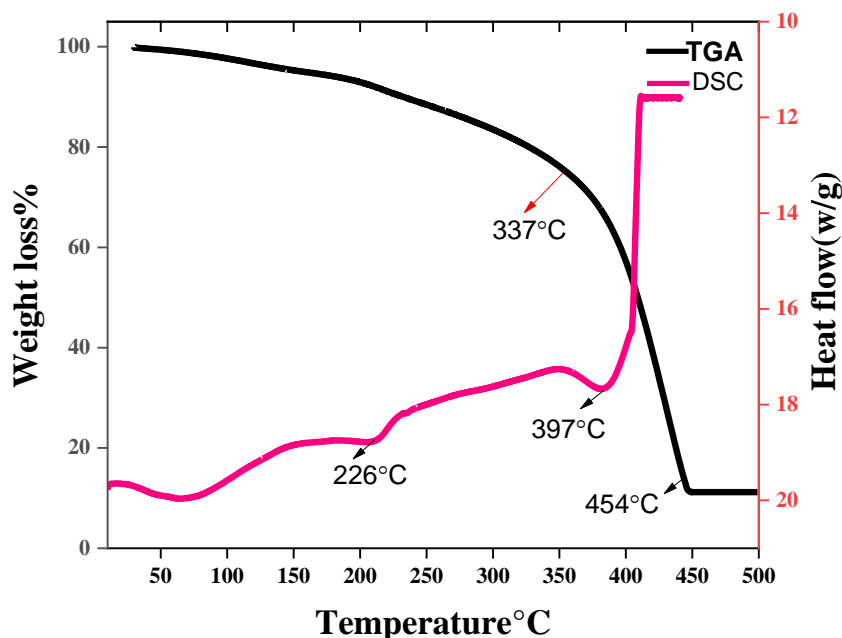


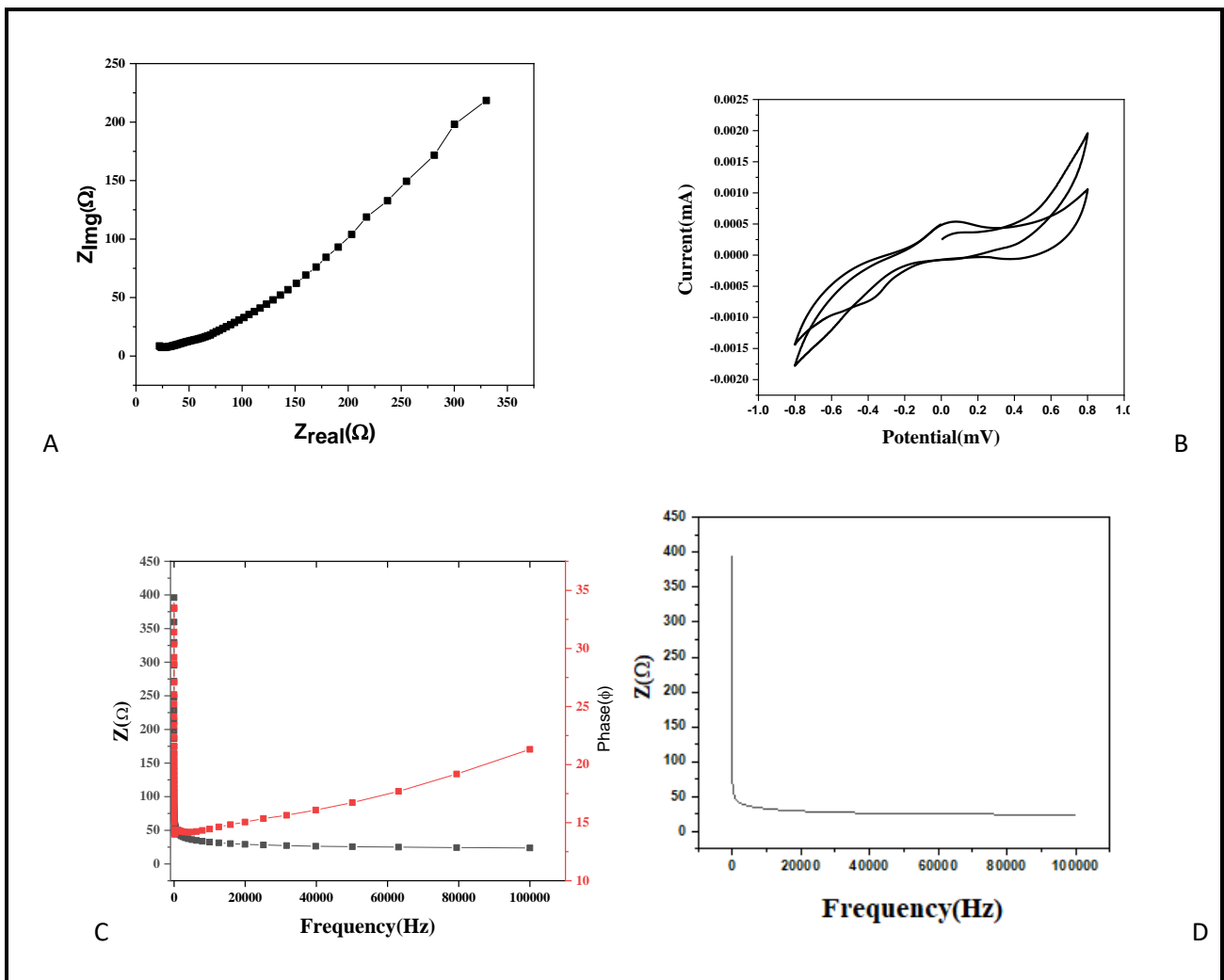
**Figure 5.** DSC- TGA of CdS MIPs CdS nanocomposite.

### 3.5 Electrochemical Analysis

The electrochemical characterization of metal oxides, nanoparticles, nanocomposite, binary metal oxides and Quantum Dots has been rapidly grown in recently years. Further the electrochemical study of Cadmium Sulfide and CdS/MIPs composite has been done using cyclic voltammetry and impedance spectra technique. Cyclic voltammetry can provide enough insight about the viability of electrode materials for supercapacitor applications. The cyclic voltammetry of CdS electrodes were recorded in the potential range from -1 to 1V in 0.1M phosphate buffer solution with different scanning rate from (10-20 mvs<sup>-1</sup>). **Figure 6** below illustrates The CV curve scan rate at 10mvs<sup>-1</sup>. From the **Figure 6** it can be seen that the redox peak pairs are well defined which is the transition from oxidation of CdS, suggesting the energy storage capacity of the proposed material.

Electrochemical impedance spectroscopy (EIS) or ac impedance techniques have risen in favour in recent years. They were originally employed to determine double-layer capacitance and in ac polarography, but are now utilised to characterise electrode processes and complex interfaces.[172]. EIS studies the response of a system to the transmission of a periodic small

amplitude alternating current signal. The system response analysis provides details about the interface [173]. The electrochemical impedance study was performed to examine the behaviour of supercapacitor electrode. The Nyquist and Bode plot are used to analyse the EIS data. The Nyquist plot represents the frequency response of the electrode system and are plots of real impedance and imaginary part of impedance. The **Figure 6** shows the impedance spectra of CdS/MIPs and pure CdS. It can be seen that the MIPs CdS has small radius curvature indicating efficient charge transfer ability than pure CdS. The Bode plot enumerates the decrease of frequency with phase and real impedance. The Figure also reveals that the phase of tail is 23.2 and 20 which evidences capacitive behaviour of CdS and MIPs composite. The plot of frequency and impedance has also been shown below of both CdS QDs(C,D) and CdS/MIPs composite (c,d).



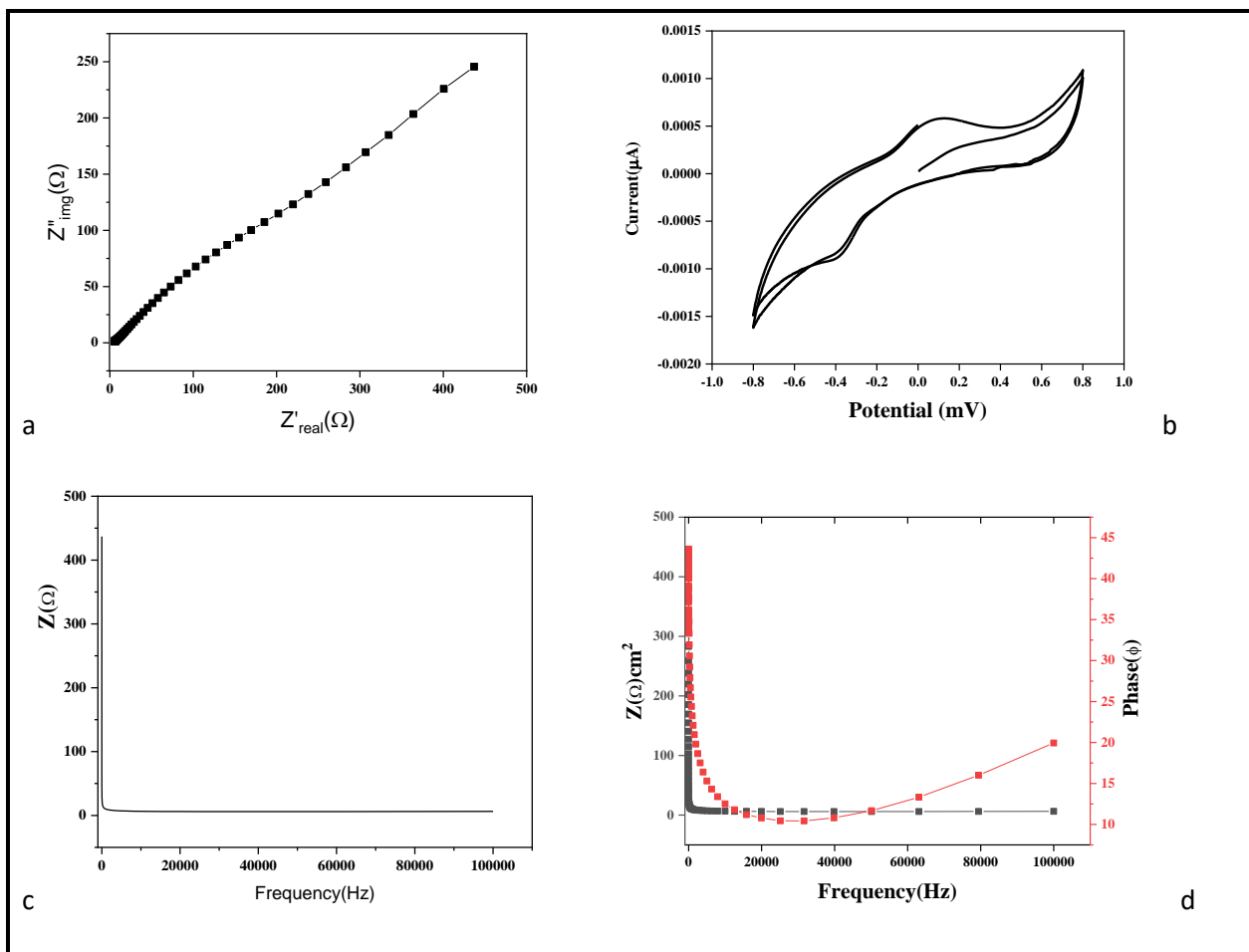


**Figure 6.** Electrochemical study of CdS QDs and CdS/MIPs composite.

### 3.6 Photocatalytic activity evaluation of Imidacloprid and buprofezin

The photocatalysis activity of CdS/MIPs and CdS/ NIPs were evaluated by monitoring photodegradation of Imidacloprid and buprofezin pesticide. The degradation of Imidacloprid and buprofezin was recorded using a Shimadzu UV-VIS spectrophotometer, which measured the change in absorption intensity at ((max)=282 nm) over time. The degradation% was estimated using equation (1) and all concentrations were prepared in double distilled water.

$$R\% = \frac{A_0 - A}{A_0}$$

$A_0$  and  $A$  are the concentration rates at  $t=0$  and time =  $t$

A stock solution was prepared by dissolving 20mg of Imidacloprid in 1000ml of aqueous solution and storing it in the dark at 4°C until use. Working standards of imidacloprid in concentrations of 10 ppm were established by dilution of the stock solution. Calibration curves

(0.05–5 ppm) were prepared by diluting aliquots of working standard solution with methanol. The buprofezin stock solution was also prepared by dissolving (20mg/1000ml) solution using 20ml methanol and was kept under dark to maintain adsorption desorption equilibrium. In order to determine the amount of imidacloprid and Buprofezin insecticide left in the solution and to examine the degradation of pesticides UV-Vis spectroscopy was used to investigate the reaction mixture.

### **3.6.1 Effects of several parameters on photocatalytic efficiency of CdS/MIPs against imidacloprid and Buprofezin pesticide.**

It was attempted to study and improve variables that affects the process of imidacloprid and buprofezin % degradation including the amount of photocatalyst, pesticide content, pH and radiation time.

#### **I. Effect of photocatalyst**

**Figure 7A** and **Figure 8A** depict the impact of initial concentration of MIPs composite on the efficiency of photo-degradation against two pesticide pollutants. The graph demonstrates that the rate of photo degradation rises with an increase in the quantity of CdS/MIPs composite. The experiment maintained a constant concentration of pesticide pollutants at 10 ppm while varying the catalyst concentration from 20 mg to 50 mg during the degradation process. The stock solution used for each experiment was 25 ml with a concentration of 10 ppm. During the initial irradiation of UV light a 50% degradation was observed with 20mg of catalyst as the concentration of nanocatalyst the degradation rate increased to its maximum upto 84% and 80% for Imidacloprids and Buprofezin. As a result, the more composite being used, the greater the photo-degradation. It is noticed that removal efficiency of CdS/NIPs has significantly decrease with 48% and 57% degradation efficiency for Imidacloprid and Buprofezin indication the decrease in specificity shown in **Figure 7A** and **8A**. As the amount of photocatalyst grows, the number of active sites on the surface increases, resulting in an increase in the number of OH• and OH' radicals, which leads to an increase in photodegradation rate[174].

#### **II. Effect of pH**

The pH of pollutant concentration plays a significant role in the production of OH radical. The photocatalytic degradation achieved under ideal conditions with a different pH range as shown in **Figure 7B** and **Figure 8B**. The best performance was obtained at **pH-9-12** for imidacloprid and for buprofezin. The removal efficiency for Imidacloprid and buprofezin was found to be 81 and 72%, While for CdS/NIPs composite the degradation was found to be 76% and 68%



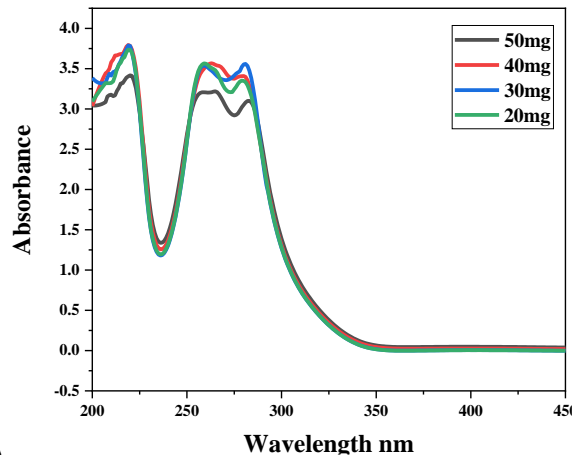
illustrated in **Figure 7B** and **8B**. The interpretation of pH role on the photodegradation is not an easy approach because pH has various roles here such as generation of charged ions during the process, maintaining electrostatic interaction between the solvent molecules, nanocomposite surface and substrate. At low pH, oxidation sites exist; at higher pH, hydroxide radicals exist than the surrounding environment ( $\text{pH} > 7$ ) As a result, when the pH is more than 7, hydroxide radicals occur on the surface of the nanocomposite, causing imidacloprid insecticides to degrade[175].

### **III. Effect of Temperature**

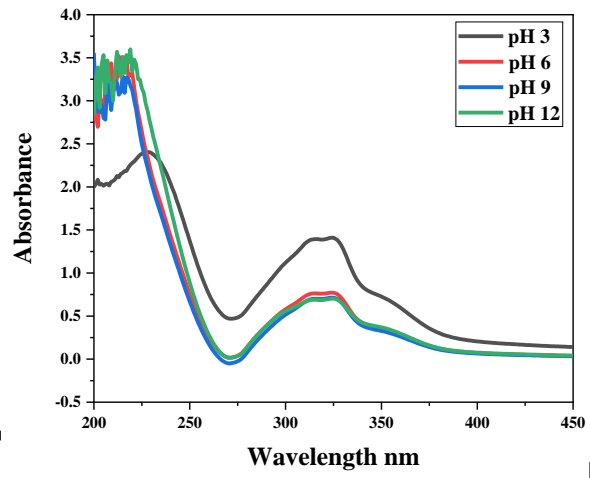
The photo-degradation is found to be temperature dependent and is favoured with increase in temperature for CdS/MIPs and CdS/NIPs. The photocatalysis was carried out at different temperature range e.g., 30°, 40°C, 50°C and 60°C. From the result analysis it was found that maintaining the temperature keeping all other parameters constant generates greater photodegradation efficiency. The maximum removal efficiency was observed at 60°C with 75% and 71% removal efficiency indicate a positive impact in photodegradation. The degradation efficiency of imidacloprid and Buprofezin follows first order kinetics at different temperatures as shown in the Figure **7C** and **Figure 8C**. Similarly, degradation efficiency was seen to follow same trend with 58 and 62% in Figure 8C and 9C.

### **IV. Pollutant concentration Impact**

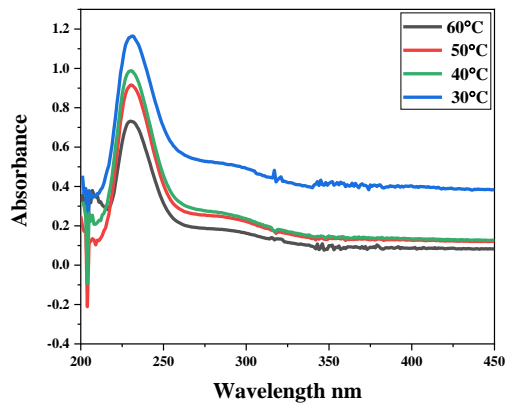
To study the effect of pollutant concentration the concentration of pollutant was varied from 10ppm to 40ppm range in **Figure 7D** and **9D** while keeping composite concentration constant. The effect of initial pesticide concentration on photo-catalytic degradation was investigated. It was discovered that when the concentration of the pesticide solution increased, the photodegradation rate decreases It was observed that degradation efficiency of Imidacloprid and Buprofezin for CdS/MIPs in Figure 10D,11D and CdS/NIPs in Figure 10D,11D decreases with increase of concentration. It was also shown that increase concentration of pollutant causes an increase in the equilibrium adsorption of pesticide on active sites of the catalyst, resulting in a decrease in competitive adsorption of  $\text{O}_2$ ,  $\text{H}_2\text{O}$ , and  $\text{OH}^-$  on the same site and less formation of OH radicals, which are the primary oxidants required for high degradation efficiency. It can be explained by the fact that when the concentration of pesticides rises, the route length of photons entering the solution shortens, resulting in less photon adsorption on catalyst surface and hence a lower degradation rate observed.



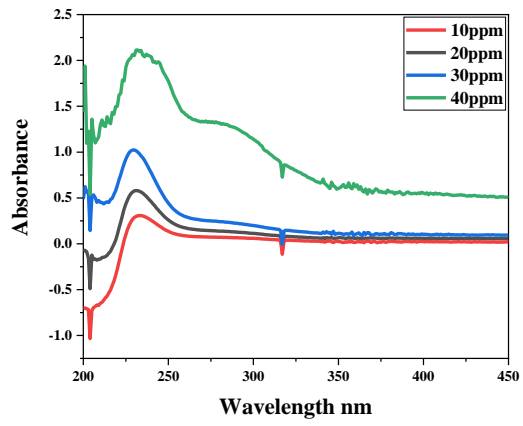
A



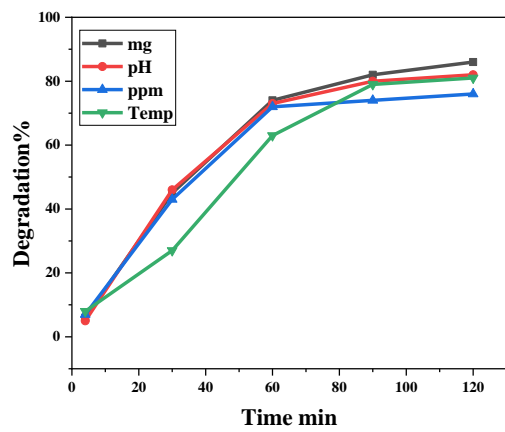
B



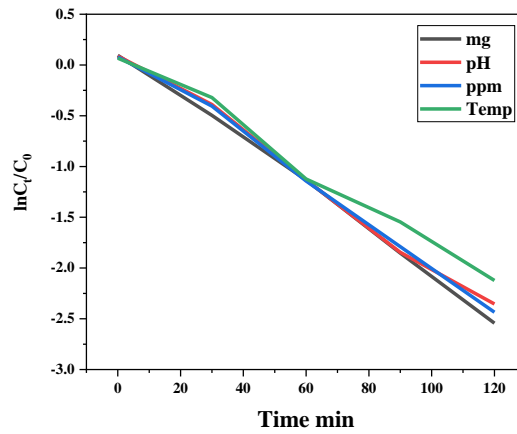
C



D



E



F

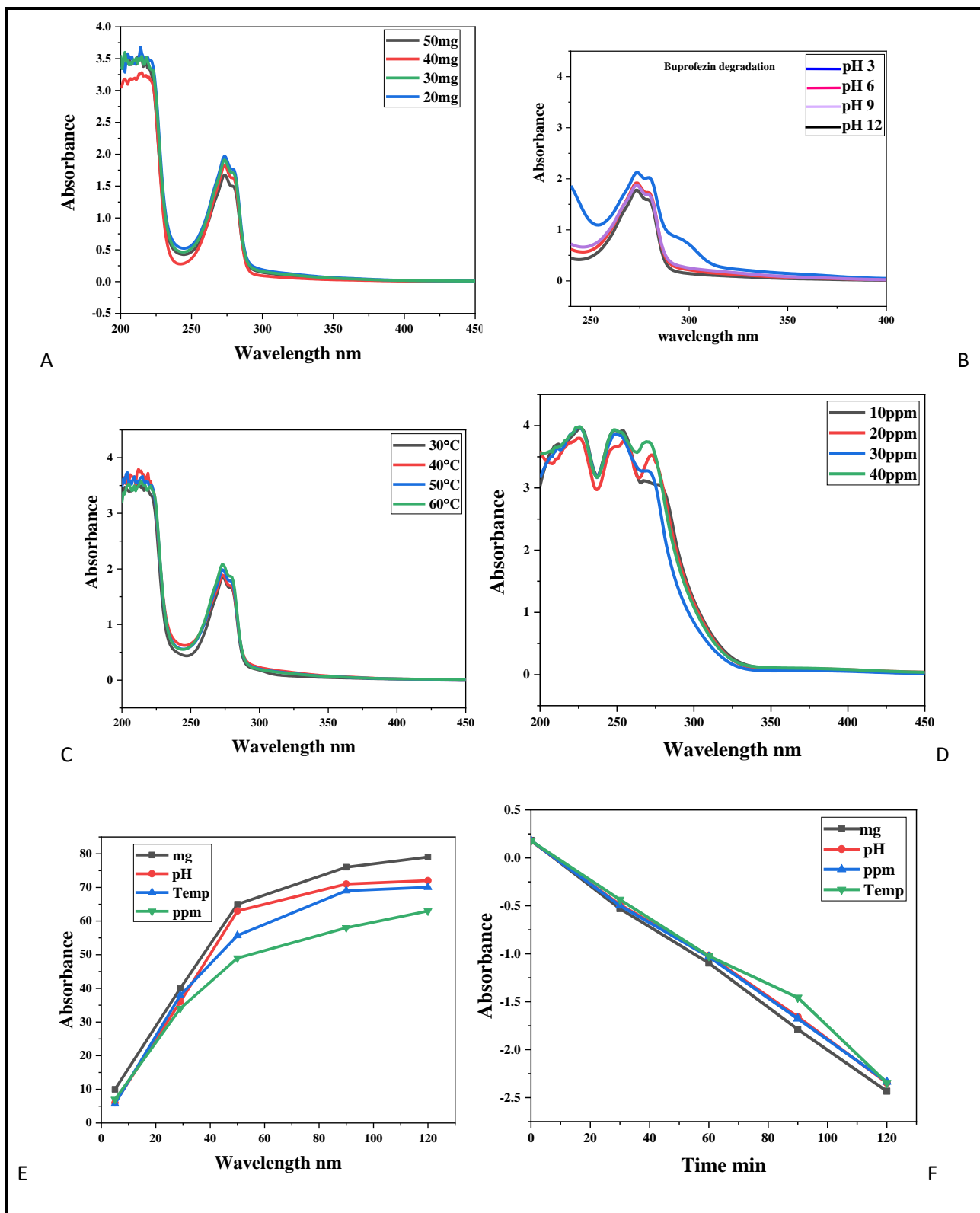
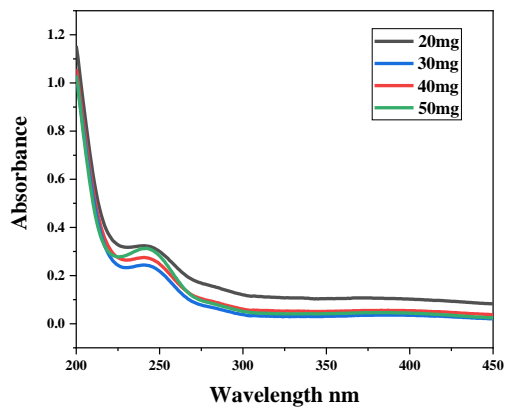
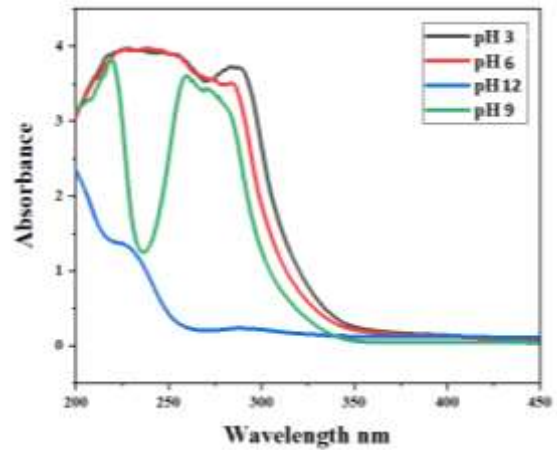


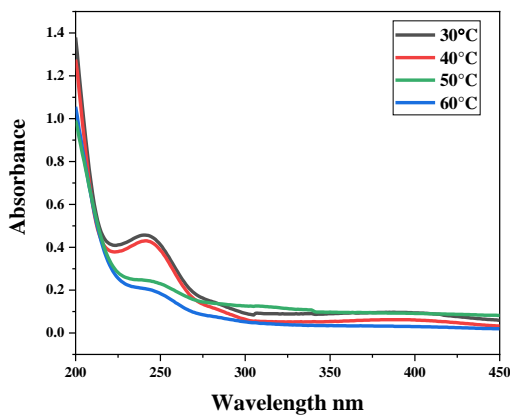
**Figure 7.** Photocatalytic degradation of Imidacloprid and Buprofezin insecticide by CdS/MIPs composite at different catalyst doses, pH values, temperature variation and pollutant concentration.



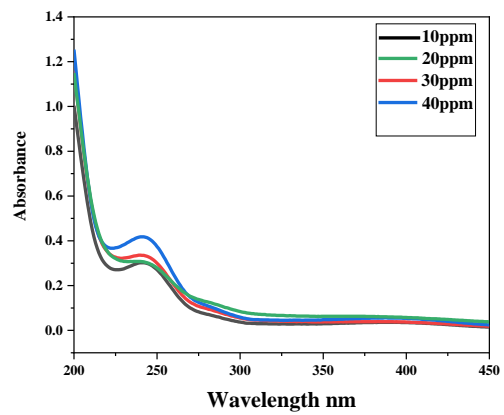
A



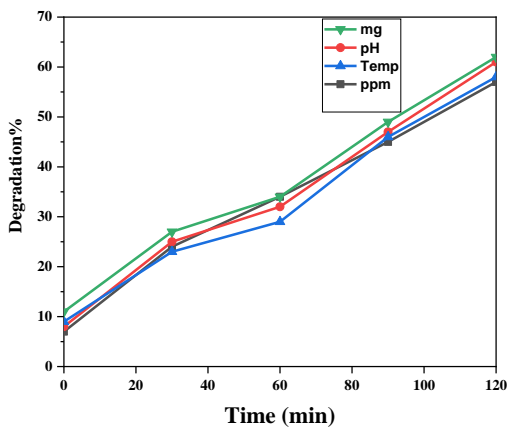
B



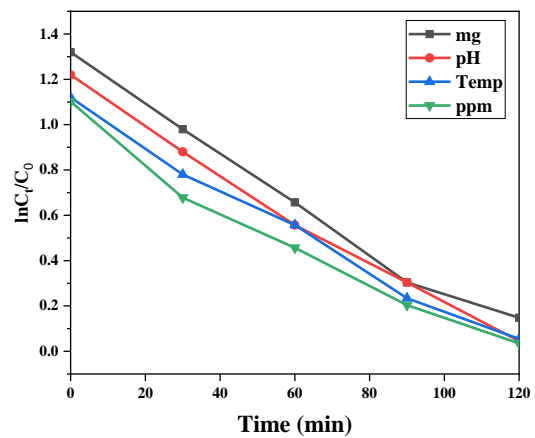
C



D



E



F

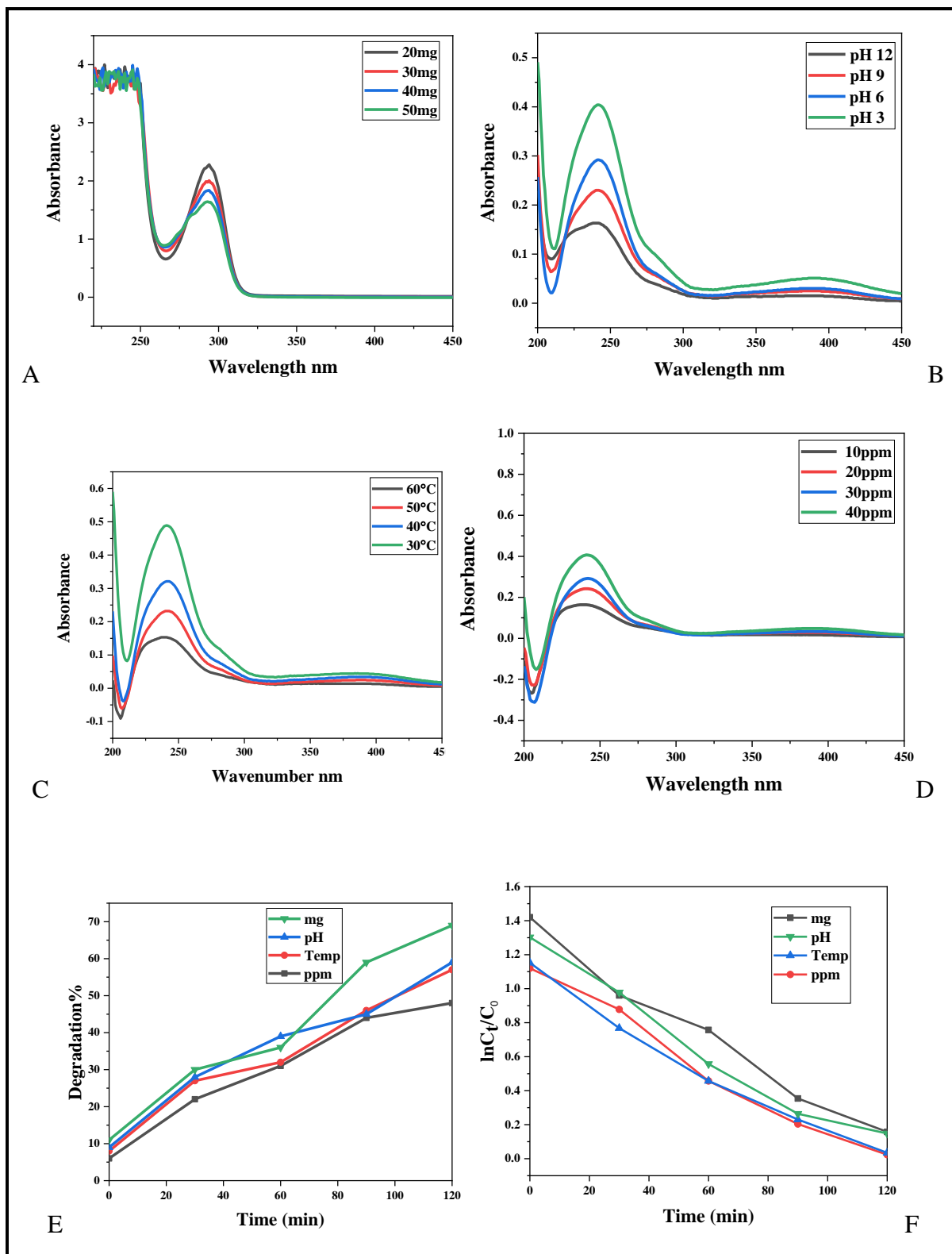


**Figure 8.** Photocatalytic removal efficiency of Imidacloprid and Buprofezin insecticide by CdS/NIPs composite at different catalyst doses, pH values, pollutant concentration and temperature variation.

### 3.7 Optical properties

The optical band gap of CdS/MIPs composite was determined using the Tauc plot shown in **Figure 9**. The energy gap of CdS/MIPs nanocomposite was found to be 2.96 eV, which is lower than the energy gap observed in this study. The larger energy gap observed in this study can be attributed to the polymer composite. The presence of CdS interstitials introduces additional charge carriers through the Burstein-Moss effect, leading to a shift of the energy gap towards higher energy levels.

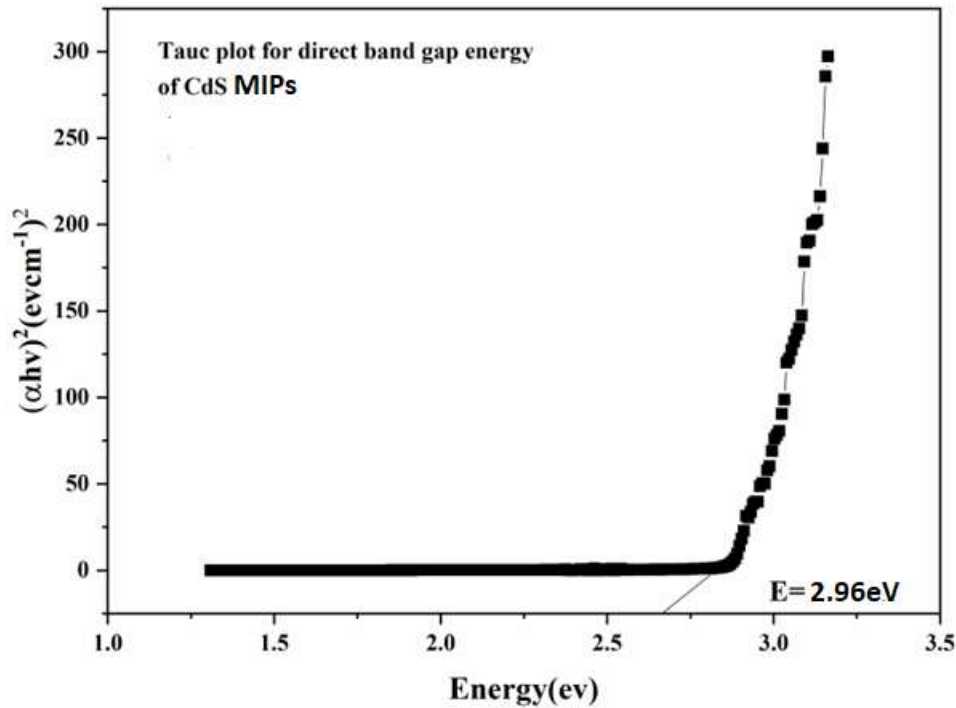


**Figure 9.** Optical band gap energy of MIP/CdS nanocomposite

### 3.8 Computational procedure

To know the effect of MIPs sensitization over the CdS matrix, a DFT modelling was carried out using a RHSEH1PBE/LANL2DZ basis set with a polarizable continuum model of water[176]. The hexagonal structure of wurtzite was utilized to identify key positions for gingerol derived MIPs union at [0001], [01-10] and [0-110] facets[177].

#### 3.8.1 Computational Studies

It has been demonstrated that different facets can develop modification in semiconductor properties of chalcogenides[178]. **Figure 10** depicts the optimized structures of CdS-MIPs and it is possible to observe that MIPs-CdS conjugation takes place as electrostatic interactions rather than covalent bonds. However, it is notable that CdS-MIPs interaction at [0 1 -1 0]

distorts Cd position in the vicinity of MIPs. This structural change may suggest a superficial crystalline rearrangement in order to achieve stability.

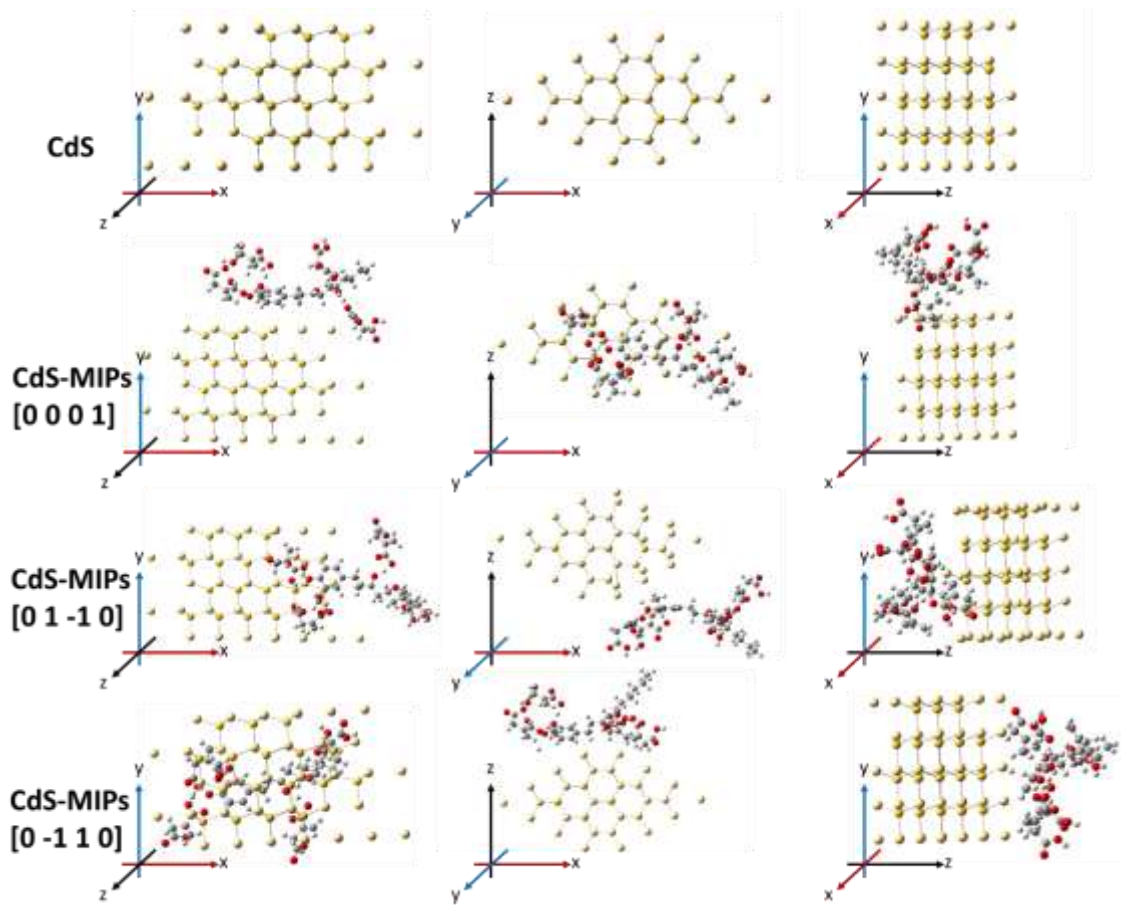


**Figure 10.** DFT energy optimization of CdS-MIPs.

Density of states analyses revealed that docking of gingerol MIPs has a marginal effect in modifying Cb-Vb position; for example, bare CdS displayed a bandgap  $\partial E \sim 2.416$  eV which guards close resemblance with reported values of 2.4 eV[98]. The introduction of MIPs decreased this value to an average bandgap  $\partial E \sim 2.256$  eV with no important differences regardless the position of organic sensitizer **Figure 11**. However, it is interesting to note that interband fluctuations decrease as MIPs are introduced which indirectly contributes to distribute  $e^-/h^+$  density throughout a wide energy range due an increased states availability.

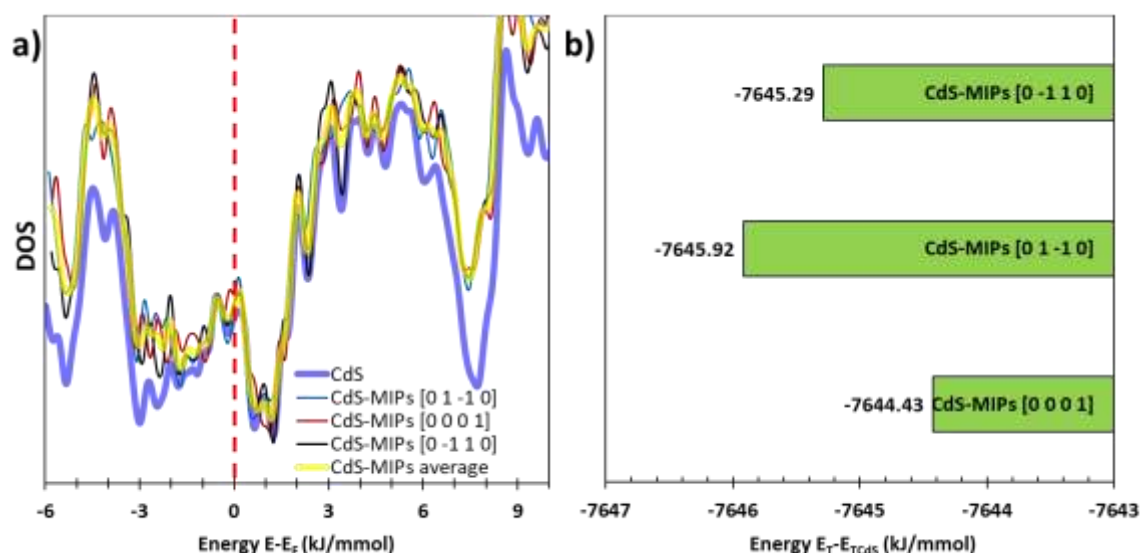


**Figure 11.** a) DOS spectrum of CdS and CdS-MIPs catalysts; b) Total energy determination for composite CdS-MIPs.

Even though sensitization of CdS QDs with MIPs does not affect semiconductor energetic features, total energy of the studied systems showed that docking position can affect stability. Bare CdS wurtzite crystal has a total energy  $E_{TCdS} = -10.399 \times 10^3$  kJ/mmol and the addition of that MIPs decreased total energy in an average of  $\partial E = 7645.21$  kJ/mmol in **Figure 12**. However, it is possible to see that different docking positions have different contributions to  $E_T$ . For instance, [0001] facet interaction in hexagonal CdS crystal reduce the stability as  $E_T - E_{TCdS} = -7644.43$  kJ/mmol which is lower in comparison with [0-110] ( $E_T - E_{TCdS} = -7645.29$  kJ/mmol) or [01-10] ( $E_T - E_{TCdS} = -7645.92$  kJ/mmol). In this case, the higher stability comes from [01-10]-MIPs interaction which supports optimization results where this system yields and structural change. Above mentioned results described the interaction of metal with organic moieties and plays an important role in lowering the energy. This energy related results also helpful in the degradation studies of agriculture waste such as pesticides. Lowering the energy accelerate the rate of photocatalytic degradation.



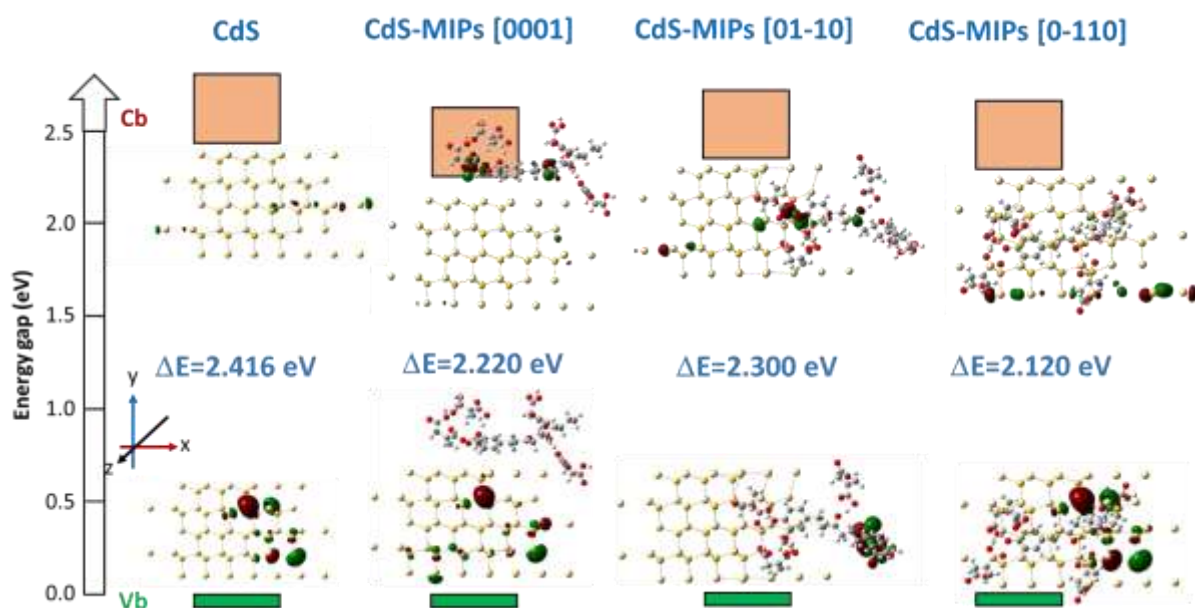


**Figure 12.** Band gap energy of CdS QDs and CdS MIPs composite.

### 3.9 Mechanism of photodegradation

The photogenerated electron-hole pair played an important role in the improved photocatalytic performance of the CdS prepared catalyst. **Figure 13.** depicts the suggested basic photocatalytic pathways (reaction mechanism). The catalyst material in our case can generate an  $e^-h^+$  (i.e., exciton) pair by absorbing visible light energy equal to or greater than the band energy gap. The superoxide radical anions ( $O_2^-$ ), which is formed by the reaction between the  $O_2$  and photogenerated electrons, can be produced when the electrons generated on the CB of the CdS NPs react with the  $O_2$  adsorbed on the surface of the photocatalyst and unpaired  $h^+$  is directly involved in the redox reaction[179]. The superoxide and hydroxyl radicals combine with organic molecules and degrade it to form by-products such as  $CO_2$ ,  $H_2O$ , and other chemicals. The MIP coating can modify the surface charge properties of the nanomaterial. MIPs can be designed with functional monomers that possess specific charges, either positive or negative, depending on the target molecule to be bound. When these charged functional monomers are polymerized onto the nanomaterial surface, they can alter the overall charge of the nanomaterial and create a favourable environment for charge carriers.

By enhancing the charge carriers, MIP-coated nanomaterials can exhibit improved electrical conductivity, charge transfer capabilities, or catalytic activities. This can be particularly useful in applications such as sensors, energy storage devices, or electrochemical systems where

efficient charge transport plays a crucial role in environmental applications. Furthermore, MIP coatings can provide stability and protection for the nanomaterials, preventing aggregation or degradation of the underlying material. The polymer matrix of the MIP acts as a protective layer, and shielding the nanomaterial from external factors and providing long-term stability to the system. Overall, the combination of MIPs and nanomaterials offers a synergistic effect, where the selectivity and binding properties of the MIPs enhanced the charge carrier transport and overall performance of the coated nanomaterial system.

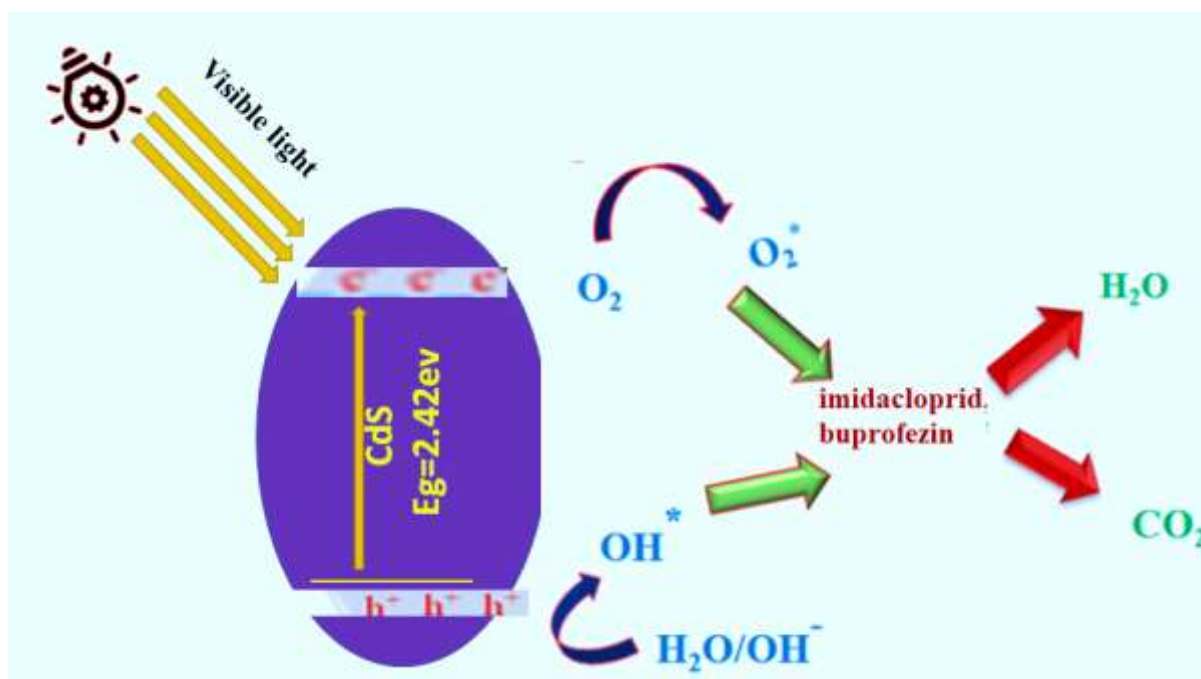


**Figure 13.** Schematic representation of photodegradation mechanism of CdS.

### 3.10 Conclusions

In this study, a novel template molecular imprinted polymer composite (CdS/MIPs), was synthesized and studied. A molecularly imprinted polymer was developed utilising [6]-gingerol as the target molecule, Itaconic acid as the monomer, EGDMA as the crosslinker, and AIBN as the initiator. Simple in-situ polymerization method with CdS QDs as a metal-organic framework was used to accomplish the synthesis. Non imprinted polymer composite was also developed by the extraction of [6]-gingerol from Molecular Imprinted polymer. IR, NMR, XRD, and SEM analysis were used to characterize the material. This material was evaluated as a photocatalyst for the degradation of imidacloprid and buprofezin, both of which are considered organic pesticide pollutant and the photocatalyst displayed good degradation efficiency. The catalyst degrades using pseudo-first-order reaction kinetics. The addition of

MIPs actively enhances semiconductor charge carriers, triggering photocatalytic degradation of pesticide medicines, according to experimental and theoretical studies.

### 3.11 References

- [157] I.A. Banerjee, L. Yu, H. Matsui, Room-Temperature Wurtzite ZnS Nanocrystal Growth on Zn Finger-like Peptide Nanotubes by Controlling Their Unfolding Peptide Structures, *J. Am. Chem. Soc.* 127 (2005) 16002–16003. <https://doi.org/10.1021/ja054907e>.
- [158] P.J. Binu, S. Muthukumaran, Band Gap Tailoring, Size Modulation and Photoluminescence Properties of Mn/Cu doped ZnS Nanostructures, *In Review*, 2021. <https://doi.org/10.21203/rs.3.rs-216184/v1>.
- [159] R.K. Chandrakar, R.N. Baghel, V.K. Chandra, B.P. Chandra, Synthesis, characterization and photoluminescence studies of Mn doped ZnS nanoparticles, Superlattices and Microstructures. 86 (2015) 256–269. <https://doi.org/10.1016/j.spmi.2015.07.043>.
- [160] T. Thi, N. Hien, D. Thu, V. Quoc Trung, Thin films containing Mn-doped ZnS nanocrystals synthesised by chemical method and study of some of their optical properties, *Journal of Experimental Nanoscience*. 8 (2013) 530–538. <https://doi.org/10.1080/17458080.2011.599045>.
- [161] L. Fang, K. Tang, D. Wei, Y. Zhang, Y. Zhou, Photocatalytic Degradation of Norfloxacin By Magnetic Molecularly Imprinted Polymers: Influencing Factors And Mechanisms, 2021. <https://doi.org/10.21203/rs.3.rs-392691/v1>.
- [162] I. Shahnavi, R. Bano, S. Musharraf, M. Sheraz, S. Hussain, S. Ahmed, H. Tahir, Q. Ul Arfeen, M.S. Bhatti, Z. Shad, Photodegradation of Norfloxacin in Aqueous and Organic Solvents: A Kinetic Study, *Journal of Photochemistry and Photobiology A Chemistry*. 302 (2015) 1–10. <https://doi.org/10.1016/j.jphotochem.2015.01.005>.
- [163] L. Li, X. Zheng, Y. Chi, Y. Wang, X. Sun, Q. Yue, B. Gao, S. Xu, Molecularly imprinted carbon nanosheets supported TiO<sub>2</sub>: Strong selectivity and synergic adsorption-photocatalysis for antibiotics removal, *Journal of Hazardous Materials*. 383 (2020) 121211. <https://doi.org/10.1016/j.jhazmat.2019.121211>.
- [164] M. Cantarella, A. Di Mauro, A. Gulino, L. Spitaleri, G. Nicotra, V. Priviter, G. Impellizzeri, Selective photodegradation of paracetamol by molecularly imprinted ZnO nanonuts, *Applied Catalysis B: Environmental*. 238 (2018). <https://doi.org/10.1016/j.apcatb.2018.07.055>.
- [165] C.A. Huerta-Aguilar, A.A. Ramírez-Alejandre, P. Thangarasu, J.A. Arenas-Alatorre, I.A. Reyes-Dominguez, M. de la L. Corea, Crystal phase induced band gap energy enhancing the photocatalytic properties of Zn–Fe<sub>2</sub>O<sub>4</sub>/Au NPs: experimental and theoretical studies, *Catal. Sci. Technol.* 9 (2019) 3066–3080. <https://doi.org/10.1039/C9CY00678H>.
- [166] G. Murugadoss, Synthesis, optical, structural and thermal characterization of Mn<sup>2+</sup> doped ZnS nanoparticles using reverse micelle method, *Journal of Luminescence*. 131 (2011) 2216–2223. <https://doi.org/10.1016/j.jlumin.2011.03.048>.
- [167] H.-J. SUN, Y.-Y. LI, S.-H. LI, Y.-X. ZHANG, S.-C. LIU, Z.-Y. LIU, B.-Z. REN, ZnSO<sub>4</sub> and La<sub>2</sub>O<sub>3</sub> as Co-Modifier of the Monoclinic Ru Catalyst for Selective Hydrogenation of Benzene to Cyclohexene, *Acta Physico-Chimica Sinica*. 30 (2014) 1332–1340. <https://doi.org/10.3866/PKU.WHXB201405072>.
- [168] S. Sapra, A. Prakash, A. Ghangrekar, N. Periasamy, D.D. Sarma, Emission Properties of Manganese-Doped ZnS Nanocrystals, *J. Phys. Chem. B*. 109 (2005) 1663–1668. <https://doi.org/10.1021/jp049976e>.
- [169] M.L. Steigerwald, L.E. Brus, Semiconductor crystallites: a class of large molecules, *Acc. Chem. Res.* 23 (1990) 183–188. <https://doi.org/10.1021/ar00174a003>.
- [170] W.-X. Wu, X.-Z. You, A.-B. Dai, S.-P. Jing, Indo/Giao calculations of the NMR shielding constant including d orbitals, *Polyhedron*. 9 (1990) 1849–1854. [https://doi.org/10.1016/S0277-5387\(00\)83997-2](https://doi.org/10.1016/S0277-5387(00)83997-2).
- [171] N. Chestnoy, R. Hull, L.E. Brus, Higher excited electronic states in clusters of ZnSe, CdSe, and ZnS: Spin-orbit, vibronic, and relaxation phenomena, *J. Chem. Phys.* 85 (1986) 2237–2242. <https://doi.org/10.1063/1.451119>.

- [172] X. Wang, H. Huang, B. Liang, Z. Liu, D. Chen, G. Shen, ZnS Nanostructures: Synthesis, Properties, and Applications, *Critical Reviews in Solid State and Materials Sciences*. 38 (2013) 57–90. <https://doi.org/10.1080/10408436.2012.736887>.
- [173] T. Liu, J. Qian, C. Wang, Y. Wang, Y. Yang, B. Kong, Y. Qian, W. Wu, Enhanced photocatalytic degradation performance of mono-disperse ZnS nano-flake on biocarbon sheets, *Inorganic Chemistry Communications*. 119 (2020) 108142. <https://doi.org/10.1016/j.inoche.2020.108142>.
- [174] M. Roushani, M. Mavaei, Graphene quantum dots as novel and green nano-materials for the visible-light-driven photocatalytic degradation of cationic dye, *Journal of Molecular Catalysis A: Chemical*. 409 (2015) 102–109. <https://doi.org/10.1016/j.molcata.2015.08.011>.
- [175] H.R. Rajabi, O. Khani, M. Shamsipur, V. Vatanpour, High-performance pure and Fe<sup>3+</sup>-ion doped ZnS quantum dots as green nanophotocatalysts for the removal of malachite green under UV-light irradiation, *J Hazard Mater*. 250–251 (2013) 370–378. <https://doi.org/10.1016/j.jhazmat.2013.02.007>.
- [176] H.R. Pouretedal, H. Eskandari, M. Keshavarz, A. Semnani, Photodegradation of organic dyes using nanoparticles of cadmium sulfide doped with manganese, nickel and copper as nanophotocatalyst, *Acta Chimica Slovenica*. 56 (2009) 353–361.
- [177] T. Oyama, A. Aoshima, S. Horikoshi, H. Hidaka, J. Zhao, N. Serpone, Solar photocatalysis, photodegradation of a commercial detergent in aqueous TiO<sub>2</sub> dispersions under sunlight irradiation, *Solar Energy*. 77 (2004) 525–532. <https://doi.org/10.1016/j.solener.2004.04.020>.
- [178] M. Montazerzohori, M. Nasr-Esfahani, S. Joohari, Photocatalytic degradation of an organic dye in some aqueous buffer solutions using nano titanium dioxide: A kinetic study, *Environment Protection Engineering*. 38 (2012) 45–55. <https://doi.org/10.5277/EPE120305>.
- [179] A. Fujishima, X. Zhang, Titanium dioxide photocatalysis: present situation and future approaches, *Comptes Rendus Chimie*. 9 (2006) 750–760. <https://doi.org/10.1016/j.crci.2005.02.055>.

## CHAPTER 4

### **Photocatalytic activity tuning in a Novel Ag<sub>2</sub>S QDs embedded in Molecular imprinted polymer matrix**

#### **4.1 Introduction**

Access to clean freshwater is an essential ingredient in healthy human life. However, 1.1 billion people across the globe lack access, and 2.7 billion experience water scarcity for at least one month per year. Due to water pollution nearly 14,000 deaths are registered per day in developing countries. Rapid rise in industrialization of the world and its high population density, the problem of addressing water contamination has attracted significant attention globally. The growing amount of industrial effluent containing various types of colours from the textile, food, drug, and other industries makes water pollution even more concerning. The discharge from these effluents into ecosystems can cause environmental damage and have negative impacts on human health, where the majority of the discharge is carcinogenic and mutagenic. Recently, water-soluble Azo dyes have been extensively employed as colouring agents in a range of products. Azo dyes are highly visible, even at extremely low concentrations. Moreover, due to their complicated molecular structure and large molecule size, these dyes are considered nonoxidizable by traditional physical and biological treatments. The colour of these dyes in water can be easily seen even at very low concentrations, making water extremely harmful to the environment and human health.[180]. The perpetual colour of dyes has a significant impact on the eyes and skin of animals. These dyes in water cause carcinogenic, mutagenic, and genotoxic disorders in humans, animals, and microorganisms. Dyes not only distort the beauty of the river, but they also reduce sunlight penetration through water, affecting photosynthesis in aquatic green plants [181]. Dyes such as Sunset yellow (Yellow 6, E 110, or SY) and Alizarin red are recorded as extremely toxic dyes in aqueous water. SY has two solubilizing sulfonate groups attached to either end of the molecule and two central aromatic groups (phenyl and naphthyl rings connected by an azo group). Because of its azo functional group (N=N) and aromatic ring formation, SY has the potential to have an impact on human health[182], Similarly AR is a potent allergen [183]. Hence their removal is necessary before discharging into environment. ppMany methods for pollutant removal and treatment have been developed and used thus far, including adsorption, electrolysis[184], biological treatments[185] and so on. Among the various pollutant treatment methods, photocatalytic degradation have been identified as operational, sustainable, and scalable technologies that could address the problem of environmental pollution.

Photocatalysis is a promising technique for capturing energy. When photon energy is more than the band gap energy of semiconductor, electrons from the valence band (VB) can be excited to the conduction band (CB), resulting in electron/hole pairs in photocatalysts. Electrons and holes migrate to the surface of the Earth to participate in chemical reactions[186].Titanium dioxide (TiO<sub>2</sub>) electrode has been used to perform the water-splitting process for the first time under ultraviolet (UV) radiation in 1972[187] .Traditional photocatalysts such as TiO<sub>2</sub>,Zinc Oxide (ZnO), cadmium sulphide (CdS) and silver phosphate (Ag<sub>3</sub>PO<sub>4</sub>) have been widely used for pollutant degradation[188]. Silver sulphide (Ag<sub>2</sub>S) is a semiconductor with various fascinating applications, including infrared detectors, optoelectronics, PV cells, superionic, magnetic, and lasers. Ag<sub>2</sub>S exists in two phases,  $\alpha$ -Ag<sub>2</sub>S and  $\beta$ -Ag<sub>2</sub>S, in which it interacts like a metal and a semiconductor, respectively [189]. Ag<sub>2</sub>S is a semiconductor with a narrow band gap (1.5 eV) and a high absorption coefficient (about 10<sup>4</sup> m<sup>-1</sup>) [190]. Despite its broad-spectrum applicability, Ag<sub>2</sub>S is non-selective sorbents and toxic in nature which limits their use in photocatalysis[191].To counter the selective applicability issue, Molecular imprinted polymer (MIPs) plays an eminent role. The Ag<sub>2</sub>S QDs embedded in MIPs for effective photodegradation has the potential to alter the activity and increase the photocatalyst's selectivity[192]. The benefits of molecular imprinting polymers (MIPs) over natural identification materials are, their chemical stability,Thermal resistance, high pressure resistance, good organic solvent resistance and cost effective. Deng et al. used a surface molecular imprinting approach to make conductive polypyrrole/TiO<sub>2</sub> composites while removing methyl orange (MO) from wastewater[193]. Li et al. used nanoscale TiO<sub>2</sub> immobilised in a molecularly imprinted chitosan matrix to create a new adsorbent with molecular imprinting and photodegradation which breaks down organic dyes[194]. Shen et al. developed a film in an aqueous solution containing molecular recognition sites and photocatalytic sites in the presence of Fe<sub>3</sub>O<sub>4</sub> magnetic nanoparticles [195]. During photodegradation, the MIPs first detected the target molecules and then moved to the photocatalytic domains, resulting in the successful degradation of the bound target pollutant [196]. Vary less work has been done in the synthesis and application of MIPs nanocompositeusing organic naturally extracted organic template molecule.We have focussed on the extraction of [6]-gingerol from ginger. Ginger contains a variety of gingerols, which are pungent phenolic compounds found in the fresh roots. These gingerols have different chain lengths, ranging from 6 to 10 carbon atoms. The most abundant gingerol is 6-gingerol, characterized by its unbranched alkyl chain of 6 carbon atoms. It is considered the primary bioactive compound responsible for the pungent taste and aroma of ginger.[6]-Gingerol

possesses several therapeutic effects, including antioxidant, anti-inflammatory, antipyretic (fever-reducing), and antibacterial properties.[6]-gingerol possesses aromatic -OH group which helps in the crosslinking formation with monomer molecule increasing the rigidity and specificity of Molecular imprinted polymer towards host molecule and encapsulation of QDs in the MIPs will have greater potency as photocatalyst.

In this work, Ag<sub>2</sub>S-MIPs composite was prepared and used for the first time as a photocatalyst for the degradation of Alizarin red S (ARS) dye and yellowish Sunset azo dye under visible light source. The preparation was conducted to enhance the performance of Ag<sub>2</sub>S and also to focus on the extraction of [6]-gingerol organic natural molecule from ginger, by using Soxhlet method isolated by acid base method.

## **4.2 Experimentation**

### **4.2.1. Reagents and chemicals**

The chemical reagents used in this study were of analytical grade. Sigma Aldrich supplied the Butyl acrylate, Ethylene glycol dimethacrylate (EGDMA), Azobisisobutyronitrile (AIBN) and TCI provided acetonitrile and diethyl ether. The template molecule was [6]-gingerol, which was isolated from ginger.

### **4.2.2. Instruments**

The infrared spectra (4000-400 cm<sup>-1</sup>) in KBr was recorded using an FTIR instrument (Lpu). <sup>1</sup>HNMR measurements were performed on Bruker-500 and 400MHz instruments, using DMSO-d<sub>6</sub> as the solvent and tetramethyl-silane as the internal reference standard. X-ray diffraction and FESEM were used to examine the crystalline size and morphological shape of the synthesised sample. Thermogravimetric analysis-differential scanning calorimetry was carried out in a N<sub>2</sub> environment on Perkin Elmer DSC-7 equipment at a heating rate of 10 °C with 1 to 2 mg of material.

### **4.2.3. Extraction of [6]-gingerol by Soxhlet method**

Soxhlet extraction apparatus was employed for 20g of grounded ginger with 200ml of ethanol in distillation flask ground. The extraction was conducted at 78.1°C for 6 h with 5-6 heating cycle in a heating mantle. The procedure was repeated till 200g of extract was obtained. The extracted compound contained non-volatile homologues compounds in which [6]-gingerol is the major bioactive component. The extraction was precipitated by adding a 20 ml of H<sub>2</sub>O which were then cooled to 5-10°C. The yellow oily precipitation mixture was then poured into



a separating funnel. The pH of the immiscible compound was increased to an 11-12 range by adding a standard solution of sodium hydroxide. Ethyl acetate was also added until two layers were obtained. Here, an upper organic layer and aqueous layer formed below. The aqueous layer was separated and HCl was added until the pH became less than 1. After few minutes of separation precipitates started collecting downward which were collected and filtrated further for analysis.

#### **4.2.4 Synthesis of Ag<sub>2</sub>S**

The preparation of various precursor solutions is the first step in the synthesis of silver sulphide nanoparticles. First, 50 mL of deionized water solvent was used to dissolve 1.698 g (0.1 M) of silver nitrate hexahydrate (AgNO<sub>3</sub>·6H<sub>2</sub>O), 0.4 g (0.1 M) of sodium sulphide (Na<sub>2</sub>S·6H<sub>2</sub>O), and 3.0 g of PVP. The solutions of sodium sulphide and PVP were added drop-wise to the silver nitrate solution and was stirred continuously for 3h. The resultant precipitate was then centrifuged and washed with deionized water and ethanol, respectively. Finally, the precipitate was dried in an oven at 80 °C for 2–3 h.

#### **4.2.5. Synthesis of molecular imprinted polymer encapsulated with silver sulphide QDs**

1.16g of [6]-gingerol was used as a targeted template and was dissolved in a conical flask with 10ml of tetrahydrofuran and acetonitrile. Because [6]-gingerol is poorly soluble in tetrahydrofuran, a mixture of tetrahydrofuran and acetonitrile was used as a Porogenic solvent in the reaction. 4.43g of monomer butyl acrylate was added in the same manner as in the conical flask, followed by 7.8ml of crosslinking agent Ethylene glycol dimethyl acrylate (EGDMA). The molar ratio was kept constant at 1:4:16 and 0.05g of 2,2-azobisisobutyronitrile (AIBN) was used as a polymer initiator to initiate the reaction via free radical polymerization. The reaction was carried out in the presence of a nitrogen atmosphere by purging N<sub>2</sub> gas for 15 minutes with an access flow of 0.1L/min and was continued for 3 hours until an amorphous polymer was obtained, after which Cadmium sulphide QDs were added. The contents of the conical flask containing the mixture were allowed to polymerize for 3 hours on a hotplate at 80°C. The polymer was purified using methanol. This results in a molecular imprinted polymer (MIPs) composite. The obtained solid polymer was ground and crushed with a mortar and pestle into a fine powder, which was then analysed using FTIR, XRD, and FESEM.

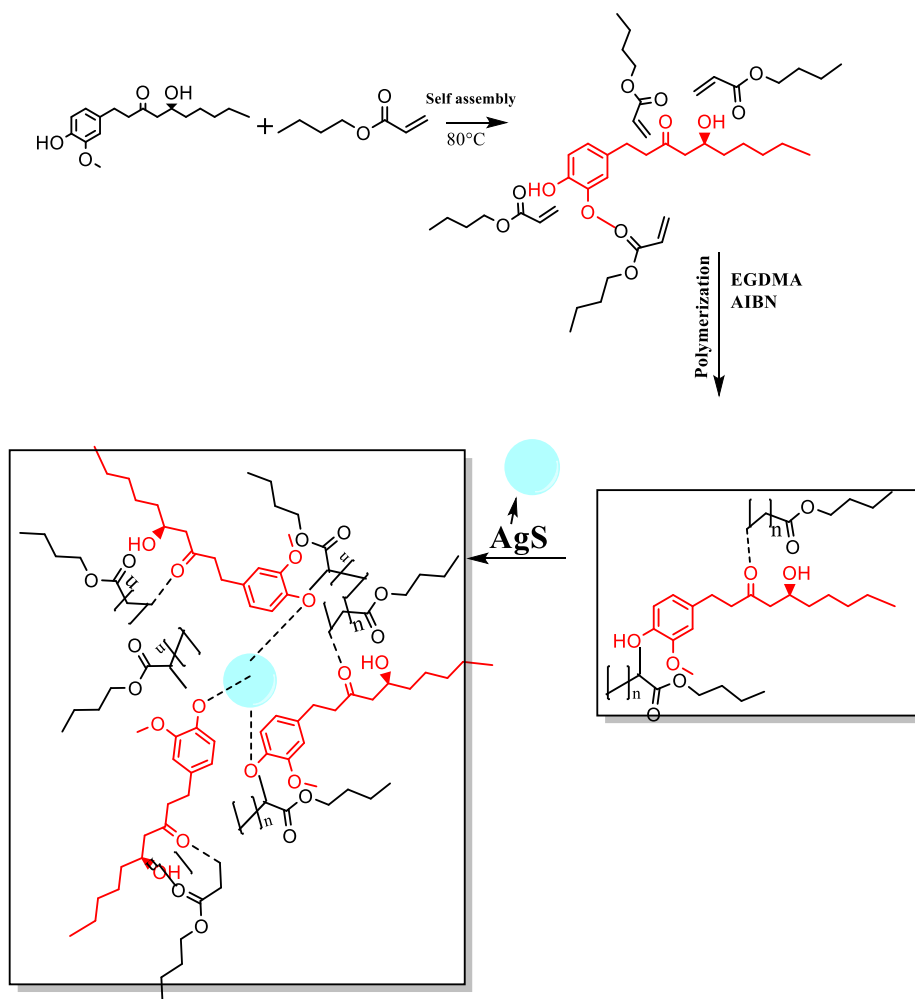


**Figure 1.** Schematic representation of Ag<sub>2</sub>S-MIPs.

## 4.3 Results and Discussion

### 4.3.1. Structural and morphological study

The crystalline structure of silver sulphide Quantum dots was investigated using XRD data (see in Fig. 2). The diffraction lattice was analysed in the range 20° to 70° resulting in the appearance of several major peaks within the chosen range. The major peaks are  $2\theta = 25.8, 28.9, 31.45, 33.01, 34, 36.80, 38.019, 40.78, 43.42, 45.504, 46.14, 47.7, 48.03, 53.34, 58.28, 64.529$  are the prominent peaks. These peaks correspond to diffraction from lattice planes (101), (111), (-112), (120), (-121), (121), (103), (031), (200), (023), (113), (311), (21-2), (22-2), (042), (034). When compared to the results from the previous study, the diffraction patterns appear to imply the presence of a monoclinic Ag<sub>2</sub>S phase with lattice parameters of  $a = 4.22900\text{\AA}$  and  $c = 7.86200\text{\AA}$ . (JCPDS Card File: 00-014-0072). The average crystallite size of silver sulphide nanoparticles Ag<sub>2</sub>S was calculated using Full-Width half maxima measurements. The Debye-

Scherer equation and the Full-Width at Half Maximum (FWHM) of X-Ray diffraction peaks were used to calculate the average crystallite size of silver sulphide nanoparticles Ag<sub>2</sub>S [41].

$$D = K\lambda / \beta \cos\theta \quad (1)$$

where  $\lambda$  is the X-ray wavelength (1.5405),  $k$  is the Scherrer constant ( $k = 0.89$ ),  $\beta$  is the diffraction peak's full width at half maximum (FWHM) in radians, and  $\theta$  is the Bragg angle corresponding to the maximum of the diffraction peak in degrees.  $D = 6-7$  nm is the average crystallite size obtained. The fabrication peaks of Ag<sub>2</sub>S-MIPs and Ag<sub>2</sub>S-NIPs were almost identical to pristine Ag<sub>2</sub>S but the corresponding peaks were found weaker suggesting the embedding of MIPs would impair the intensity of diffraction peaks.

The TEM images of Ag<sub>2</sub>S reveals smooth surface but offers uniform opportunity for the fabrication of MIPs shell. The elemental and crystalline composition of silver sulphide QDs is revealed by the EDX pattern. The elemental mapping of the same powder revealed consistently distributed silver and sulphur components in the medium. The elemental analysis based on EDX data is shown in **Figure 2**, which clearly shows two strong peaks linked with the presence of silver in the produced nano-particles.

The TEM image of the prepared Ag<sub>2</sub>S QDs in **Figure 3** shows that the QDs are homogeneous and uniformly dispersed in the solution. The approx. Ag<sub>2</sub>S QD size was estimated to be 6-7 nm, though the boundaries were not perfectly defined due to the presence of capping agents on the Ag<sub>2</sub>S QD surfaces. FESEM was used to examine the surface morphology of Ag<sub>2</sub>S-MIP composite, and the images are shown in **Figure 4**. **Figure 4 (A, B)** depicts the morphological characteristics of Ag<sub>2</sub>S-MIP and **Figure 4(C, D)** shows Ag<sub>2</sub>S NIPs. The coating of MIPs has increased cross linking network of polymeric composite with rough and porous surfaces of average size 50-60 nm, whereas in Ag<sub>2</sub>S-NIPs removal of porosity was observed in SEM images indicating lack in crosslinking of polymeric network. When the particle sizes of Ag<sub>2</sub>S-functionalized QDs and Ag<sub>2</sub>S-MIP obtained from XRD and FESM are compared, it can be concluded that the increase in particle size demonstrated the formation of a polymeric network on the surface of Ag<sub>2</sub>S-functionalized QDs.

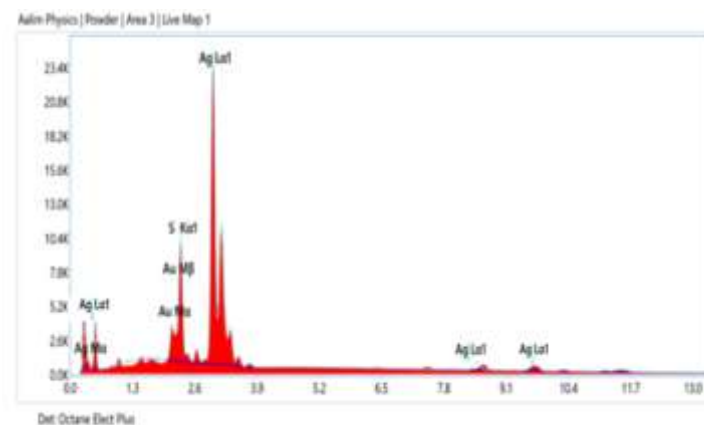
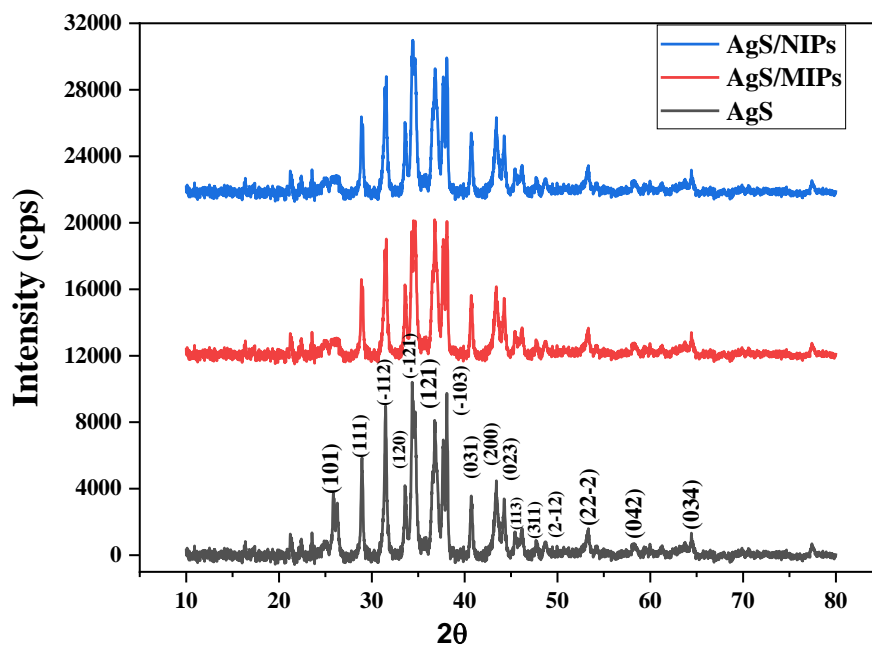


Figure 2. XRD and EDX of Ag<sub>2</sub>S (B)XRD of Ag<sub>2</sub>S-MIPS composite

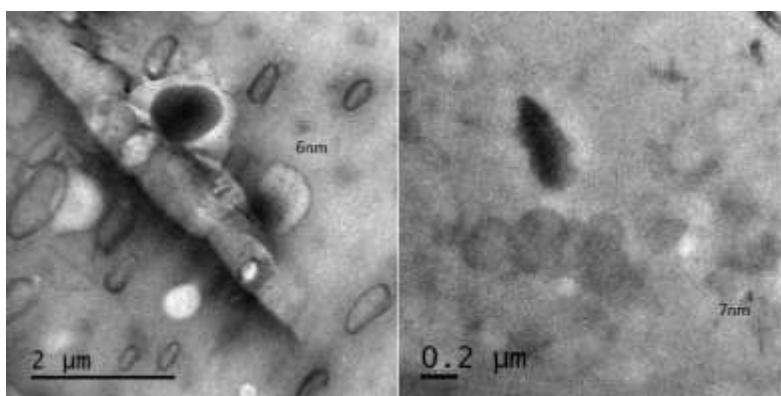
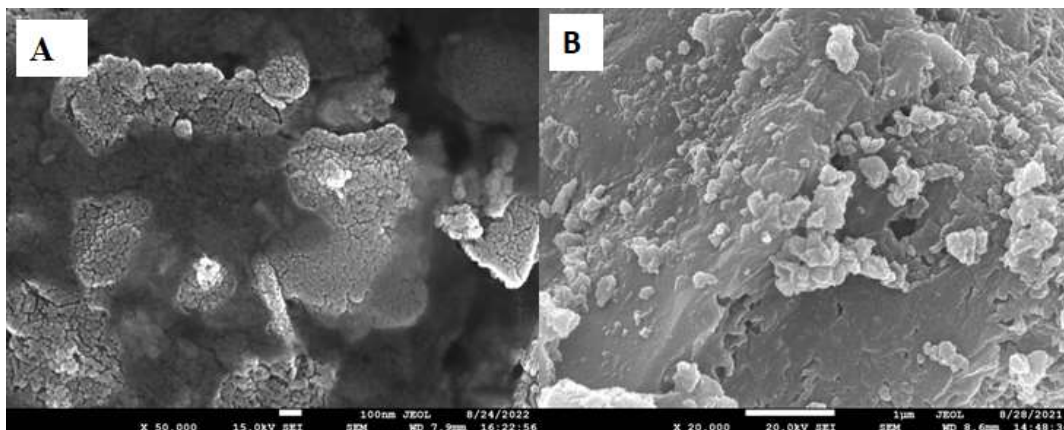


Figure 3. TEM images Ag<sub>2</sub>S Quantum Dots



**Figure 4.** FESEM images of (A) Ag<sub>2</sub>S-MIPs and (B) Ag<sub>2</sub>S-NIPs composite.

The spectrum analysis of bioactive compounds was performed using FTIR. The spectrum of ginger extracts revealed the phenol group [14]. As shown in **Figure 4 Chapter 2**, the trend of spectrums for 4, 6, and 8 hours was almost identical, indicating the presence of aliphatic O-H groups in the 3000 to 3600 cm<sup>-1</sup> range. However, after 10 hours of extraction, the aliphatic O-H absorption was completely absent. This was due to the dehydration of gingerol to shogaol, as shogaol lacks aliphatic O-H groups. At lower extraction times of 4 and 6 hours, respectively, the bands at 2800 to 2950 cm<sup>-1</sup> showed two stretching peaks. The CH<sub>2</sub> and CH<sub>3</sub> stretching were well separated (2944 and 2832 cm<sup>-1</sup>). Because of the changes in compound structure over time, the bands became a broad peak. While the C-O group was well represented at 1030 cm<sup>-1</sup> for all extraction times. <sup>1</sup>HNMR shows the following peaks in : 0.6-1.5 (3H, t, j=6.6Hz, H-10), 1.6-1.9 (8H, m, H-6, H-7, H-8, H-9), 2.2-2.45 (1H, d, j=8Hz, H-4), 2.67-2.85 (2H, s, H-2), 3.847 (3H, s, -OCH<sub>3</sub>) 6.631 (1H, dd, J=6Hz, 2Hz, H-6'), 6.772 (1H, d, J=8Hz, H-5'), 6.78 (1H, s, H-2'). In this spectrum HNMR exhibits separate signals for the presence of -OCH<sub>3</sub> group with a chemical shift at 3.837 and signals of three aromatic protons were assigned to H2', H5' and H6'. In this spectrum δ value at 0.6-1.5 is relevant to -CH<sub>3</sub> groups and the rest of protons such as δ value at 1.6-1.9, 2.2-2.5, 2.67-2.85 is corresponds to -CH<sub>2</sub>- groups in aliphatic region

FT-IR spectroscopy was used to determine major functional groups present in the compound as shown in **Fig 5**. A hydroxyl (-OH) group was assigned to the band at 3308 cm<sup>-1</sup>. The vibrations of the hydrocarbon chains' methyl and methylene are located at 2095 and 2921 cm<sup>-1</sup>. The presence of the S-O group is indicated by the IR spectrum's strong absorption bands in the 1030–1107 cm<sup>-1</sup> (sulphate) and 1350–1490 cm<sup>-1</sup> (sulfoxide) ranges. Metal-sulphur, known as Ag-S, is responsible for the peaks in the 500–750 cm<sup>-1</sup> range.

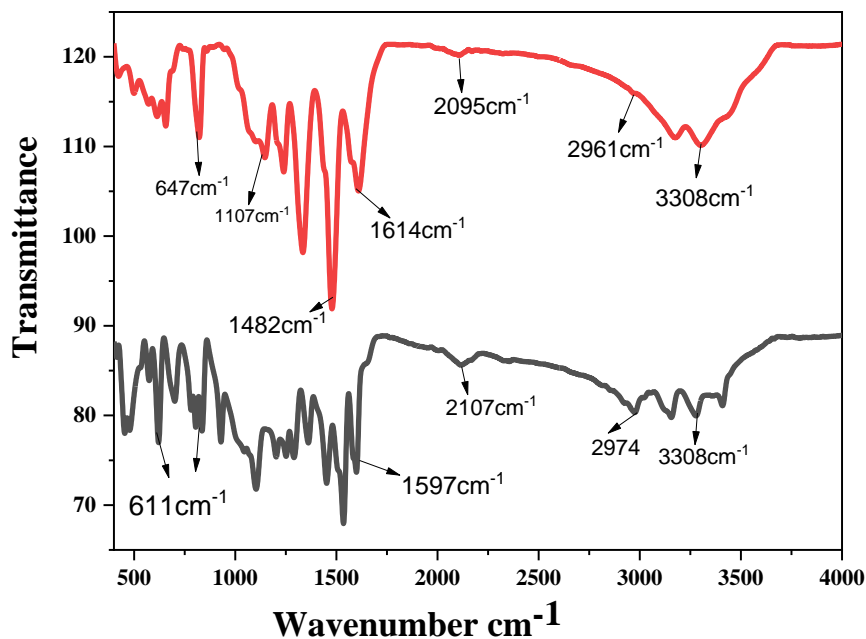


**Figure 5.** FTIR Spectra of Ag<sub>2</sub>S QDs and AgS-MIPs composite

#### 4.4 Fluorescence Spectra

The fluorescence emission spectra of the Ag<sub>2</sub>S MIPs nanocomposite were recorded and are displayed in **Fig 6a**. Ag<sub>2</sub>S MIPs had a fluorescence emission peak at 834 nm both at room temperature and in an ethanol solution. the fluorescence emission peak is observed both at room temperature and in an ethanol, solution suggests that the fluorescence properties of the nanocomposite are not significantly affected by the surrounding environment or solvent. This stability is beneficial for applications where consistent fluorescence emission is desired.

The zeta potential of the dispersed nanoparticles was ascertained through electrophoretic light scattering. The particles' zeta potentials were found to be -6.5mV as shown in **Fig.6c** by electrophoresis. The carboxylate groups on the surface of the particles give them a strong negative zeta potential, and they have shown excellent stability. Zeta potential measurements as well as particle size distributions were performed on each sample in a comparable manner. The zeta potential not only indicates the electrical charge on the particle surface, but it also indicates the stability of colloidal dispersions. The average particle size is about 60nm, which is larger than the untreated particle size (6 nm), indicating more agglomeration of Ag<sub>2</sub>S-MIPs as shown in **Figure 6b and bd**. The particle size distributions' results agree with the zeta potential measurement.

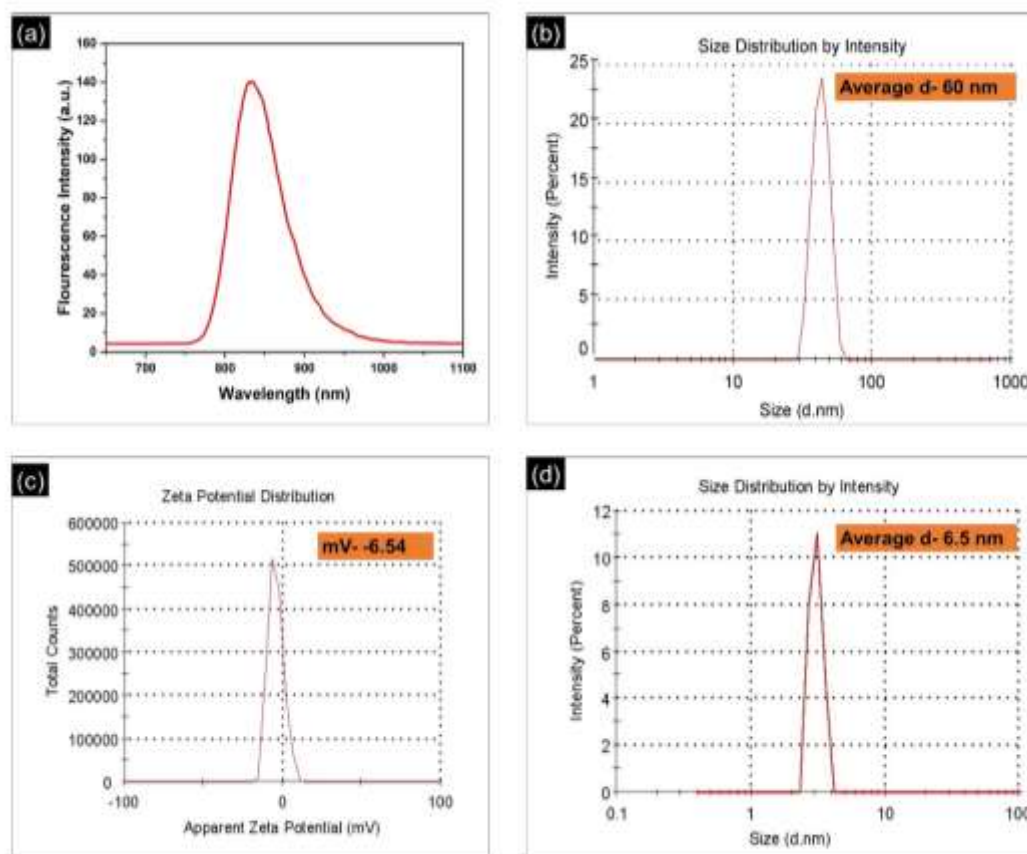


**Figure 6a.** Fluorescence spectra and Zeta potential analysis of Ag<sub>2</sub>S-MIPs composite (a,b,d) and Zeta potential of Ag<sub>2</sub>S QDs(c).

#### 4.5 TGA-DSC Study

Thermal Study of MIPs composite was done to analyze the melting transition, crystalline nature, components and thermal stability where some physical variable is measured against temperature. Thermogravimetric analysis (TGA) is a type of thermal analysis employed to examine sample degradation temperature, moisture content, chemical changes, and thermal stability of components. The stability of MIPs-Ag<sub>2</sub>S composite was determined using TGA plot in **Figure 7**. The composites began to disintegrate at 248°C and were completely decomposed at 352°C. All of the composites' residual weights were found to be 18%. Differential scanning calorimetry (DSC) characterization was also performed to evaluate different transitions such as melting, crystallization and glass transition temperature. TGA–DSC coexistence measurement not only improves output values but also simplifies interpretation. DSC data allows for the distinguishing endothermic and exothermic states. The endothermic peaks at 99.8°C can be observed in DSc curves revealing indicates a phase transition, such as melting. The peak corresponds to the absorption of heat energy required to

overcome the intermolecular forces holding the solid together the dip at 338°C accompanied significant weight loss indicates major decomposition of MIPs composite in **Figure 7**.

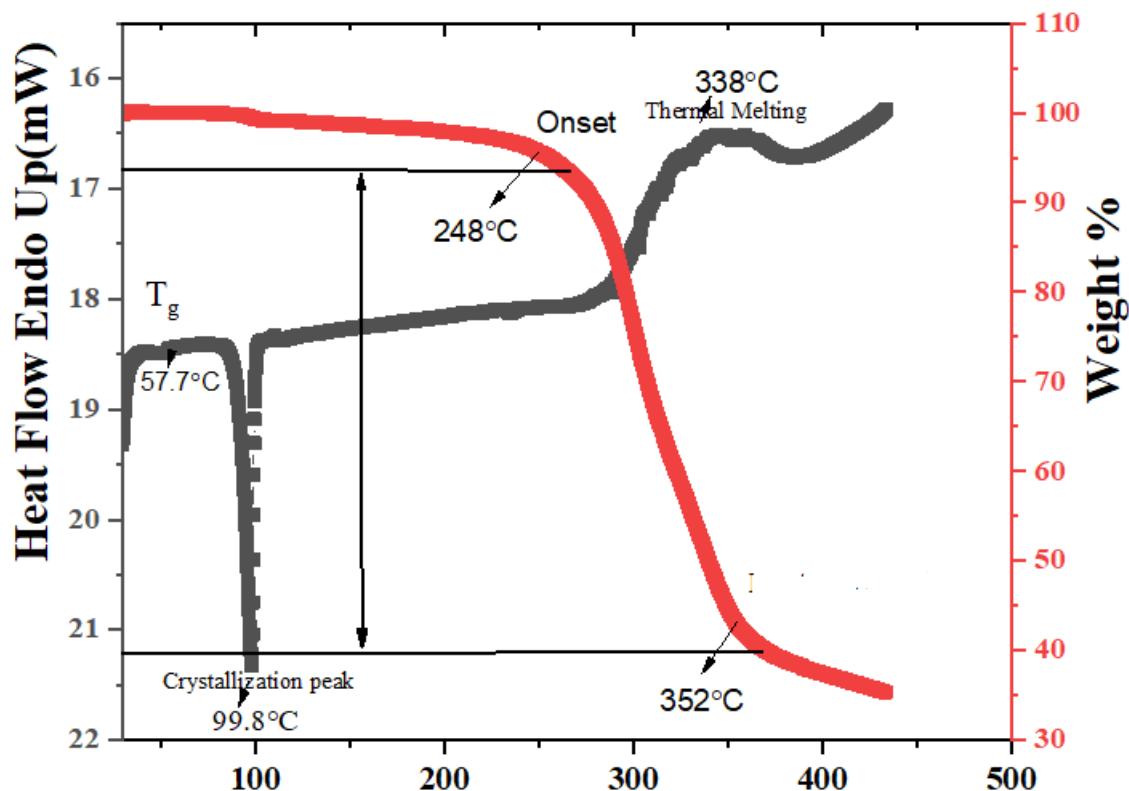


**Figure 7.**TGA-DSC analysis of AgS-MIPs composite

#### 4.6 Photocatalysis activity

Stock solution of Alizarin red and Sunset yellow dye solutions were prepared by dissolving 20mg of both in 1000ml of deionized water. Then 100ml solution was taken from both and stirred for 30minutes to ensure adsorption equilibrium. The photocatalytic degradation experiment was carried out on the water bath placed inside box with visible source at room temperature. A UV-1800 (Shimadzu) spectrophotometer was used to measure the absorbance of the response result during the experiment. Decolorization is defined as

$$\% \text{Degradation} = (C_0 - C) * 100 / C_0 \quad (2)$$

where,  $C_0$  is the initial concentration of dye concentration at  $\lambda_{\text{max}}$ . The Visible spectra revealed that the irradiation time and dye photodegradation increase in both cases. **Figure 8A** depicts the percentage degradation of AR and SY dye photodegraded by photocatalyst composite at



increasing time intervals. **Figure 8B<sub>1</sub>** and **B<sub>2</sub>** of AR and SY shows a plot of  $\ln C_0/C_t$  versus irradiation time, which indicates a linear relationship and pseudo-first-order kinetics. The results show that AgS-MIPs composite degraded dye by approximately 32.75-37% within 30 minutes of analysis, which increases to 75.51% and 61% when the irradiation time increased to 120 minutes as shown in **Figure 8(A)**. The degradation percentage was also calculated for Ag-S MIPs and AgS-NIPs using effect of Catalyst, pH and concentration illustrated in **Figure 9 (E1,e1)** and **Figure10(E2,e2)**

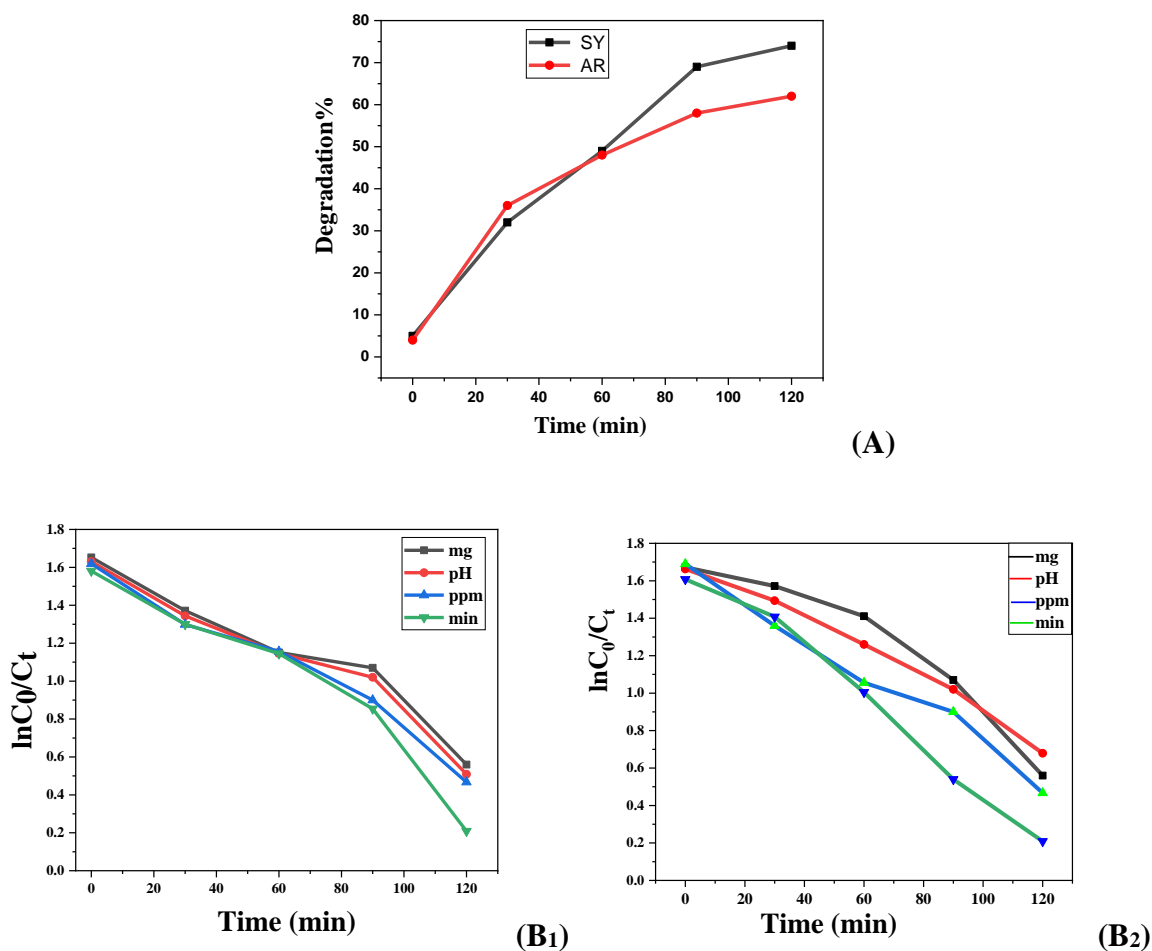


**Figure 8.** (A) Degradation % of Alizarin red and Sunset at different time and (B)  $\ln C_0/C_t$  versus irradiation time

### (i) Effect of Catalyst

When analysing the degradation of AgS-MIPs and AgS-NIPs in **Fig. 9(A1, a1)** and **Fig. 10(A2, a2)** one of the main parameters that should be considered is the amount of catalyst used. To avoid using too much catalyst, the optimum loading for dye molecule removal must be determined. The effect of catalyst amount on photocatalytic degradation of AR and SY was

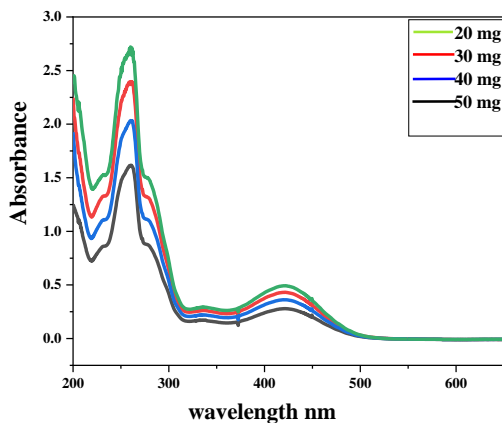
studied using 20-50 mg of catalyst per 100 ml of solution. When the amount of AgS-MIPs catalyst was increased from 20 to 50 mg the degradation increased to 82 to 84.5% for Alizarin red and Sunset yellow at 120 minutes of irradiation time. This increase in degradation was due to an increase in the quantity of nanocomposite, which increases photon absorption and dye molecule adsorption. The removal rate decreases as the nanocomposite concentration increases. The screening effect may occur if the catalyst loading exceeds 50 mg/25mL (i.e., 5 g/L), which reduces the catalyst's specific activity (aggregation of particle may also reduce catalytic activity at high catalyst loadings [197]). However, the optimum amount of catalyst loading for the degradation of AR and SY was found to be 50mg/25ml. It is noticed that removal efficiency of AgS/NIPs has significantly decrease with 62% and 65% degradation efficiency for Alizarin red and Sunset yellow dye indication the decrease in specificity shown in Figure **Fig. 10(A2, a2)**.

#### **(ii) Effect of pH**

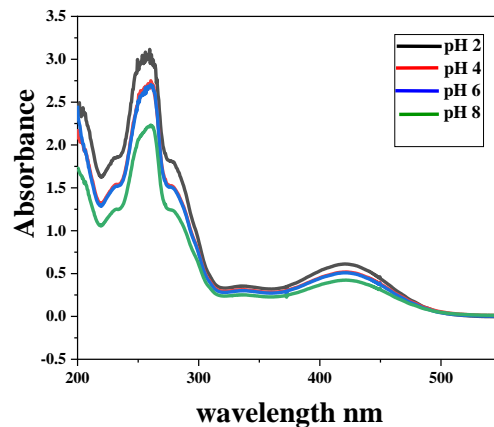
The effect of pH is critical in the photocatalytic degradation of various pollutants. The pH of the dye determines the surface charge properties of Ag<sub>2</sub>S-MIPs composite. The effect of pH solution on the photodegradation rate of Alizarin red and sunset yellow dye was studied at different pH values (2-8) as shown in **Figure 9(B1, b1)**. The pH of the solution was adjusted before visible irradiation, but was not monitored during the reaction. The increase in pH value from 2 to 8 has changed surface properties of catalyst and increased the degradation% to 80% (alizarin red) and 81% (Sunset yellow Azo), respectively, after 120 minutes of visible source. The results confirmed that the photodegradation rate increased as the pH of the medium increased. The results reveal that photodegradation of the dye was slightly higher in basic medium than in acidic medium, which is postulated to have been caused by the increased formation of hydroxyl radicals (strong oxidising species. While for AgS/NIPs composite, the degradation was found to be 59% and 62% illustrated in **Figure10 (B2, b2)**. The interpretation of pH role on the photodegradation is not an easy approach because pH has various roles here such as generation of charged ions during the process, maintaining electrostatic interaction between the solvent molecules, nanocomposite surface and substrate. The maximum degradation of AR dye was obtained by Saeed et al. at pH 12, which was attributed to dye oxidation by positive hole and hydroxyl radicals in the basic medium[198]. Similarly, Rajamanickam et al obtained maximum degradation of Sunset yellow at pH 7[199].

#### **(iii) Effect of Dye Concentration**

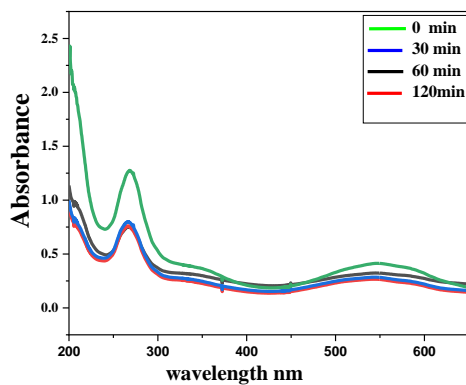
The impact of pollutant concentration on photodegradation rate at constant catalyst amount was studied at varying ppm concentrations (5, 10, 15, and 20 ppm). The degradation rate was reduced with increase in the dye concentration from 5ppm to 20ppm as shown in **Figure 9(D1, d1)**. The same trend was followed with percentage degradation less efficient in Ag-SMIPs as shown **Figure10(D2, d2)**. The rate of degradation is directly proportional to the formation of OH radicals on the surface of the catalyst and the likelihood of OH radicals reacting with dye molecules. The probability of a dye molecule reacting with hydroxyl radical decreases as the generation of hydroxyl radical remains constant. Furthermore, as the initial dye concentrations increase, the path length of photons entering the solution decreases. As a result, photocatalytic degradation efficiency decreases. The opposite effect, or an increase in photon absorption by the catalyst, is seen at low concentrations, though. The adsorption of oxygen and OH<sup>•</sup> onto the catalyst surface may also be hindered by the high concentration of dye that has been adsorbed[200].



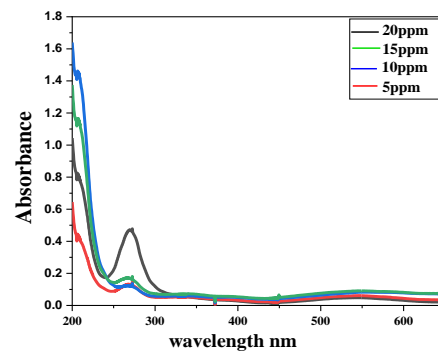
(A1)



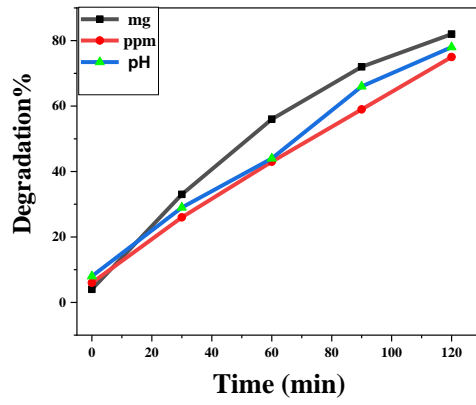
(B1)



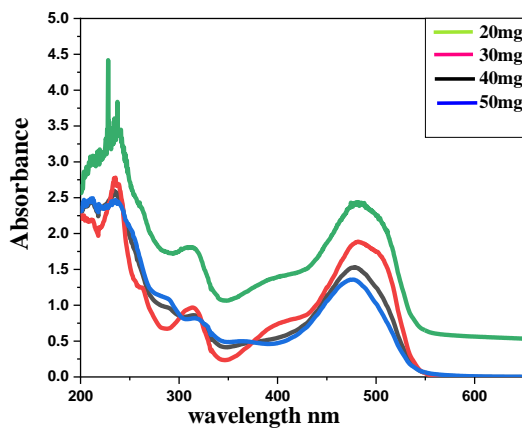
(C1)



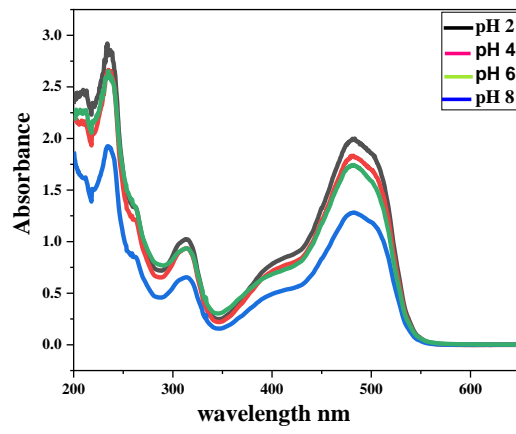
(D1)



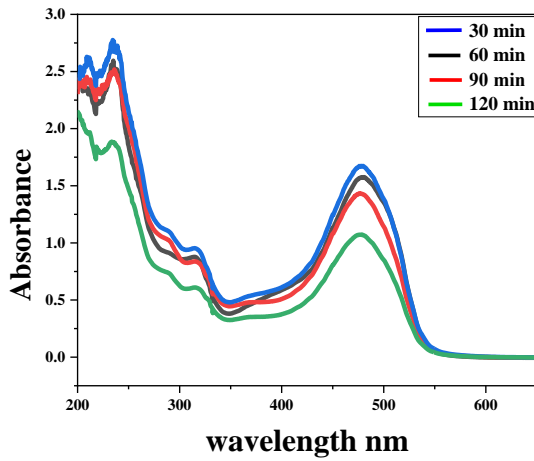
(E1)



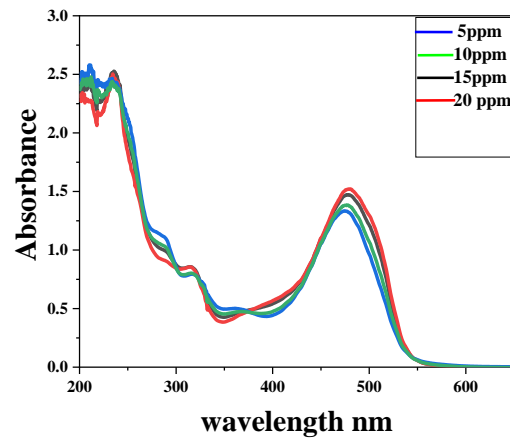
(a1)



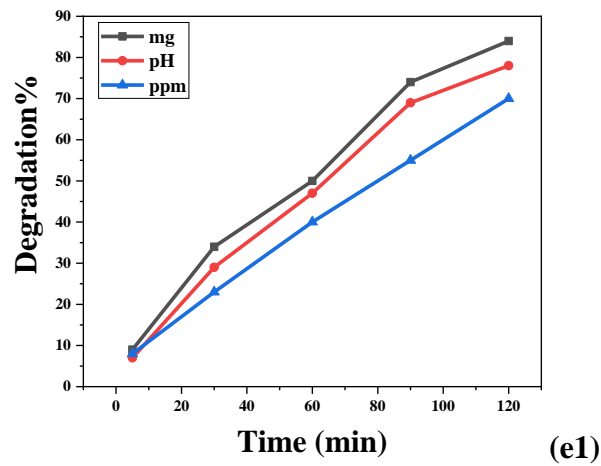
(b1)



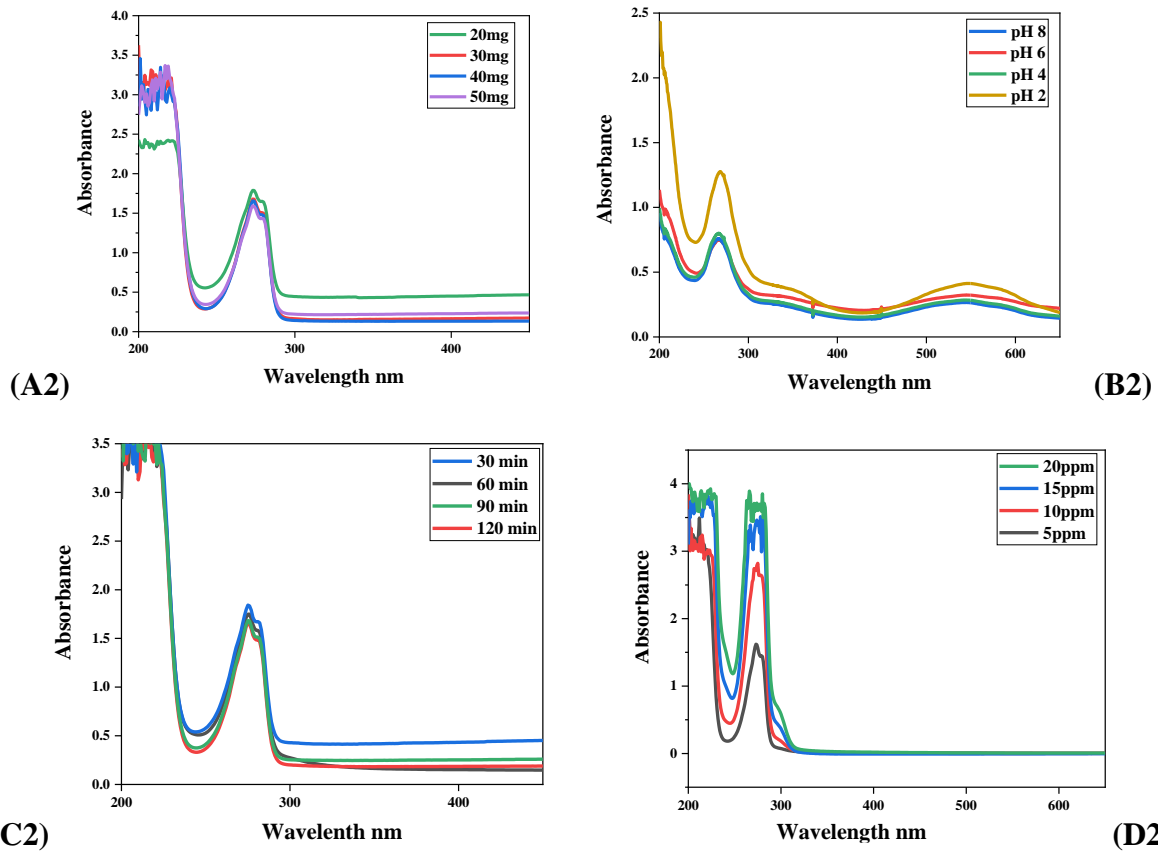
(c1)

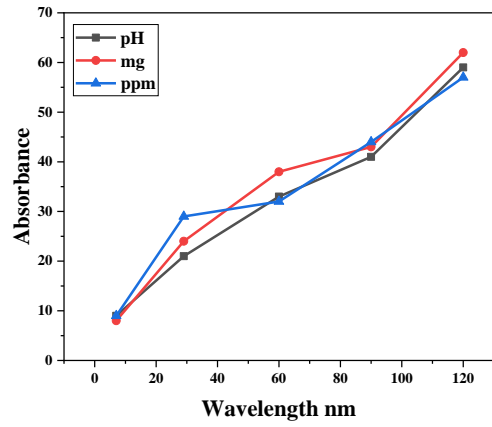


(d1)

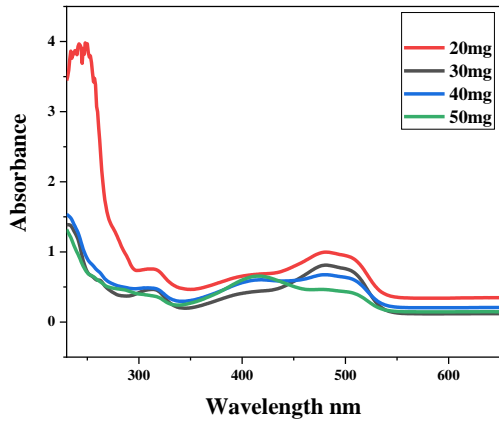


**Figure 9.** Photodegradation of alizarin red and yellowish sunset yellow by Ag<sub>2</sub>S-MIPs composite under different parameters.

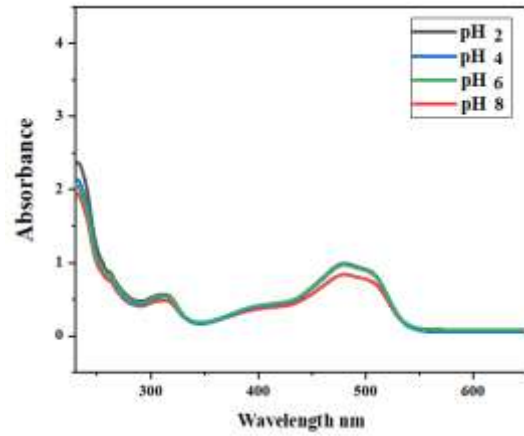




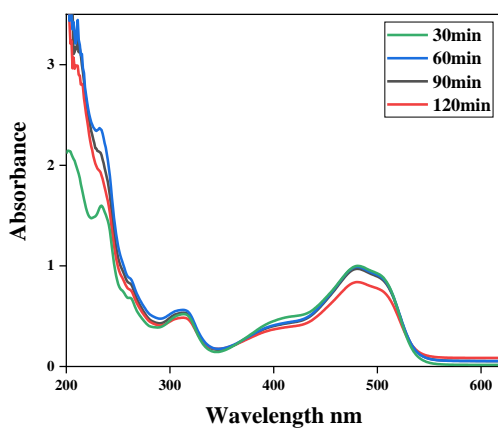
(E2)



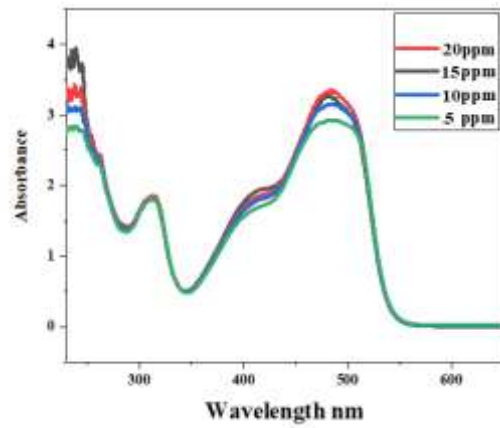
(a2)



(b2)



(c2)



(d2)

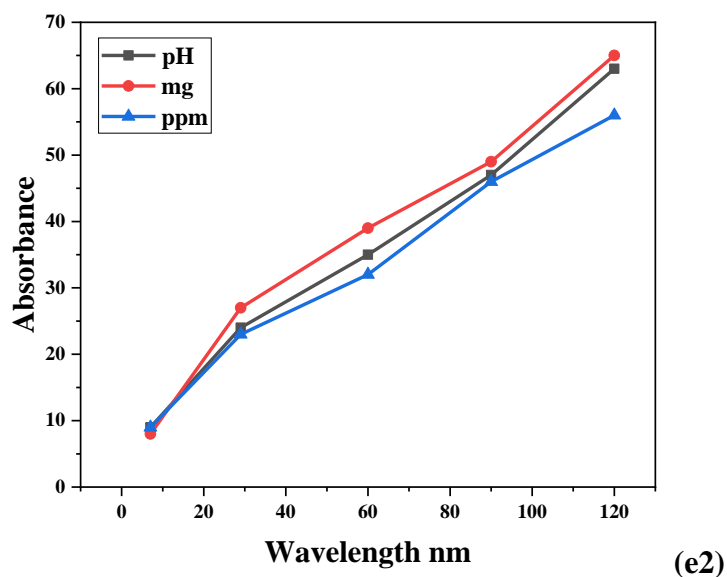


**Figure 10.** Photodegradation of alizarin red and yellowish sunset yellow by Ag<sub>2</sub>S-NIPs composite under different parameters.

#### 4.7 Conclusion

QDs developed were combined with MIPs to form Ag<sub>2</sub>S-MIPs as a photocatalyst for alizarin red and yellowish sunset dye degradation. Ag<sub>2</sub>S-MIPs demonstrated highly selective alizarin red and sunset yellow recognition. XRD, SEM, TEM and FT-IR spectroscopy were used to determine crystalline size, morphology and structure of the composite. UV spectrophotometry and mathematical analysis were used to assess the photocatalytic degradation of Ag<sub>2</sub>S-MIPs. The degradation rate of Alizarin red and Sunset yellow by Ag<sub>2</sub>S-MIP was found to be 82.8% and 84.7%.

## 4.8 References

- [180] M. Ajaz, S. Shakeel, A. Rehman, Microbial use for azo dye degradation—a strategy for dye bioremediation, *International Microbiology*. 23 (2020) 1–11. <https://doi.org/10.1007/s10123-019-00103-2>.
- [181] N.A. Ahmad, P.S. Goh, A.K. Zulhairun, T.W. Wong, A.F. Ismail, CHAPTER 1 The Role of Functional Nanomaterials for Wastewater Remediation, (2021) 1–28. <https://doi.org/10.1039/9781839165283-00001>.
- [182] M. Ghaedi, A. Hekmati Jah, S. Khodadoust, R. Sahraei, A. Daneshfar, A. Mihanidoost, M.K. Purkait, Cadmium telluride nanoparticles loaded on activated carbon as adsorbent for removal of sunset yellow, *Spectrochimica Acta Part A: Molecular and Biomolecular Spectroscopy*. 90 (2012) 22–27. <https://doi.org/10.1016/j.saa.2011.12.064>.
- [183] P.K. Gautam, P.M. Shivapriya, S. Banerjee, A.K. Sahoo, S.K. Samanta, Biogenic fabrication of iron nanoadsorbents from mixed waste biomass for aqueous phase removal of alizarin red S and tartrazine: Kinetics, isotherm, and thermodynamic investigation, *Environmental Progress & Sustainable Energy*. 39 (2020) e13326. <https://doi.org/10.1002/ep.13326>.
- [184] C. Chen, Z. Zhang, G. Li, L. Li, Z. Lin, Recent Advances on Nanomaterials for Electrocatalytic CO<sub>2</sub> Conversion, *Energy Fuels*. 35 (2021) 7485–7510. <https://doi.org/10.1021/acs.energyfuels.1c00448>.
- [185] O.V. Salata, Applications of nanoparticles in biology and medicine, *J Nanobiotechnol*. 2 (2004) 1–6. <https://doi.org/10.1186/1477-3155-2-3>.
- [186] K. Wenderich, G. Mul, Methods, Mechanism, and Applications of Photodeposition in Photocatalysis: A Review, *Chem. Rev.* 116 (2016) 14587–14619. <https://doi.org/10.1021/acs.chemrev.6b00327>.
- [187] G. Singh, Z. Desta, ChemInform Abstract: Isatins As Privileged Molecules in Design and Synthesis of Spiro-Fused Cyclic Frameworks, *Chemical Reviews*. 112 (2012). <https://doi.org/10.1021/cr300135y>.
- [188] M.A. Hayat, Y. Chen, A Brief Review on Nano Phase Change Material-Based Polymer Encapsulation for Thermal Energy Storage Systems, in: I. Mporas, P. Kourtessis, A. Al-Habaibeh, A. Asthana, V. Vukovic, J. Senior (Eds.), *Energy and Sustainable Futures*, Springer International Publishing, Cham, 2021: pp. 19–26. [https://doi.org/10.1007/978-3-030-63916-7\\_3](https://doi.org/10.1007/978-3-030-63916-7_3).
- [189] S.I. Sadovnikov, A.I. Gusev, A.A. Rempel, Artificial silver sulfide Ag<sub>2</sub>S: Crystal structure and particle size in deposited powders, Superlattices and Microstructures. 83 (2015) 35–47. <https://doi.org/10.1016/j.spmi.2015.03.024>.
- [190] Q. Ren, Y. Ma, S. Zhang, L. Ga, J. Ai, One-Step Synthesis of Water-Soluble Silver Sulfide Quantum Dots and Their Application to Bioimaging, *ACS Omega*. 6 (2021) 6361–6367. <https://doi.org/10.1021/acsomega.0c06276>.
- [191] S.A. Mirsalari, A. Nezamzadeh-Ejhieh, CdS–Ag<sub>3</sub>PO<sub>4</sub> nano-catalyst: A brief characterization and kinetic study towards methylene blue photodegradation, *Materials Science in Semiconductor Processing*. 122 (2021) 105455. <https://doi.org/10.1016/j.mssp.2020.105455>.
- [192] X. Li, J. Wang, M. Li, Y. Jin, Z. Gu, C. Liu, K. Ogino, Fe-doped TiO<sub>2</sub>/SiO<sub>2</sub> nanofibrous membranes with surface molecular imprinted modification for selective photodegradation of 4-nitrophenol, *Chinese Chemical Letters*. 29 (2018) 527–530. <https://doi.org/10.1016/j.cclet.2017.09.007>.
- [193] F. Gao, X. Hou, A. Wang, G. Chu, W. Wu, J. Chen, H. Zou, Preparation of polypyrrole/TiO<sub>2</sub> nanocomposites with enhanced photocatalytic performance, *Particuology*. 26 (2016) 73–78. <https://doi.org/10.1016/j.partic.2015.07.003>.
- [194] M. Ahmed, N. Abdelbar, A. Mohamed, Molecular imprinted chitosan-TiO<sub>2</sub> nanocomposite for the selective removal of Rose Bengal from wastewater, *International Journal of Biological Macromolecules*. 107 (2017). <https://doi.org/10.1016/j.ijbiomac.2017.09.082>.



- [195] Y. Wei, B. Han, X. Hu, Y. Lin, X. Wang, X. Deng, Synthesis of Fe<sub>3</sub>O<sub>4</sub> Nanoparticles and their Magnetic Properties, *Procedia Engineering*. 27 (2012) 632–637. <https://doi.org/10.1016/j.proeng.2011.12.498>.
- [196] T. ul Gani Mir, A.Q. Malik, J. Singh, S. Shukla, D. Kumar, An Overview of Molecularly Imprinted Polymers Embedded with Quantum Dots and Their Implementation as an Alternative Approach for Extraction and Detection of Crocin, *ChemistrySelect*. 7 (2022) e202200829. <https://doi.org/10.1002/slct.202200829>.
- [197] V. Kuzhalosai, B. Subash, A. Senthilraja, P. Dhatshanamurthi, M. Shanthi, Synthesis, characterization and photocatalytic properties of SnO<sub>2</sub>–ZnO composite under UV-A light, *Spectrochimica Acta. Part A, Molecular and Biomolecular Spectroscopy*. 115C (2013) 876–882. <https://doi.org/10.1016/j.saa.2013.06.106>.
- [198] K. Saeed, Zada, I. Khan, Photocatalytic degradation of alizarin red dye in aqueous medium using carbon nanotubes/Cu–Ti oxide composites, *Separation Science and Technology*. 54 (2018) 1–9. <https://doi.org/10.1080/01496395.2018.1552296>.
- [199] D. Rajamanickam, M. Shanthi, Photocatalytic degradation of an azo dye Sunset Yellow under UV-A light using TiO<sub>2</sub>/CAC composite catalysts, *Spectrochimica Acta Part A: Molecular and Biomolecular Spectroscopy*. 128 (2014) 100–108. <https://doi.org/10.1016/j.saa.2014.02.126>.
- [200] K. Balu, K. Selvam, R. Velmurugan, M. Swaminathan, Influence of operational parameters on photodegradation of Acid Black 1 with ZnO, *Desalination and Water Treatment*. 24 (2012) 132–139. <https://doi.org/10.5004/dwt.2010.1466>.

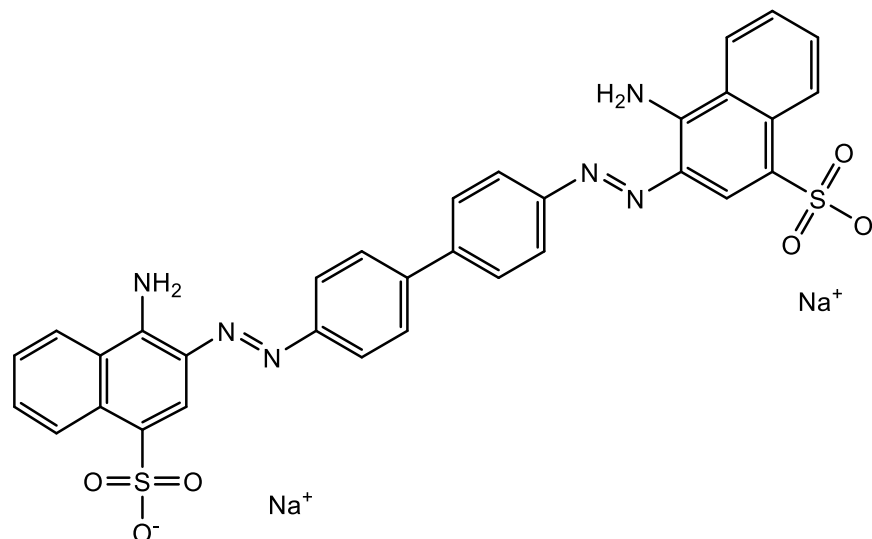
## Chapter 5

### Synthesis, Characterization, Photocatalytic effect of CuS-ZnO nanocomposite on photodegradation of Congo Red and phenol pollutant

#### 5.1 Introduction

Dye wastewater from industrial effluents is a serious threat to aquatic ecosystem due to high content of organic pollutants, high alkalinity, high chemical abundance and high chromaticity[201]. The large percentage of dyes are synthetic, including cationic, anionic and non-ionic dyes. They are classified based on their chemical composition as azo, Nitro, Nitroso, anthraquinone, indigoid dyes. The discharge of dyes effluents into natural water poses a significant environmental threat due to their elemental composition including toxic components such as heavy metal ions and aromatic compounds. Dyes are the most prevalent pollutant model for evaluating the degradation efficiency of photocatalyst. Many organic dyes, such as azo dyes (methyl orange, rhodamine, congo red, acid orange), thiazine, and cationic dyes (methylene blue), have been examined in light-assisted photodegradation. Congo red (sodium 3,3'-(1E,1'E)-biphenyl-4,4'-diylbis(diazene-2,1-diyl) bis(4-aminonaphthalene-1-sulfonate)) introduced in 1884 is one of the most prominent benzidine secondary diazo dyes. Benzidine is a poisonous metabolite of Congo red that causes cancer in humans. Congo red toxic by-products are strongly pigmented, have a low biological oxygen demand (BOD) and a high chemical oxygen demand (COD), and include a high concentration of dissolved solids. Congo red degradation involves not only basic organic reactions (addition, elimination, and substitution), but also complex organic reactions because of its intricate molecular structure and large number of functional groups. As a result, degrading Congo red is quite difficult. Similarly, phenol, which is widely used as a raw material in a various sector, is one of the most prevalent contaminants found in industrial wastewater and is mentioned in the refractory wastewater category. Due to its toxicity, carcinogenic and mutagenesis potentials, it is one of the most important pollutant in the aquatic environment [202]. As a result, Congo red and phenol, two key refractory organics, were chosen as the study's target contaminants. Several techniques for removing Congo red and phenol from wastewater have been investigated, including adsorption ([203]electrochemistry [204], and biological processes [180]. The photocatalytic degradation has recently gotten a lot of interest due to its efficient catalytic degradation of organic pollutants into carbon

dioxide, water and other tiny inorganic molecules without causing secondary pollution. various nanomaterials such as TiO<sub>2</sub>/montmorillonite and Au-TiO<sub>2</sub>, have been developed to degrade organic pollutants ([205]. However, many of the photocatalysts developed were stimulated by UV energy, which was less beneficial in modern application.



### Structure of Congo Red

Zinc oxide (ZnO) has received a lot of attention recently among metal oxide Nanoparticles (NPs)[206]. ZnO has unique physical and chemical properties for instance high photostability, chemical stability, Paramagnetism, broader absorption and higher electrochemical impedance [207,208]. However, in actual practice, ZnO's performance is hampered by a number of variables, including its broad band gap energy of 3.2eV, Low Quantum yield and poor photocatalysis reaction rate[209,210]. To improve the photodegradation efficiency of ZnO, A lot of work has been done to narrow the band gap and prevent photogenerated electron hole pairs from recombination, such as doping ZnO with group p type or n type metal or nonmetal ions[208,211]. Many studies have focused on ZnO being doped with various elements to increase its photocatalytic activity over the last several decades, including SnO<sub>2</sub>[212], CdS[213] and GaN [214]. However, so far of our knowledge only one article has been found of ZnO combined with CuS [215]. CuS is a popular semiconductor nanoparticle among metal chalcogenides due to its unique morphology[216]. The direct band gap energy of CuS is 1.220 eV and is therefore used widely in applications such as photocatalysis, chemical sensors, optics, energy storage material, supercapacitors, solar cells, lithium ion storage, thermoelectric cooling material and is ideal for solar energy absorption [217,218].It has also gained lot of interest in waste water treatment, water splitting and elimination of pollutants from aqueous

solution. CuS/ZnS has been used to degrade the biodegradable rhodamine B dye[219]. It was discovered that type II heterojunction ZnO/CuS had a higher visible-light photocatalytic effectiveness in MB degradation [220]. The CuS nanostructure was decorated on the surface of ZnO nanotubes using a wet-chemical approach at low temperature to form the ZnO/CuS photocatalyst[221]. The photocatalytic studies revealed that under Vis's light irradiation, ZnO has no photocatalytic activity, CuS however degrades the MB to 63% [222]. The photocatalytic efficiency with ZnO/CuS composite catalyst improved to 87%, a nearly 28% increase. The increased photocatalytic activity is attributable to the ZnO/CuS p-n heterojunction formation, which supports the effective separation of photoinduced charge carriers. In this paper, the photocatalytic activity of CuS/ZnO nanocomposite was investigated using a simple two-step solution approach. CuS/ZnO was discovered to significantly increase the visible light photocatalytic degradation of Congo red and Phenol organic pollutant.

## **5.2 Experimental Details**

The chemicals used were Zn (NO<sub>3</sub>)<sub>2</sub>·6H<sub>2</sub>O, Urea, Cu (Ac)<sub>2</sub> and Sodium Sulfide (Na<sub>2</sub>S). Phenol and Congo red were used pollutant, Distilled water, Ethanol was used as solvent to wash our compound.

### **5.2.1 Characterization**

Fourier transform infrared (FTIR) spectra of CuS/ZnO were recorded using FTIR spectrophotometer in the range of 400-4000cm<sup>-1</sup>. X ray Diffraction was used to investigate the crystalline structure of compound. FESEM images was carried out along with EDX to determine morphology and elemental composition of nanocomposite. UV-Vis's absorption spectra were recorded using double beam spectrophotometer. Electrochemical study of CuS/ZnO was performed using impedance spectra and cyclic voltammetry.

### **5.2.2 Synthesis**

The ZnO/CuS composite was synthesized by dissolving 0.02 mol of Zn (NO<sub>3</sub>)<sub>2</sub>·6H<sub>2</sub>O and a 0.015mol of urea in distilled water. The solution was kept at a constant temperature of 60°C for 1 hour. The temperature was then increased to 80°C and stirred for 3 hours. The white precursor of ZnO obtained was washed several times and then dried at 60°C. The precursor was calcined at 400°C for 1 hour to obtain ZnO nanoparticle.

Preparation of CuS was done by dissolving 0.1mol of Cu (Ac)<sub>2</sub> and 20mg of Na<sub>2</sub>S in a water/alcohol (3:1) solution, respectively. Two different solutions were then mixed and

stirred for 30min at 38°C maintaining pH value of the solution at 4-5. The colloidal precipitates obtained were being washed with ethanol several times and dried at 70°C, the required black CuS particles were prepared. CuS/ZnO nanocomposite particles were obtained by mechanically grinding ZnO and CuS nanoparticles together for 30 minutes.

### 5.3 Results and Discussions

**Figure.1.** Shows the FT-IR spectra of all ZnO/CuS nanocomposites. Water molecules physisorbed on the surface produce IR bands that correspond to O–H stretching and bending about 3300–3500  $\text{cm}^{-1}$  and 1624–1637  $\text{cm}^{-1}$ , respectively. The peak at 1012  $\text{cm}^{-1}$  is due to the stretching vibration of the C–O bond. Cu–S and Zn–O links were identified as peaks spanning from 400 to 850  $\text{cm}^{-1}$ , confirming the production of metal–sulphur bonds. As a result, a ZnO/CuS nanocomposite is created.

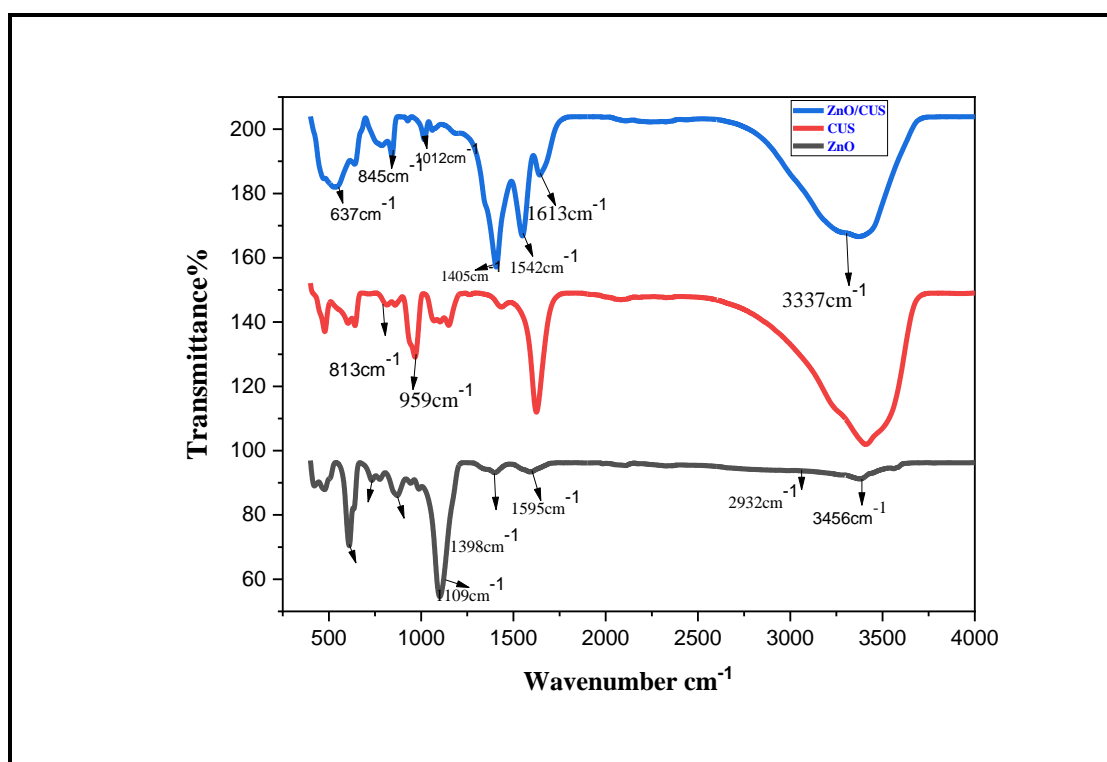


**Figure 1.** FTIR spectrum of IR spectra of CuS, ZnO and ZnO/CuS nanocomposites

X-Ray diffraction was used to determine the crystallinity and average particle size of synthesised nanoparticles. The XRD pattern of zinc oxide nanoparticles are shown in the following figures. The number of Bragg reflections for ZnO NPs. At  $2\theta = 30.77^\circ$  (100),  $34.44^\circ$  (002),  $36.27^\circ$  (101),  $47.62^\circ$  (102),  $55.73^\circ$  (110),  $62.96^\circ$  (103),  $68.06^\circ$  (112),  $69.13^\circ$  (201) and  $77.04^\circ$  (201). The planes accord well with the JCPDS file 80-0075. This

reveals hexagonal wurtzite structure of zinc oxide nanoparticles. The average particle size of synthesized particles was calculated to be 23.4 nm for ZnO NPs using FWHM the Debye-Scherrer equation.

$$D = 0.9\lambda/\beta\cos\theta \quad (1)$$

Where  $\beta$  is full width half maxima,  $\lambda$  is the wavelength and  $\theta$  is the angle obtained from  $2\theta$  values.

The Copper sulphide diffraction peaks were found at  $2\theta$  values of  $17^\circ$ ,  $30^\circ$ ,  $31^\circ$ ,  $36^\circ$ ,  $37^\circ$ ,  $47^\circ$ ,  $50.4^\circ$ , and  $62.9^\circ$ , which corresponded to the (101), (102), (006), (103), (104), (110), (108) and (116) crystal planes of copper sulphide. The data matches well with (JCPDS No. 06-0464) respectively. The slight broader peaks in CuS inwardly suggest the smaller the smaller size of nanoparticle. The average crystalline size was calculated and was found to be to be in the range of 8-9.7 nm. All the diffraction peaks of CuS are reprocessed in the nanocomposite CuS/ZnO which clearly indicates that the crystalline phase and structure of CuS has not changed even after embedding ZnO nanoparticles. The intense peaks reveal the crystallinity of our Composite material. The corresponding peaks reveals that there was no transformation in the structure of ZnO and CuS nor any additional peak of any intermediate was observed. The doping of ZnO has successfully deposited on CuS and increased surface of grain boundaries which leads to large scattering effect.

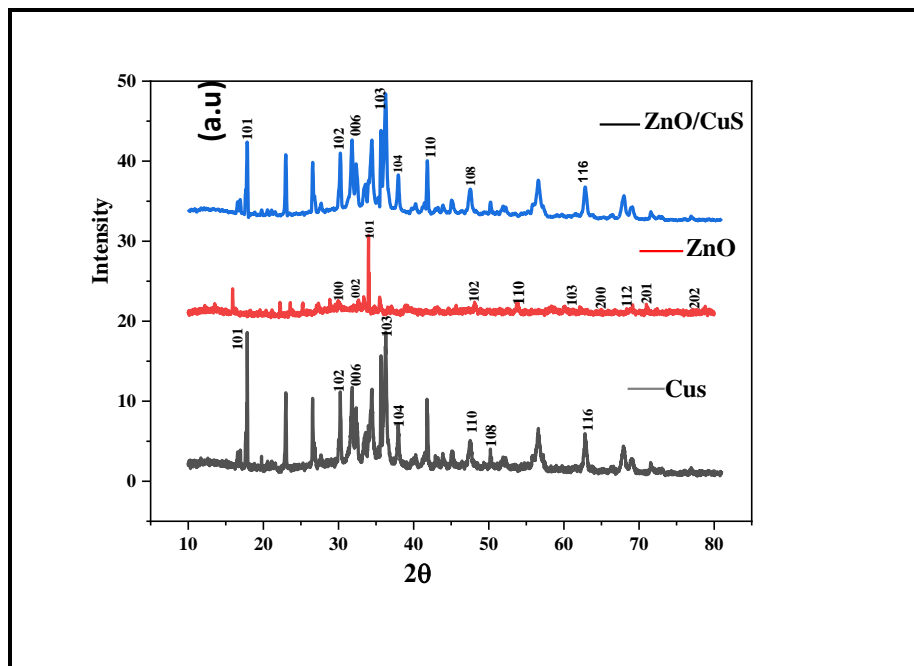


**Figure 2.** XRD pattern of CuS, ZnO and ZnO/CuS composite

SEM images of pure ZnO and CuS were shown in **Figure 3**. respectively. The majority of pure ZnO QDs were clearly spherical with average particle size of 27-28nm, whereas CuS QDs appeared to be more like nanorods with a significantly lower particle size of 6nm than ZnO.

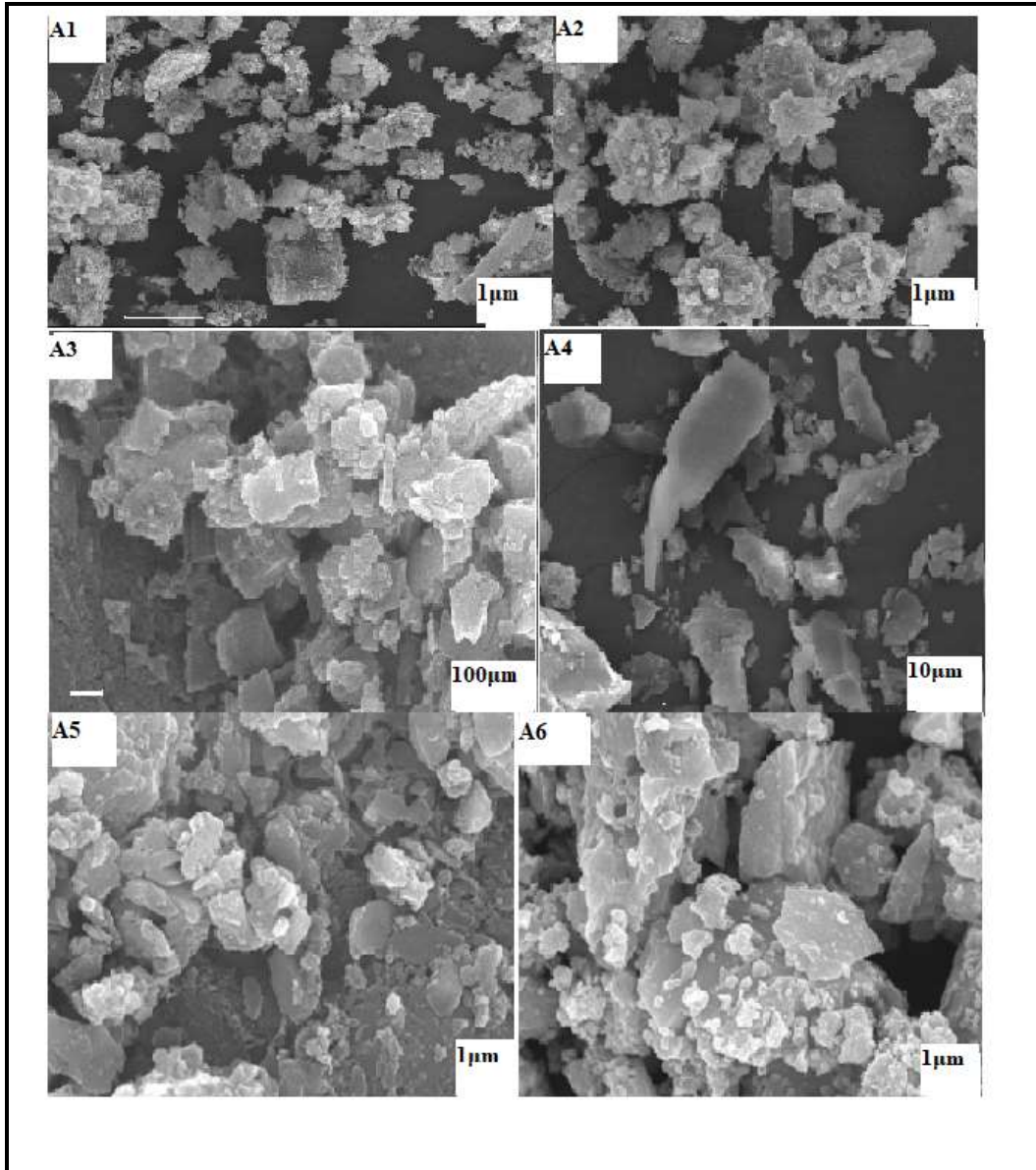


**Figure 3.** FESEM images of synthesized crystalline forms of ZnO and CuS QDs

Similarly, the SEM image of composite material were also taken with different resolution in **Figure 4**. CuS were found on ZnO nanoparticles, indicating that CuS was present in the nanocomposite particles, although it had no effect on the shape of ZnO. The average particle size of nanocomposite particles was around 30-32nm, which agrees with Scherrer's formula values.

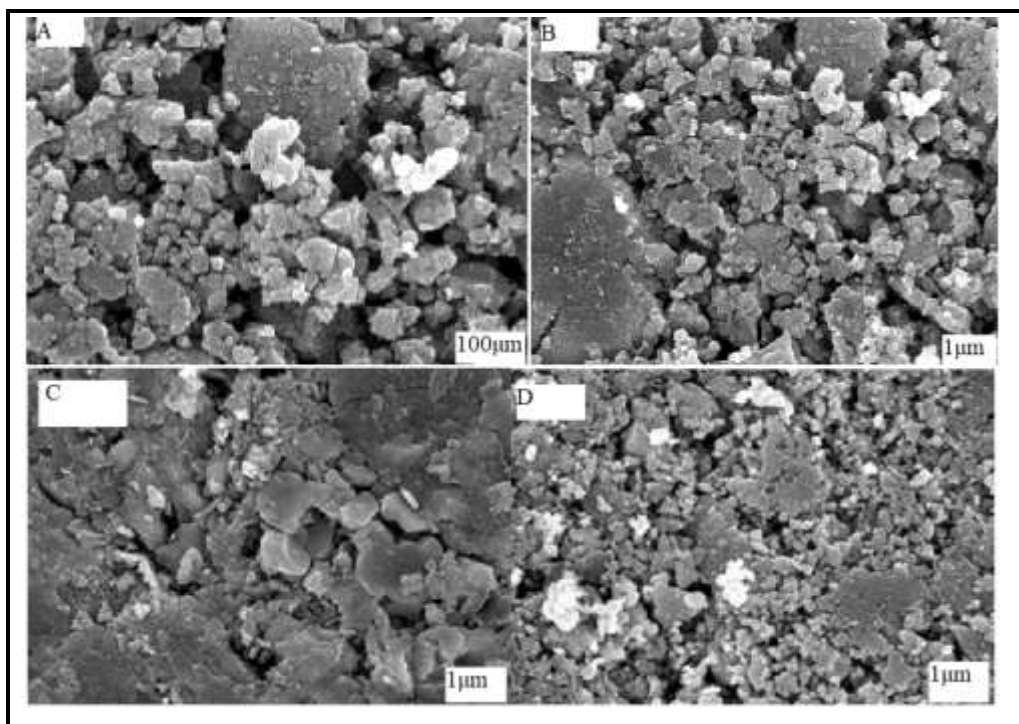


**Figure 4.** SEM images of prepared CuS/ZnO Nanocomposite.

#### 5.4 Electrochemical study

The electrochemical study was done using AUTOLAB electrochemical workstation. 1 M phosphate buffer solution was used as an electrolyte, the electrochemical characteristics were investigated. CuS modified stainless steel substrates served as the working electrode, platinum was used as the counter electrode and Ag/AgCl served as the reference electrode in the electrochemical study. The active material was used to make the working electrode. The activate carbon was coated on a stainless-steel electrode and dried, while the CuS/ZnO composite was coated uniformly on the electrode surface with a polyvinyl alcohol solution made from 1g of PVA in 50ml of water. The active substance in the working electrode has a weight of 2 mg. The numerous studies on the electrochemical characteristics of nanostructured materials such as carbon, metal oxides, binary metal oxides and composite materials has increased dramatically in recent years [223]. Using cyclic voltammetry and electrochemical impedance spectroscopy, the electrochemical characteristics of the produced CuS nanoparticles are also investigated. CuS electrode cyclic voltammetry was measured at varied scan rates ( $20\text{--}300\text{ mV s}^{-1}$ ) in a 1 M solution of phosphate buffer electrolyte from -1 to 1 mV potential range. The CV curve of CuS at different scan rate is shown in Figure below. The presence of a well-defined pair of redox peaks, which represents the transition, is readily visible.



**Figure.5.** CuS NPs cyclic voltammetry profiles (a) at  $20 \text{ mV s}^{-1}$  scan rate and (b) at varied scan rates from  $20\text{--}300 \text{ mV s}^{-1}$ . according to copper's oxidation state, implying the material's pseudocapacitive nature. At lower scan rates, the oxidation and reduction peaks are clearly visible, however at higher scan rates, the redox peaks are not visible, as shown in Figure 3. (b). Due to the sluggish diffusion rates of ions, the electrode material is not fully utilised at high scan rates, which may result in the redox disappearing[224].

Nyquist and Bode graphs were used to examine the EIS data. Nyquist plots reveal the frequency response of the electrode system by plotting the imaginary component ( $Z''$ ) of the impedance against the real component ( $Z'$ ). Figure shows the Nyquist plot of the CuS electrodes (a). The presence of a semicircle zone at higher frequencies and a linear slope at lower frequencies can be seen. The solution resistance is demonstrated by the semicircle's starting point in the high frequency zone. The charge transfer resistance ( $R_{ct}$ ) of the electrode material and electrolyte interfaces is also represented by the diameter of the semicircle. CuS nanoparticles have low  $R_{ct}$  value indicating that the material is pseudocapacitive. The tail visible at low frequencies, on the other hand, indicates the material's capacitive behaviour. The decrease in resistance with increasing frequency is enumerated by the Bode plot (as shown in Fig 5(c) reveals that the tail phase is about  $52^\circ$ , indicating that the electrode material is capacitive.

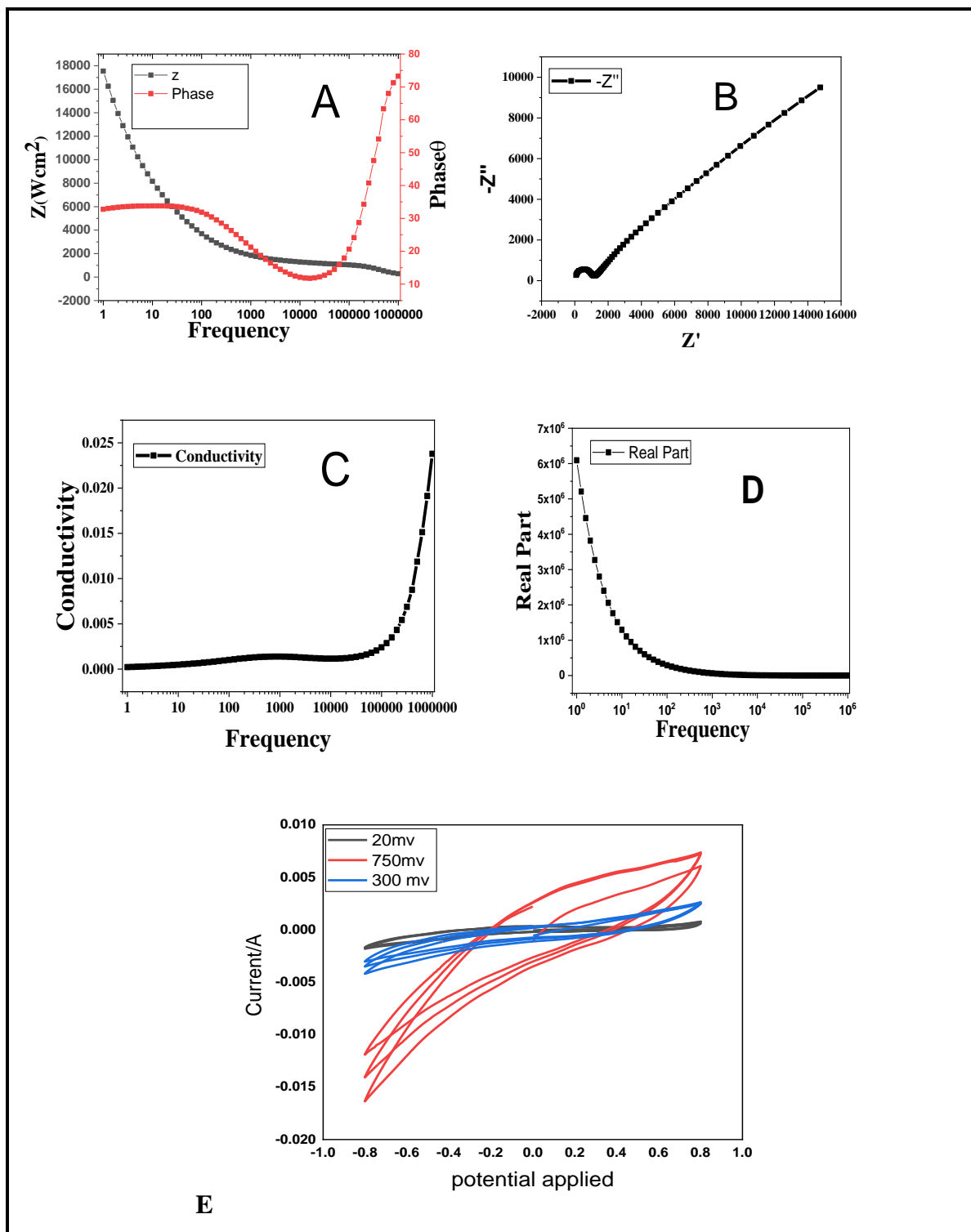


**Figure 5.** Electrochemical impedance spectroscopy and Cyclic Voltammetry of CuS-ZnO nanocomposite

### 5.5 photodegradation efficiency

The CuS/ZnO nanocomposites were tested as a photocatalyst for the degradation of aqueous congo red dye and organic phenol pollutant in presence of a visible light. 1000 ppm stock solution of Congo red and phenol was prepared by dissolving (20mg/1000ml

and 50mg/1000ml) solution. The contents were exposed to visible light for 30 minutes in the dark to allow adsorption desorption equilibrium. The photocatalytic studies were carried out by taking sample aliquots at regular intervals and were measured under UV-Vis's spectrum to observe absorbance at corresponding wavelength. Catalyst dosage and pH value was discovered to be a viable catalyst for the degradation of Congo red and phenol in order to maximise degradation efficiency. Reactions were carried out with different catalyst quantities (CuS-ZnO) ranging from 20 to 50 mg. Similarly, pH of the reaction was varied at constant pollutant concentration. The effect of photocatalyst loading and pH value was studied on the degradation of Congo red dye and phenol at constant pollutant concentration.

(i) Effect of Catalyst dose

The impact of nanocomposite on the photodegradation of congo red dye and phenol was investigated by varying the amount of dose (20–50 mg) under visible light. The photocatalyst dose had a significant impact on the photodecomposition of congo red and phenol pollutant at constant concentration of pollutant. It is clear from the **Figure 6A and 6B** that the degradation rate increases with increase in the number of catalysts which may be due to introduction of more photoactive sites in the medium. The presence of photocatalytic sites generates radical ions responsible for the degradation. However Due to the particles' surface energy, there will not be enough space for the nanocrystals to disperse in the solution when the photocatalyst quantity surpasses a critical barrier and the particles will adhere to each other and aggregate. As a result, most of the photocatalytic active sites will be occupied, reducing the degrading efficacy of nanocomposite. The degradation rate of both substrates accelerates as the mass of catalyst increases Because the excess addition of catalyst makes the solution more turbid and light penetration is slowed.

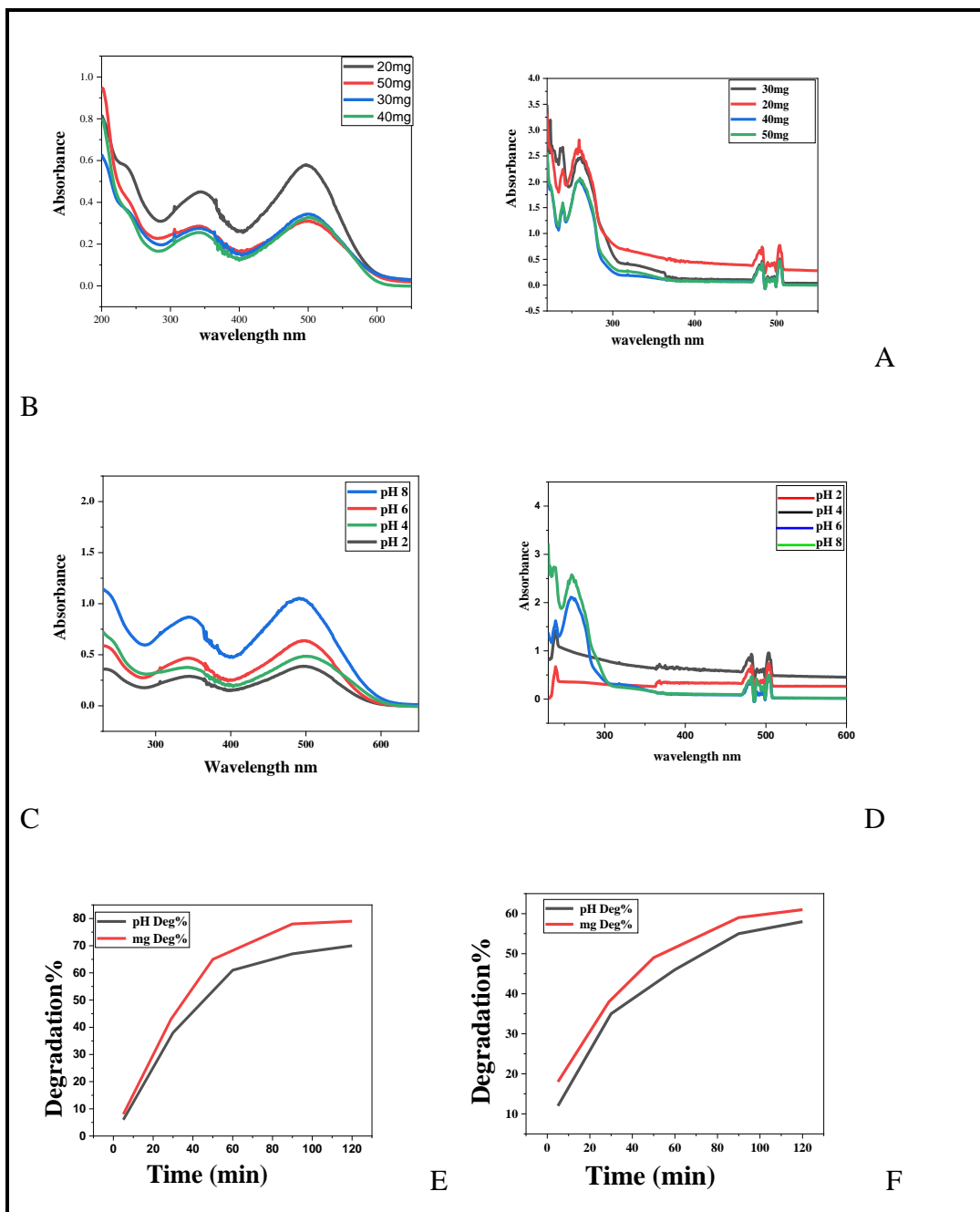


**Figure.6.** CuS/ZnO as an efficient photocatalyst for Congo Red and phenol degradation(b) Effect of pH on photodegradation of Congo Red and phenol under Visible light influence

(ii) Effect of initial pH

The pH values of wastewater may differ and therefore effect the photocatalytic efficiency of catalyst. The pH of the solution is one of the most critical parameters in the photocatalytic degradation of organic dyes. **Figure 6C and D** below shows the pH effect on the photodegradation of congo red dye and Phenol. The rate of degradation of both pollutants is highest at acidic pH and

decreases as pH rises. The degradation efficiencies of Congo red and Phenol reduces with increasing pH from 2 to 8 in a reaction period of 180 minutes, this could be related to a decrease in Nanocomposite activity. Negatively charged ionic chemicals such as phenolate could be adsorbed on CuS/ZnO surfaces.

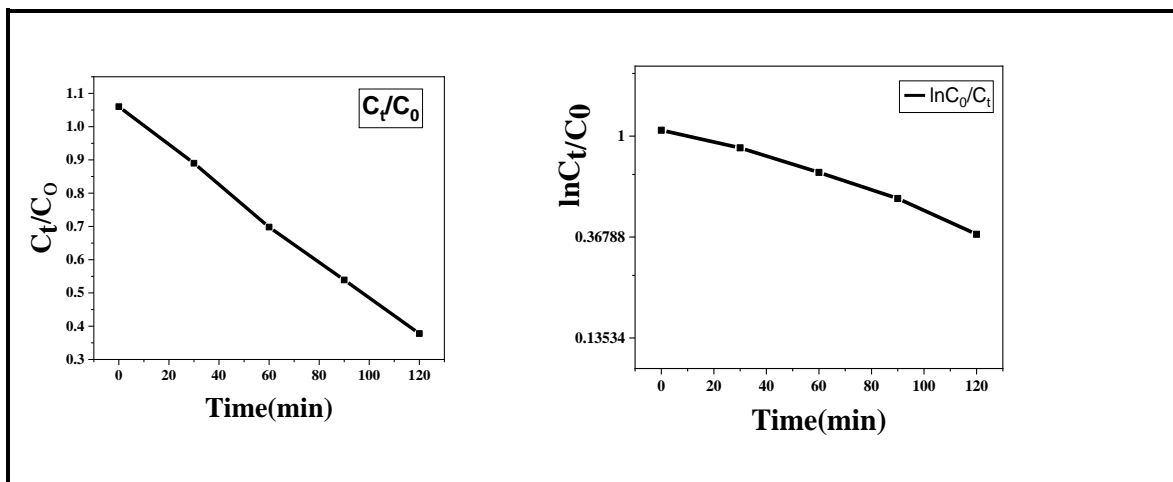


**Figure 7.** kinetics curves of degradation of Congo red under visible light

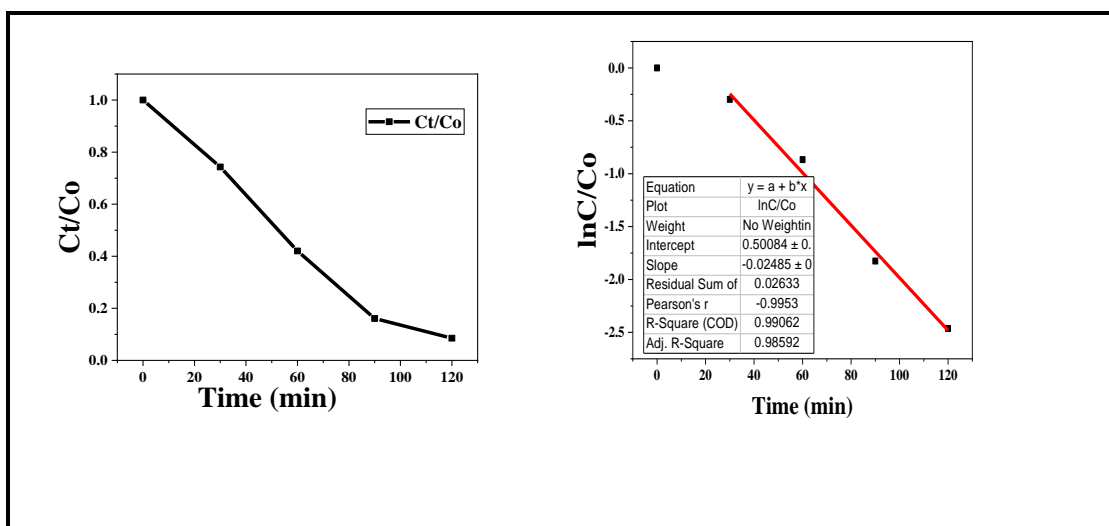


**Figure 8.** UV-Vis results demonstrating reaction rate kinetics of phenol under the influence of Visible light.

The kinetics of photodegradation reactions are studied based on the dye concentration change in the visible range (400–700 nm), all typical dyes have their own unique absorption characteristics. The photocatalytic degradation of Congo red and phenol in

suspension solution was investigated using photocatalytic experiments. The degradation% was calculated using **Equation (1)**:

$$\text{Degradation\%} = \frac{C_0 - C}{C_t} \times 100$$

where  $C_0$  and  $C$  are initial and final concentration of phenol, respectively. Similar experimental analysis was carried out with variation of initial phenol concentration.

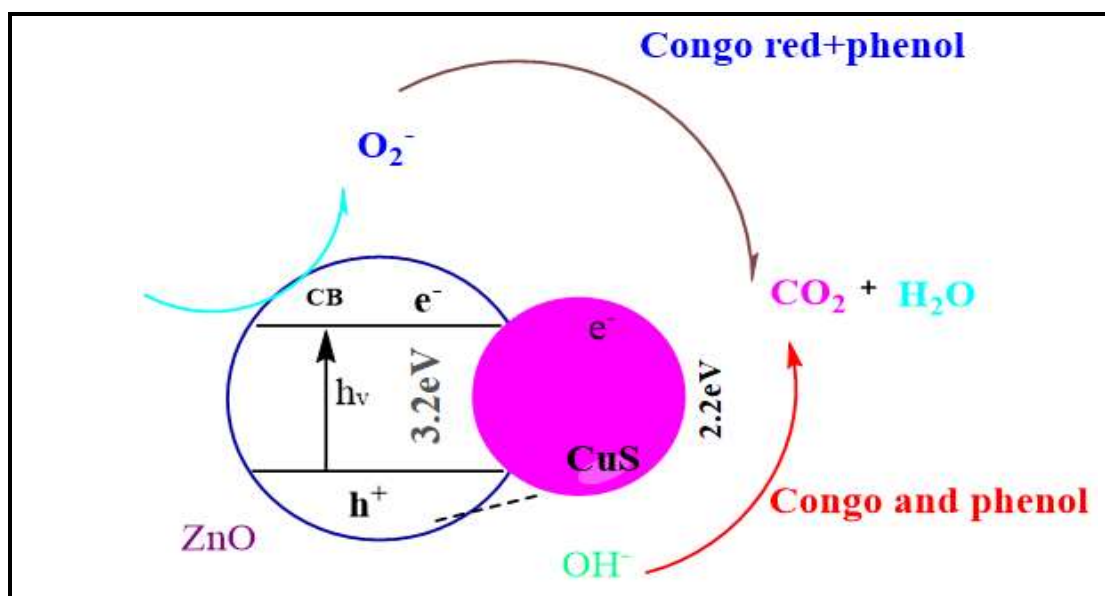


**Figure 9.** photocatalytic degradation mechanism of ZnO/CuS.

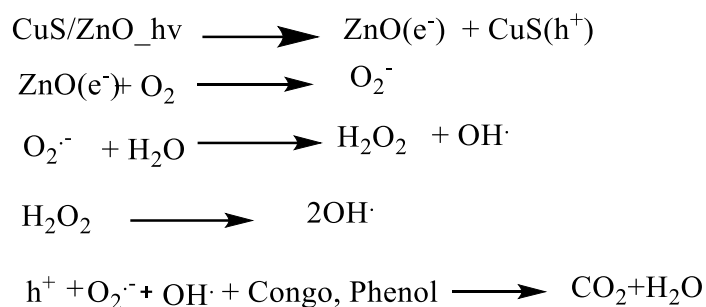
**Table 1.** Photocatalytic activity of Different catalyst against Congo red and phenol in aqueous solution

Pollutants	Photocatalyst	Light source	Photodegradation rate	References
Congo red	Mn-TiO <sub>2</sub>	UV	0.33	Gong et al. (2017)
	$\alpha$ -Fe <sub>2</sub> O <sub>3</sub>	UV	0.3	Jiang et al. (2016)

	Cd/Ba-CuO	Visible	1.36	Arunadevi et al. (2018)
	Au-TiO <sub>2</sub>	UV	1.99	Zhao et al. (2018)
Phenol	Biocl	Visible	0.76	Mao et al. (2018)
	TiO <sub>2</sub>	UV	0.32	Yao et al. (2015)
	Fe <sub>3</sub> O <sub>4</sub> /TiO <sub>2</sub>	Visible	0.28	Teng et al. (2016)
Congo red/phenol	CuS/ZnO	Visible	0.8 and 0.6	This study

## 5.6 Mechanism of Photodegradation

**Figure 9.** Depicts the photocatalysis process of CuS/ZnO nanocomposite particles. ZnO exhibited a large band gap, with a valence band of 2.415 eV and a conduction band of 0.855 eV [225]. but CuS had a small band gap of 0 eV [226]. The photogenerated electrons may transfer to CuS nanoparticles loaded on the surface of ZnO because the band gap of CuS is narrower than that of ZnO. The transferred electrons were then confined by CuS because to its great electron accepting ability, resulting in effective electron and hole separation [227]. CuS particles can transmit electrons to oxygen molecules adsorbed on the surface, resulting in free oxygen radicals. The photocatalyst efficiency is enhanced due to increased charge separation at the interface of CuS/ZnO catalyst. The schematic representation of photodegradation mechanism can be expressed as follows.



### 5.7 Conclusion

CuS/ZnO was successfully synthesized by grinding the ZnO and CuS, which were synthesised by using the precipitation method. CuS precisely existed in the nanocomposite particles, according to SEM images and XRD analysis. The nanocomposite's average size was around 35nm. Cyclic voltammetry and electrochemical impedance spectra were used to evaluate the electrochemical study of CuS/ZnO. Under visible light irradiation, the CuS-modifying ZnO can function as an outstanding improved photocatalyst when compared to pure ZnO. The improved photocatalytic activity was expected to be due to the charge separation between CuS and ZnO. Because of their exceptional photocatalytic stability and electrochemical research, CuS/ZnO nanoparticles are potential for practical applications.



## 5.8 References

- [201] I. Halomoan, Y. Yulizar, R.M. Surya, D.O.B. Apriandanu, Facile preparation of CuO-Gd<sub>2</sub>Ti<sub>2</sub>O<sub>7</sub> using *Acemella uliginosa* leaf extract for photocatalytic degradation of malachite green, *Materials Research Bulletin*. 150 (2022) 111726. <https://doi.org/10.1016/j.materresbull.2021.111726>.
- [202] S. Chakraborty, B. Basak, S. Dutta, B. Bhunia, A. Dey, Decolorization and biodegradation of congo red dye by a novel white rot fungus *Alternaria alternata* CMERI F6, *Bioresource Technology*. 147 (2013). <https://doi.org/10.1016/j.biortech.2013.08.117>.
- [203] T. Aysu, M. Küçük, Removal of crystal violet and methylene blue from aqueous solutions by activated carbon prepared from *Ferula orientalis*, *International Journal of Environmental Science and Technology*. 12 (2014). <https://doi.org/10.1007/s13762-014-0623-y>.
- [204] K.A. Madurani, S. Suprpto, N.I. Machrita, S.L. Bahar, W. Illiya, F. Kurniawan, Progress in Graphene Synthesis and its Application: History, Challenge and the Future Outlook for Research and Industry, *ECS J. Solid State Sci. Technol.* 9 (2020) 093013. <https://doi.org/10.1149/2162-8777/abbb6f>.
- [205] Y. Tang, Y. Shao, N. Chen, X. Liu, S.Q. Chen, K.F. Yao, Insight into the high reactivity of commercial Fe–Si–B amorphous zero-valent iron in degrading azo dye solutions, *RSC Adv.* 5 (2015) 34032–34039. <https://doi.org/10.1039/C5RA02870A>.
- [206] S. Yousaf, S. Zulfiqar, M.I. Din, P.O. Agboola, M.F. Aly Aboud, M.F. Warsi, I. Shakir, Solar light irradiated photocatalytic activity of ZnO–NiO/rGO nanocatalyst, *Journal of Materials Research and Technology*. 12 (2021) 999–1009. <https://doi.org/10.1016/j.jmrt.2021.03.012>.
- [207] L. Zhu, M. Zheng, J. Lu, M. Xu, H.J. Seo, Synthesis of CuS/ZnO Nanocomposite and Its Visible-Light Photocatalytic Activity, *Journal of Nanomaterials*. 2014 (2014) e126475. <https://doi.org/10.1155/2014/126475>.
- [208] Elviera, Y. Yulizar, D.O.B. Apriandanu, R. Marcony Surya, Fabrication of novel SnWO<sub>4</sub>/ZnO using *Muntingia calabura* L. leaf extract with enhanced photocatalytic methylene blue degradation under visible light irradiation, *Ceramics International*. 48 (2022) 3564–3577. <https://doi.org/10.1016/j.ceramint.2021.10.135>.
- [209] S. Deka, P. Joy, Synthesis and magnetic properties of Mn doped ZnO nanowires, *Solid State Communications*. 142 (2007) 190–194. <https://doi.org/10.1016/j.ssc.2007.02.017>.
- [210] K. Chaudhary, M. Aadil, S. Zulfiqar, S. Ullah, S. Haider, P.O. Agboola, M.F. Warsi, I. Shakir, Graphene oxide and reduced graphene oxide supported ZnO nanochips for removal of basic dyes from the industrial effluents, *Fullerenes, Nanotubes and Carbon Nanostructures*. 29 (2021) 915–928. <https://doi.org/10.1080/1536383X.2021.1917553>.
- [211] K. Chaudhary, N. Shaheen, S. Zulfiqar, M.I. Sarwar, M. Suleman, P.O. Agboola, I. Shakir, M.F. Warsi, Binary WO<sub>3</sub>-ZnO nanostructures supported rGO ternary nanocomposite for visible light driven photocatalytic degradation of methylene blue, *Synthetic Metals*. 269 (2020) 116526. <https://doi.org/10.1016/j.synthmet.2020.116526>.
- [212] W. Cun, Z. Jincai, X. Wang, M. Bixian, G. Sheng, P. Ping'an, F. Jiamo, Preparation, characterization and photocatalytic activity of nano-sized ZnO/SnO<sub>2</sub> coupled photocatalysts, *Applied Catalysis B: Environmental*. 39 (2002) 269–279. [https://doi.org/10.1016/S0926-3373\(02\)00115-7](https://doi.org/10.1016/S0926-3373(02)00115-7).
- [213] C. Chen, Z. Li, H.-N. Lin, G. Wang, J. Liao, M. Li, L. Shasha, W. Li, Enhanced visible light photocatalytic performance of ZnO nanowires integrated with CdS and Ag<sub>2</sub>S, *Dalton Transactions*. 45 (2016) 3750–3758. <https://doi.org/10.1039/C5DT04533A>.
- [214] § Kazuhiko Maeda, § Tsuyoshi Takata, ‡ Michikazu Hara, † Nobuo Saito, † Yasunobu Inoue, || Hisayoshi Kobayashi, § Kazunari Domen\*, GaN:ZnO Solid Solution as a Photocatalyst for Visible-Light-Driven Overall Water Splitting, *ACS Publications*. (2005). <https://doi.org/10.1021/ja0518777>.

- [215] M. Lee, K. Yong, Highly efficient visible light photocatalysis of novel CuS/ZnO heterostructure nanowire arrays, *Nanotechnology*. 23 (2012) 194014. <https://doi.org/10.1088/0957-4484/23/19/194014>.
- [216] F. Castellón-Barraza, M. Farías, J. Coronado-López, M. Encinas-Romero, M. Pérez-Tello, A. Posada-Amarillas, Synthesis and Characterization of Copper Sulfide Nanoparticles Obtained by the Polyol Method, *Advanced Science Letters*. 4 (2011) 596–601. <https://doi.org/10.1166/asl.2011.1249>.
- [217] P. Kumar, M. Gusain, R. Nagarajan, Synthesis of Cu<sub>1.8</sub>S and CuS from Copper-Thiourea Containing Precursors; Anionic (Cl<sup>-</sup>, NO<sub>3</sub><sup>-</sup>, SO<sub>4</sub><sup>2-</sup>) Influence on the Product Stoichiometry, *Inorg. Chem.* 50 (2011) 3065–3070. <https://doi.org/10.1021/ic102593h>.
- [218] H. Sabeeh, M. Aadil, S. Zulfiqar, A. Rasheed, N.F. Al-Khalli, P.O. Agboola, S. Haider, M.F. Warsi, I. Shakir, Hydrothermal synthesis of CuS nanochips and their nanohybrids with CNTs for electrochemical energy storage applications, *Ceramics International*. 47 (2021) 13613–13621. <https://doi.org/10.1016/j.ceramint.2021.01.220>.
- [219] L. Song, Y. Zeng, Y. Cheng, G. Luo, Synthesis of CuS microspheres from constituent elements and its photocatalytic application, *Materials Research Innovations*. 21 (2017) 232–236. <https://doi.org/10.1080/14328917.2016.1207043>.
- [220] M. Basu, R. Nazir, P. Fageria, S. Pande, Construction of CuS/Au Heterostructure through a Simple Photoreduction Route for Enhanced Electrochemical Hydrogen Evolution and Photocatalysis, *Sci Rep.* 6 (2016) 34738. <https://doi.org/10.1038/srep34738>.
- [221] M. Basu, N. Garg, A. Ganguli, A type-II semiconductor (ZnO/CuS heterostructure) for visible light photocatalysis, *J. Mater. Chem. A*. 2 (2014). <https://doi.org/10.1039/C3TA15446G>.
- [222] Y.-T. Kao, S.-M. Yang, K.-C. Lu, Synthesis and Photocatalytic Properties of CuO-CuS Core-Shell Nanowires, *Materials*. 12 (2019) 1106. <https://doi.org/10.3390/ma12071106>.
- [223] Y. Lu, Y. Huang, M. Zhang, Y. Chen, Nitrogen-doped graphene materials for supercapacitor applications, *J Nanosci Nanotechnol.* 14 (2014) 1134–1144. <https://doi.org/10.1166/jnn.2014.9102>.
- [224] G. Guo, L. Huang, Q. Chang, L. Ji, Y. Liu, Y. Xie, W. Shi, N. Jia, Sandwiched nanoarchitecture of reduced graphene oxide/ZnO nanorods/reduced graphene oxide on flexible PET substrate for supercapacitor, *Appl. Phys. Lett.* 99 (2011) 083111. <https://doi.org/10.1063/1.3629789>.
- [225] Y. Yulizar, D.O.B. Apriandanu, F.L. Hakim, Two-Phase Synthesis in n-Hexane–Water, Characterization, and Photocatalytic Activity of ZnO/Bi<sub>2</sub>Sn<sub>2</sub>O<sub>7</sub> Nanocomposite, *JOM*. 73 (2021) 441–449. <https://doi.org/10.1007/s11837-020-04475-z>.
- [226] Y. Xu, M.A.A. Schoonen, The absolute energy positions of conduction and valence bands of selected semiconducting minerals, *American Mineralogist*. 85 (2000) 543–556. <https://doi.org/10.2138/am-2000-0416>.
- [227] X. Lin, F. Rong, X. Ji, D. Fu, C. Yuan, Preparation and enhanced visible light photocatalytic activity of N-doped titanate nanotubes by loaded with Ag for the degradation of X-3B, *Solid State Sciences*. 13 (2011) 1424–1428. <https://doi.org/10.1016/j.solidstatesciences.2011.05.005>.

## CHAPTER 6

### **Preparation of Cadmium Sulphide Quantum Dots and their mechanistic investigations towards aqueous 2-Chlorophenol degradation and antimicrobial activity**

#### **6.1 INTRODUCTION**

The perversion of feedable and groundwater by toxic organic chemicals is a major remonstrance to the world. The portable water has been contaminated with various hazardous chemical including organics and metal ions among which phenol derivatives are one of the major organic pollutants such as chlorinated phenols. A chlorophenol is any derivative of phenol possessing chlorine covalently bonded to phenol ring. Chlorophenols are distinct in their in their applications such as herbicides, insecticides, fungicides, bactericides and other industrial applications[228]. The chlorinated compounds present in aqueous ecosystem has caused serious environmental pollution problems. Among which 2-chlorophenol is one of the representative organic pollutant compounds (2-CP)[229]. 2CP is slightly soluble in water and its challenging to remove 2-CP from water, several techniques have been employed such as flocculation, adsorption, and conventional methods to eliminate 2-CP from water[230]. Currently semiconductor nanoparticles have been found to play efficient role in removal of organic wastes from aqueous solution. Quantum dots in the presence of visible light or UV light act as promising candidate for the purification and treatment of such organic pollutants through the degradation process[231]. Several sulphide based quantum dots have been used for Photodegradation process among which Cadmium Sulphide is one of the most efficient photocatalysts, due to its stability and being inexpensive photosensitive material[232] . Cadmium is a transition metal with good electrical conductivity and corrosion resistance. CdS material has been synthesized as colloidal fluorescent crystalline material. CdS are well known QDs among the synthesized nanomaterials due to their excellent electrochemical and optical performance which makes them vital catalyst in the variety of applications like biosensing, photovoltaic cell, nanomedicine and drug delivery[6]. The CdS have numerous benefits as semiconductors: discrete energy levels, tunable bandgap, optoelectronic properties, good chemical stability, and simple preparation methods[234]. They have a high photosensitivity, allowing them to detect visible radiation and so improving the efficiency of solar cells in LEDs and

functioning as photoconductors. Quantum Dots are a type of CdS that is extensively used in the manufacture of lasers, LED, photovoltaic cell, and in the medical industry for in vitro and in vivo bio-imaging and biofilm suppression[235]. Majority of Quantum dots possess nonlinear optical properties and band gap energy of CdS lies in the range of (2.42 eV), ideal material for the photodegradation of hazardous chemicals. These properties make more interesting towards photocatalytic activity in visible region[236]. The use of QDs as photocatalysts has garnered a lot of interest due to its high degradation efficiency, high photostability, and good quantum yields. CdS QDs has been used as photocatalyst against degradation of organic pollutants in various literature sources. Anjum et al. showed that semiconductor Nano catalysts remove organic colours from water effluents more effectively when exposed to visible light[237].Shan et.al have reported photodegradation of penicillin under visible light by CdS modified with TiO<sub>2</sub> QDs [238]. Organic pollutants are photodegraded by lighting semiconductor solutions with visible light; however, the energy of light source must be greater than the energy of the required band gap to get better results. The photo redox reaction is stimulated during photon absorption due to narrow band gap energy. The conduction band (CB) valence band (VB) of semiconductors facilitate redox reactions during irradiation process and produces electron hole recombination[239]. The electron transfer from conduction band to valence band results in high reduction and oxidation potential which results in reduction process[240]. These generate free radicals within the substrate's oxidoreduction system. The resulting free radicals (OH) are effective organic oxidizers[241]. Several techniques employed to synthesize CdS, e.g., precipitation reaction[242], photochemical method [243], solvothermal method[244], hydrothermal[245],and one-pot synthesis method[246]. Amongst, chemical precipitation method is the simple and cost-effective method to obtain CdS nanoparticles.

In this paper, the photodegradation activity of the synthesised CdS QDs samples were determined by calculating the removal efficiency of 2-CP in aqueous solution under visual radiation. The influence of catalyst crystallinity, optical absorbance, pH of solution, and catalyst concentration have been investigated during the photodegradation process. Antimicrobial activity of CdS QDs was done against *E. coli* and *Aeromonas hydrophilia*. The antimicrobial activity was performed by using well disc method[247].

## **6.2 Characterization**

X-ray diffraction has been performed over a range of 20°-70° to determine crystalline size of cadmium sulphide QDs. FESEM analysis was employed to determine morphology of the synthesized sample. Fourier infrared spectroscopy was used to record FTIR spectrum of the compound. *Aeromonas hydrophila* with *E. coli* and *Aeromonas hydrophilia* bacteria were tested to perform antibacterial activity of nanomaterial.

### 6.3 Materials and method

Ammonium nitrate ( $\text{NH}_4\text{NO}_3$ ), potassium hydroxide (KOH), cadmium chloride ( $\text{CdCl}_2$ ) and thiourea were purchased from TCI chemicals, which were used without purification. Firstly, prepared an aqueous solution of 0.732 g of  $\text{CdCl}_2$  (0.02 M) in 20ml of distilled water. The other aqueous solution of KOH (0.5M) and thiourea (0.2 M) were prepared in distilled water. 0.02 M  $\text{CdCl}_2$  and 0.2 M thiourea solution were gradually poured into 0.5 M KOH solution and stirred for 2 hr for uniformity. Then,  $\text{NH}_4\text{NO}_3$  was added dropwise in above solution, solution turned white milky to light yellow after 30 minutes. The yellow precipitates were filtered, washed with distilled water and calcined at 400°C, yellow powder was obtained.

### 6.4 Results and Discussions

#### 6.4.1 FTIR of CdS

The FTIR investigation of cadmium sulphide QDs was performed using Fourier transform infrared spectroscopy as shown in **Figure 1**.  $3367\text{cm}^{-1}$  peak corresponds to the free O-H group, similarly narrow peak at  $1649\text{cm}^{-1}$  depicts the presence of hydroxyl group of moisture, and a peak at  $621\text{cm}^{-1}$  corresponds to the S-S bond. The peak at  $546\text{cm}^{-1}$  is due to Cd-S bond. The other peaks observed at 1395,  $1542\text{cm}^{-1}$  may be due to Sulfide compounds, amide bands of proteins.

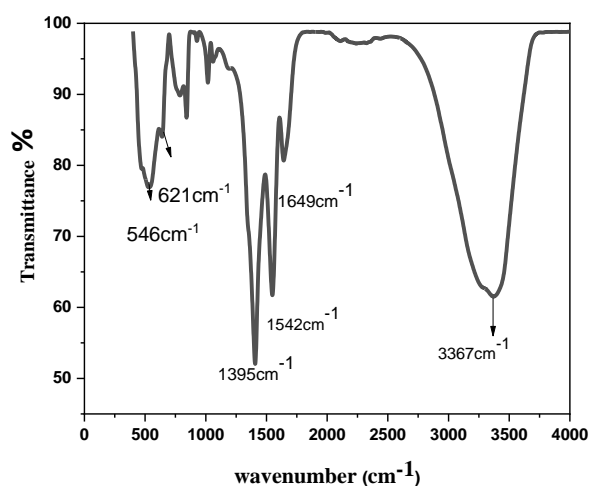


**Figure 1.** FTIR spectra of Cadmium Sulphide QDs

The crystallite structure and size of CdS was studied with the help of XRD. **Figure 2.** depicts the XRD diffraction pattern of CdS QDs. In this spectrum, diffraction peaks are obtained and planes (1 0 0), (0 0 2), (1 0 1), (1 1 0), (1 0 3), (1 1 2) respectively and the shape of the QDs are hexagonal which is well matched with JCPDS card (File No. 41-1049).

$a=4.143$ ,  $b=4.143$ , and  $c=6.719$  are the lattice parameters for the CdS hexagonal system. From the Debye Scherrer equation[248], we found the average crystalline size of the QDs was 6-7 nm. The morphological studies of the CdS QDs were examined with (SEM) involving the formation of hexagonal CdS QDs which is well match with XRD spectrum. SEM images of CdS was taken at different resolution to reveal the average particle size of QDs within the range of 7-10 nm with hexagonal morphology. Data obtained imply that the quantum size CdS particles were successfully synthesized in the present alkaline medium. The increased size of particle may be due to agglomeration of particles.

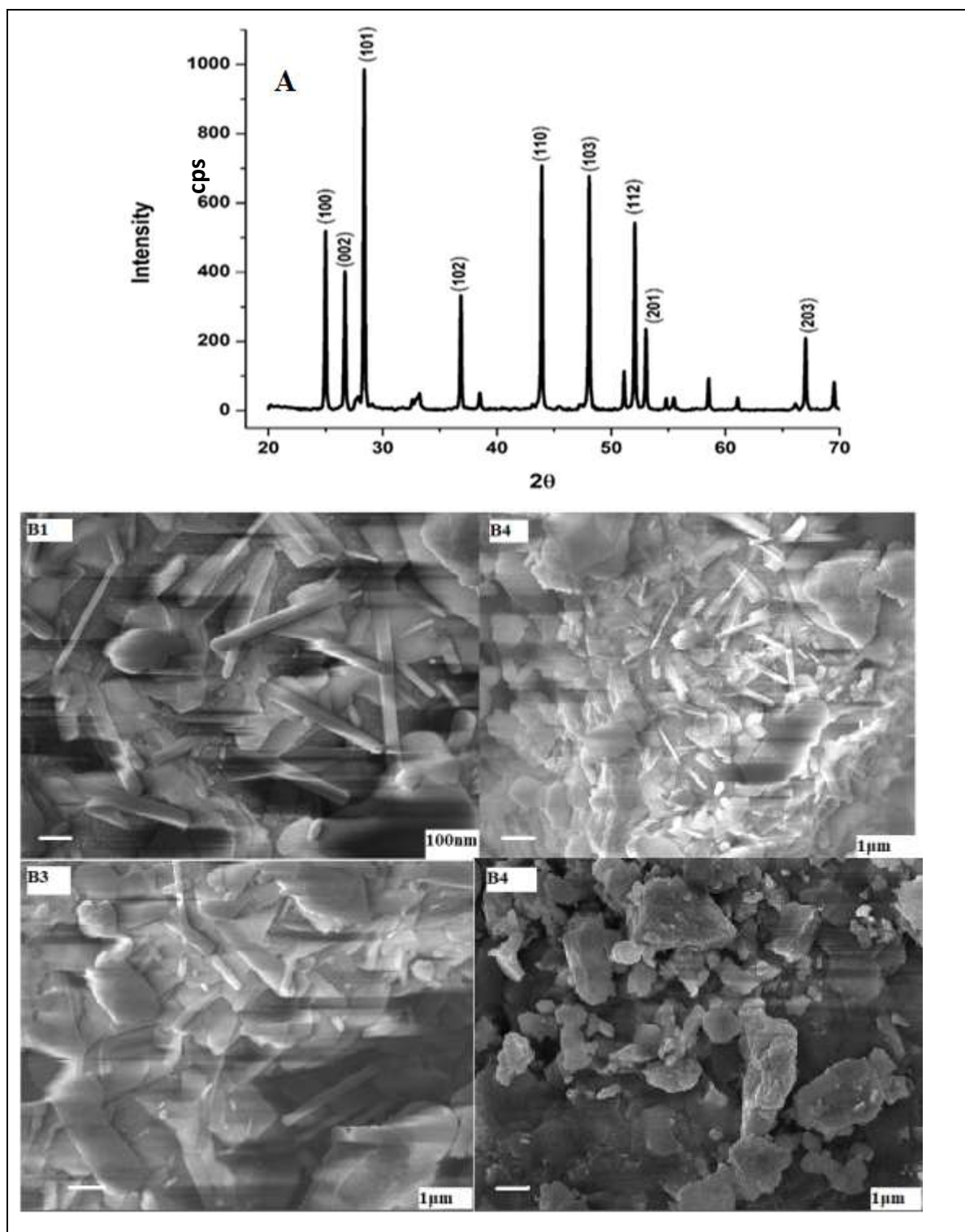


**Figure 2.** (A) XRD Spectrum of CdS (B)-SEM images of CdS Quantum Dots at different resolution.

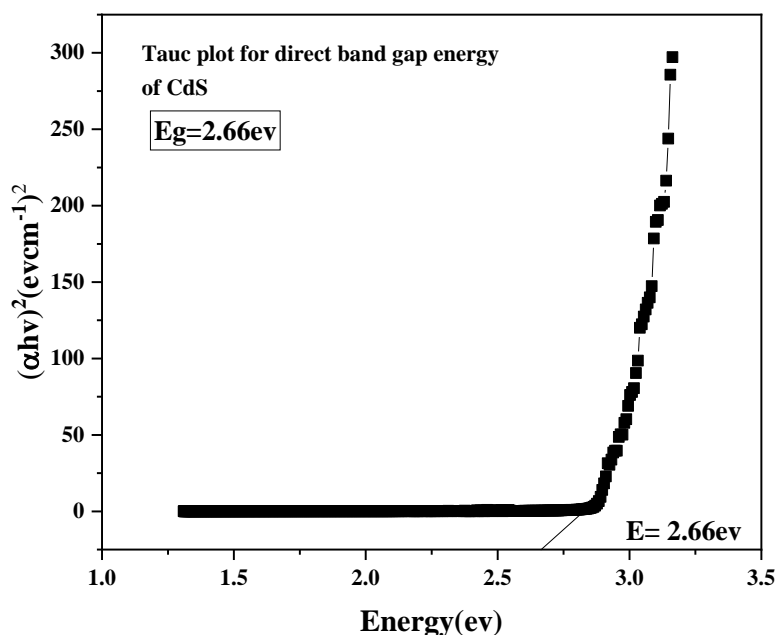


**Figure 3.** Tauc Plot to obtain band gap energy of CdS QDs

The Optical band energy of CdS QDs was calculated employing Tauc plot by using the equation below

$$(\alpha h\nu)^n = A (h\nu - E_g)$$

The direct band gap energy was calculated by plotting graph between  $(\alpha h\nu)^2$  vs.  $(h\nu)$ , where  $h$  represents the energy of the photon molecule and  $n = 2$  for a direct band gap transition. Extrapolation of the linear portion of the curve to the x-axis results in the  $E_g$  intercept [249]. The correspond band gap value obtained for CdS nanoparticles is 2.42eV and the observed value obtained here is 2.66eV which could be due to a quantization size effect in the sample in **Figure 3**. As envisaged, particle size reduction causes a shift in the sample's optical band gap.

## 6.5 TGA-DSC

Thermal characterizations of material components are investigated in order to assess quality, components, and thermal stability in situations where some physical variable is measured against temperature. TGA is a type of thermoanalytical analysis used to determine the degradation temperature of a sample[250]. TGA is commonly used to determine component degradation, moisture content, chemical changes, and thermal stability. TGA curves are properties of a substance that are the result of a specific set of physiochemical reactions related to molecular structure and composition[251]. The



breaking and/or formation of physical and chemical bonds causes weight changes, as a result of which a volatile or heavier product may be formed [252]. The thermal stability of the nanomaterials, as well as the percentage of CdS present, were determined using TGA shown in **Figure 4**. The composites began to disintegrate at 297°C and were completely decomposed at 451°C. The residual weights of all the composites were found to be 20%. Differential scanning calorimetry (DSC) analysis was also carried out to evaluate various transitions such as glass transition temperature, melting temperature, and crystallisation temperature. TGA-DSC coexistence measurement not only improves output values but also simplifies interpretation. DSC data allows for the differentiation of endothermic and exothermic states. The two peaks at 94°C and 370°C reveal endothermic associated with area under sharp dips. The dip at 370°C, which was accompanied by significant weight loss, indicates that the MIPs composite has been significantly decomposed.

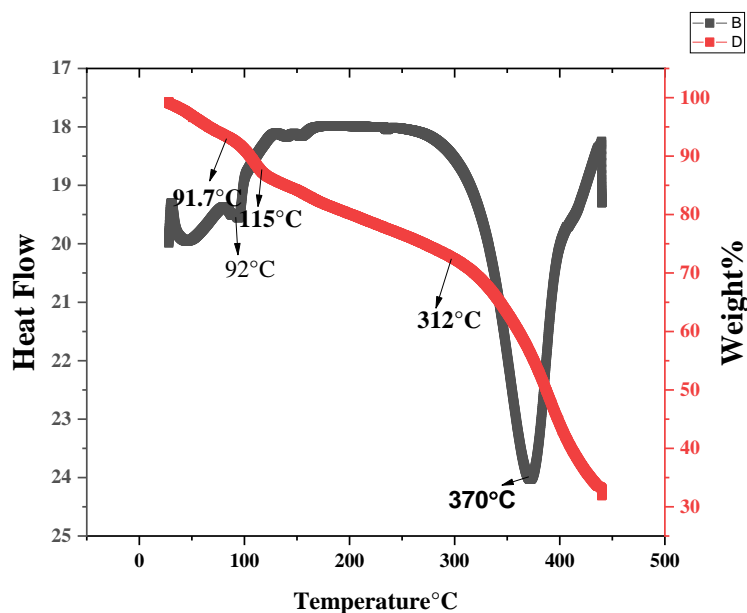


**Figure 4.** TGA-DSC characterization of CdS QDs

### 6.6 Photodegradation of 2-CP in the visible region

The elimination efficiency of CdS was used to assess photodegradation activity. The photocatalytic process was carried out in a thermostatic water bath with visible light sources provided by Xe-lamps up to 130 minutes of reaction time containing different concentration of 5,10,20,30 mg of photocatalyst. The degradation efficiency enhances

with increase in the concentration of photocatalyst. Optimum degradation results were obtained at 20 mg concentration of photocatalyst, therefore pH studies measured with time at 0.1 M NaOH or HCl solution. The solution was placed in a water bath under visible conditions. To extract the QDs at predefined time intervals, the solutions were centrifuged and filtered with Whatman (0.45 mm) filter paper. The filtrate was then analysed using a UV-Vis spectrophotometer at a wavelength (max) of 280-800nm. The effects of experimental conditions such as pH and concentration change on 2-CP elimination were investigated.

The removal percentage was calculated during the experiment by using formula[253].

$$\text{Removal of 2-CP (\%)} = (C_0 - C_e) \times 100 / C_0$$

Where  $C_0$  and  $C_e$  denote the starting and ultimate concentrations of 2-CP in milligrammes per litre, respectively.

#### *(I) pH effect*

The role of different pH on degradation efficiency of CdS QDs in 2-CP under visible light was measured. 2-CP's removal efficacy improves with increasing pH up to 6 and subsequently decreases as pH rises to 8.0, as seen in **Figure 5(D)**. The solution should be mild acidic at pH 6. The surface of the photocatalyst material becomes positively charged at an acidic pH (pH 6) which is responsible for an electrostatic repulsion shift towards the cationic moiety. The photocatalyst's surface material becomes negatively charged at alkaline pH and an electrostatic repulsion shifts towards anionic chemicals enhancing the light power 100 to 200 W. CdS QDs, a photocatalytic elimination of 2-CP enhanced from 18.2% to 80%, respectively. After that, the removal efficiencies remained constant.

#### *(II) Effect of contact time and light source*

The removal efficiency increased linearly in first 60 minutes then increases slowly with time till maximum degradation. 30mg of initial of 2-CP was used to study for the photodegradation kinetics. The reaction follows pseudo first order kinetics and equilibrium adsorption of 2-CP removal was obtained around 120 minutes, with a maximum removal efficiency of 80% in **Figure 5(C)**. The photodegradation of 2-CP for CdS nanocomposite increased from 18.2-80% when the visible light power was increased from 20 to 100W.

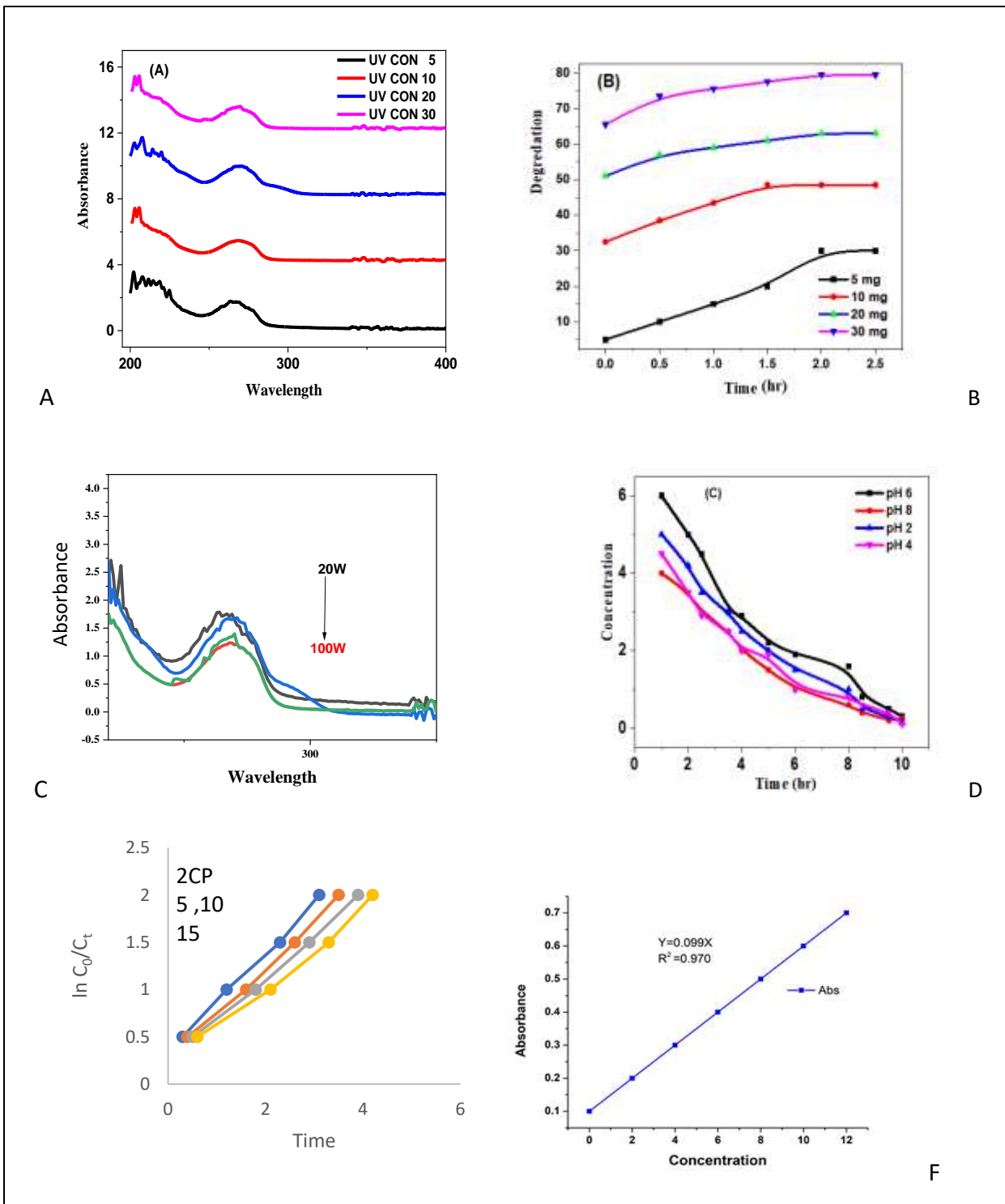


**Figure 5** (A) Calibration curve showing a plot of electronic absorbance vs. conc. (ppm). The maximum wavelength was 280 nm (B) Graph showing degradation effect of concentration on 2-CP. (C) Effect of concentration of nanoparticles on organic pollutant with respect to time. (D) calibration curve was drawn against the concentration of 2-chlorophenol

### 6.6.1 Calibration curve of 2 C.P.

Different concentrations of 2-chlorophenol solution were prepared. The electronic absorption spectra were measured for varying concentrations at  $\lambda_{\text{max}}$  280nm. A calibration curve was drawn against the concentration of 2-chlorophenol in ppm (i.e., calibration graph) was linear, and therefore Beers lambert law was employed as shown in **Figure 5F**.

#### 6.6.2 *Degradation mechanism of photocatalytic activity*

Quantum dots have been successfully employed to reduce band difference between valence and conduction band accompanying photocatalytic processes. Nanomaterials in presence of oxygen are quite efficient in removing different types of organic pollutants, when irradiated with visible or UV source. Electron hole pairs are generated by photon of light which activates semiconductor on the surface of the catalyst and participate in redox reaction of adsorbed substrates. Photocatalysis could benefit from CdS QDs with a direct band gap of 2.42 eV. The oxygen molecule on the catalyst's surface attracts an electron trapped on the metal surface, resulting in the formation of a superoxide radical. The OH group (existing on the surface) combines with the hole in the valence band to form OH•[254] .

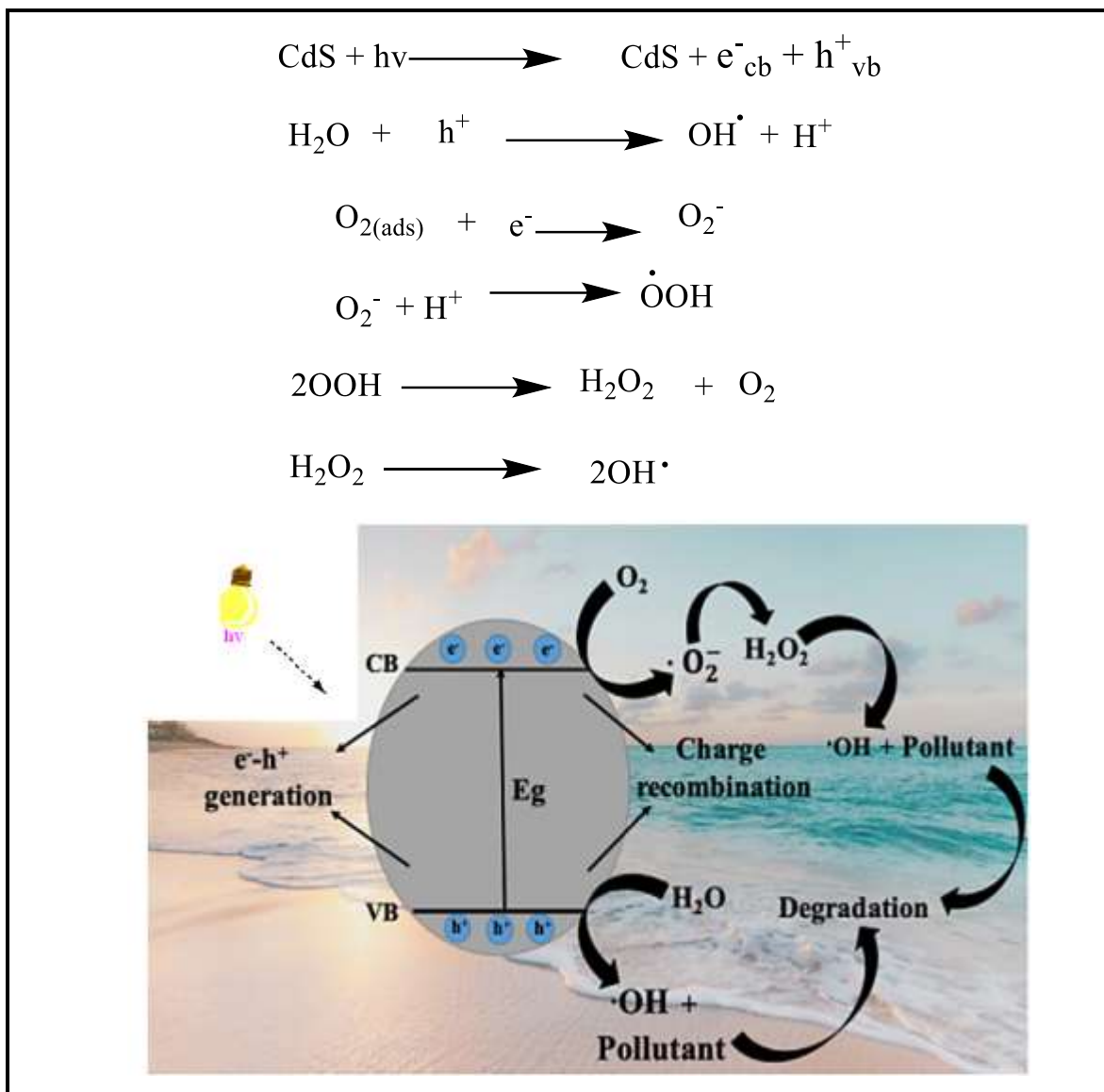


**Figure 6:** Mechanistic Investigation of Photodegradation by CdS

### 6.7 Antibacterial activity of CdS nanoparticles using disc diffusion process

The disc diffusion process

was used to investigate the antibacterial activity of synthesised CdS nanoparticles against *Aeromonas hydrophila* and *Escherichia coli*. The culture was first inoculated in nutrient broth and incubated in an incubator for 24 hours at 37 °C. Following that, different doses of CdS nanoparticles, such as 10 mg/ml and 20 mg/ml in DMSO, were prepared. Positive and negative controls were ampicillin (10 mg/ml) and DMSO, respectively. The Whatman filter paper discs were then submerged in the dissolved CdS nanoparticles overnight. This was followed by the spread plating of bacterial inoculum and four different discs. In each spread-plated plate, place a 10mg CdS QDs, a 20mg CdS QDs,

a positive control, and a negative control. The zone of inhibition around the discs was measured using a calibrated scale after incubation. **Figure 7.** illustrate the antibacterial activity against both bacterial strains. It shows that CdS QDs have bactericidal activity against *E. coli*. *Aeromonas hydrophila* with *E. coli* and *Aeromonas hydrophilia* has clear zone with a ZOI of 20mm when there is a larger concentration of CdS QDs.



**Figure 7.** Bactericidal Images of *E. coli* and *Aeromonas hydrophilia*

## 6.8 Conclusions

For the preparation of CdS QDs chemical precipitation method was adopted and well characterized. This material performed good photocatalytic degradation efficiency in the presence of 2-Chloro phenol in the visible region. The pH effect and concentration effect of the pollutant was measured at various concentrations and pH. The maximum removal effectiveness of 2-CP (10 mg/L) in the visible area with CdS photocatalyst was about 80% at the optimum pH of 6.0. The photocatalysis degradation follows Pseudo first order reaction. The CdS QDs also maintained its high efficacy against *E. coli* and *Aeromonas hydrophilia* bacterial growth.

## 6.9 References

- [228] S.P. Onkani, P.N. Diagboya, F.M. Mtunzi, M.J. Klink, B.I. Olu-Owolabi, V. Pakade, Comparative study of the photocatalytic degradation of 2-chlorophenol under UV irradiation using pristine and Ag-doped species of TiO<sub>2</sub>, ZnO and ZnS photocatalysts, *Journal of Environmental Management*. 260 (2020) 110145. <https://doi.org/10.1016/j.jenvman.2020.110145>.
- [229] M.M. Ba-Abbad, M.S. Takriff, A.W. Mohammad, Enhancement of 2-chlorophenol photocatalytic degradation in the presence Co<sup>2+</sup>-doped ZnO nanoparticles under direct solar radiation, *Res Chem Intermed*. 42 (2016) 5219–5236. <https://doi.org/10.1007/s11164-015-2352-3>.
- [230] N.N. Rao, A.K. Dubey, S. Mohanty, P. Khare, R. Jain, S.N. Kaul, Photocatalytic degradation of 2-chlorophenol: a study of kinetics, intermediates and biodegradability, *Journal of Hazardous Materials*. 101 (2003) 301–314. [https://doi.org/10.1016/S0304-3894\(03\)00180-8](https://doi.org/10.1016/S0304-3894(03)00180-8).
- [231] E. Amouyal, Photochemical production of hydrogen and oxygen from water: A review and state of the art, *Solar Energy Materials and Solar Cells*. 38 (1995) 249–276. [https://doi.org/10.1016/0927-0248\(95\)00003-8](https://doi.org/10.1016/0927-0248(95)00003-8).
- [232] G.Z. Wang, W. Chen, C.H. Liang, Y.W. Wang, G.W. Meng, L.D. Zhang, Preparation and characterization of CdS nanoparticles by ultrasonic irradiation, *Inorganic Chemistry Communications*. 4 (2001) 208–210. [https://doi.org/10.1016/S1387-7003\(01\)00172-1](https://doi.org/10.1016/S1387-7003(01)00172-1).
- [233] S. Wang, J. Yu, P. Zhao, S. Guo, S. Han, One-Step Synthesis of Water-Soluble CdS Quantum Dots for Silver-Ion Detection, *ACS Omega*. 6 (2021) 7139–7146. <https://doi.org/10.1021/acsomega.1c00162>.
- [234] Y. Fazli, S.M. Pourmortazavi, I. Kohsari, M.S. Karimi, M. Tajdari, Synthesis, characterization and photocatalytic property of nickel sulfide nanoparticles, *J Mater Sci: Mater Electron*. 27 (2016) 7192–7199. <https://doi.org/10.1007/s10854-016-4683-2>.
- [235] Z. Shalabayev, M. Baláž, N. Khan, Y. Nurlan, A. Augustyniak, N. Daneu, B. Tatykayev, E. Dutková, G. Burashev, M. Casas-Luna, R. Džunda, R. Bureš, L. Čelko, A. Ilin, M. Burkitbayev, Sustainable Synthesis of Cadmium Sulfide, with Applicability in Photocatalysis, Hydrogen Production, and as an Antibacterial Agent, Using Two Mechanochemical Protocols, *Nanomaterials (Basel)*. 12 (2022) 1250. <https://doi.org/10.3390/nano12081250>.
- [236] D. Ayodhya, G. Veerabhadram, Facile fabrication, characterization and efficient photocatalytic activity of surfactant free ZnS, CdS and CuS nanoparticles, *Journal of Science: Advanced Materials and Devices*. 4 (2019) 381–391. <https://doi.org/10.1016/j.jsamd.2019.08.006>.
- [237] M. Anjum, R. Miandad, M. Waqas, F. Gehany, M. Barakat, Remediation of wastewater using various nano-materials, *Arabian Journal of Chemistry*. 12 (2016). <https://doi.org/10.1016/j.arabjc.2016.10.004>.
- [238] S. Wang, D. Liu, J. Yu, X. Zhang, P. Zhao, Z. Ren, Y. Sun, M. Li, S. Han, Photocatalytic Penicillin Degradation Performance and the Mechanism of the Fragmented TiO<sub>2</sub> Modified by CdS Quantum Dots, *ACS Omega*. 6 (2021) 18178–18189. <https://doi.org/10.1021/acsomega.1c02079>.
- [239] M. Iqbal, A. Ali, N.A. Nahyoon, A. Majeed, R. Pothu, S. Phulpoto, K.H. Thebo, Photocatalytic degradation of organic pollutant with nanosized cadmium sulfide, *Materials Science for Energy Technologies*. 2 (2019) 41–45. <https://doi.org/10.1016/j.mset.2018.09.002>.
- [240] P. Wang, S. Xu, J. Wang, X. Liu, Photodeposition synthesis of CdS QDs-decorated TiO<sub>2</sub> for efficient photocatalytic degradation of metronidazole under visible light, *Journal of Materials Science: Materials in Electronics*. 27 (2020) 1–12. <https://doi.org/10.1007/s10854-020-04504-2>.
- [241] R.S. Ganesh, S.K. Sharma, E. Durgadevi, M. Navaneethan, S. Ponnusamy, C. Muthamizhchelvan, Y. Hayakawa, D.Y. Kim, Growth, microstructure, structural and optical properties of PVP-capped CdS nanoflowers for efficient photocatalytic activity of Rhodamine B, *Materials Research Bulletin*. 94 (2017) 190–198. <https://doi.org/10.1016/j.materresbull.2017.05.059>.

- [242] R.A. Devi, M. Latha, S. Velumani, G. Oza, P. Reyes-Figueroa, M. Rohini, I.G. Becerril-Juarez, J.-H. Lee, J. Yi, Synthesis and Characterization of Cadmium Sulfide Nanoparticles by Chemical Precipitation Method, *J Nanosci Nanotechnol.* 15 (2015) 8434–8439. <https://doi.org/10.1166/jnn.2015.11472>.
- [243] A.M. Larionov, L.P. Yeryomin, Synthesis of cadmium sulfide by ultraviolet irradiation technique, in: *Proceedings. The 8th Russian-Korean International Symposium on Science and Technology, 2004. KORUS 2004.*, 2004: pp. 235–237 vol. 2. <https://doi.org/10.1109/KORUS.2004.1555605>.
- [244] M. Shakouri-Arani, M. Salavati-Niasari, Synthesis and characterization of cadmium sulfide nanocrystals in the presence of a new sulfur source via a simple solvothermal method, *New J. Chem.* 38 (2014) 1179–1185. <https://doi.org/10.1039/C3NJ00996C>.
- [245] N. Loudhaief, H. Labiadh, E. Hannachi, M. Zouaoui, M.B. Salem, Synthesis of CdS Nanoparticles by Hydrothermal Method and Their Effects on the Electrical Properties of Bi-based Superconductors, *J Supercond Nov Magn.* 31 (2018) 2305–2312. <https://doi.org/10.1007/s10948-017-4496-4>.
- [246] C. Tura, N. Coombs, Ö. Dag, One-Pot Synthesis of CdS Nanoparticles in the Channels of Mesosructured Silica Films and Monoliths, *Chemistry of Materials.* 17 (2005). <https://doi.org/10.1021/cm048484b>.
- [247] T.K. Jana, S.K. Maji, A. Pal, R.P. Maiti, T.K. Dolai, K. Chatterjee, Photocatalytic and antibacterial activity of cadmium sulphide/zinc oxide nanocomposite with varied morphology, *Journal of Colloid and Interface Science.* 480 (2016) 9–16. <https://doi.org/10.1016/j.jcis.2016.06.073>.
- [248] K. Zhang, Z. Mou, S. Cao, S. Wu, X. Xu, C. Li, Well-designed NiS/CdS nanoparticles heterojunction for efficient visible-light photocatalytic H<sub>2</sub> evolution, *International Journal of Hydrogen Energy.* 47 (2022) 12605–12614. <https://doi.org/10.1016/j.ijhydene.2022.02.009>.
- [249] M. Imran, Dr.M. Ikram, A. Shahzadi, S. Dilpazir, H. Khan, I. Shahzadi, S. Yousaf, S. Ali, J. Geng, Y. Huang, High-performance solution-based CdS-conjugated hybrid polymer solar cells, *RSC Advances.* 8 (2018). <https://doi.org/10.1039/C8RA01813H>.
- [250] G.V. Jucá Dantas, N.P. de Moraes, R. Bacani, L.Á. Rodrigues, Facile synthesis of cadmium sulfide and the effect of thermal annealing in N<sub>2</sub>-rich atmosphere on its structural, morphological, chemical, and optical properties, *Materials Chemistry and Physics.* 277 (2022) 125492. <https://doi.org/10.1016/j.matchemphys.2021.125492>.
- [251] S. Wang, Q. Liu, Z. Lu, L. Xu, X. Liu, Y. Hu, L. Qian, S. Xu, A.E.-F. Abomohra, Visible light-driven conversion of carboxylic acids into esters for enhanced algal bio-crude oil catalyzed by cadmium sulfide quantum dots (CdS-QDs), *Fuel Processing Technology.* 216 (2021) 106778. <https://doi.org/10.1016/j.fuproc.2021.106778>.
- [252] Y.M. Arababab, C.K. Sheng, M.F. Hassan, Influence of ammonium nitrate concentration on structural evolution and optical properties tuning of CdS nanoparticles synthesized by precipitation method, *Nano-Structures & Nano-Objects.* 19 (2019) 100344. <https://doi.org/10.1016/j.nanoso.2019.100344>.
- [253] H. Shi, X. Jiang, Y. Li, D. Chen, C. Hou, Z. Zhang, Q. Zhang, J. Shen, Enhanced bio-photodegradation of p-chlorophenol by CdS/g-C<sub>3</sub>N<sub>4</sub> 3D semiconductor-microbe interfaces, *Sci Total Environ.* 807 (2022) 151006. <https://doi.org/10.1016/j.scitotenv.2021.151006>.
- [254] E. El-Fawal, O. Elshamy, Photodegradation enhancement of 2-chlorophenol using ZnO–CdS@CS nanocomposite under visible light, *International Journal of Environmental Science and Technology.* 16 (2019). <https://doi.org/10.1007/s13762-019-02249-y>.



## CHAPTER 7

### Facile synthesis of ZnS and Ni doped ZnS Quantum dots and enhanced photocatalytic property of Ni doped ZnS nanoparticle

#### 7.1. Introduction

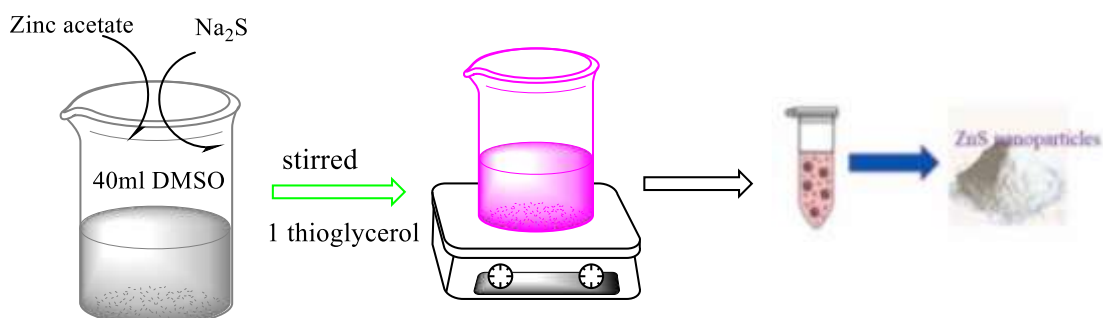
Quantum dots (QDs) are unique nanocrystal semiconductor materials having a size in the range of few nanometres. This domain of nanomaterial study has rapidly grown and drawn substantial study over the last two decades due to their distinctive structural, electronic, magnetic and optical properties arising from their enormous surface-to-volume ratio and quantum confinement [255–257]. Doping semiconductor nanomaterials with transition metals or rare earth ions improves their efficiency output, which is significant for applications such as LEDs, lasers, and composites [258–260]. ZnS is a prominent II–VI semiconductor with a large exciton-binding energy (40 meV) and a wide bandgap of 3.67 eV (bulk). ZnS and its doped have been extensively used nowadays in various photocatalytic process and its efficiency has been found to be interesting to degrade certain toxin materials in aqueous solution. Toxic and nonbiodegradable wastes are the primary cause of soil, water, and air pollution. The formulations that are water soluble are the most harmful. as they have a direct effect on living things [261]. Synthetic dyes in waste waters from industrial and other sectors have been a key contributor to this. Many colours are safe on their own, but when mixed with water, they quickly produce highly hazardous compounds in the aqueous waste, polluting the water. When synthetic dyes (azo dyes) dissolve in water, for example, their degradation or intermediate products include carcinogenic or mutagenic aromatic compounds including such benzidine, naphthalene and others. Photodegradation is an emerging technology among the several ways for removing textile dyes from wastewater, such as adsorption, biodegradation, chlorination and ozonation. The significant advantage of this technique is the total mineralization of most organic contaminants [262–264]. One important strategy for enhancing the rate of destruction is to use semiconductors such as ZnS, CdS, TiO<sub>2</sub>, ZnO, Fe<sub>2</sub>O<sub>3</sub> and others as photocatalysts in the photodegradation process [265,266]. An appropriate photocatalyst has strong photocatalytic activity, resistance to photo corrosion, cheap cost, non-toxicity and a favourable band-gap energy. As a result, the synthesis of diverse photocatalysts with varying compositions, as well as the investigation of organic pollutants annihilation, could be an appealing subject of research. Photocatalytic methods that breakdown organic contaminants into simple metallic inorganic species have gotten a lot of attention in the last year as a potential solution to a variety

of water pollution issues. Semiconductor compounds of group II–VI elements with direct band gaps have a high tendency as effective photocatalysts due to their ability to rapidly generate electron holes by absorption of photons with energy equal to or greater than their band gap. Such produced electron-hole pairs can generate free radical ions in the system when used to redox the chemicals adsorbed on the photocatalyst surface. Free radicals (OH) are a potent organic compound oxidant that can aid in the breakdown of pollutants in the environment. As a result, there has been a lot of interest in developing new II–VI group semiconductors as photocatalysts, as well as adapting existing ones for the decoloration of hazardous organic dyes. Hamid Reza Rajabi and Mohammad Farsi used a chemical preparation approach to make ZnS quantum dots, which showed high photodegradation activity on methylin violet [267]. According to Chen et al. (2013) the photocatalytic degradation of as-synthesised ZnS rods in the breakdown of methyl orange was the highest [268]. We used a simple wet chemical precipitation approach to create pristine and Ni doped ZnS QDs in this study. XRD and SEM analyses are used to characterise the produced samples. In addition, the photocatalytic capabilities of pure and Ni<sup>2+</sup> doped ZnS QDs were tested on methylene red dye (a model pollutant) degradation under visual illumination.

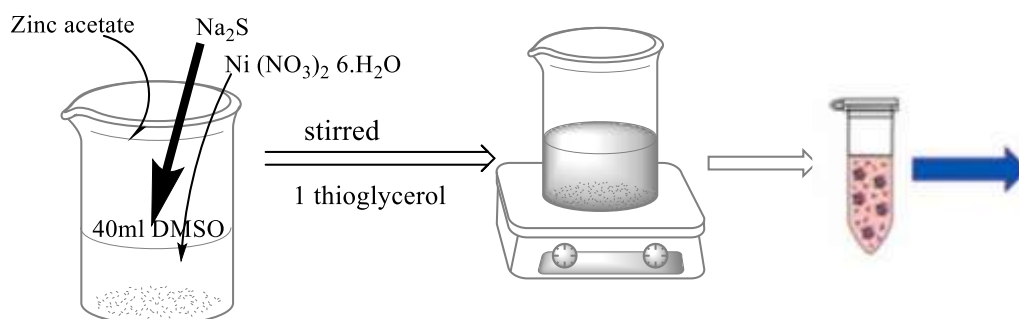
## 7.2 Experimental Section

The simple wet chemical procedure was employed for the preparation of ZnS and Ni doped ZnS. Standard Zn (CH<sub>3</sub>COO)<sub>2</sub>H<sub>2</sub>O and Na<sub>2</sub>S were utilised to make ZnS QDs, with no further purification required. 1-thioglycerol was utilised as the stabilizing agent to prevent any aggregation of produced QDs. Synthesis of ZnS was obtained by dissolving 0.1 M Zn (CH<sub>3</sub>COO)<sub>2</sub>H<sub>2</sub>O in 40 ml dimethyl sulfoxide (DMSO). The solution was stirred and 0.5 ml of 1-thioglycerol was pipetted at room temperature to the mixture. The solution was then injected with 10 ml of aqueous Na<sub>2</sub>S solutions. A homogenous mixture of ZnS was obtained by stirring the solution at room temperature for many hours. The non-solvent acetone was used to extract the ZnS QDs from the solution, which was subsequently centrifuged and washed several times to eliminate any un-reacted ions that remained outside the clusters. To generate Ni: ZnS QDs, 0.003M aqueous Ni (NO<sub>3</sub>)<sub>2</sub> 6.H<sub>2</sub>O solutions were added to a solution of Zn (CH<sub>3</sub>COO)<sub>2</sub>H<sub>2</sub>O, and then the procedure described above was performed.

## Stage 1



## Stage 2



Powder

Ni doped ZnS

**Figure 1.** Scheme representation of Synthesis of ZnS and Ni doped ZnS

## 7.3 Results and discussions

### Structural analysis

The crystal structure and grain size were studied using XRD signals. The XRD patterns for ZnS and Ni: ZnS QDs are shown in **Figure 2**. The (1 1 1), (2 2 0) and (3 1 1) planes were discovered to have three major diffraction peaks. The diffraction patterns discovered can be

categorised as cubic phase ZnS crystalline structure, which matches the standard data quite well (JCPD No: 65-9585). It was revealed that when Ni is doped into ZnS QDs, the structure does not change. The presence of Ni in the ZnS lattice has no effect on the cubic structure of ZnS QDs, as demonstrated by this condition. The identical size of Zn led to the discovery of a comparable crystal size, a stable cubic structure and the absence of an impurity phase. The diameters of the ZnS and Ni: ZnS QDs are shrinking as shown by the ZnS and Ni: ZnS QD diffraction peaks. **Eq. 1** the average particle sizes of the QDs [269] was determined by using Scherrer equation based on the peak widths of the moderately strong (111), (220), and (311) diffractions.

$$D = 0.9\lambda / (\beta \cos\theta) \quad (1)$$

where D is the average size of the QDs, X-ray wavelength, broadening measured in radians as the full width half maxima (FWHM) and Bragg's diffraction angle ZnS and Ni: ZnS QDs had diameters of 6 and 9.8 nm, respectively as determined by XRD peak width.

To determine the morphology, grain size, and shape of cubic pristine ZnS and Ni doped ZnS, QDs were analysed using SEM in **Figure 2**. The ZnS QDs were detected by SEM to have a high surface area with well-defined mesopores, as shown in Fig. Small granules of about 7–9 nm was found on the surface of undoped ZnS. The particle size of ZnS grows somewhat as the Ni doping level increases, reaching higher nanometres. A well-defined particle-like morphology with a significant number of spherical sized particles is revealed upon close observation.

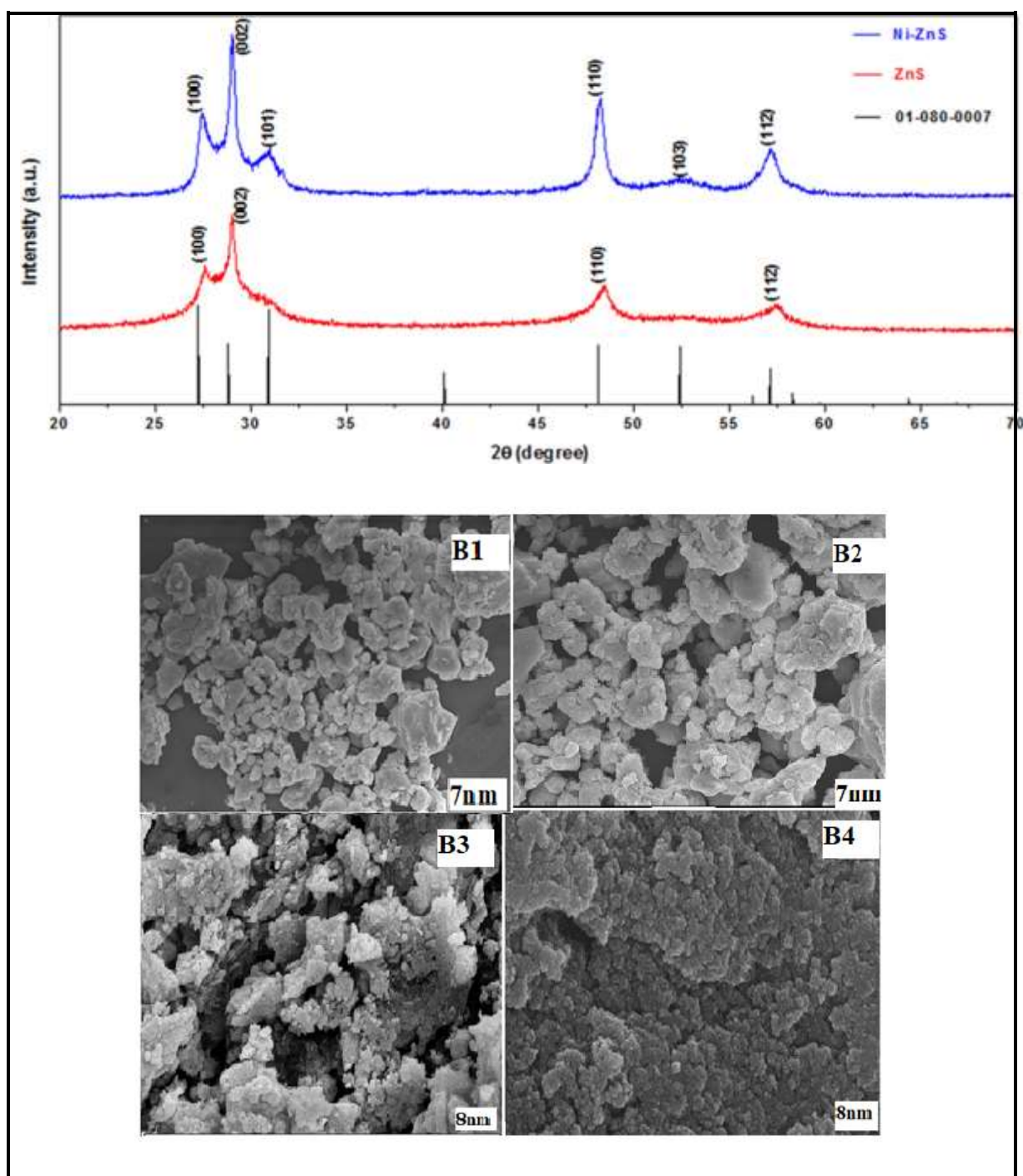


**Figure 2.** XRD and FESEM images of cubic pristine and Ni doped ZnS QDs.

#### 7.4 Photocatalytic activity

The Photodegradation efficiency of pure and Ni doped ZnS samples was assessed by measuring methylene red (MR) photodegradation in aqueous solution. Both ZnS and Ni doped ZnS photocatalyzed degradation of methyl-red under visible light results in a progressive lowering

of the absorbance maximum at 430 nm, as shown in the Figure. These findings are consistent with prior findings that revealed a first-order, or pseudo-first-order kinetic. MR was chosen because of its high adhesion to metal oxide surfaces and outstanding light degradation resistance. Stock solution of 1000 ppm was prepared by dissolving 1g in 1000ml of aqueous solution. The suspensions were magnetically agitated for 30 minute to achieve adsorption–desorption equilibrium between dye and ZnS. Visible light was used to irradiate the combined liquids. Few aliquots of sample were taken after every 30 minutes (up to 120 minutes) and centrifuged to separate the photocatalyst from the mixing solution followed by a UV–Vis’s spectrophotometer analysis of the clarified solutions. The absorbance of MR solution was measured in nanometres in Uv spectra, which is the wavelength at which it absorbs the most.

### **i) Effect of Dopant on Photocatalytic activity**

The optimal catalyst concentration has been calculated to minimize catalyst waste and achieve 100% photon absorption. Experiments with varied doses of ZnS catalyst (20,30,40,50mg) in **Figure 3** and the same concentration of Ni doped ZnS were carried out as shown in **Figure 4**. When the amount of catalyst was increased to 50mg/25mL, the rate of degradation rose linearly. The increased concentration of catalyst dosage increases the quantum yield of photons absorbed by the catalyst, resulting in more electron and hole generation and hence more hydroxyl radicals. Increased catalyst dose also boosts the number of organic pollutants absorbed, making photocatalytic activity easier. Figure also compare the Photodegradation efficiency of Ni doped ZnS in Figure 3. Under visible light irradiation, the doped sample has shown better photocatalytic efficiency than pristine ZnS. As a result, it is clear that doping has boosted ZnS photocatalytic activity.

### **ii) Effect of pH**

The figure below shows the percentage degradation of methyl red as a function of time at various pH values. The effect of pH was used to identify the impact of QDs at a constant dye concentration (20 mg/L) and catalyst weight (1g/1L) using the sample with the best photocatalytic reactor. The photocatalytic activity of this anionic dye was faster at **pH- 4** as seen in the **Figure 3** and **4**. The pH of the solution has a significant impact on the electrostatic interactions between a semiconductor surface, substrate and charged radicals during photocatalytic oxidation. Positive charge on the ZnS surface increases in an acidic environment, enhancing dye molecule adsorption on the surface of catalyst. Furthermore, an acidic medium reduces recombination.

### **iii) Effect of Dye concentration**

Experiment was conducted with varied concentrations of 10ppm, 20ppm, 30ppm and 40ppm of dye in aqueous solution for ZnS and Ni doped ZnS in **Figure 3** and **4**. The impact of concentration was observed at a fixed catalyst dosage and pH. The ideal starting dye concentration was discovered to be 10ppm and increasing the dye concentration slowed down the rate of deterioration. The following is a plausible explanation: if pollutant concentrations rise, the appropriate reactive species ratio may not be generated at the fixed photocatalyst dosage. The breakdown of methyl red may be controlled by limiting surface active spots for the catalytic process.

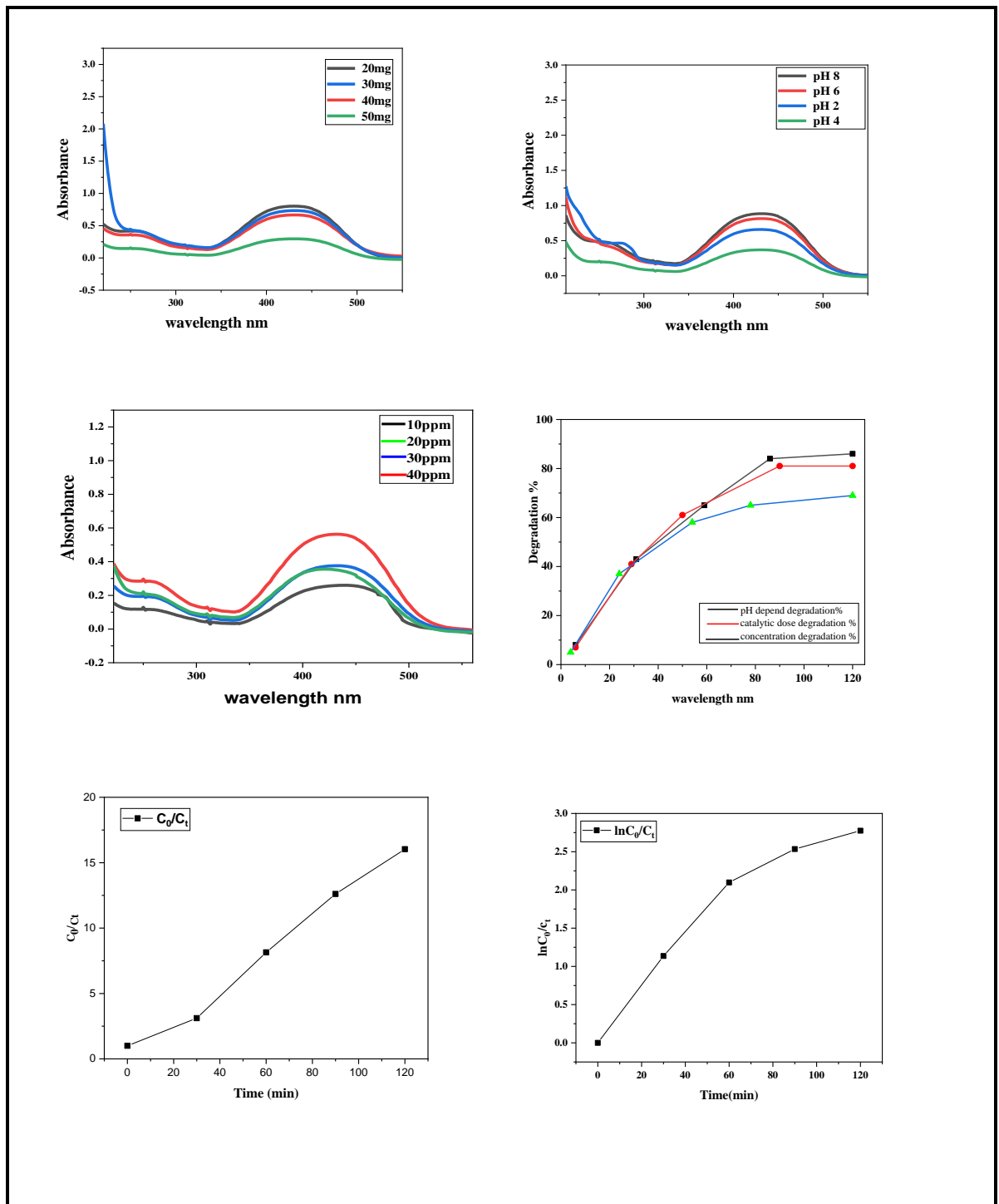


Figure 3. Photodegradation of Methyl Red by ZnS.



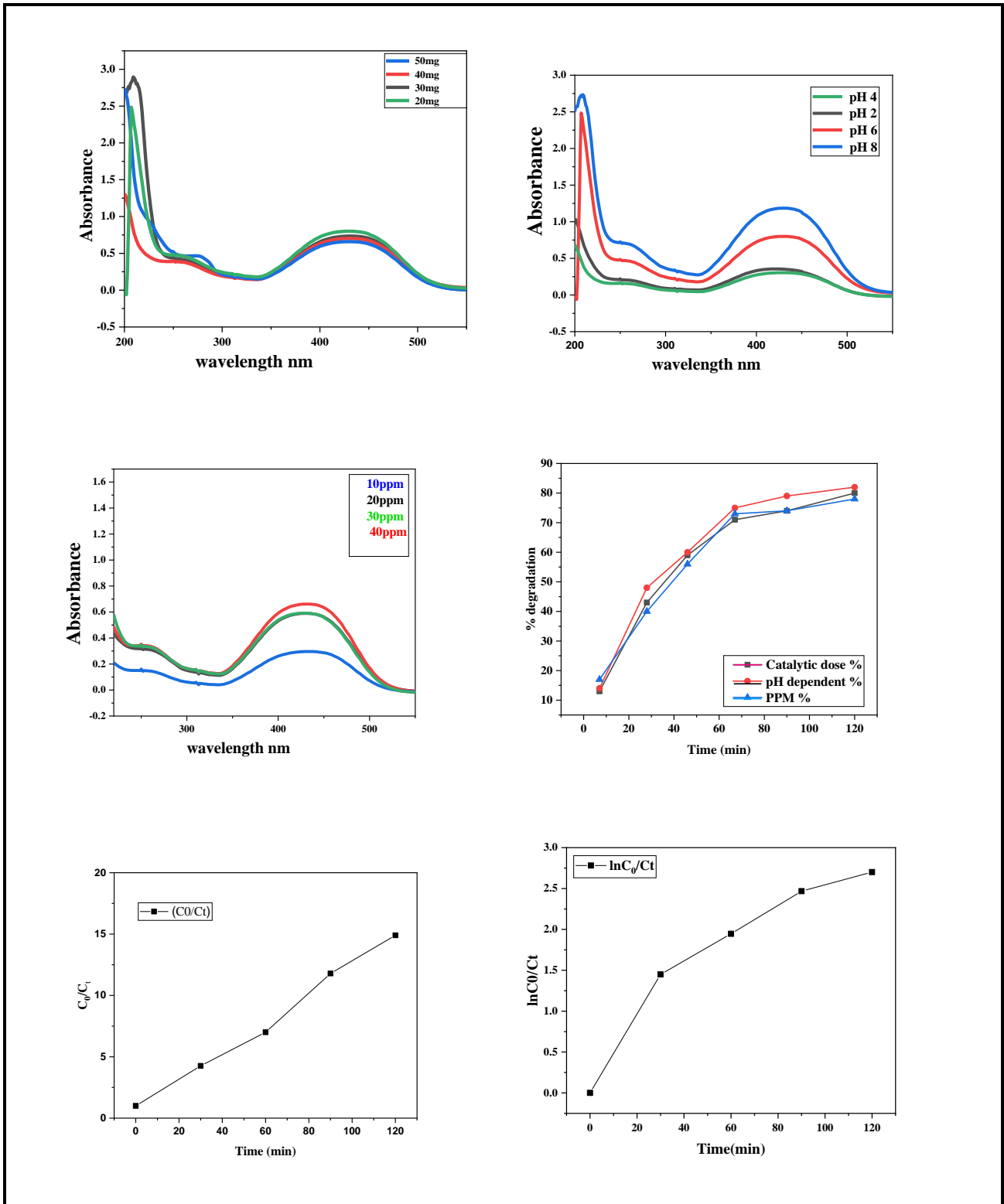


Figure 4. Effect of Ni doped ZnS on photodegradation of Methyl Red.

### 7.5 Photocatalytic activity

The photocatalytic efficiency is known to be influenced by Crystallinity, surface area and shape, which might be increased by reducing photogenerated electron-hole pair recombination, lowering the excitation wavelength and increasing the number of surface-adsorbed reactant

species. In most situations, photocatalysis begins with the adsorption of supra-band gap photons, culminating in the creation of electron-hole pairs in semiconductor particles. The charge carriers then diffuse to the surface of the particle, where they combine with water molecules to create highly reactive peroxide (O<sub>2</sub>) and hydroxyl radicals (OH·) [270,271]. The kinetics of Methyl red dye photodegradation by ZnS nanoparticles was investigated and the results are depicted in above Figure. The rate constant (k) for MR breakdown by ZnS nanoparticles was calculated using the pseudo-first-order rate equation. The rate constant value is obtained by plotting ln (C<sub>0</sub>/C<sub>t</sub>) as a function of irradiation time. To learn more about photocatalytic mechanisms, Researchers used ZnS nanoparticles to create a photocatalytic system for Methyl red dye. The (e-) hole (h<sup>+</sup>) combination produces ZnS nanoparticles. Light radiation that can be observed by photovoltaic diluted with ZnS nanoparticles can create e- and h<sup>+</sup> at the topmost of the ZnS nanoparticles with spectroscopic radiation.

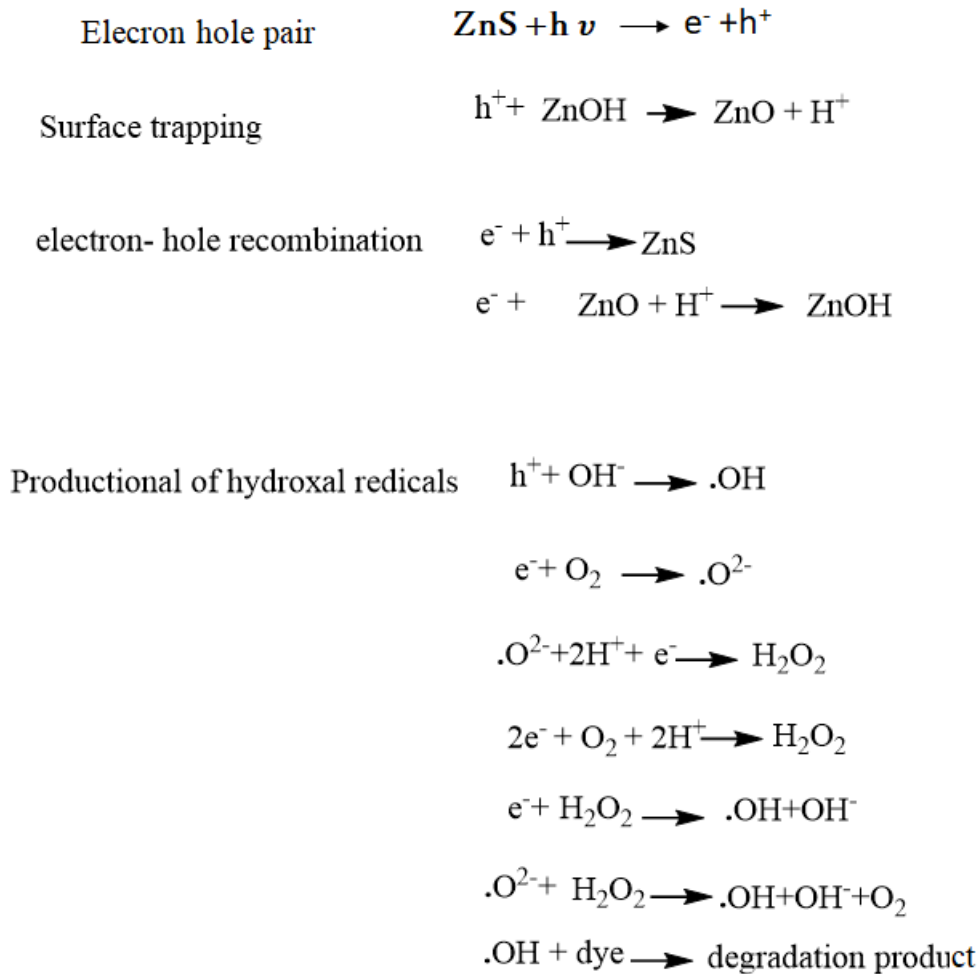
#### Photocatalytic activity

The degradation of natural dyes by photocatalysts is thought to be primarily governed by pseudo first-order kinetics.

$$\ln C_0/C_t = kt \quad (1)$$

$$C_0 = C_e - kt$$

where k is the reaction rate constant and K is the reactant's adsorption co-efficient. The slope of the relationship curve between ln (C<sub>0</sub>/C<sub>t</sub>) and time (t) equals the observable first-order rate constant k (16,18).



## 7.6 Conclusion

The ZnS and Ni doped ZnS were synthesized by simple solid-state method. The QDs were characterized by XRD SEM to determine size and Morphology of compound. The crystalline size increases by doping with Ni in ZnS. In this work the synthesized QDs were employed to check photocatalytic activity of sample against Methylene Red dye and it has been concluded that Ni doped on ZnS nanostructures increases the percentage of degradation and reaction rate constant, according to photocatalytic measurements. As a result, we believe that Ni-ZnS nanoparticles are a promising photocatalyst for the breakdown of methylene red dye, which was used as a model pollutant in this investigation.

## 7.7 References

- [255] M. Afzaal, M.A. Malik, P. O'Brien, Chemical routes to chalcogenide materials as thin films or particles with critical dimensions with the order of nanometres, *J. Mater. Chem.* 20 (2010) 4031–4040. <https://doi.org/10.1039/B923898K>.
- [256] X. Fang, L. Wu, L. Hu, ZnS Nanostructure Arrays: A Developing Material Star, *Advanced Materials*. 23 (2011) 585–598. <https://doi.org/10.1002/adma.201003624>.
- [257] M. Jothibas, C. Manoharan, S. Johnson Jeyakumar, P. Praveen, I. Kartharinal Punithavathy, J. Prince Richard, Synthesis and enhanced photocatalytic property of Ni doped ZnS nanoparticles, *Solar Energy*. 159 (2018) 434–443. <https://doi.org/10.1016/j.solener.2017.10.055>.
- [258] J.M. Kikkawa, D.D. Awschalom, Lateral drag of spin coherence in gallium arsenide, *Nature*. 397 (1999) 139–141. <https://doi.org/10.1038/16420>.
- [259] Y.S. Didosyan, H. Hauser, G.A. Reider, W. Toriser, Fast latching type optical switch, *Journal of Applied Physics*. 95 (2004) 7339–7341. <https://doi.org/10.1063/1.1669350>.
- [260] I. Žutić, J. Fabian, S. Das Sarma, Spintronics: Fundamentals and applications, *Rev. Mod. Phys.* 76 (2004) 323–410. <https://doi.org/10.1103/RevModPhys.76.323>.
- [261] M.V. Encinas, A.M. Rufs, M.G. Neumann, C.M. Previtali, Photoinitiated vinyl polymerization by safranin T/triethanolamine in aqueous solution, *Polymer*. 37 (1996) 1395–1398. [https://doi.org/10.1016/0032-3861\(96\)81137-2](https://doi.org/10.1016/0032-3861(96)81137-2).
- [262] A. Kistan, V. Kanchana, L. Sakayasheela, J. Sumathi, A. Premkumar, A. Selvam, Titanium dioxide as a Catalyst for Photodegradation of Various Concentrations of Methyl Orange and Methyl Red dyes using Hg Vapour Lamp with Constant pH, *Oriental Journal of Chemistry*. 34 (2018) 1000–1010.
- [263] L.M. Ahmed, F.T. Tawfeeq, M.H.A. Al-Ameer, K.A. Al-Hussein, A.R. Athaab, Photo-Degradation of Reactive Yellow 14 Dye (A Textile Dye) Employing ZnO as Photocatalyst, *Journal of Geoscience and Environment Protection*. 4 (2016) 34–44. <https://doi.org/10.4236/gep.2016.411004>.
- [264] B.M. Al-Sakkaf, S. Nasreen, N. Ejaz, Degradation Pattern of Textile Effluent by Using Bio and Sono Chemical Reactor, *Journal of Chemistry*. 2020 (2020) e8965627. <https://doi.org/10.1155/2020/8965627>.
- [265] M. Pawar, S. Topcu Sengođdular, P. Gouma, A Brief Overview of TiO<sub>2</sub> Photocatalyst for Organic Dye Remediation: Case Study of Reaction Mechanisms Involved in Ce-TiO<sub>2</sub> Photocatalysts System, *Journal of Nanomaterials*. 2018 (2018) e5953609. <https://doi.org/10.1155/2018/5953609>.
- [266] M.B. Tahir, M. Sohaib, M. Sagir, M. Rafique, Role of Nanotechnology in Photocatalysis, Reference Module in Materials Science and Materials Engineering. (2020) B978-0-12-815732-9.00006–1. <https://doi.org/10.1016/B978-0-12-815732-9.00006-1>.
- [267] V. Vatanpour, O. Karatas, S. Amiri, H.R. Rajabi, I. Koyuncu, A. Khataee, Different metal-doped ZnS quantum dots photocatalysts for enhancing the permeability and antifouling performances of polysulfone membranes with and without UV irradiation, *Chemosphere*. 294 (2022) 133705. <https://doi.org/10.1016/j.chemosphere.2022.133705>.
- [268] A. Kumar, Photodegradation of Methyl Orange in Aqueous Solution by the Visible Light Active Co:La:TiO<sub>2</sub> Nanocomposite, *Journal of Chemical Sciences*. 8 (2017). <https://doi.org/10.4172/2150-3494.1000164>.
- [269] B. Poornaprakash, U. Chalapathi, S.V.P. Vattikuti, Compositional, morphological, structural, microstructural, optical, and magnetic properties of Fe, Co, and Ni doped ZnS nanoparticles, *Appl. Phys. A*. 123 (2017) 275. <https://doi.org/10.1007/s00339-017-0865-x>.
- [270] Y. Badr, M.G. Abd El-Wahed, M.A. Mahmoud, Photocatalytic degradation of methyl red dye by silica nanoparticles, *Journal of Hazardous Materials*. 154 (2008) 245–253. <https://doi.org/10.1016/j.jhazmat.2007.10.020>.

- [271] T. Welderfael, O.P. Yadav, A.M. Taddesse, J. Kaushal, Synthesis, characterization and photocatalytic activities of Ag-N-codoped ZnO nanoparticles for degradation of methyl red, *Bulletin of the Chemical Society of Ethiopia*. 27 (2013) 221–232.  
<https://doi.org/10.4314/bcse.v27i2.7>.

## Chapter 8

### Assessment of photocatalytic efficiency and antifungal activity of Zinc doped Copper Sulfide composite embedded with Graphene Oxide nanosheets

#### 8.1. Introduction

Photocatalytic mechanisms on semiconducting nanoparticles with different light sources are very important due to their pertinency in the degradation of hazardous unprocessed dyes in aqueous media such as Rhodamine-B (RhB), Methyl orange (MO), Methyl Red, Methylene blue (MB) etc[272]. Extensive efforts have been made over the last recent years to develop more stable and powerful photocatalysts that operate under the visible source of light and are promised catalysts for waste water treatment by degrading pollutant species into harmless compounds[273]. Various metal based photocatalysts, including CdS,  $\text{Ag}_3\text{PO}_4$ , MnS,  $\text{CeO}_2$ ,  $\text{WO}_3$ ,  $\text{BiVO}_4$ , AgS/RGO and CuO and CuS, have been employed in visible light extensively in the past due to their excellent disintegration abilities[274].

Covellite segment copper monosulfide (CuS) is one of the p-type semiconducting nanoparticle photocatalytically active under visible light that is non-toxic, affordable, and sustainable[275]. Copper sulphide (CuS) is an essential semiconductor material with adaptive stoichiometric composition among semiconducting nanoparticles[276]. CuS nanoparticles have gained a lot of attention due to their unusual qualities CuS has been recognized as an efficient nanomaterial component employed in nanophase energy storage, gas sensing, sensors, Optics, photocatalysis and lithium-ion batteries[277]. So far, there has been a lot of effort put towards enhancing the efficiency of pure CuS and its nanocomposite towards photodegradation of organic dyes and subsequent water treatment. CuS/ZnS nanocomposite hollow spheres have been developed for this pathway using an ion exchange technique to improve the photocatalytic efficiency for the degradation of RhB dye pollutant CuS/ZnS nanocomposite hollow spheres have been developed for this pathway using an ion exchange technique, to improve the photocatalytic efficiency for the degradation of RhB dye pollutant according to J. Yu et al. [278]. while X. Hui Guan et al. prepared hierarchical CuS/ZnS nanocomposite through hydrothermal method having photocatalytic and microwave absorption capacity and it has shown photocatalytic efficiency at 4% Zn doped CuS [279]. Y. Zhang et al. used one-pot synthesis to prepare graphene modified CuS nanocomposite to investigate the degradation of methylene blue dye

[280]. K. Joyjit et al. demonstrated methylene blue degradation in the absence of light using CuS nanostructure catalysts [94].

Copper sulphide doped with transition metals and its composite formation is a fascinating topic since it can exhibit novel physicochemical properties and is potential for the creation of nanostructures with advanced functions. The inclusion of dopant and substitution of nanomaterial could function as electron trap and can improve its properties[281]. Further, a metal ion doped can affect the electronic structure and transition probabilities of the nanomaterial. Pristine and doped CuS nanoparticle has been synthesized by various Chemical methods such as solvo thermal methods, hydro thermal methods, sol gel methods, ball milling, physical vapour deposition and sputtering[282].

Graphene is a single layer of  $sp^2$ -hybridized carbon atoms arranged in a two-dimensional hexagonal lattice. GO has a significant number of hydrophilic functional groups on its surface and can be interspersed in water. GO is now being used to prepare many graphene-based nanocomposites. GO is also a potential material for electric, photonic, and optoelectronic devices due to its good electrical conductivity, flexibility, and optical transparency[283]. However, developing Zn.CuS/GO composite in a facile and cost-effective way is still challenged to produce.

To the best of our knowledge, Zn dopedCuS/GO nanocomposite with photocatalytic performance and antimicrobial agent have not yet been studied in terms of academic and applied interest. In this work Zn doped CuS has been synthesized and on the other hand GO has been prepared by Hammers method and both have been mixed mechanically. The Nanocomposite has been employed in the photodegradation of Rhodamine B. We encountered that Zn doped CuS with GO nanoparticles has better photocatalytic performance and stability than pristine host lattice of CuS; This could be due to photoinduced charge transfer and electron hole separation being efficient.

## **8.2 Experimental Section**

### **8.2.1 Chemicals and Reagents**

All the chemicals used were of analytical grade and of high purity and were used with further purification. Copper acetate  $Cu (CO_2CH_3)_2 \cdot 2H_2O$ , Zinc chloride  $ZnCl_2$ , and Sodium Sulfide  $Na_2S$  were obtained from Sigma Aldrich. All the solution were prepared in double distilled water.

### **8.2.2 Characterization**

FTIR spectrum of nanocomposite was used to determine the composition and chemical bonds by measuring the absorption or emission of the infrared spectrum using Fourier-transform infrared spectroscopy (FTIR) (SHIMADZU IRAFFINITY). The as-prepared Zn-CuS nanoparticles were examined using various characterization techniques. Scanning electron microscopy (SEM) with an EDX attachment A Seifert 3003 TT was used to know the morphological and chemical composition of the synthesised samples. X-ray diffractometer with Cu-K radiation at 1.542 wavelength was used to investigate structural properties and estimate crystallite size from XRD patterns. The optical absorption was measured using a JASCO-V-670 spectrophotometer.

### **8.2.3. Synthesis of Zn doped CuS**

The Synthesis was performed by using Analytical grade chemicals with deionized water serving as the reaction medium. The Zn doped CuS nanoparticles were developed using a Facile Co-precipitation method.  $\text{Cu}(\text{CO}_2\text{CH}_3)_{22}\text{H}_2\text{O}$  and  $\text{Na}_2\text{S}$  were dissolved in aqueous media at a concentration of 0.2 M with a stoichiometric ratio of 1:1 and stirred for more than 25 minutes before adding 0.005 (5% Zn dopant)  $\text{ZnCl}_2$ . The anionic solution of sodium sulphide precursors was then gradually incorporated into the Cu and Zn solutions in a burette. 0.5ml of (EDTA) was used as capping agent to prevent agglomeration of reagents and control size of the prepared nanostructures. The resulting precipitate was washed with deionized water and methanol and dehydrated at 110°C for 8 hours, yielding high-quality QDs.

### **8.2.4 Synthesis of GO**

Hummer's method was employed to synthesize Graphene oxide nanoparticle as previously reported[284]. In brief, Graphite powder(1g) was used as starting material treated with concentrated  $\text{H}_2\text{SO}_4$ (16.3ml) and  $\text{NaNO}_3$ (1g 0.5 wt eq). To keep the temperature in an ice bath below 20°C,  $\text{KMnO}_4$  (3g) solution was slowly added to the reaction mixture. The reaction was then heated at 30°C for 5 h and diluted with deionised water(130ml) producing exothermic 98°C. Another exotherm was produced by adding more water (150 mL) and 30%  $\text{H}_2\text{O}_2$  (3 mL). The addition of a 30%  $\text{H}_2\text{O}_2$  solution confirmed the completion of the reaction. Acetone and then deionized water were used to wash the resulting mixture. The graphite oxide was sonicated for 30 minutes in a water-ethanol solution after filtering and drying to create GO nanosheets.

### **8.2.5 Synthesis of Zn.CuS/GO**



Utilizing the oxidation of powdered graphite, Hummers' method produces GO. By using a modified precipitation method, including the Ex-situ method, the GO/Zn.CuS composites were created as shown in **Figure 1**. Usually, 20 ml of dimethylformamide had a 0.05g of as-prepared GO dispersed in it after 30 minutes of ultrasonication, then 0.12g of Zn.CuS was added and stirred continuously for 1 hour at room temperature. Filtered, heated deionized water and absolute ethanol were used to wash the finished product multiple times, and it was then dried at 60°C for 12 hours.

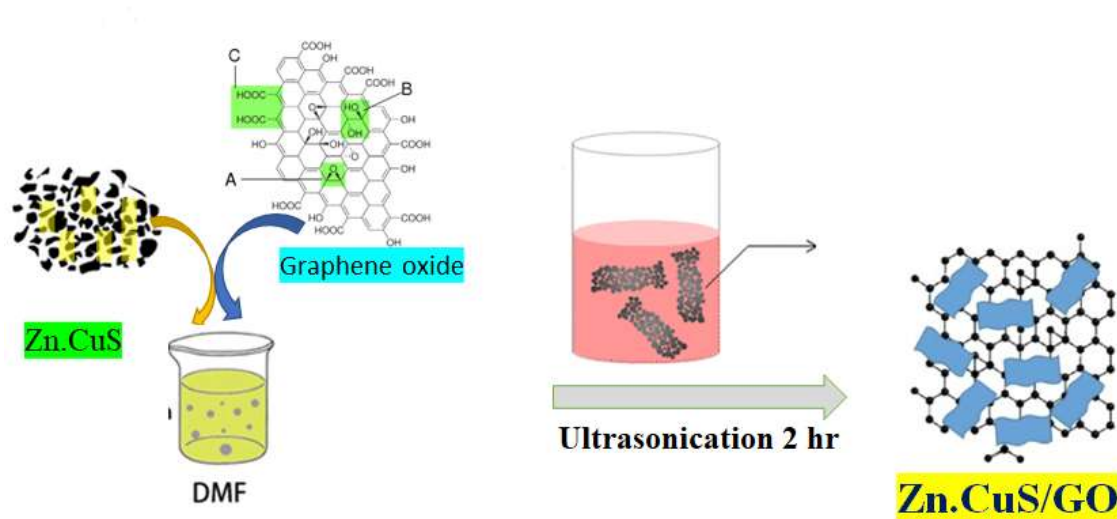


**Figure 1.** Schematic representation of synthesis of Zn. CuS/GO

## 8.3 Results and Discussions

### 8.3.1. Structure and Morphology

The XRD of sample was recorded in order to assess the crystalline purity of the nanomaterial as well as crystalline size of Zn doped CuS. **Figure 2.** depicts the XRD patterns of Zn.CuS, GO and Zn.CuS-GO composite. The obtained diffraction peaks could be well indexed with hexagonal Zn doped CuS phase. The standard diffraction patterns observed in the representative XRD pattern of Zn.CuS were at  $2\theta = 27.2, 27.7, 29.4, 32.0, 33.0, 48.2, 52.8,$  and  $59.4$  corresponds to the (1 0 0), (1 0 1), (1 0 2), (1 0 3), (0 0 6), (1 1 0), (1 0 3), and (5 3 3) reflections of Zn doped CuS (JCPDS No. 06-0464). All of the diffraction patterns are well matched to hexagonal Zn.CuS and size of Zn.CuS was found to be 8-10nm indicating of formation of Zn doped CuS Quantum Dot. Furthermore, the XRD analysis revealed the appearance of a sharp peak at  $2\theta = 10.8$  that corresponded to the (0 0 1) planes of GO with crystalline size 9-13nm. The XRD plot of Zn.CuS/GO was plotted and the presence of

diffraction values of Zn.CuS and GO peaks indicate successful preparation of nanocomposite material. The good agreement between the observed pattern confirmed the successful preparation of Zn.CuS/GO. The crystalline peaks are substantially narrower than the typical peaks, indicating the creation of larger crystallites. The diffraction peaks were correlated with the hexagonal CuS crystal phase. The average crystallite size has been estimated using the Debye-Scherrer formula as mentioned below[285].

$$D = 0.9\lambda/\beta \text{ Cos}\theta \quad (1)$$

In this equation, D stands for crystallite size (nm), X-ray wavelength ( $\lambda$ ),  $\beta$  is full width at half maximum, and  $\theta$  is angle of diffraction (radian). The average crystalline size was found to be 8-20nm.

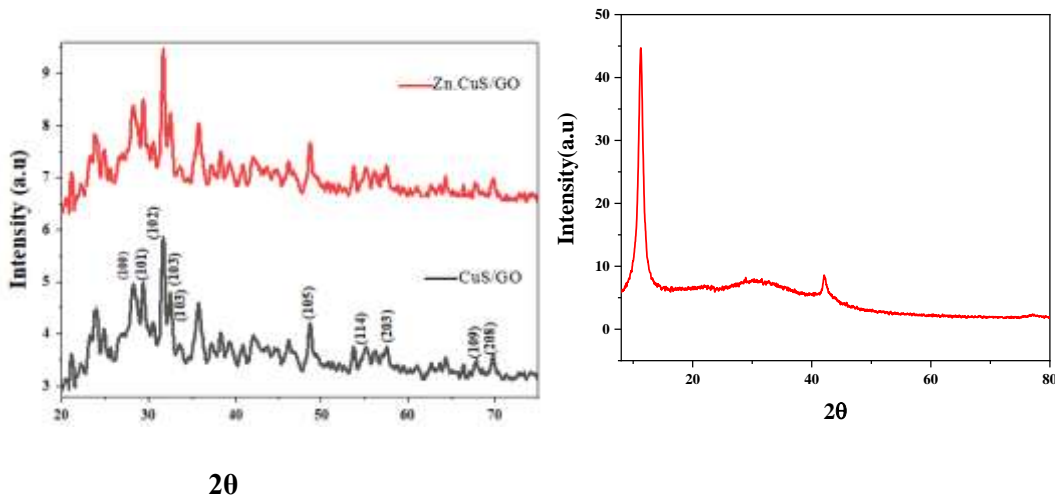


**Figure 2.** XRD analysis of GO nanosheets, Zn-CuS QDs and Zn-CuS-GO nanocomposite

The characteristic SEM images of Zn doped CuS, GO and Zn.CuS-GO nanocomposite are shown in **Figure 3**. FESEM analysis was used to examine the morphologies of Zn-doped CuS and GO samples. The FESEM image of the Zn doped CuS reveals Quantum Dots with irregular shapes and clear edges in the size range of 9-10 nm were discovered. Surface morphology deformation suggests the presence of defect centres and non-uniform growth. The layered structure of synthesised GO with nanometer sizes was clearly confirmed by the SEM image, indicating the formation of GO sheets. When GO was added to the reaction, however, monodispersing, nanosized and uniform elliptical nanoparticles could be produced. GO acted as a surface modifier as well as a support for nanoparticle growth. The prepared composite's morphology clearly demonstrates immobilised cubic Zn doped CuS crystals on layered GO

sheets that are evenly distributed without agglomeration. This demonstrates that the crystalline nature of the Zn.CuS crystals is well preserved even after the addition of graphene oxide during the preparation of the composite and that they are evenly dispersed between the graphene oxide sheets and results confirms increased surface area of Zn.CuS/GO with average size 50 nm and size was also confirmed by using Zeta potential analysis.

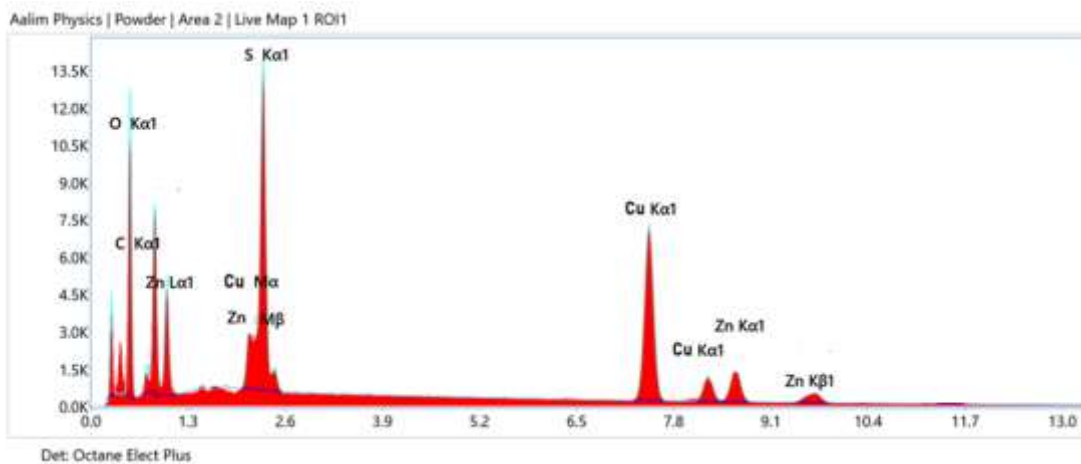
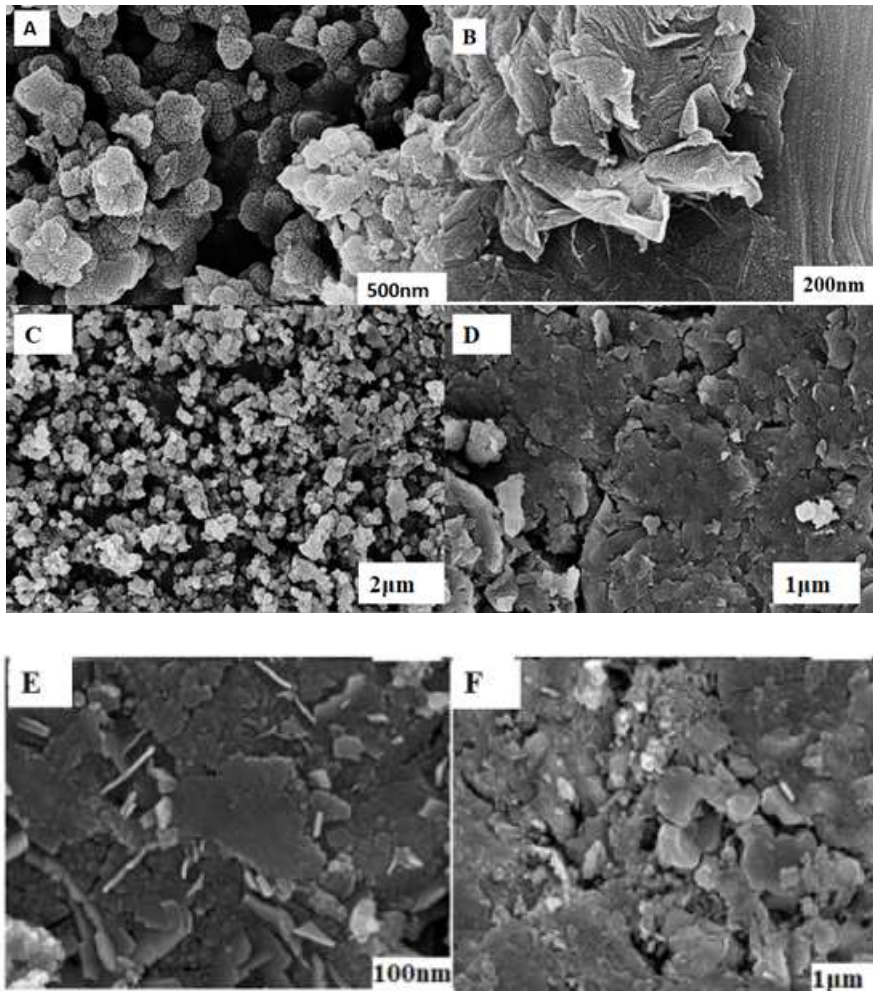


**Figure 3.** SEM and EDS analysis of (a, b) GO, (c, d) Zn-CuS and (E,F) Zn-CuS-GO.

Fourier transform infrared spectroscopy of ZnCuS-GO composite in the range 400 to 4000  $\text{cm}^{-1}$  was used to confirm the FTIR spectrum of the prepared nanomaterial shown in **Figure 4**. The corresponding peaks of GO exhibit strong and broad OH stretching vibration bands at 3399  $\text{cm}^{-1}$ , presence of 1597  $\text{cm}^{-1}$  band peak reveals presence of carboxyl group CHO stretching bond, Due to extensive oxidation OH deformation vibration bands at 1404  $\text{cm}^{-1}$ , and CO stretching vibration bands at 1109  $\text{cm}^{-1}$  in its FTIR spectrum[286]. The broad and significant absorption peaks in the FTIR spectra of Zn doped CuS nanoparticles are attributed to the symmetric stretching vibrations of the hydroxyls of the adsorbed water content, which produce significant intermolecular hydrogen bonded O-H stretches at about 3405  $\text{cm}^{-1}$ . The bending mode at 1644  $\text{cm}^{-1}$  may be due to bending of  $\text{H}_2\text{O}$ . a relatively small lower intensity absorption peak at 1089  $\text{cm}^{-1}$  was discovered and linked to stretching vibrations in the C=S bond[287]. The host lattice's Zn.CuS-S bond corresponds to the absorption peak at 628  $\text{cm}^{-1}$ .

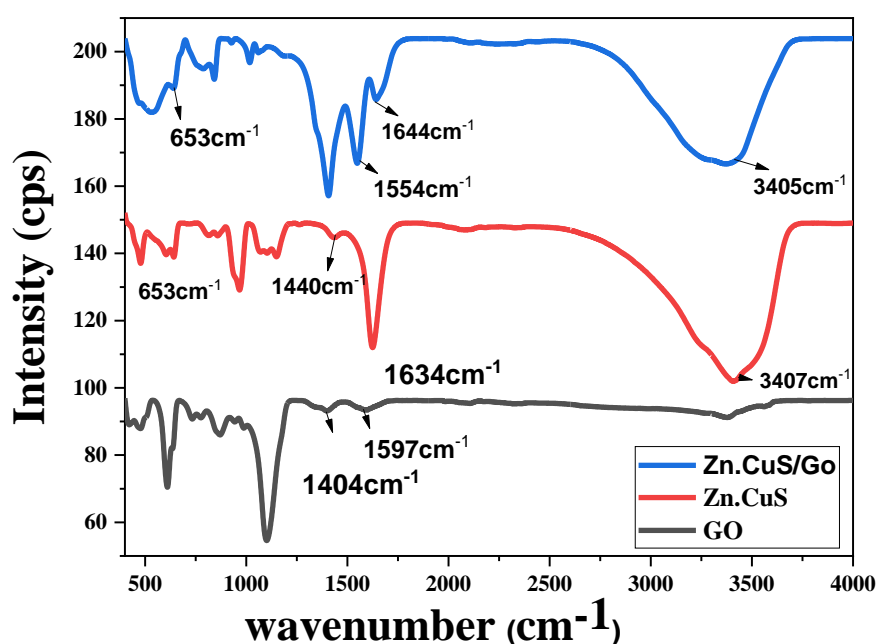


**Figure 4.** FTIR spectrum of GO, Zn/CuS and Zn.CuS/GO nanomaterial.

#### 8.4 TGA-DSC

Thermogravimetric analysis is a technique in which a substance is degraded in the presence of heat, causing molecules' bonds to break. As the reaction progresses, the sample weight initially

declines slowly, then comparatively faster over a relatively small temperature range, and then levels off as the reactants run out. The kinetics parameters have the greatest influence on the TGA curve's form[288]. **Figure 5.** shows TGA thermogram and TGA as function of temperature. The thermograms for ZnCuS-GO composites made by mixing powdered metals and salts of various transition metals were recorded. It is evident from the TGA curve that the primary decomposition of composite begins at its melting point of 235°C with steady weight reduction. with constant weight loss up to 330 °C, displaying approximately 69.45% weight loss. Gradual decomposition with a 12.01% weight loss occurs between 350 and 450C. It's possible that the initial weight loss (4%) was caused by the breakup of big polymer chains into smaller bits. CuS suffers a minor mass loss at 92 °C due to the partial conversion of CuS to Cu<sub>2</sub>S. It was followed by a mass increase of 20% at 369°C, which is attributed to the oxidation of copper sulphides (CuS, Cu<sub>2</sub>S) to CuSO<sub>4</sub>, and another 10% mass increase due to CuO. The two exothermic peaks in DSC curve reveals glass transition and melting crystallization of our nanocomposite.

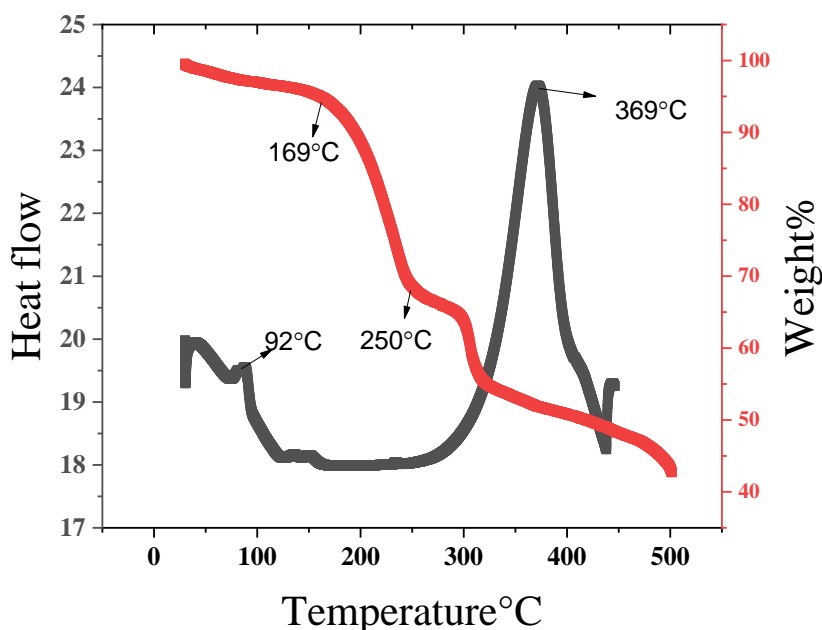


**Figure 5.** TGA-DSC characterization of ZnCuS-GO nanocomposite

### 8.5 Electrochemical Characterization

Cyclic Voltametric (CV) tests were recorded at a potential range from -0.003 and 0.003 V in 1M Na<sub>2</sub>SO<sub>4</sub> solution with scan rate 5-10mVs<sup>-1</sup>. The presence of redox peaks reveals electrochemical nature of crystalline Zn.CuS/GO. The peaks of Zn.CuS/GO (up to the second

cycle) for the half-cell configuration at the scan rate of  $5 \text{ mVs}^{-1}$  are shown in **Figure 6**. We deduced from the results that the conversion reaction's two peaks are discovered for the cathodic process at 0.0012 and 0.0016V. The reversible reaction of the cathodic process is represented by the anodic process peak values of -0.009 and -8.2V. The presence of peaks indicates super capacitive nature of our sample in aqueous electrolyte[289].

We explore electrochemical impedance spectroscopy (EIS), which is shown in Figure, in order to provide a clearer understanding of the electrochemical analysis of Zn.CuS/GO nanocomposite material. The Nyquist plots illustrates the frequency response of the electrode system and are plots of the imaginary component ( $Z$ ) of impedance versus the real component ( $Z$ ). The semicircle of the Nyquist plot in high frequency region is evidence to resistance and linearity at lower frequency is attributed to the less charge-transfer resistance ( $R_{ct}$ ) which enumerates capacitive behaviour. Similarly, The Bode plot which is plotted between frequency at x axis and impedance and phase angle at y axis shows that resistance decreases with increasing frequency. Figure 5(c) shows that the phase of the tail is approximately 15, indicating that the electrode material is capacitive. The cyclic voltametric curve can be used to calculate the electrodes' specific capacitance using the following formula[290].

$$C_s = \frac{Q}{\Delta V \cdot m}$$

$C_s$  is the specific capacitance represented by the specific capacitance based on the mass of electrode materials,  $m$  is the mass of the active material (g) in the electrodes,  $Q$  is the anodic and cathodic charges on each scanning and  $\Delta V$  is the applied voltage window of the voltametric curve ( $\text{mVs}^{-1}$ ).

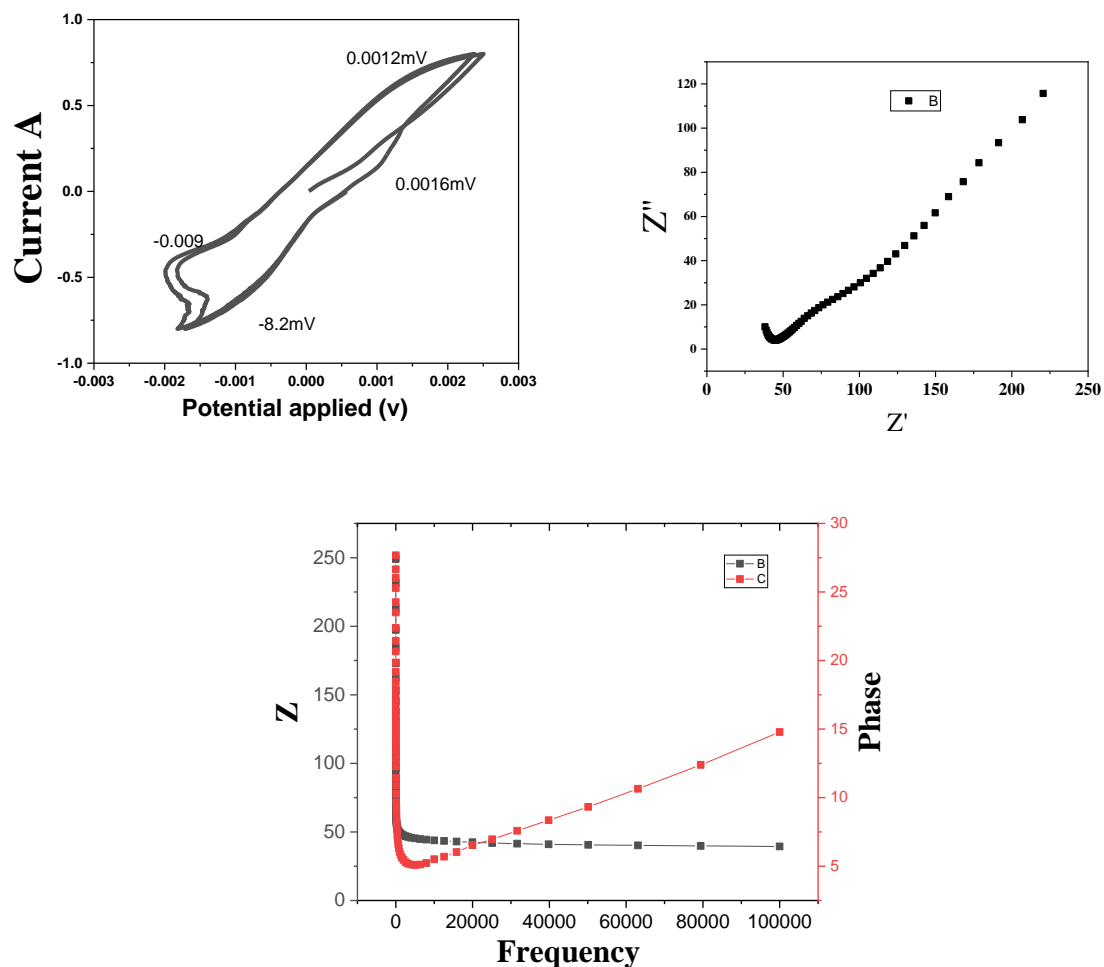
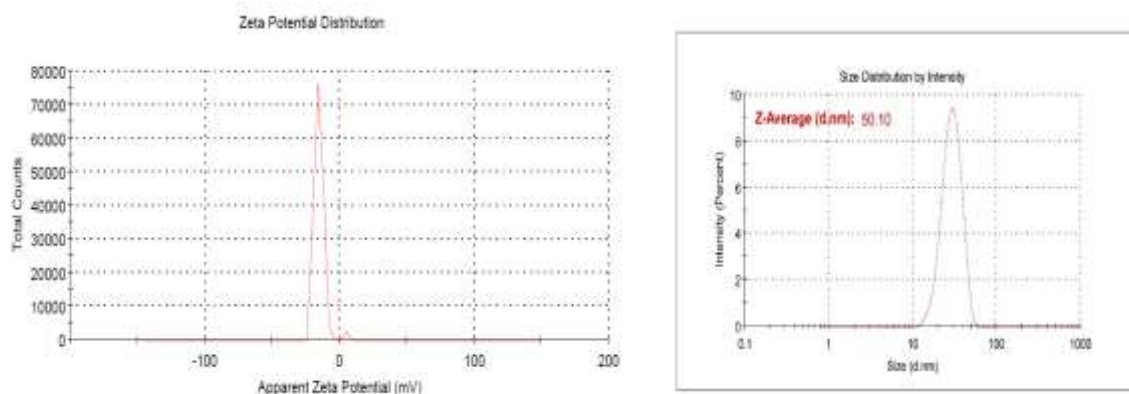


**Figure 6.** Electrochemical study of Zn.CuS-GO nanocomposite using CV and Impedance spectroscopy.

### 8.6 Zeta Potential

The zeta potential of the dispersed nanoparticles was ascertained through electrophoretic light scattering as show in **Figure 7**. The particles' zeta potentials were found to be -15.2mV by electrophoresis. The carboxylate groups on the surface of the particles give them a strong negative zeta potential, and they have shown excellent stability. Zeta potential measurements as well as particle size distributions were performed on each sample in a comparable manner. The zeta potential not only indicates the electrical charge on the particle surface, but it also indicates the stability of colloidal dispersions[291]. The average particle size is about 185 nm, which is larger than the untreated particle size (50-52 nm), indicating more agglomeration of Zn/CuS-GO. The particle size distributions' results agree with the zeta potential measurement.





**Zeta Potential (mV): -15.2**

**Zeta Deviation (mV): 4.16**

**Figure 7.** Zeta potential of Zn.CuS/GO composite.

### 8.7 Optical properties

**Figure 8.** Tauc plot was used to calculate optical band gap of Zn.CuS QDs and Zn.CuS/GO composite. The optical  $E_g$  of  $Cu_2S$  film has been found to be 2.37 eV, which is less than the energy gap observed in this study. The quantum size effect is responsible for the larger energy gap observed in this study than in previous studies. When GO is substituted for CuS, the band gap value (blue shift) increases from 2.7 eV to 3.4 eV. Zn interstitials provide an additional charge carrier due to the Burstein-Moss effect, which causes the energy gap to shift to the higher energy side. The enhanced  $E_g$  permitted the replacement of GO with Zn.CuS.



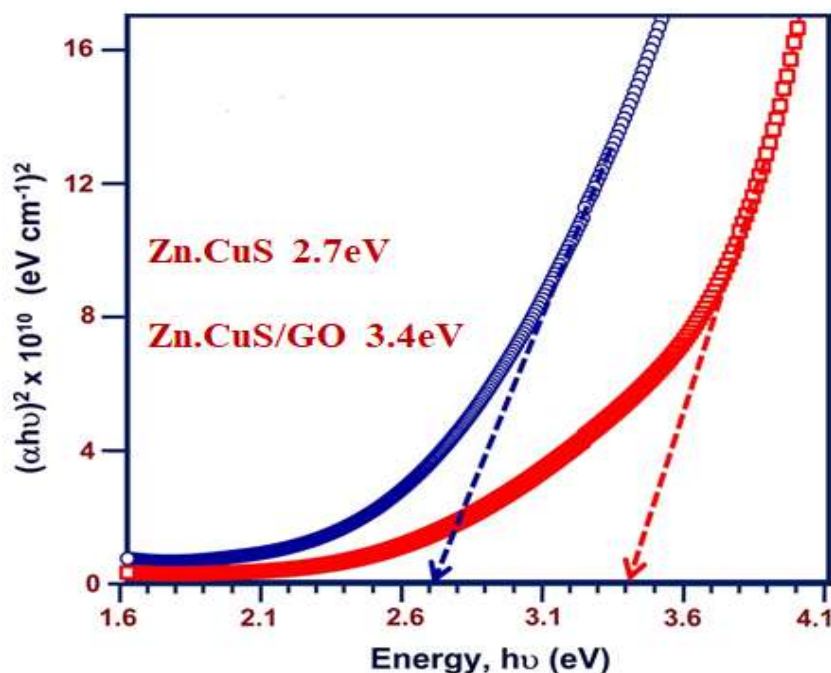


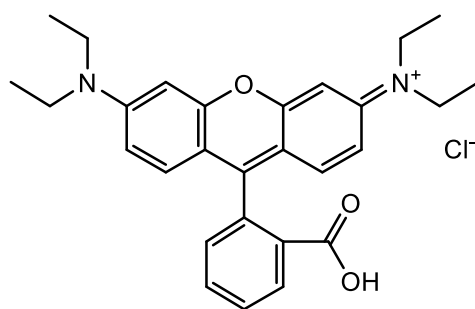
**Figure 8.** A plot between  $(\alpha h\nu)^2$  versus  $h\nu$  of Zn.CuS and Zn.CuS/GO nanocomposite for energy gap calculation.

### 8.8. Photocatalytic Efficiency and effect of different parameters

The photocatalytic activity of synthesised nanomaterials was investigated at room temperature using the photodegradation method with Rhodamine blue (Rh-B) in presence of a visible-light source. The Rh-B solution was made prior to light irradiation by dissolving 3 mg of dye in 300 ml DI water, then adding a predetermined amount of catalyst and agitating the mixture in absence of light to stabilize and equilibrate Rh-B adsorption onto the surface of the catalyst. 10 mL of the suspension from the reaction mixture was taken, centrifuged, and subjected to UV-vis spectrometer analysis. The reaction mixture was stirred (Shimadzu 3100 PC spectrophotometer, Japan). With an increase in Rh-B degradation, the absorption fell. The photodegradation % of Rh B was calculated using the following equation[292]:

$$D (\%) = (C_1 - C_0) / C_0 \times 100$$

where  $C_0$  and  $C_1$  are the concentrations of Rh B at time 0 and time  $t$  (s), respectively, and  $t$  is the time of degradation. Centrifugation was used to recover the catalyst, which was then re-dispersed in the Rh B solution for the recycling tests.



**Structure of Rhodamine b**

### **I. Effect of pH**

The pH of various pollutants appears to have a major role in the photocatalytic process. The influence of pH on Rhodamine-B was investigated in the pH range 3-12 shown in **Figure 9D**. The pH of the solution is adjusted before to adsorption and is not controlled during the reaction. The cationic Rhodamine-B dye uptake by Zn.CuS/GO nanocomposite was found to be greater at lower pH, i.e., pH-3 It could be because polarisation of the adsorbent occurs in acidic medium, resulting in dye aggregation on the adsorbent surface.

### **II. Catalyst dosage effect**

To investigate the effect of catalyst dosage on photodegradation efficiency, photocatalytic experiment was conducted by varying the amount of Zn.CuS/GO nanoparticles from 20mg to 50mg in a stock solution 0.3g/L of Rhodamine B while maintaining a contact time of 120 minutes. As shown in **Figure. 9A**, the photodegradation efficiency increases with increasing catalyst dosage. The crystalline nature of the sample and the increase in catalyst dose both contribute to increasing active surface area and reducing the rate at which the photogenerated electron and hole pair produced by a visible light source recombine.

### **III. The impact of initial dye concentration**

The effect of initial Rhodamine B concentration on degradation rate was investigated by varying the initial dye concentration from 10ppm to 50ppm while maintaining a constant catalyst concentration shown in **Figure 9B**. As the concentration of dye increases, the degradation efficiency decreases due to a decrease in the number of photons approaching the catalyst surface active site, which further inhibits the rate of formation of holes, hydroxyl radicals, and super oxide ions ( $O^{2-}$ ).



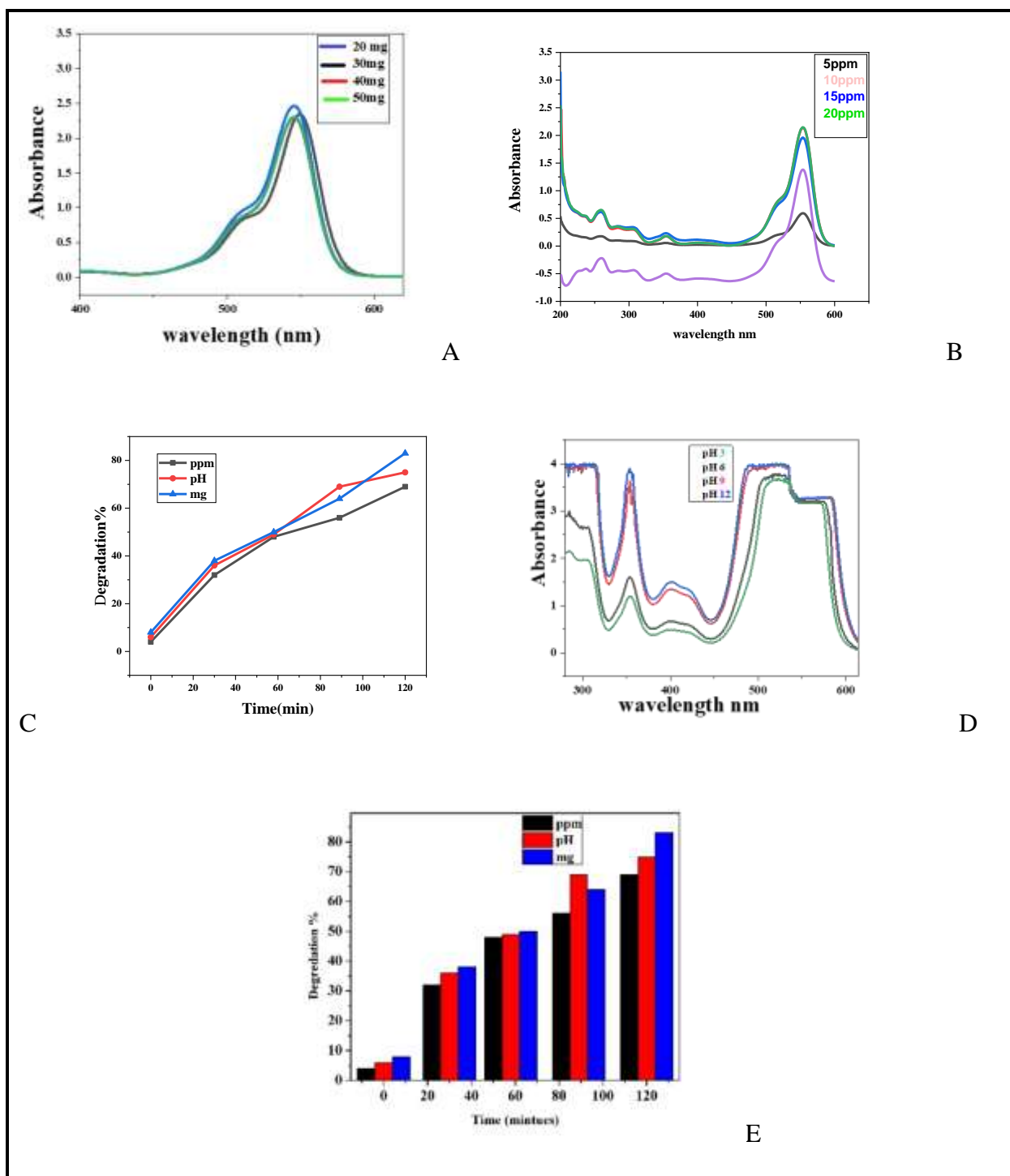


**Figure 9.** Effect of catalyst at different concentrations, at different pH values, varying pollutant concentration and different time period.

### 8.9 Minimum Inhibitory Concentration

Fungal strain such as *Candida albicans* (MTCC183) *Candida parapsilosis* (MTCC998) *Candida tropicalis* (MTCC184) were used in this study. The strains were tested against Zn.CuS/GO and

GO. At 4°C, all organisms were kept afloat on plates of sabouraud dextrose (SD) agar. Using the broth micro-dilution assay, the MIC of Zn.CuS/GO against fungal bacteria was determined. The standardisation of test organisms was done to meet the 0.5 McFarland requirement. 100 L of SD broth were put into a 96-well microtiter plate. A 50 mg/ml stock solution of each compound was prepared in DMSO and diluted to give final concentrations of 25, 12.5, 6.5, 3.125, 1.565, 0.781, 0.390, 0.195, 0.097, 0.048, 0.024 mg/mL were added on the A1 to A11 wells, also same for B to F wells. The positive control was amphotericin-B (stock 128 g/mL). The plates were incubated at 37°C overnight. The MIC was defined as the lowest amount of extract that, after 24 hours of incubation, prevented the microorganisms from showing visible growth[293].

#### 4.1. Minimum fungicidal concentration

The MICs of Zinc doped copper sulphide (Zn-CuS/GO) were determined from the MIC broth microdilution assay, after MIC determination. 15µL from each not-growing well were spot inoculated onto fresh SD agar plates. The number of colonies was counted after the plates had been incubated for 24-48 hours. The MFC was determined to be the lowest concentration of doped Zn.CuS/GO that killed at least 99.9% of the inoculums as measured by initial viable counts. (ales).

#### 4.2. Antifungal activity

Antifungal activity Zn.CuS/GO were quantitatively tested by determining their MIC and MBC against *Candida albicans* (MTCC183) *Candida parapsilosis* (MTCC998) *Candida tropicalis* (MTCC184). Results of MIC and MFC tests shown in Table 1 confirmed high antifungal activity of Zn.CuS against *Candida albicans* (MTCC183) *Candida parapsilosis* (MTCC998) *Candida tropicalis* (MTCC184) as compared to GO.

**Table 1:** Minimum Inhibitory Concentration (MIC) and Minimum fungicidal concentration (MFC) of Doped Zn.CuS/GO and GO.

MIC of Doped Zn.CuS/GO and GO			
Test Fungus	Test antifungal agent		
	Doped Zn.CuS/GO (mg/ml)	GO (mg/ml)	Amphotericin-B (µg/mL)
<i>Candida albicans</i>	0.048	6.5	0.5

<i>Candida parapsilosis</i>	0.097	6.5	0.5
<i>Candida tropicalis</i>	0.024	6.5	0.25
<b>MFC of Doped Zn.CuS/GO and GO</b>			
<b>Test Fungus</b>	<b>Test antifungal agent</b>		
	<b>Doped Zn.CuS/GO (mg/ml)</b>	<b>GO (mg/ml)</b>	<b>Amphotericin-B (µg/mL)</b>
<i>Candida albicans</i>	0.390	12.5	1
<i>Candida parapsilosis</i>	0.781	12.5	1
<i>Candida tropicalis</i>	0.048	12.5	1`

## 8.10 RESULTS

### 8.10.1 Antifungal activity

Antifungal activity of Zinc doped copper sulphide (Zn.CuS) and Graphene oxide (Z) were quantitatively tested by determining their MIC and MBC against *Candida albicans* (MTCC183) *Candida parapsilosis* (MTCC998) *Candida tropicalis* (MTCC184). Results of MIC and MFC tests shown in Table 1 confirmed high antifungal activity of Zinc doped copper sulphide (Zn.CuS) against *Candida albicans* (MTCC183) *Candida parapsilosis* (MTCC998) *Candida tropicalis* (MTCC184) as compare to Graphene Oxide.

### 8.11 Conclusion

The Zn doped CuS QDs and its fabrication with GO were successfully synthesised using simple, cost-effective chemicals in water as the reaction medium. The XRD, SEM, EDX and FTIR demonstrated successful inclusion of Zn and GO in Hybrid composite. The UV absorption illustrates the band gap energy of nanocomposite to be in the range of 2.7-3.4 eV. The nanocomposite prepared was found to effective in photodegradation of the Rh-B dye in aqueous media in visible light. The best system achieves 82% degradation in the removal of dye with a concentration of 10ppm with 50mg nanocomposites in 120 minutes. The nanocomposite is proposed as a potential candidate for removing organic pollutants from water using simple photocatalysis at room temperature. The antimicrobial study also revealed that the nanocomposites are effective against certain pathogens.

## 8.12 References

- [272] E. Hannachi, Y. Slimani, M. Nawaz, R. Sivakumar, Z. Trabelsi, R. Vignesh, S. Akhtar, M.A. Almessiere, A. Baykal, G. Yasin, Preparation of cerium and yttrium doped ZnO nanoparticles and tracking their structural, optical, and photocatalytic performances, *Journal of Rare Earths*. (2022). <https://doi.org/10.1016/j.jre.2022.03.020>.
- [273] M. Jouyandeh, S.S.M. Khadem, S. Habibzadeh, A. Esmaeili, O. Abida, V. Vatanpour, N. Rabiee, M. Bagherzadeh, S. Irvani, M.R. Saeb, R.S. Varma, Quantum dots for photocatalysis: synthesis and environmental applications, *Green Chem.* 23 (2021) 4931–4954. <https://doi.org/10.1039/D1GC00639H>.
- [274] A.H. Reshak, Quantum dots in photocatalytic applications: efficiently enhancing visible light photocatalytic activity by integrating CdO quantum dots as sensitizers, *Phys. Chem. Chem. Phys.* 19 (2017) 24915–24927. <https://doi.org/10.1039/C7CP05312F>.
- [275] N. Nasseh, F.S. Arghavan, N. Daglioglu, A. Asadi, Fabrication of novel magnetic CuS/Fe<sub>3</sub>O<sub>4</sub>/GO nanocomposite for organic pollutant degradation under visible light irradiation, *Environ Sci Pollut Res Int.* 28 (2021) 19222–19233. <https://doi.org/10.1007/s11356-020-12066-3>.
- [276] C. Behera, R. Samal, A.K. Panda, C.S. Rout, S.L. Samal, Synthesis of flower and biconcave shape CuS: Enhancement of super-capacitance properties via Ni–CuS nanocomposite formation, *Solid State Sciences.* 117 (2021) 106631. <https://doi.org/10.1016/j.solidstatesciences.2021.106631>.
- [277] Y. Fazli, S.M. Pourmortazavi, I. Kohsari, M. Sadeghpur, Electrochemical synthesis and structure characterization of nickel sulfide nanoparticles, *Materials Science in Semiconductor Processing.* 27 (2014) 362–367. <https://doi.org/10.1016/j.mssp.2014.07.013>.
- [278] J. Yu, J. Zhang, S. Liu, Ion-Exchange Synthesis and Enhanced Visible-Light Photoactivity of CuS/ZnS Nanocomposite Hollow Spheres, *J. Phys. Chem. C.* 114 (2010) 13642–13649. <https://doi.org/10.1021/jp101816c>.
- [279] X.-H. Guan, P. Qu, X. Guan, G.-S. Wang, Hydrothermal synthesis of hierarchical CuS/ZnS nanocomposites and their photocatalytic and microwave absorption properties, *RSC Adv.* 4 (2014) 15579–15585. <https://doi.org/10.1039/C4RA00659C>.
- [280] Y. Wang, L. Zhang, H. Jiu, N. Li, Y. Sun, Depositing of CuS nanocrystals upon the graphene scaffold and their photocatalytic activities, *Applied Surface Science.* 303 (2014) 54–60. <https://doi.org/10.1016/j.apsusc.2014.02.058>.
- [281] N. Ahmad, A.M. Alshehri, I. Ahmad, M. Shkir, P.M.Z. Hasan, A.A. Melaibari, In doping effect on the structural, morphological, optical and enhanced antimicrobial activity of facilely synthesized novel CuS nanostructures, *Surfaces and Interfaces.* 27 (2021) 101536. <https://doi.org/10.1016/j.surfin.2021.101536>.
- [282] A. Sudhaik, P. Raizada, S. Rangabhashiyam, A. Singh, V.-H. Nguyen, Q. Van Le, A.A.P. Khan, C. Hu, C.-W. Huang, T. Ahamad, P. Singh, Copper sulfides based photocatalysts for degradation of environmental pollution hazards: A review on the recent catalyst design concepts and future perspectives, *Surfaces and Interfaces.* (2022) 102182. <https://doi.org/10.1016/j.surfin.2022.102182>.
- [283] L. Li, S. Xue, P. Xie, H. Feng, X. Hou, Z. Liu, Z. Xu, R. Zou, Facile Synthesis and Characterization of GO/ZnS Nanocomposite with Highly Efficient Photocatalytic Activity, *Electron. Mater. Lett.* 14 (2018) 739–748. <https://doi.org/10.1007/s13391-018-0082-6>.
- [284] N.I. Zaaba, K.L. Foo, U. Hashim, S.J. Tan, W.-W. Liu, C.H. Voon, Synthesis of Graphene Oxide using Modified Hummers Method: Solvent Influence, *Procedia Engineering.* 184 (2017) 469–477. <https://doi.org/10.1016/j.proeng.2017.04.118>.
- [285] C.V.V.M. Gopi, S. Sambasivam, R. Vinodh, H.-J. Kim, I.M. Obaidat, Nanostructured Ni-doped CuS thin film as an efficient counter electrode material for high-performance quantum dot-sensitized solar cells, *J Mater Sci: Mater Electron.* 31 (2020) 975–982. <https://doi.org/10.1007/s10854-019-02608-y>.

- [286] D. Kala, T.K. Sharma, S. Gupta, V. Verma, A. Thakur, A. Kaushal, A.V. Trukhanov, S.V. Trukhanov, Graphene Oxide Nanoparticles Modified Paper Electrode as a Biosensing Platform for Detection of the htrA Gene of *O. tsutsugamushi*, *Sensors*. 21 (2021) 4366. <https://doi.org/10.3390/s21134366>.
- [287] S.M.H. Al-Jawad, A.A. Taha, A.M. Redha, N.J. Imran, INFLUENCE OF NICKEL DOPING CONCENTRATION ON THE CHARACTERISTICS OF NANOSTRUCTURE CuS PREPARED BY HYDROTHERMAL METHOD FOR ANTIBACTERIAL ACTIVITY, *Surf. Rev. Lett.* 28 (2021) 2050031. <https://doi.org/10.1142/S0218625X20500316>.
- [288] S.Y. Attia, S.G. Mohamed, Detergent-free micelle-assisted synthesis of carbon-containing hexagonal CuS nanostructures for efficient supercapacitor electrode materials, *Electrochimica Acta*. 407 (2022) 139918. <https://doi.org/10.1016/j.electacta.2022.139918>.
- [289] S. Asaithambi, V. Balaji, M. Karuppaiah, P. Sakthivel, K. Muhil Eswari, R. Yuvakkumar, P. Selvakumar, D. Velauthapillai, G. Ravi, The electrochemical energy storage and photocatalytic performances analysis of rare earth metal (Tb and Y) doped SnO<sub>2</sub>@CuS composites, *Advanced Powder Technology*. 33 (2022) 103442. <https://doi.org/10.1016/j.apt.2022.103442>.
- [290] S.I. El-Hout, S.G. Mohamed, A. Gaber, S.Y. Attia, A. Shawky, S.M. El-Sheikh, High electrochemical performance of rGO anchored CuS nanospheres for supercapacitor applications, *Journal of Energy Storage*. 34 (2021) 102001. <https://doi.org/10.1016/j.est.2020.102001>.
- [291] K.B.A. Ahmed, V. Anbazhagan, Synthesis of copper sulfide nanoparticles and evaluation of in vitro antibacterial activity and in vivo therapeutic effect in bacteria-infected zebrafish, *RSC Advances*. 7 (2017) 36644–36652. <https://doi.org/10.1039/C7RA05636B>.
- [292] M.S. Rohokale, D. Dhaliya, T. Sathish, V. Vijayan, N. Senthilkumar, A novel two-step co-precipitation approach of CuS/NiMn<sub>2</sub>O<sub>4</sub> heterostructured nanocatalyst for enhanced visible light driven photocatalytic activity via efficient photo-induced charge separation properties, *Physica B: Condensed Matter*. 610 (2021) 412902. <https://doi.org/10.1016/j.physb.2021.412902>.



## **Chapter 9.**

### **Conclusion and Future Recommendations**

#### **9.1. Chapter overview**

This thesis is designed to explore the development of efficient Molecular imprinted polymer embedded with Quantum Dots and their application in photodegradation. The identified research objectives are adequately emphasized and the relevant discussion are included in the previous chapters. This chapter covers the final part of the thesis. Research conclusion.

This chapter outlines the approaches taken to address the research aim. It also summarises the major findings specifically to each research objective, with emphasis on the key novelties. Finally, this chapter discusses the research limitations and provides limitations for further research that builds on the finding of this work.

#### **9.2. Summary of the Key findings**

This research addresses the rational design and development of novel MIPs embedded with QDs for the photodegradation of pollutants. A series of experiments were carried out to complete the following research objectives

- Research Objective 1; To develop Molecular imprinted polymers (MIPs) through [6]-gingerol extracted from natural herbs.
- Research Objective 2: To synthesize sulphide based pristine and doped Quantum Dots.
- Research objective 3: To develop MIPs embedded by Quantum Dots and polymers.
- Research objective 4: To evaluate potential applications of MIPs in environmental aspects

Based on the extensive literature review conducted as discussed in chapter 2, the research gaps related to the development of MIPs hybrid composite. Literature survey on Synthesis of Molecular imprinted polymer embedded with Quantum Dots has been done successfully and application in the photocatalysis has been identified. Currently no scientific work has been done on the use of [6]-gingerol as template and its implication in environment aspects. Also, it is noted that there is a lack of studies on ensuring charge transfer kinetics in MIPs composite. Furthermore, very less analysis has been done on the application of MIPs hybrid composite in the photocatalytic degradation.

After identifying the area of research, Chapter 1 we have discussed various polymerization methods for the synthesis of MIPs and Quantum dots. The chapter 2 we have performed the extraction of [6]-gingerol for MIPs preparation which was prepared through Insitu polymerization and embedded with QDs through insitu polymerization.

### **9.3. Recommendations for future work**

Although the extensive research work has been conducted on the development of MIPs composite, their long-term stability still poses one of the biggest challenges. Further improvement strategies, such as the use of technologically advanced synthesis techniques and the employment of highly stable surface co-catalysts, should be researched to bridge the gap and progress towards scaling up and commercialisation. Besides, it is also believed that the areas of research on the use of hybrid materials, such as synergistic inorganic-organic composite and metal-organic frameworks, should be delved deeper into, especially on their potential application in elevating the water splitting application, hydrogen production, electrocatalysis and photocatalytic degradation.

On the other hand, to advance the development of the MIPs composite and its application in organic molecule degradation. It is suggested that there should be a paradigm shift from a material-oriented research focus to an overall integrated system research focus. The construction of MIPs composite and aits application requires technical considerations, especially in the aspects of system parameters and components. For instance, further research studies can be conducted on the optimum pH environment and the influence of catalyst. A comparative study on the synthesis of MIPs embedded with Quantum Dots and the effect of doping constituents on the synthesis of QDs.

## PUBLICATIONS

- [1] A.Q. Malik, T. ul G. Mir, O. Amin, M. Sathish, D. Kumar, Synthesis, characterization, photocatalytic effect of CuS-ZnO nanocomposite on photodegradation of Congo red and phenol pollutant, *Inorganic Chemistry Communications*. 143 (2022) 109797. <https://doi.org/10.1016/j.inoche.2022.109797>.
- [2] A.Q. Malik, H. Singh, A. Kumar, R. Aepuru, D. Kumar, T. ul G. Mir, Q. ul Ain, A.A. Bhat, A. Mubayi, An Overview on Magnetic Separable Spinel as a Promising Materials for Photocatalysis and Waste Water Treatment, *ES Energy & Environment*. Volume 19 March 2023 (2022) 744. <https://www.espublisher.com/journals/articledetails/744>
- [3] T. ul Gani Mir, A.Q. Malik, J. Singh, S. Shukla, D. Kumar, An Overview of Molecularly Imprinted Polymers Embedded with Quantum Dots and Their Implementation as an Alternative Approach for Extraction and Detection of Crocin, *ChemistrySelect*. 7 (2022) e202200829. <https://doi.org/10.1002/slct.202200829>.
- [4] A.Q. Malik, P.E. Lokhande, D. Kumar, J. Mooney, A. Sharma, T.U. Gani Mir, Photocatalytic and Antimicrobial activity study for Cadmium Sulphide Quantum Dots, *Materials Research Innovations*. 0 (2023) 1–9. <https://doi.org/10.1080/14328917.2023.2180570>.
- [5] Rani, S., Sharma, A., Tabasum, S. et al. Highly Efficient Photocatalytic Properties of La-Doped ZnO over Pristine ZnO for Degradation of 2-Chlorophenol from Aquatic Agriculture Waste. *Chemistry Africa* (2023). <https://doi.org/10.1007/s42250-023-00630-6>.
- [6] A. Q. Malik, T.U.G. Mir, D. Kumar, An Overview of Paclitaxel and Molecular Imprinted Polymers Capped with Quantum Dots as an Alternative Approach for Paclitaxel Extraction and Detection, *Current Materials Science*. 15 (2022). <https://doi.org/10.2174/2666145415666220928111532>.
- [7] Mir, T.u.G., Shukla, S., Malik, A.Q. et al. Microwave-assisted synthesis of N-doped carbon quantum dots for detection of methyl orange in saffron. *Chem. Pap.* 77, 3641–3649 (2023). <https://doi.org/10.1007/s11696-023-02726-2>.
- [8] Bhat AA, Shakeel A, Rafiq S, Farooq I, Malik AQ, Alghuthami ME, Alharthi S, Qanash H, Alharthy SA. *Juglans regia* Linn.: A Natural Repository of Vital Phytochemical and Pharmacological Compounds. *Life*. 2023; 13(2):380. <https://doi.org/10.3390/life13020380>
- [9] A. Malik, R. Thakur, Extraction, characterization and detection of [6]-gingerol from Ginger

officinale, (2022).

[10] Malik, A.Q., Mir, T.u.G., Kumar, D. et al. A review on the green synthesis of nanoparticles, their biological applications, and photocatalytic efficiency against environmental toxins. *Environ Sci Pollut Res* (2023). <https://doi.org/10.1007/s11356-023-27437-9>

[11] Tabasum, S & Sharma, A & Rani, S & Chaudhary, S & Malik, Azad & Kumar, D & Deshpande, T. (2023). Prolific fabrication of lanthanum oxide with graphitic carbon/graphene oxide for enhancing photocatalytic degradation of carbofuran from aqueous solution. 2023. <https://doi.org/10.31788/RJC.2023.1628266>.

[12] Mir, T., Malik, A.Q., Shukla, S. et al. Facile Synthesis of S-doped Carbon Quantum Dots and Their Application in the Detection of Sudan I in Saffron. *J Fluoresc* (2023). <https://doi.org/10.1007/s10895-023-03264-6>

[13] Suman Rani, Sahima Tabasum, Ajit Sharma, Pawanpreet Singh, Prabal Pratap Singh, Priyanka Reehl, Azad Qayoom Malik, Deepak Kumar & Hema Singh (2023) Effects of Cu substitution on photocatalytic performance of ZnO nanorods synthesized via hydrothermal route for the degradation of chlorobenzene, *International Journal of Environmental Analytical Chemistry*, <https://doi.org/10.1080/03067319.2023.2215695>

[14] Malik, A.Q., Tabasum, S., Rani, S. *et al.* Fluorescent CdS QDs Modified With Molecular Imprinted Polymer for the Photodegradation of Imidacloprid and Buprofezin Pesticides Under Visible Light. *J Inorg Organomet Polym* (2023). <https://doi.org/10.1007/s10904-023-02753-2>

[15] I. Mir, Q. Ain, T. Qadir, A. Malik, S. Jan, S. Shahverdi, S. Nabi, A review of semicarbazone-derived metal complexes for application in biomedicine and related fields, *Journal of Molecular Structure*. (2023) 136216. <https://doi.org/10.1016/j.molstruc.2023.136216>.

[16] Suman Rani, Sahima Tabasum, Ajit Sharma, Pawanpreet Singh, Prabal Pratap Singh, Priyanka Reehl, Azad Qayoom Malik, Deepak Kumar & Hema Singh (2023) Effects of Cu substitution on photocatalytic performance of ZnO nanorods synthesized via hydrothermal route for the degradation of chlorobenzene, *International Journal of Environmental Analytical Chemistry*, <https://doi.org/10.1080/03067319.2023.2215695>

[17] A.Q. Malik, T.U.G. Mir, Q.U. Ain, D. Kumar, Facile synthesis of ZnS and Ni doped ZnS quantum dots and enhanced photocatalytic property of Ni doped ZnS nanoparticle, *AIP Conference Proceedings*. 2800 (2023) 020045. <https://doi.org/10.1063/5.0163406>.

[18] S. Tabasum, S. Rani, A. Thakur, M. Sindhu, K.S. Maan, Upasana, V. Patel, Sarika, A. Malik, P. Gajbhiye, D. Kumar, A. Sharma, Photo-catalytic detoxification of chlorpyrifos pesticide from the aquatic environment using g-C<sub>3</sub>N<sub>4</sub> doped with GO nano-composite, in: 2023: p. 020079. <https://doi.org/10.1063/5.0163717>.